



Bayesian characterization of seismic sources : from earthquake initiation to seismic ruptures

Emmanuel Caballero Leyva

► To cite this version:

Emmanuel Caballero Leyva. Bayesian characterization of seismic sources: from earthquake initiation to seismic ruptures. Earth Sciences. Université de Strasbourg, 2022. English. NNT: 2022STRAH003 . tel-03813880

HAL Id: tel-03813880

<https://theses.hal.science/tel-03813880v1>

Submitted on 13 Oct 2022

HAL is a multi-disciplinary open access archive for the deposit and dissemination of scientific research documents, whether they are published or not. The documents may come from teaching and research institutions in France or abroad, or from public or private research centers.

L'archive ouverte pluridisciplinaire **HAL**, est destinée au dépôt et à la diffusion de documents scientifiques de niveau recherche, publiés ou non, émanant des établissements d'enseignement et de recherche français ou étrangers, des laboratoires publics ou privés.

ÉCOLE DOCTORALE 413

Institut Terre et Environnement de Strasbourg UMR 7063

THÈSE présentée par :

Emmanuel CABALLERO LEYVA

soutenue le : 05 juillet 2022

pour obtenir le grade de : **Docteur de l'université de Strasbourg**

Discipline/ Spécialité : Sciences de la Terre / Géophysique

Caractérisation bayésienne de la source sismique: De l'initiation du séisme à la rupture sismique

THÈSE dirigée par :
M. RIVERA Luis

Professeur, Université de Strasbourg

RAPPORTEURS :
Mme. LYON-CAEN Hélène
Mme. SOCQUET Anne

Directrice de recherche CNRS, Laboratoire de Géologie, ENS
Physicienne CNAP, ISTerre

AUTRES MEMBRES DU JURY :
M. BLETERY Quentin
M. BODIN Thomas
Terre, Planètes, Environnement
M. LENGLINÉ Olivier

Chargé de recherche IRD, Géoazur
Chargé de recherche CNRS, Laboratoire de Géologie de Lyon:
Maitre de conférences, Université de Strasbourg

INVITÉS : M. Duputel Zacharie

Université de Strasbourg

Thèse de doctorat

en vue de l'obtention du titre de Docteur de l'Université de
Strasbourg

École doctorale des Sciences de la Terre et de l'Environnement
N° 413

Discipline: Géophysique

Bayesian characterization of seismic sources: from earthquake initiation to seismic ruptures

Présentée par Emmanuel Caballero Leyva

Préparée à l'Institut Terre et Environnement de Strasbourg UMR 7063

- dirigée par:

Luis Rivera directeur
Zacharie duputel co-encadrant

- présentée et soutenue publiquement le **05 juillet 2022**

- devant le jury composé de:

Hélène, Lyon-Caen rapporteuse, directrice de recherche CNRS, Laboratoire
de Géologie, ENS, Paris
Anne, Socquet rapporteuse, physicienne CNAP, ISTerre
Quentin, Bletery examinateur, chargé de recherche IRD, Géoazur
Thomas, Bodin examinateur, chargé de recherche CNRS, Laboratoire
de Géologie de Lyon: Terre, Planètes, Environnement
Olivier, Lengliné examinateur, maitre de conférences, Université de
Strasbourg

Bayesian characterization of seismic sources: from earthquake initiation to seismic ruptures.

par Emmanuel Caballero Leyva

Extended Abstract

Earthquakes are complex natural phenomena that can cause numerous victims and significant material damage. Earthquake characterization is essential to understand the mechanisms that cause such events and the physics behind the seismic rupture. Like many areas of geophysics, the determination of the seismic source is affected by various uncertainties and by the fact that there are often several models that can explain the observations. The general objective of this thesis is to conduct a thorough study of different aspects of the earthquake source. First, I focus on the initiation phase of earthquakes, trying to glimpse details about the early stages of seismic ruptures. Specifically, I analyze the initiation phase of the 2017 $M_W = 6.9$ Valparaíso earthquake. This earthquake is an interesting event since it was preceded by a transient displacement accompanied by a foreshocks sequence. We demonstrate that the pre-seismic GNSS signal cannot be explained by the co-seismic and post-seismic displacements induced by foreshocks. We show that this earthquake was probably preceded by an aseismic preslip on the fault. In the second part of my thesis, I focus on the detailed characterization of the coseismic slip distribution associated with large earthquakes. In particular, I examine the 2014 $M_W = 8.3$ Illapel earthquake, where several works have led to different conclusions about the rupture process. We use a Bayesian slip inversion approach to characterize this seismic rupture. We account for observational and forward model uncertainties. In particular, we focus on the impact of Earth model inaccuracies on the forward problem, especially for seismological data. Our kinematic models indicate a high complexity in the source process, with significant slip at shallow depth supported by breakdown energy estimates, and an asperity encircling rupture that have been previously suggested by high-frequency back-projection studies.

Initiation phase of the 2017 Valparaíso earthquake

Transient deformations before several large earthquakes have been observed using geodetic measurements. These signals are observed simultaneously with the occurrence of foreshock sequences (i.e., seismic events preceding the mainshock). Two conceptual models have been proposed to explain the role of foreshocks during the initiation phase of earthquakes [Mignan, 2014]. A first model considers the existence of an aseismic slip gradually accelerating until the occurrence of the main earthquake. According to this model, this pre-seismic slip would trigger the foreshocks. The second model considers a cascade of foreshocks. In this model, the foreshock events are triggered by each other (through static stress transfer and possibly through postseismic slip) and contribute to a cascade of random ruptures, finally leading to the mainshock. This model could explain the pre-seismic geodetic signals by considering that these observations actually correspond to the accumulation of coseismic and postseismic deformation associated with each foreshock.

On 24 April 2017, a $M_W = 6.9$ earthquake occurred offshore Valparaíso in the central segment of the Chilean subduction zone (33.089°S, 72.116°W, 21:38:28 UTC; Centro Sismológico Nacional, CSN). This earthquake was preceded by a transient

displacement observed by continuous GNSS stations four days before the mainshock [Ruiz et al., 2017]. Foreshocks were also identified with a significant increase in seismicity rate two days before the mainshock (Figure 1). The primary goal of this study is to assess the relative contribution of seismic and aseismic slip during the few days preceding the 2017 Valparaíso earthquake.

For this purpose, we process GPS data of 68 stations in the South America region. Figure 1-b shows the resulting horizontal displacements for stations in the vicinity of the study area. There is a clear westward motion starting about three days before the mainshock. In Figure 1-b, we can see that the slope of the cumulative seismicity rate does not change significantly at the beginning of the transient displacement. The increase in seismicity rate is delayed by about 24 hours and only starts with the occurrence of a $M_W = 6.0$ foreshock on April 23 (purple star in Figure 1-b).

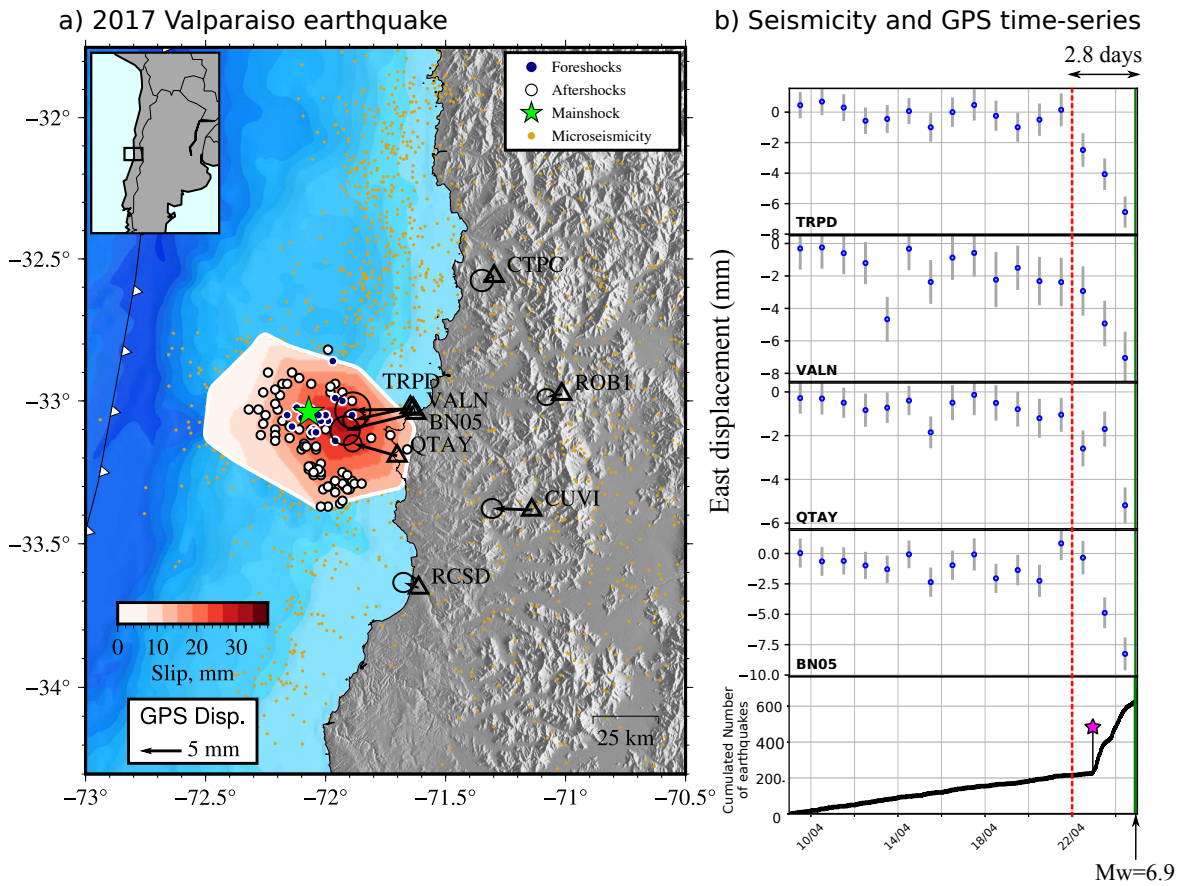


Figure 1: The 2017 Valparaíso earthquake sequence. (a) Earthquake locations including foreshocks (blue circles), mainshock (green star), and aftershocks (white circles). The red colormap indicates the preslip distribution resulting from the inversion of GPS data. The black arrows show the cumulative observed GPS surface displacements (up to one hour before the mainshock). Orange dots indicate the seismicity distribution from 2017/01/01 until 2017/10/05 according to the microseismicity catalog obtained by S. Ruiz et al. (2017). (b) GPS Time-series in the vicinity of Valparaíso. The vertical red dashed line indicates approximate onset of the transient displacement visible on the timeseries. The cumulative number of earthquakes from S. Ruiz et al. (2017) is shown at the bottom of the figure. The purple star represents the largest $M_W = 6.0$ foreshock.

To constrain the contribution of foreshocks to the observed GPS displacement, we estimate Centroid Moment Tensor (CMT) parameters for moderate to large earthquakes during the Valparaíso earthquake sequence (from 2017/04/05 up to 2017/05/30). We use a modified version of the W-phase algorithm adapted to regional distances and the magnitude range of the Valparaíso sequence [Kanamori and Rivera, 2008, Zhao et al., 2017]. Estimated parameters are the deviatoric moment tensor, the centroid location, the centroid time, and the half-duration of an isosceles triangular moment rate function. The resulting CMT catalog is shown in Figure 2.

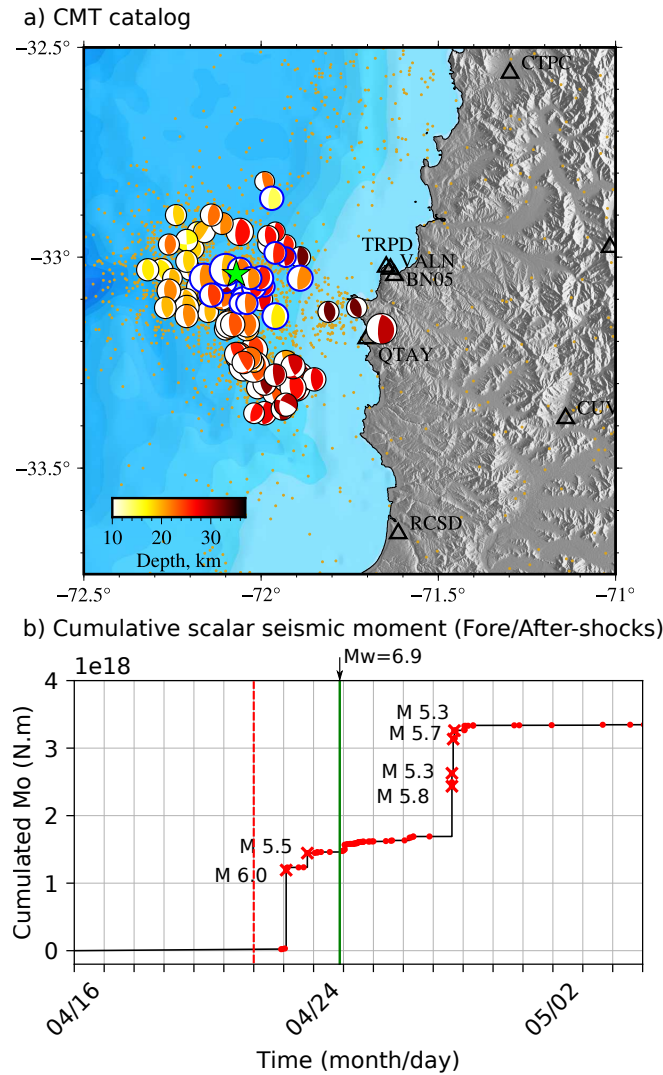


Figure 2: CMT solutions of the 2017 Valparaíso earthquake sequence and cumulative moment (a) CMT solutions of the 2017 Valparaíso earthquake sequence. Focal mechanisms are contoured in blue and black for foreshocks and aftershocks respectively. The size of beach balls scales with the moment magnitude. Color of the compressive quadrants represents the event depth. (b) Cumulative scalar seismic moment of the 2017 Valparaíso sequence. The mainshock scalar moment is not included in this figure. The red dashed line outlines the approximate onset of transient displacements visible on GPS time-series. The green line indicates the origin time.

To evaluate the contribution of foreshocks to observed surface displacements, we calculate synthetic static displacements using our CMT catalog. Synthetics are computed using the CSI package, incorporating the approach of Zhu and Rivera [2002] to compute static displacement in a layered model. The largest foreshock ($M_W = 6.0$) largely dominates the co-seismic contribution to the observed GPS transient, while $M_W < 6.0$ events in our catalog generate relatively small surface displacement. Since the $M_W = 6.0$ foreshock plays an important role in the sequence, we assess uncertainties associated with the corresponding CMT parameters. The posterior ensemble of plausible source locations and moment tensors is appraised using a strategy similar to Sambridge [1999] while accounting for Earth model uncertainty using the approach of Duputel et al. [2012a, 2014].

To evaluate the uncertainty on the predicted co-seismic displacement, we simulate static displacement for each model samples from the $M_W = 6.0$ foreshock. The resulting stochastic co-seismic displacements are shown in Gray in Figure 3a for the closest GPS stations to the mainshock epicenter. Even though we account for uncertainties, the predicted cumulative co-seismic offsets are still significantly smaller than the observed pre-seismic displacements (~ 6 to 8 mm of the east component for the closest stations).

To get a total budget of seismic and aseismic displacement before the mainshock, we compare GPS data one hour before the mainshock with the corresponding cumulative foreshock displacement (Figure 3b). Observed displacements are on average, between 4 and 6 mm larger than co-seismic offsets. Such differences cannot be explained by uncertainties in the observations and the predictions. These results clearly suggest that a significant portion of the observed pre-seismic deformation is actually aseismic and cannot be explained by foreshocks. We estimate that about $51 \pm 11\%$ of the displacement measured at the GPS stations originates from aseismic slip on the fault. The portion of aseismic deformation is consistent between neighboring stations (Figure 3c), suggesting a common source located in the vicinity of the foreshocks.

Finally, we perform two slip inversions: a first slip inversion with the total GPS pre-seismic displacement and another inversion after removing the foreshocks contribution (i.e., aseismic displacement only). The distribution of aseismic preslip spreads toward the west of Valparaíso city with an extension of about 50×90 km and a scalar moment of $M_0 = 3.08 \times 10^{18}$ N.m (i.e., $M_w = 6.26$). This aseismic motion represents about 50% of the moment calculated for the slip model derived from uncorrected GPS data ($M_0 = 5.67 \times 10^{18}$ N.m, Figure 3e). Given the cumulative moment of foreshocks ($M_0 = 1.48 \times 10^{18}$ N.m), we estimate that nearly 70% of the scalar moment released during the preparation phase of the Valparaíso mainshock is aseismic, which is roughly in agreement with estimates from Ruiz et al. [2017]. The smaller portion of aseismic moment derived from the comparison of slip models in Figure 3e-f likely results from the simplistic assumption in Figure 3e that all foreshocks are located on the plate interface.

Different numerical and experimental studies have pointed out the influence of aseismic preslip in the triggering of foreshocks [e.g., Kaneko et al., 2016, McLaskey and Kilgore, 2013]. If such observations apply on natural faults, foreshock locations could potentially inform us about the overall spatial extent of the nucleation

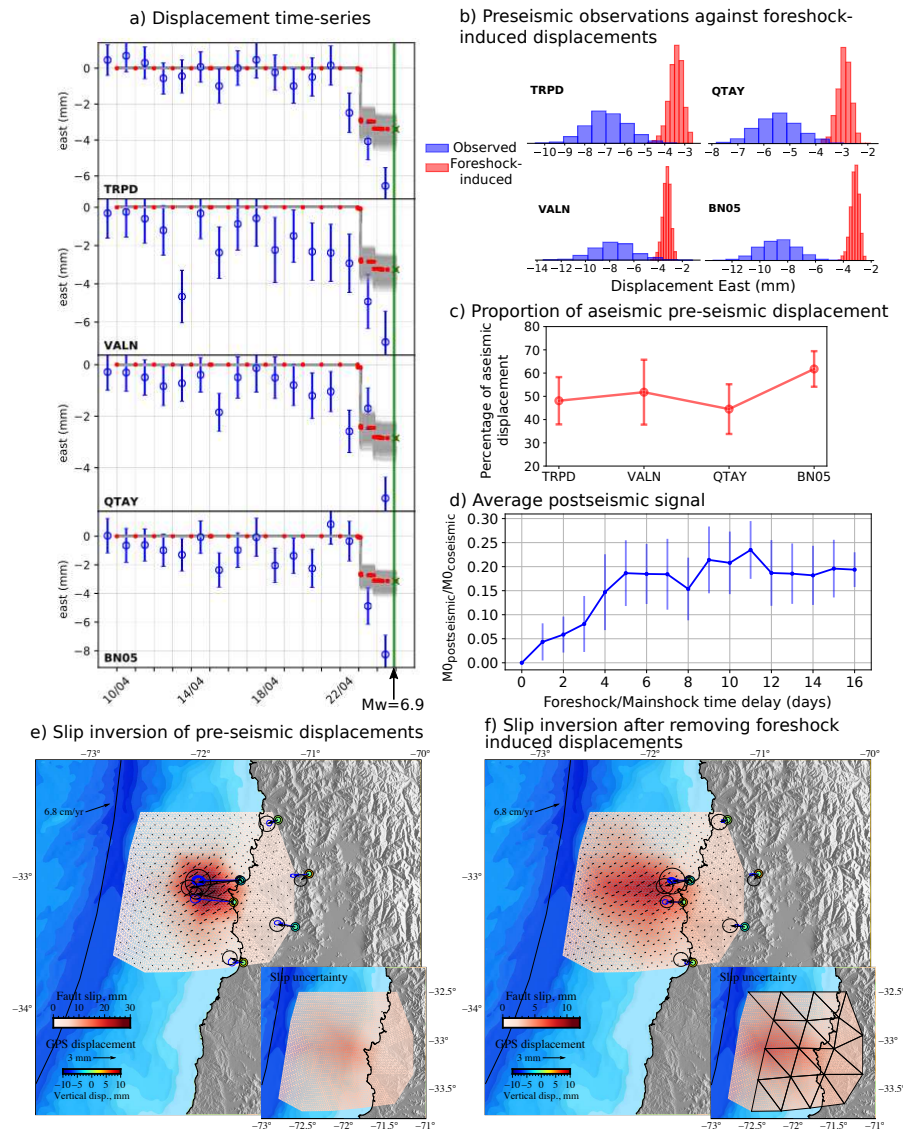


Figure 3: Slip during the Valparaíso foreshock sequence. a) Time series of GNSS data (blue) and stochastic foreshock-induced co-seismic displacement (gray). Red dots represent the average of stochastic co-seismic offsets. Green cross corresponds to the total foreshock displacement, including the contribution of earthquakes below the magnitude of completeness. b) Distributions of observed pre-seismic displacement and predicted cumulative co-seismic offsets caused by foreshocks. Blue histograms represent observations assuming Gaussian uncertainties from standard errors estimated at each station. Red histograms correspond to the posterior distribution of cumulative foreshock-induced co-seismic displacement. c) Percentage of aseismic displacement for each station. d) Average postseismic signal measured on stations TRPD, VALN, BN05 and QTAY. e) Slip inversion of pre-seismic GPS data. f) Slip inversion of GPS data after removing foreshock-induced displacement. Black and blue arrows are observed and predicted horizontal GPS displacements along with their ellipses (representing observational and prediction uncertainties, respectively). Colored circles are observed (outer circles) and predicted (inner circles) vertical displacements from GPS.

zone prior to an earthquake. This idea is in fairly good agreement with our results suggesting a first-order correlation between preslip distribution and the location of foreshocks (Figure 1 and Figure 3). Even if preslip appears to be an important mechanism in the triggering of foreshocks, part of the foreshock activity likely results from cascading phenomena due to stress changes of neighboring events. In addition, we still need to understand why most earthquakes are not preceded by foreshock activity and even less with observable pre-seismic motion.

Revisiting the 2015 $M_W=8.3$ Illapel earthquake. From kinematic rupture inversion to rupture dynamics.

The 2015 $M_W = 8.3$ Illapel earthquake is one of the largest recorded earthquakes in the Chilean subduction zone [Ruiz et al., 2016]. Previous studies indicate a rupture propagation from the hypocenter to the superficial part of the fault, with a maximum slip varying between 10 and 16 meters [see e.g., Heidarzadeh et al., 2016, Melgar et al., 2016b, Tilmann et al., 2016]. The slip distributions previously reported show a significant disparity, depending on the data used and the adopted inversion technique. Thus for some models, the slip magnitude in the surface part of the fault is almost zero, while others show significant slip at shallow depth.

In this work, we revisit the 2015 $M_W = 8.3$ Illapel earthquake by combining a comprehensive data set including permanent and survey GPS stations corrected for post-seismic and aftershock signals, ascending and descending Sentinel 1A InSAR images along with high-rate GPS and doubly integrated strong-motion waveforms. We perform a kinematic slip inversion following a Bayesian approach in which we obtain an ensemble of models and not a unique solution. The inversion is done using the cascading capability of the Altar code (<https://altar.readthedocs.io>). This approach can incorporate different uncertainty assessments: observational uncertainties and forward modeling uncertainties. The observational uncertainty is commonly related to errors in measurements, while forward modeling uncertainties are associated with imperfect modeling. In the present study, we focus on accounting uncertainties due to Earth structure modeling. Specifically, we evaluate the impact of inaccuracies in the 1D velocity model employed to compute static and kinematic predictions. We follow three different schemes to map Earth model uncertainty into prediction uncertainty. The first straightforward approach is to empirically calculate the prediction uncertainty covariance matrix C_p using predictions computed for a large number of random Earth models $\Psi_i, (i = 1, \dots, n)$. Then, we follow the first-order approximation approach proposed by Duputel et al. [2014]. Finally, we explore the possibility of using a 2nd order perturbation approach, previously introduced by Caballero et al. [2021] for point source inversions. In Figure 4, we compare the diagonal of the C_p matrix for HRGPS and strong motion stations. The 1st and 2nd order C_p matrices seem to capture the main features of the

empirical C_p matrix. However, there are differences that could play an important role in complex inversion problems. For this reason, in the next section, we explore the impact of the C_p matrix on the coseismic models of the 2015 $M_W = 8.3$ Illapel earthquake.

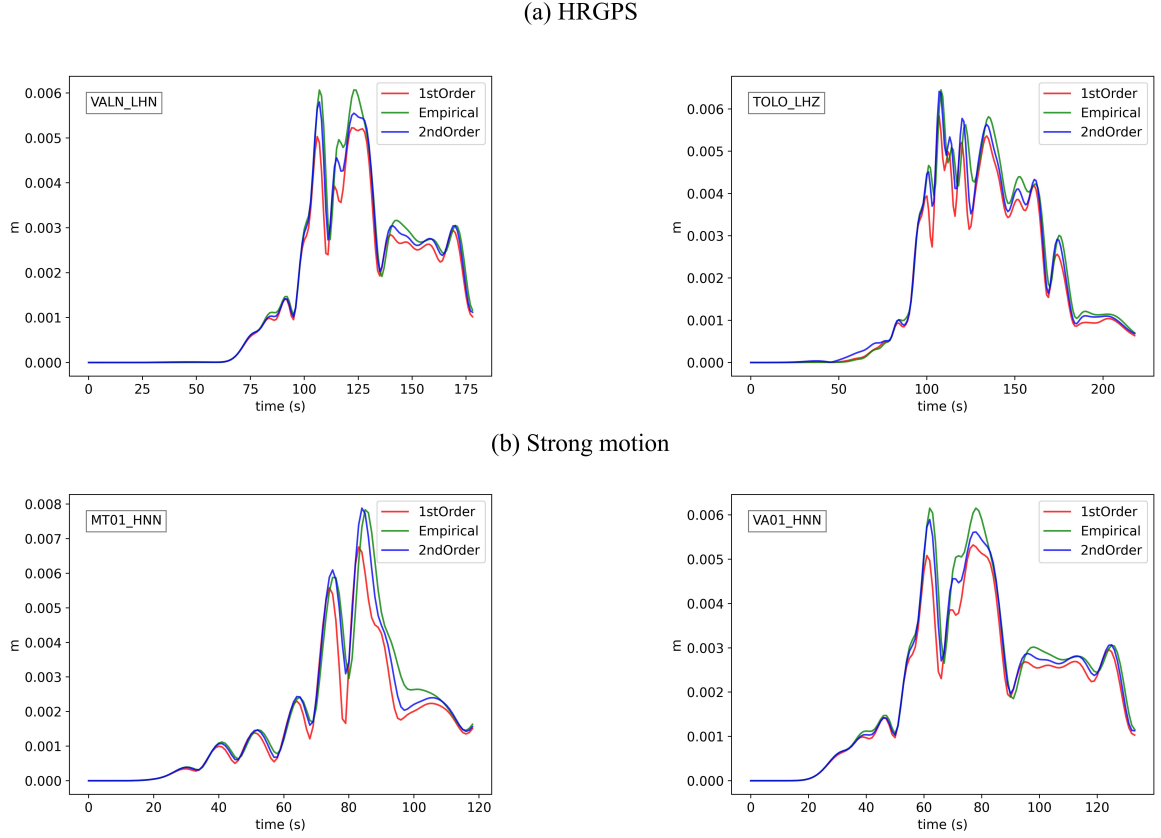


Figure 4: Covariance matrix comparison for HRGPS records (a) and Strong Motion stations (b). The green line represents the diagonal of the empirical covariance matrix (i.e., the matrix created from an ensemble of models). The red and blue line represents the diagonal of the matrix calculated using the 1st and 2nd order approximation approach.

We obtain a static slip inversion *a posteriori* PDF model and use the distribution samples as seeds to make three different joint inversions: one using an empirical C_p matrix and two others using a C_p matrix calculated using the first and second order perturbation approach. The final slip distributions obtained using these different approaches are shown in Figure 5. The solution based on 1st order C_p shows a slip patch that is quite compact at shallow depth, while the shallow slip is more broadly distributed when considering 2nd order or empirical C_p matrices. This results in a larger peak slip value for the 1st order C_p solution (21.07 \pm 2.03 m), while empirical C_p (17.35 \pm 1.96 m) and 2nd order C_p (18.52 \pm 2.74 m) display smaller peak slips.

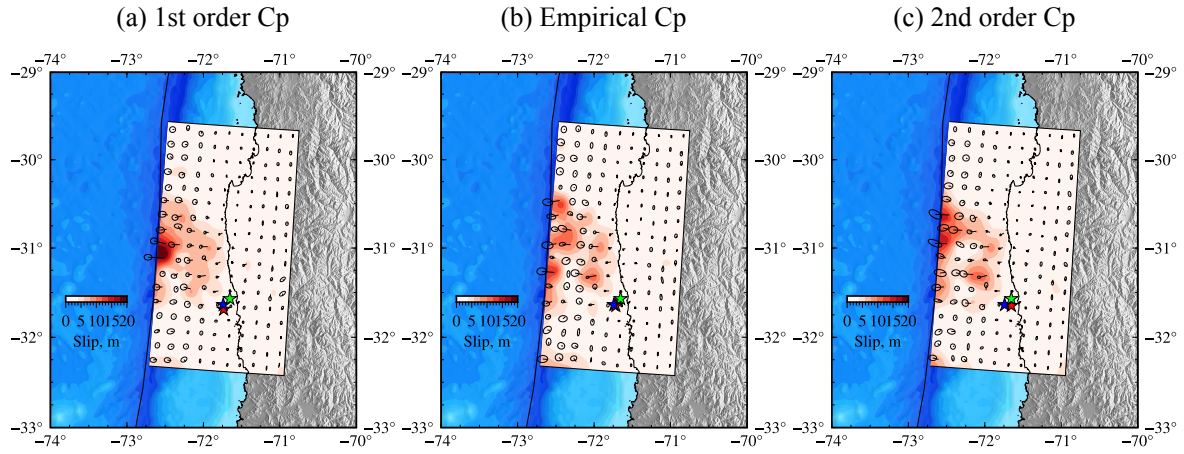


Figure 5: Comparison of co-seismic slip distributions obtained using different prediction error covariances C_p . Red colors are the final slip distributions. Arrows represent the slip directions with their corresponding uncertainty. The red star is the inverted hypocenter location (empirical, 1st, and 2nd order approximation, respectively). The blue star is the CSN hypocenter, and the green star is the USGS hypocenter.

Details of the solution obtained using a 2nd order C_p are shown in Figure 6. Stochastic rupture propagation fronts in Figure 6 (a) suggest a complex rupture pattern. It slowly grows close to the hypocenter, and then propagates northwestward to a shallower area of the subduction interface. Stochastic moment rate functions in Figure 6 (b) indicate an overall rupture duration of 120 seconds approximately. The average scalar seismic moment is $M_0 = 3.20 \times 10^{21} \text{ N} \cdot \text{m}$, i. e., a moment magnitude of $M_W = 8.27$. The centroid time propagation is not homogenous, displaying complex patterns, especially to the west of the hypocenter. We examine individually different aspects of the Illapel earthquake rupture: (i) shallow slip distribution, (ii) observed encircling rupture patterns, and (iii) fracture energy assessed from our posterior ensemble of slip models.

To explore the contribution of shallow slip on the inversion, we perform a static slip inversion imposing the shallow slip to be very small (a small prior in shallow sub faults). In this manner, we obtain a slip model for which the shallow part is significantly different due to the new prior. We compare the difference in tsunami waveform fits. We can see that the solution without shallow slip cannot fit the tsunami waveforms as well as our initial model. The existence of large shallow slips supports the fact that the 2015 event is not a simple repeat of the earthquake that affected the region in 1943 [Tilman et al., 2016]. This is consistent with historical reports indicating that the tsunami generated in 1943 was much smaller than what was observed in 2015. In addition, the differences in the duration of teleseismic body-wave arrivals for both events suggest that the 1943 rupture did not involve shallow slip

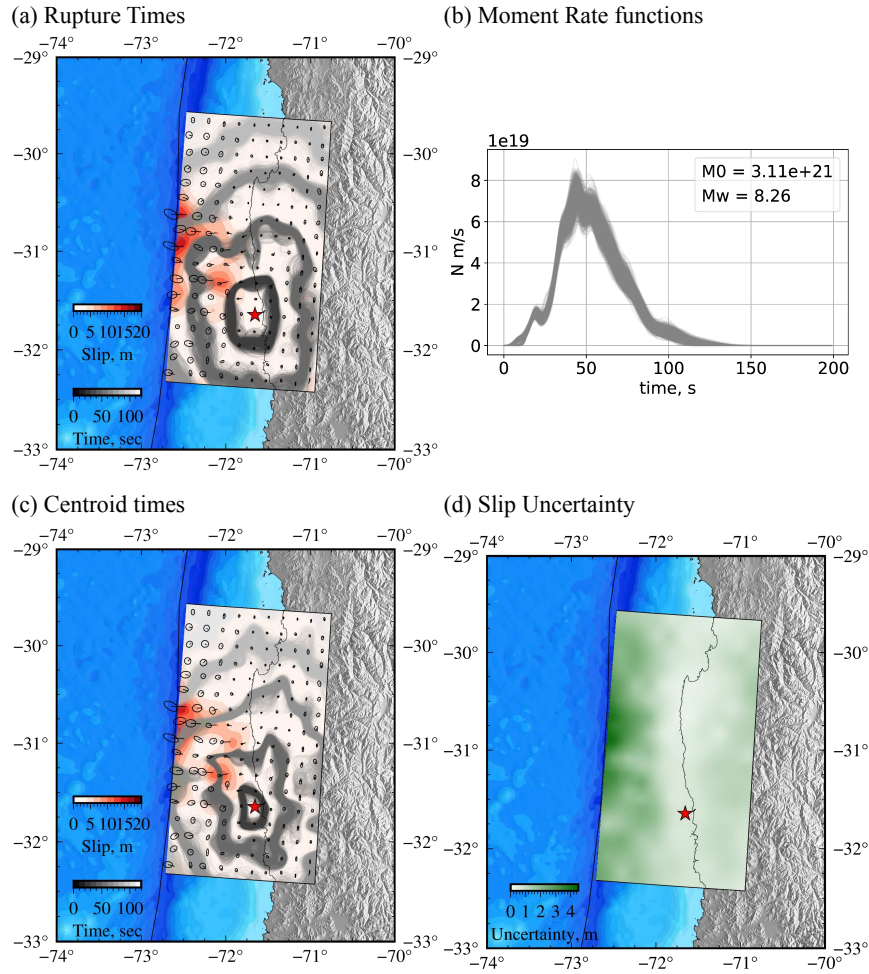


Figure 6: Impact of using a 2nd order approximation C_p in slip inversion. (a) Posterior mean coseismic slip model, arrows represent the slip directions and the ellipses its corresponding uncertainty. Contours show stochastic rupture fronts samples from the *a posteriori* distribution. (b) Stochastic moment rate functions. (c) Posterior mean coseismic slip model with contours that represent stochastic centroid time fronts samples from the *a posteriori* distribution. (d) Uncertainty of the ensemble of coseismic slip models. The red star in the figures represents the inverted hypocenter location.

[Tilman et al., 2016].

Results in Figures 6 (a) and (c) show a possible encircling behavior northward from the hypocenter location. We use the posterior coseismic mean model to investigate the slip and slip rate evolution. The observed rupture slowly grows propagating to the northwest during 35 seconds. Around 40 seconds, the rupture splits into three slip-rate pulses depicting a first encircling pattern west of the hypocenter (cf., slip rate snapshots between 40 and 50 seconds) and another encircling pattern to the northwest (cf., slip rate snapshots between 45 and 60 seconds). These encircling slip pulse contour fault areas with small slip amplitudes (cf., final slip distribution in Figures 6. Both slip branches finally join together generating a large

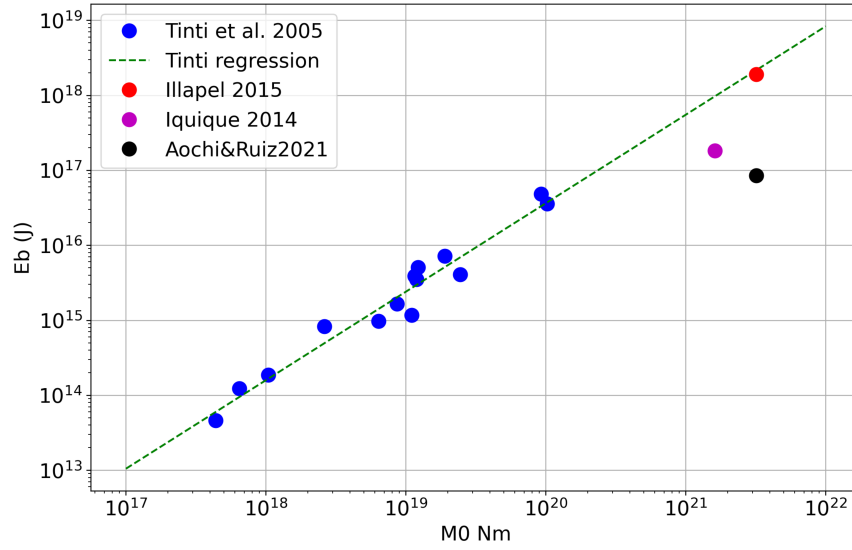
slip-rate pulse around 60 sec continuing at shallow depth toward the north until the end of the rupture. The encircling slip pulses visible in our solution between 40 and 60 seconds are consistent with previous back-projection results that suggest such complexities in the rupture.

Some studies have reported a low radiation efficiency for tsunami earthquakes [Venkataraman and Kanamori, 2004]. This is related to the presence of sediments, which dissipate a large part of the available energy. This is relevant for the 2015 Illapel earthquake as our solution suggests an important amount of slip at shallow depth. To further investigate the rupture dynamics of the 2015 Illapel earthquake, we follow an approach similar to Tinti et al. [2005a] and use kinematic models to compute the breakdown work W_b . We follow the same methodology to obtain the breakdown work of the 2014 $M_W = 8.1$ Iquique earthquake. We compare the average breakdown energy of both earthquakes with the solution and scaling relationship from Tinti et al. [2005a] (Figure 7 a). With our calculated breakdown energy, we estimate a radiation efficiency of $\eta_R = 0.015$. Such low radiation efficiency is consistent with our modeling results requiring significant slip at a shallow depth to explain tsunami observations.

We also compare the average breakdown work of both earthquakes with the solution and scaling relationship from Tinti et al. [2005a] and the scaling relationship from Causse et al. [2014] (Figure 3.14 b). Even though there is a general agreement, we can clearly see that the breakdown work averaged over the fault is small compared with the scaling relationships. We suggest that such underestimation results from the fact that the averaging of W_b is done over the entire fault used for slip inversion (even in regions that did not slip). To mitigate this effect, we decided to weight the averaging of the breakdown work by the corresponding slip in subfaults. We see that for the Illapel earthquake, the estimated value is more consistent with the aforementioned scaling relationships. In the case of the Iquique earthquake, there is still a significant offset, which could be then due to the compactness of the rupture [Duputel et al., 2015].

To get insights into breakdown work scaling relationships, we calculate the fracture energy G for a self-healing slip pulse model [Rice et al., 2005] for both earthquakes, the 2014 Iquique and the 2015 Illapel earthquake. In both cases, the breakdown work distributions seem to follow the same scaling relationship expected for fracture energy calculated for self-healing pulses.

(a) Breakdown Energy



(b) Average Breakdown

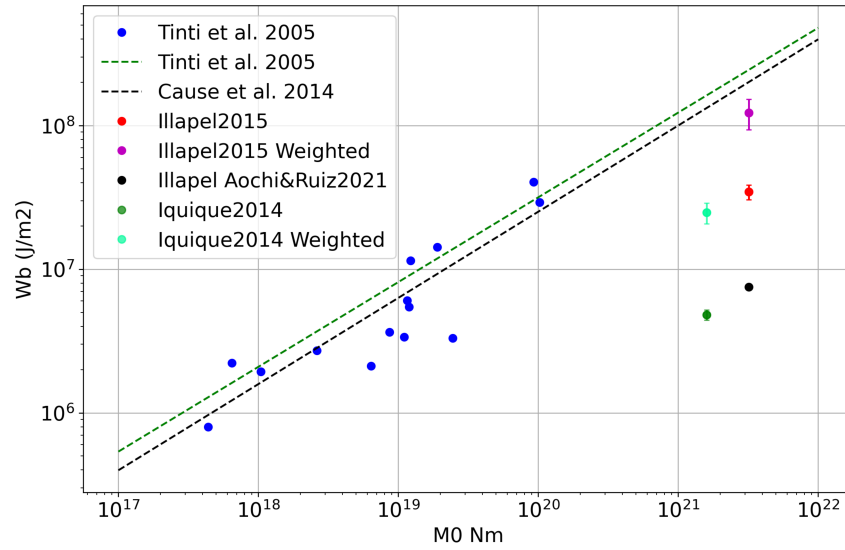


Figure 7: Average breakdown energies (a) and average breakdown work (b) for the 2015 $M_W = 8.3$ Illapel earthquake and the 2014 $M_W = 8.1$ Iquique earthquake. For the breakdown energy, purple and red dots represent the average breakdown energies calculated in this study. For the breakdown work, green and red dots represent the average breakdown work calculated in this study. Cyan and purple dots represent the average breakdown work weighted by the corresponding slip. Blue dots represent the breakdown energies and breakdown work calculated by Tinti et al. [2005a] respectively. The dashed green line represents the scaling relationship from the same study while the dashed black line represents the scaling relationship is from Causse et al. [2014].

Résumé étendu *(en français)*

Les séismes sont un phénomène naturel complexe qui peuvent provoquer de nombreuses victimes et des dégâts matériels importants. La caractérisation des séismes est essentielle pour comprendre les mécanismes et la physique des ruptures sismiques. Comme d'autres domaines en géophysique, la détermination de la source sismique est affectée par différentes sources d'incertitudes et par le fait qu'il existe souvent plusieurs modèles permettant d'expliquer les observations. L'objectif général de cette thèse est de mener une étude approfondie de la source, couvrant différents aspects de la caractérisation des séismes. Premièrement, je me suis focalisé sur la phase d'initiation des tremblements de terre, en essayant d'entrevoir des détails concernant la préparation des ruptures sismiques. Spécifiquement, j'ai analysé la phase d'initiation du séisme de Valparaíso en 2017 (magnitude $M_W = 6.9$). Ce séisme est un cas d'étude intéressant car il a été précédé par un déplacement transitoire accompagnée par de nombreux séismes pré-chocs. En démontrant que le signal GNSS pré-sismique ne peut pas être expliqué par les déplacements co-sismiques et post-sismiques induit par les séismes pré-chocs, nous montrons que ce séisme a vraisemblablement été précédé par un glissement asismique sur la faille. Dans une deuxième partie de ma thèse, je me suis intéressé à la caractérisation détaillée de la distribution de glissement co-sismique associée aux grands séismes. En particulier, j'examine le séisme d'Illapel en 2014 ($M_W = 8.3$), dont plusieurs travaux ont conduit à des conclusions différentes sur le processus de rupture. La caractérisation cinématique de la source de ce séisme est donc effectuée via une approche d'échantillonnage bayésien qui s'est avérée utile pour caractériser l'incertitude a posteriori. C'est également l'occasion de discuter la meilleure façon de caractériser l'incertitude de modélisation (liée au problème direct) en particulier pour les données sismologiques. Nos modèles cinématiques indiquent une forte complexité dans le processus de rupture, associé à des "encerclements d'aspérités" qui ont été précédemment suggérées par des études utilisant des méthodes de rétro-projection.

Phase d'initiation du séisme de Valparaíso en 2017

L'utilisation de mesures géodésiques a permis de découvrir des déformations transitoires avant plusieurs grands séismes. Ces signaux sont observés simultanément à l'occurrence de séquences de séismes pré-chocs (c-à-d. des événements sismiques précédant le séisme principal). Deux modèles conceptuels ont été construits pour expliquer ces observations [Mignan, 2014]. Un premier modèle considère l'existence d'un glissement asismique qui s'accélère graduellement jusqu'à l'occurrence du séisme principal. Selon ce modèle, ce glissement pré-sismique dé-

clencherait les séismes pré-chocs. Le deuxième modèle considère une cascade de séismes pré-chocs. Dans ce modèle, les séismes pré-chocs se déclenchent de proche en proche (par transfert de contrainte statique et possiblement par l'intermédiaire de glissement post-sismique) et contribuent à une cascade de ruptures aléatoires qui conduit finalement au déclenchement du séisme principal. Ce modèle pourrait expliquer les signaux géodésiques pré-sismiques en considérant que ces observations correspondent en réalité à l'accumulation des déformations co-et post-sismiques associées à chaque séisme pré-choc.

Le séisme de Valparaíso s'est produit le 24 avril 2017 (magnitude $M_W = 6,9$), dans le segment central de la zone de subduction chilienne (33.089°S , 72.116°W , 21:38:28 UTC ; Centro Sismológico Nacional, CSN). Ce séisme a été précédé d'un déplacement transitoire observé par des stations GNSS permanentes, trois jours avant le choc principal [Ruiz et al., 2017]. Des séismes pré-choc ont également été identifiés avec une augmentation significative du taux de sismicité deux jours avant le choc principal (Figure 8). L'objectif principal de cette étude est d'évaluer la contribution relative du glissement sismique et asismique pendant les jours précédants le séisme de Valparaíso en 2017.

Pour ce faire, nous traitons les données GPS de 68 stations de la région d'Amérique du Sud. La figure 1-b montre les déplacements horizontaux pour les stations situées à proximité de la zone d'étude. On observe clairement un mouvement vers l'ouest, qui commence environ trois jours avant le choc principal. Dans la figure 8-b, on peut voir que la pente du taux de sismicité cumulé ne change pas de manière significative au début du déplacement transitoire. L'augmentation du taux de sismicité est décalé d'environ 24 heures et ne commence qu'avec l'apparition d'un séisme pré-choc le 23 avril (magnitude $M_W = 6.0$) (cf., étoile violette sur la figure 8-b).

Pour contraindre la contribution des séismes pré-choc aux déplacements GPS observés, nous estimons les paramètres du tenseur de moment barycentrique (Centroid Moment Tensor CMT, en anglais) pour les séismes de magnitude $M_W > 3.6$ la séquence de séismes de Valparaíso (de 2017/04/05 à 2017/05/30). Nous utilisons une version modifiée de l'algorithme W-phase adaptée aux distances régionales et à la gamme de magnitude de la séquence de Valparaíso [Kanamori and Rivera, 2008, Zhao et al., 2017]. Les paramètres estimés sont le tenseur de moment déviatorique, la localisation barycentrique, le temps barycentrique, et la demi-durée d'un triangle isocèle qui représente la fonction de taux de moment sismique. Le catalogue CMT résultant est présenté dans la Figure 9.

Pour évaluer la contribution des séismes pré-chocs aux déplacements superficiels, nous calculons le déplacement statique synthétique en utilisant notre catalogue

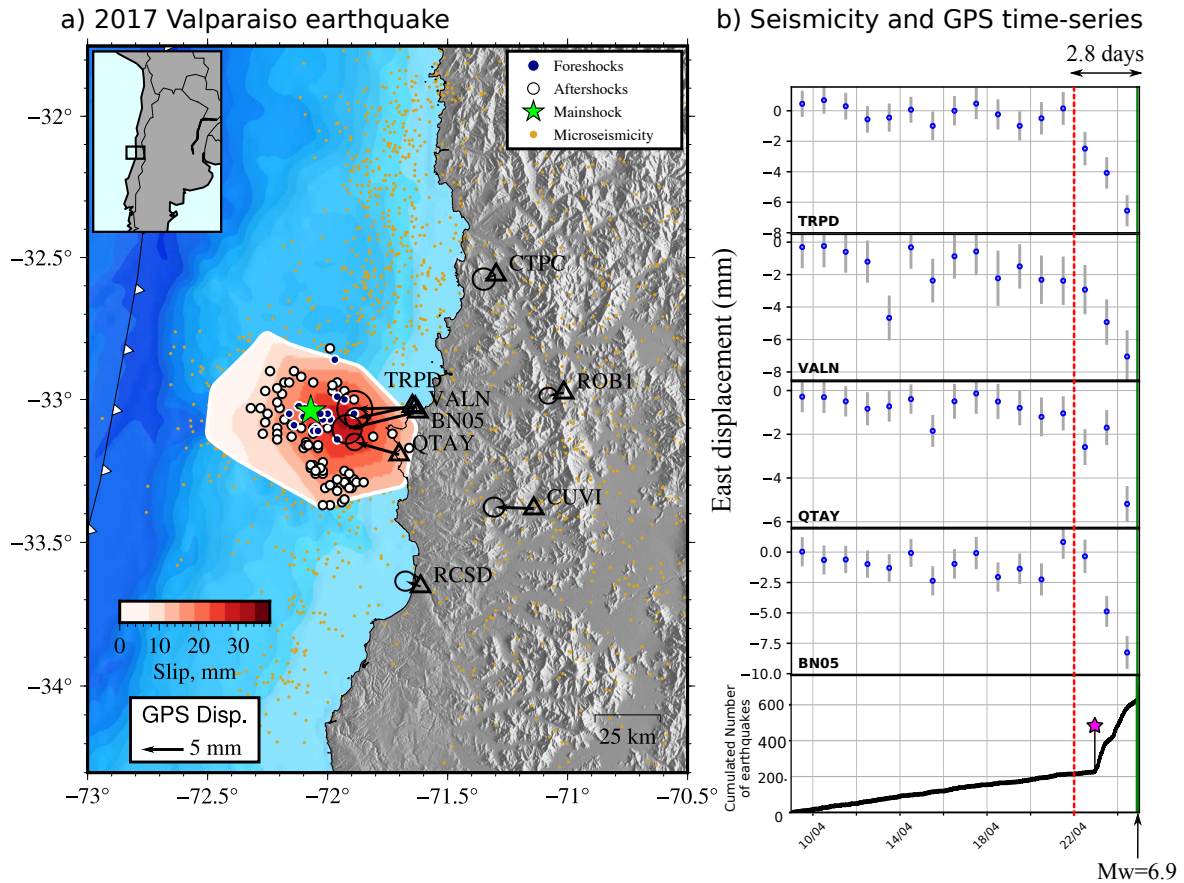


Figure 8: La séquence du séisme de Valparaíso de 2017. (a) Localisations des séismes, y compris les pré-chocs (cercles bleus), le choc principal (étoile verte) et les répliques (cercles blancs). La carte de couleur rouge indique la distribution de glissement présismique résultant de l'inversion des données GPS. Les flèches noires montrent les déplacements GPS observés cumulés (jusqu'à une heure avant le choc principal). Les points orange indiquent la distribution de la sismicité du 2017/01/01 au 2017/10/05 selon le catalogue de microsismicité obtenu par S. Ruiz et al. (2017). (b) Séries temporelles GPS dans les environs de Valparaíso. La ligne verticale en pointillés rouges indique le début approximatif du déplacement transitoire visible sur la série temporelle. Le nombre cumulé de séismes de S. Ruiz et al. (2017) est indiqué en bas de la figure. L'étoile violette représente le plus grand pré-choc $M_W = 6.0$.

CMT. Nous utilisons le code CSI pour le calcul (<http://www.geologie.ens.fr/~jolivets/csi>), et nous suivons l'approche de Zhu and Rivera [2002] pour obtenir des déplacements statiques dans un milieu stratifié. Le plus grand événement pré-choc (magnitude $M_W = 6.0$) prédomine largement la contribution cosismique au déplacement transitoire observé dans les GPS. Puisque le pré-choc de magnitude $M_W = 6.0$ joue un rôle important dans la séquence, nous évaluons les incertitudes associées aux paramètres CMT correspondants. Afin d'évaluer ces incertitudes, nous effectuons une nouvelle inversion du CMT dans un cadre bayésien, en suivant l'approche proposée par Duputel et al. [2012a, 2014]. L'ensemble a posteriori

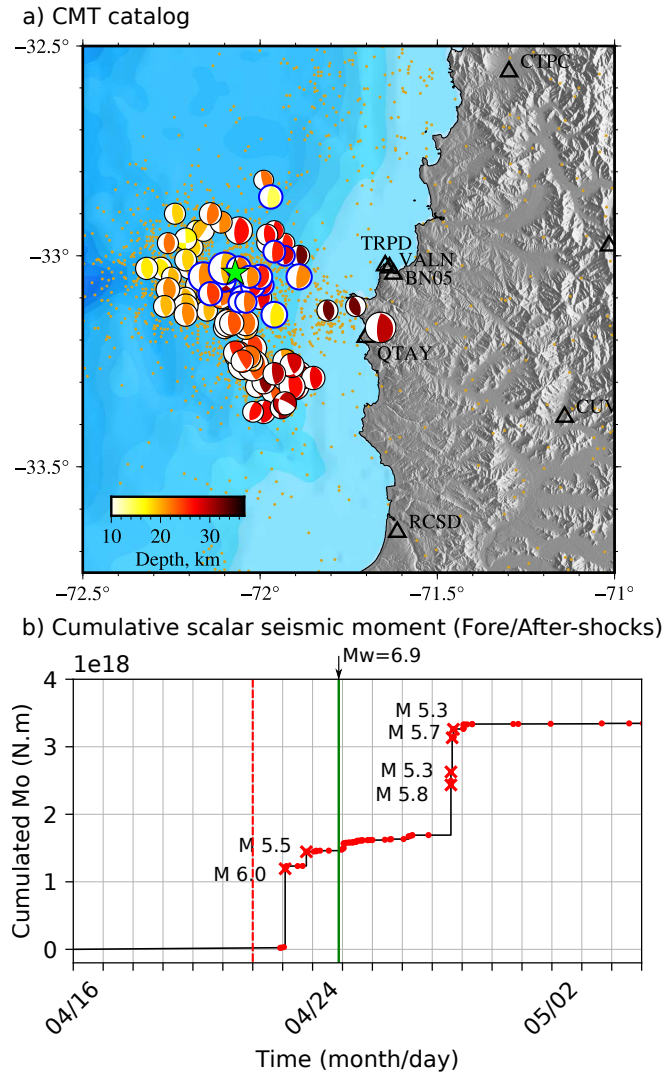


Figure 9: Solutions CMT de la séquence du séisme de Valparaíso de 2017 et moment cumulé. (a) Solutions CMT de la séquence du séisme de Valparaíso de 2017. Les mécanismes aux foyers sont délimités en bleu et en noir pour les pré-chocs et les répliques respectivement. La taille de chaque mécanisme est proportionnelle à la magnitude du moment. La couleur des mécanismes représente la profondeur de l'événement. (b) Moment sismique scalaire cumulé de la séquence Valparaíso 2017. Le moment scalaire du choc principal n'est pas inclus dans cette figure. La ligne pointillée rouge souligne le début approximatif des déplacements transitoires visibles sur les séries temporelles GPS. La ligne verte indique l'heure d'origine.

des localisations de sources plausibles et des tenseurs de moment est évalué en utilisant une stratégie similaire à celle de Sambridge [1999].

Pour évaluer l'incertitude sur le déplacement cosismique prédit, nous simulons des déplacements statiques pour chaque échantillon du modèle du séisme pré-choc $M_W = 6.0$. Les déplacements cosismiques stochastiques résultants sont représentés en gris sur la figure 10a pour les stations GPS les plus proches de l'épicentre du choc principal. Même en prenant en compte les incertitudes, les déplacement co-

sismiques cumulés prédits sont encore inférieurs aux déplacements présismiques observés (~ 6 à 8 mm de la composante Est pour les stations les plus proches).

Pour obtenir un bilan total du déplacement sismique et asismique avant le choc principal, nous comparons les données GPS une heure avant le choc principal avec le déplacement synthétique cumulé généré par les pré-chocs (Figure 10b). Les déplacements observés sont en moyenne entre 4 et 6 mm plus grands que les déplacements synthétiques cosismiques. De telles différences ne peuvent pas être expliquées par les incertitudes liées aux observations et aux prédictions. Ces résultats suggèrent clairement qu'une partie importante de la déformation pré-sismique observée est en fait asismique et ne peut pas être expliquée par les pré-chocs. Nous estimons qu'environ 51 % du déplacement mesuré aux stations GPS provient d'un glissement asismique sur la faille. La partie liée à la déformation asismique est cohérente entre les stations voisines (Figure 10c), ce qui suggère une source commune située à proximité des pré-chocs.

Finalement, nous effectuons deux inversions de glissement : une première inversion de glissement avec le déplacement présismique GPS total et une autre inversion après avoir supprimé la contribution des pré-chocs (c'est-à-dire le déplacement asismique uniquement). La distribution du glissement présismique s'étend vers l'ouest de la ville de Valparaíso avec une extension d'environ 50×90 km et un moment scalaire de $M_0 = 3.08 \times 10^{18}$ N.m (c'est-à-dire, $M_w = 6.26$). Ce mouvement asismique représente environ 50 % du moment calculé pour le modèle de glissement dérivé des données GPS non corrigées ($M_0 = 5,67 \times 10^{18}$ N.m, Figure 3e). Compte tenu du moment cumulé des pré-chocs ($M_0 = 1,48 \times 10^{18}$ N.m), nous estimons que près de 70 % du moment scalaire libéré pendant la phase de préparation du choc principal de Valparaíso est asismique, ce qui est à peu près en accord avec les estimations de Ruiz et al. [2017]. La plus petite part de moment asismique dérivée de la comparaison des modèles de glissement dans la figure 3e-f résulte probablement de l'hypothèse simpliste de la figure 3e selon laquelle toutes les pré-chocs sont situées à l'interface des plaques.

Différentes études numériques et expérimentales ont mis en évidence l'influence d'un glissement pré-sismique dans le déclenchement de séismes pré-chocs [par exemple, Kaneko et al., 2016, McLaskey and Kilgore, 2013]. Si telles observations s'appliquent aux failles naturelles, les localisations des pré-chocs pourraient potentiellement nous informer sur l'étendue spatiale globale de la zone de nucléation avant un séisme. Cette idée est en accord avec nos résultats suggérant une corrélation du premier ordre entre la distribution du glissement pré-sismique et la localisation des pré-chocs (Figure 1 et Figure 3). Même si le glissement pré-sismique

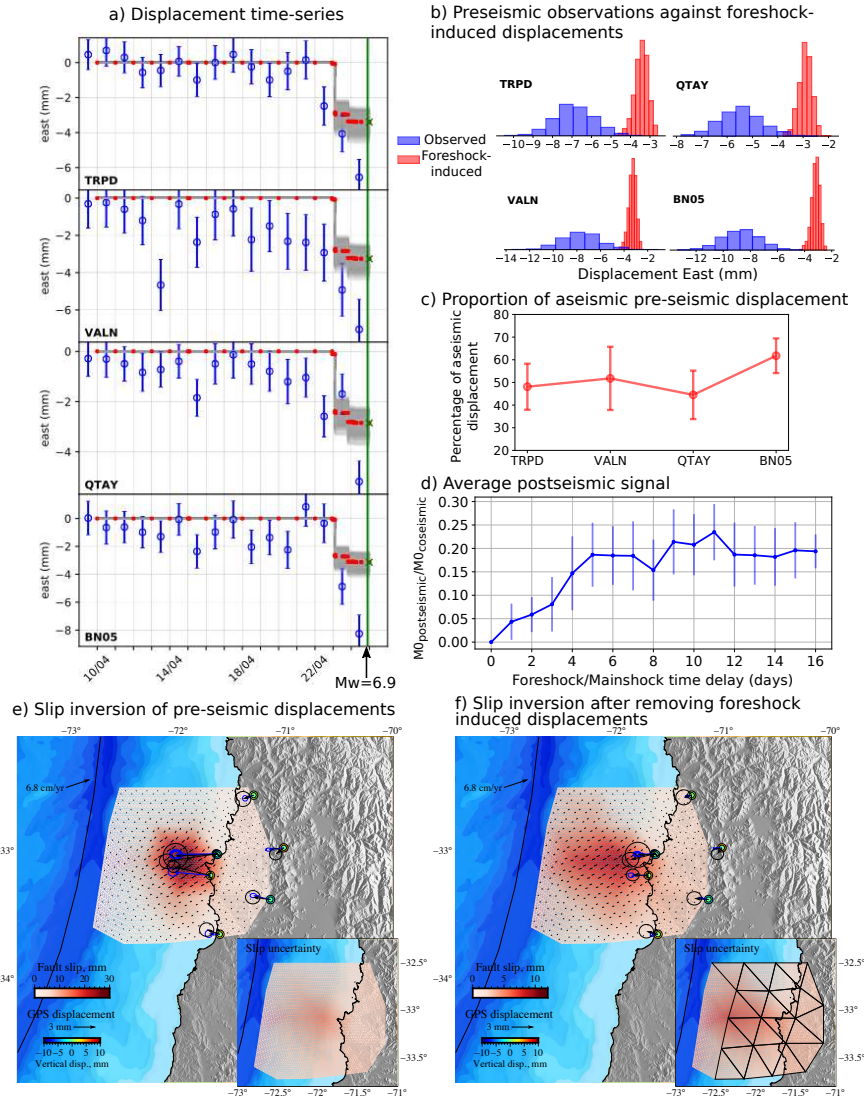


Figure 10: Glissement pendant la séquence de séismes pré-chocs de Valparaíso. a) Séries temporelle des données GNSS (bleu) et déplacement cosismique stochastique induit par le pré-choc $M_W = 6.0$ (gris). Les points rouges représentent les déplacements moyens cosismiques stochastiques. La croix verte correspond au déplacement présismique total, y compris la contribution des séismes inférieurs à la magnitude de complétude. b) Distributions des déplacements pre-sismiques observés (blue) et des déplacements cosismiques cumulés générés pour les séismes pré-chocs (rouge) une heure avant le choc principal. Pour les observations, on suppose des incertitudes gaussiennes à partir des erreurs standard estimées à chaque station. c) Pourcentage de déplacement asismique pour chaque station. d) Signal post-sismique moyen mesuré sur les stations TRPD, VALN, BN05 et QTAY. e) Inversion de glissement des données GPS présismiques. f) Inversion de glissement des données GPS sans la contribution des séismes pré-chocs. Les flèches noires et bleues représentent les déplacements GPS horizontaux observés et prédits, ainsi que leurs ellipses $1-\sigma$ (représentant les incertitudes respectives). Les cercles colorés représentent les déplacements verticaux observés (cercles extérieurs) et prédits (cercles intérieurs) à partir du GPS.

semble être un mécanisme important dans le déclenchement des pré-chocs, une partie de l'activité des pré-chocs résulte probablement des phénomènes en cascade liés aux changements de contraintes des événements voisins. De plus, nous devons encore comprendre pourquoi la plupart des tremblements de terre ne sont pas précédés d'une activité pré-choc et encore moins d'un mouvement présismique observable.

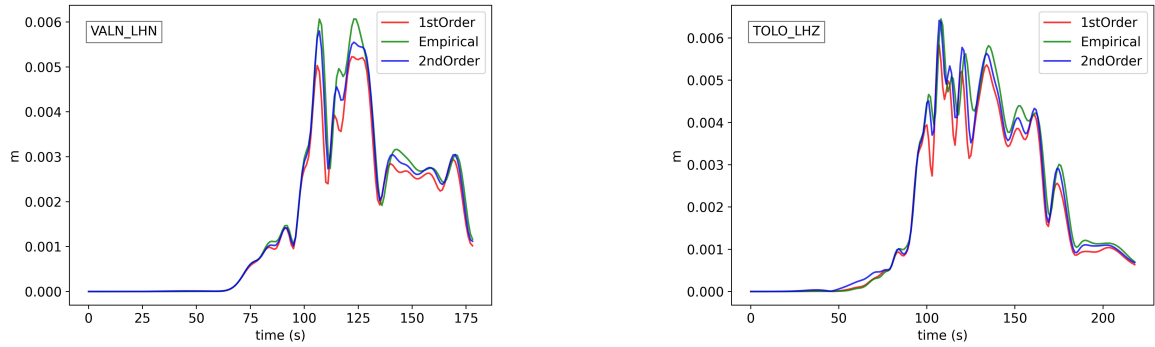
Réexamen du séisme d'Illapel en 2015

Le séisme d'Illapel en 2015 (Chili, $M_W = 8,3$) est l'un des plus grands séismes enregistré dans la zone de subduction chilienne [Ruiz et al., 2016]. Les études précédentes indiquent une propagation de la rupture depuis l'hypocentre jusqu'à la partie superficielle de la faille, avec un glissement maximal variant entre 10 et 16 mètres [voir par exemple, Heidarzadeh et al., 2016, Melgar et al., 2016b, Tilmann et al., 2016]. Les distributions de glissement obtenues précédemment montrent une disparité importante, en fonction des données utilisées et de la technique d'inversion adoptée. Ainsi pour quelques modèles, la magnitude de glissement dans la partie superficielle de la faille est presque nulle, alors que d'autres présentent un glissement superficiel significatif.

Dans ce travail de thèse, nous réexaminons cet événement en combinant un ensemble de données comprenant: (i) des stations GNSS permanentes et de campagne, corrigées des signaux post-sismiques et des répliques; (ii) des images InSAR ascendantes et descendantes du satellite Sentinel-1A; (iii) des données tsunami; (iv) de formes d'ondes GNSS à haute fréquence (HRGPS); (v) de formes d'ondes obtenues à partir d'enregistrements accélérométriques en champ proche. Nous effectuons une inversion du glissement cinématique en suivant une approche bayésienne, dans laquelle nous obtenons un ensemble de modèles, et non une solution unique. L'inversion cinématique est réalisée avec le code AlTar, qui permet d'obtenir une solution statique avant d'incorporer les données dans un problème conjoint. Cette approche bayésienne nous permet d'incorporer des estimations des incertitudes: (i) les incertitudes liées aux erreurs de mesures; (ii) les incertitudes liées au problème direct, particulièrement, liées aux inexactitudes dans le modèle de vitesse considéré lors de l'inversion. Dans l'étude présente, nous nous concentrons sur la comptabilisation des incertitudes dues à la modélisation de la structure de la Terre. Plus précisément, nous évaluons l'impact des inexactitudes dans le modèle de vitesse 1D employé pour calculer les prédictions statiques et cinématiques. Nous suivons trois schémas différents pour prendre en compte l'incertitude du modèle terrestre. La première approche consiste à calculer empiriquement la matrice de covariance de l'incertitude de prédiction C_p en utilisant les prédictions

calculées pour un grand nombre de modèles terrestres aléatoires $\Psi_i, (i = 1, \dots, n)$. Ensuite, nous suivons l'approche d'approximation au premier ordre proposée par Duputel et al. [2014]. Enfin, nous explorons la possibilité d'utiliser une approche de perturbation du second ordre, précédemment introduite par Caballero et al. [2021] pour les inversions de sources ponctuelles. Dans la Figure 11, nous comparons la diagonale de la matrice C_p pour les stations HRGPS et les stations de mouvement fort. Les matrices C_p du premier et deuxième ordre semblent capturer les principales caractéristiques de la matrice C_p empirique. Cependant, il existe des différences qui pourraient jouer un rôle important dans les problèmes d'inversion complexes. Pour cette raison, dans la section suivante, nous explorons l'impact de la matrice C_p sur les modèles cosismiques du séisme d'Illapel de 2015 ($M_W = 8.3$).

(a) HRGPS



(b) Strong motion

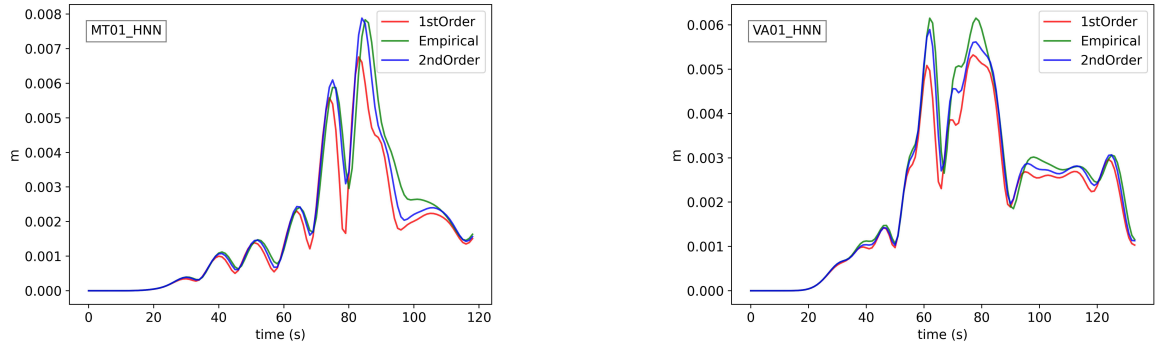


Figure 11: Comparaison des matrices de covariance pour les signaux HRGPS (a) et les stations Strong Motion (b). La ligne verte représente la diagonale de la matrice de covariance empirique (c'est-à-dire la matrice créée à partir d'un ensemble de modèles). La ligne rouge et bleue représente la diagonale de la matrice calculée en utilisant l'approche d'approximation de 1er et 2ème ordre, respectivement.

Nous obtenons une inversion de glissement statique *a posteriori* et utilisons les échantillons de distribution comme échantillons origines pour effectuer trois inversions conjointes différentes : l'une utilisant une matrice C_p empirique et deux autres avec des matrices C_p calculée en utilisant les approches de perturbation du pre-

mier et du deuxième ordre. Les distributions des glissements finales obtenues à l'aide de ces différentes approches sont présentées sur la Figure 12. La solution basée sur la matrice C_p du premier ordre montre une zone de glissement assez compacte à faible profondeur, alors que le même glissement est plus largement distribué lorsqu'on considère les matrices C_p du second ordre et empirique. Cela se traduit par un pic de glissement plus important pour la solution de 1er ordre de la matrice C_p (21,07 +/- 2,03 m), tandis que la matrice empirique C_p (17,35 +/- 1,96 m) et la matrice du 2ème ordre C_p (18,52 +/- 2,74 m) présentent des pics de glissement plus faibles.

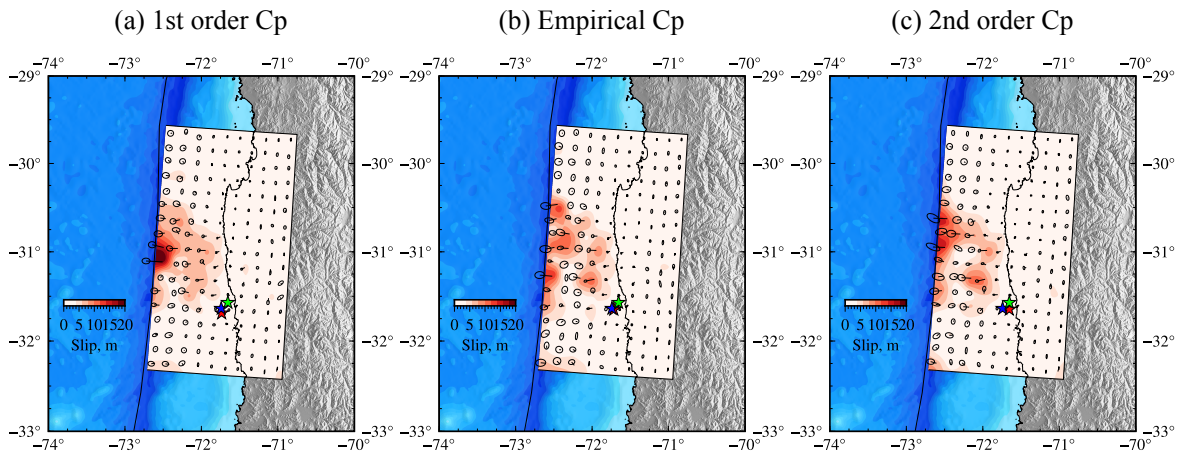


Figure 12: Comparaison des distributions de glissement cosismique obtenues en utilisant différentes matrices de covariance d'erreur de prédiction C_p . Les couleurs rouges représentent les distributions de glissement finales. Les flèches représentent les directions de glissement avec leur incertitude correspondante. L'étoile rouge représente la localisation de l'hypocentre inversé. L'étoile bleue est l'hypocentre du CSN, et l'étoile verte est l'hypocentre de l'USGS.

Les détails de la solution obtenue à l'aide d'un C_p d'ordre 2 sont présentés sur la Figure 13. Les fronts de propagation stochastiques de la rupture sur la Figure 13 (a) suggèrent un modèle de rupture complexe, où la rupture se développe lentement à proximité de l'hypocentre. Puis, elle se propage vers le nord-ouest jusqu'à une zone superficielle de l'interface de subduction. Les fonctions stochastiques de taux de moment de la Figure 13 (b) indiquent une durée de rupture globale d'environ 120 secondes. Le moment sismique scalaire moyen est $M_0 = 3,20 \times 10^{21} \text{ N} \cdot \text{m}$, soit une magnitude de moment de $M_W = 8.27$. La propagation temporelle du centre de la pulse de glissement n'est pas homogène et présente des configurations complexes, en particulier à l'ouest de l'hypocentre. Nous examinons individuellement différents aspects de la rupture du séisme d'Illapel : (i) la distribution du glissement à faible profondeur, (ii) les modèles de rupture encerclante observés, et (iii) l'énergie de fracture évaluée à partir de notre ensemble postérieur des modèles de glissement.

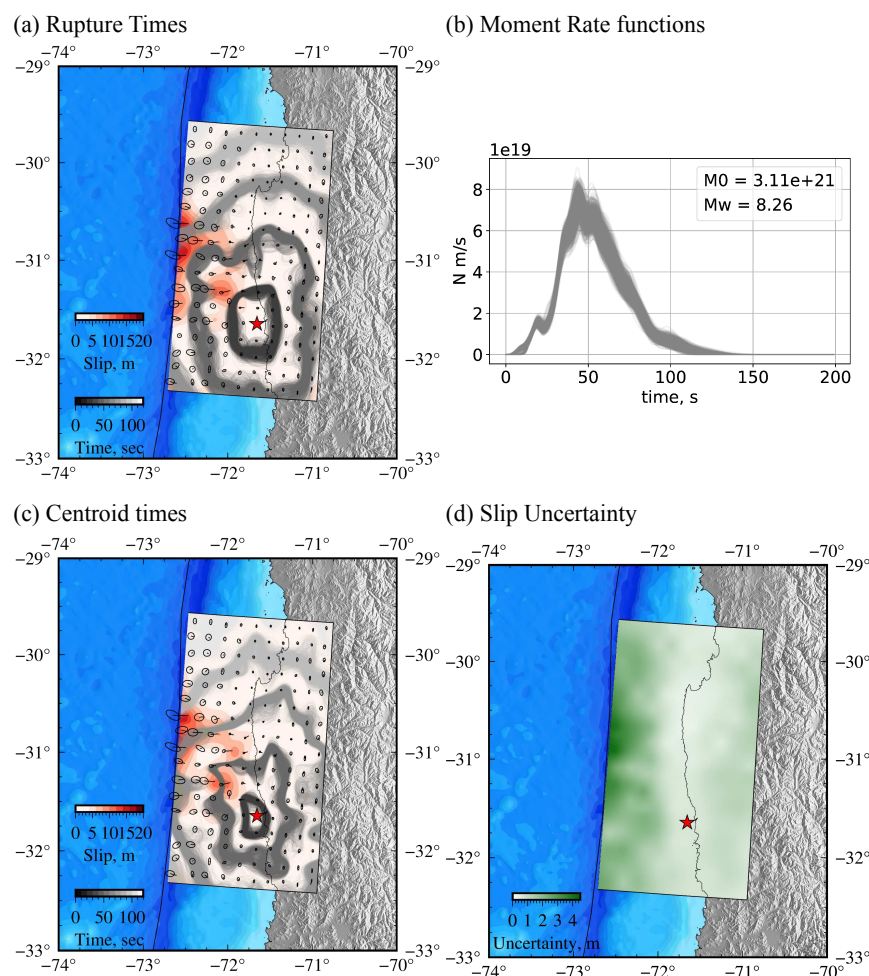


Figure 13: Impact de l'utilisation d'une approximation de 2ème ordre C_p dans l'inversion du glissement. (a) Modèle moyen *a posteriori* du glissement cosismique, les flèches représentent les directions de glissement et les ellipses l'incertitude correspondante. Les contours montrent les fronts de rupture stochastiques échantillonnés à partir de la distribution *a posteriori*. (b) Fonctions de taux de moment stochastique. (c) Modèle moyen *a posteriori* du glissement cosismique avec des contours qui représentent des échantillons de fronts de temps centroïdes stochastiques échantillonnés de la distribution *a posteriori*. (d) Incertitude de l'ensemble des modèles de glissement cosismique. L'étoile rouge dans les figures représente la localisation de l'hypocentre inversé.

Afin d'explorer la contribution du glissement superficiel sur l'inversion, nous effectuons une inversion du glissement statique en imposant un glissement superficiel faible (une distribution *a priori* proche à zéro dans les sous-failles proches de la fosse océanique). De cette manière, nous obtenons un modèle de glissement pour lequel la partie superficielle est significativement différente. Nous comparons la différence dans les ajustements de la forme d'onde des observations tsunami. Nous pouvons voir que la solution sans glissement à faible profondeur ne peut pas ajuster les formes d'onde tsunami aussi bien que notre modèle précédent. L'existence de grands glissements superficiels supportent le fait que l'événement de 2015 n'est

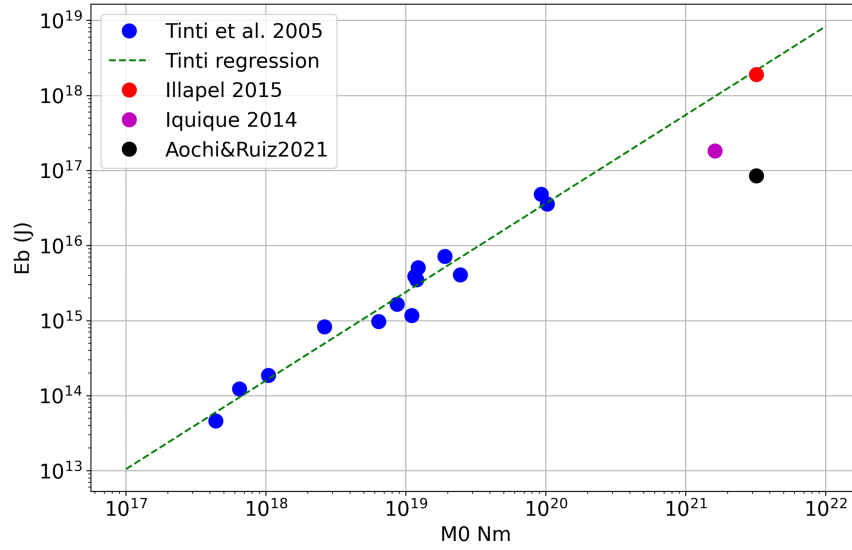
pas une simple répétition du tremblement de terre qui a touché la région en 1943 [Tilman et al., 2016]. Ceci est cohérent avec les témoignages historiques indiquant que le tsunami généré en 1943 était beaucoup plus petit que celui observé en 2015. En outre, les différences dans la durée des arrivées des ondes de corps téléseismiques pour les deux événements suggèrent que la rupture de 1943 n'a pas impliqué un glissement peu profond [Tilman et al., 2016].

Les résultats des Figures 13 (a) et (c) montrent un possible effet d'encerclement vers le nord-ouest de l'hypocentre. Nous utilisons le modèle moyen à posteriori pour étudier l'évolution du glissement et du taux de glissement. La rupture observée croît lentement en se propageant vers le nord-ouest pendant 35 secondes. Aux alentours de 40 secondes, la rupture se divise en trois pulses de taux de glissement décrivant un premier encerclement à l'ouest de l'hypocentre et un autre encerclement au nord-ouest. Ces pulses de glissement encerclantes contournent des zones de failles avec de faibles amplitudes de glissement (cf. la distribution finale du glissement dans les Figures 13). Les deux branches de glissement se rejoignent finalement en générant une grande impulsion de glissement vers 60 secondes qui se poursuit à faible profondeur vers le nord jusqu'à la fin de la rupture. Les pulses de glissement dans notre solution entre 40 et 60 secondes sont cohérentes avec les résultats précédents de rétroprojection qui suggèrent de telles complexités dans la rupture.

Certaines études ont rapporté une faible efficacité de radiation pour les séismes de type tsunami. Ceci est lié à la présence de sédiments, qui dissipent une grande partie de l'énergie disponible. Ceci est pertinent pour le séisme d'Illapel de 2015 car notre solution suggère une quantité importante de glissement à faible profondeur. Pour approfondir la dynamique de rupture du séisme de 2015 à Illapel, nous suivons une approche similaire à celle de Tinti et al. [2005a] et utilisons des modèles cinématiques pour calculer le travail de rupture W_b . Nous suivons la même méthodologie pour obtenir le travail de rupture du séisme d'Iquique de 2014 ($M_W = 8.1$). Nous comparons l'énergie de fracture moyenne des deux séismes avec la solution et la relation d'échelle de Tinti et al. [2005a] (Figure 14 a). Avec notre énergie de rupture calculée, nous estimons une efficacité de radiation de 0,015. Une efficacité de radiation aussi faible est cohérente avec les résultats de notre modélisation nécessitant un glissement superficiel important pour expliquer les observations tsunamis.

Nous comparons également la densité d'énergie de fracture des deux séismes avec les solution et la relation d'échelle de Tinti et al. [2005a] et la relation d'échelle de Causse et al. [2014] (Figure 14 b). Bien qu'il y ait un accord général, nous pouvons clairement voir que la densité d'énergie moyenné sur la faille est faible par rapport

(a) Breakdown Energy



(b) Average Breakdown

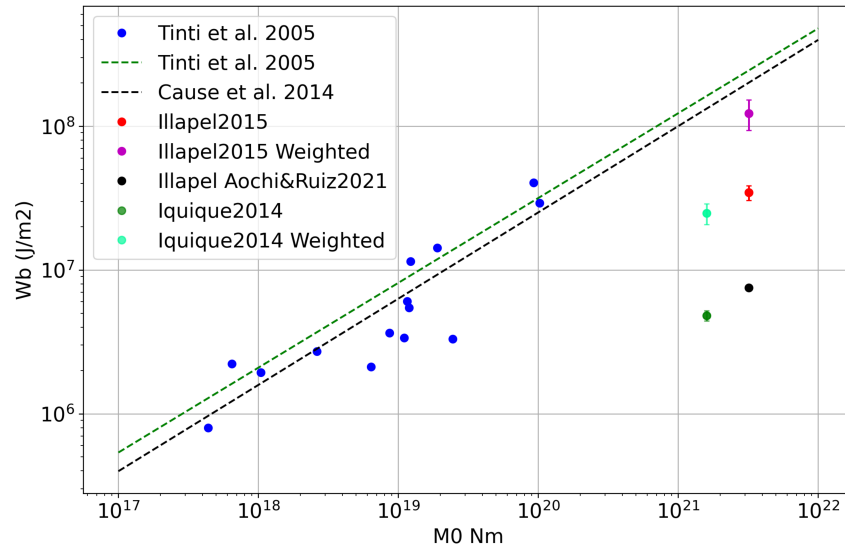


Figure 14: Energies moyennes de rupture (a) et travail moyen de rupture (b) pour le séisme de 2015 $M_W = 8.3$ Illapel et le séisme de 2014 $M_W = 8.1$ Iquique. Pour l'énergie de rupture, les points violets et rouges représentent les énergies de rupture moyennes calculées dans cette étude. Pour le travail de rupture, les points verts et rouges représentent le travail de rupture moyen calculé dans cette étude. Les points cyan et violet représentent le travail de rupture moyen pondéré par le glissement correspondant. Les points bleus représentent les énergies de rupture et le travail de rupture calculés par Tinti et al. [2005a] respectivement. La ligne verte en pointillé représente la relation d'échelle de la même étude tandis que la ligne noire en pointillé représente la relation d'échelle de Causse et al. [2014].

aux relations d'échelle. Nous suggérons que cette sous-estimation résulte du fait que le calcul de la moyenne de W_b est effectué sur l'ensemble de la faille utilisée pour l'inversion du glissement (même dans les régions qui n'ont pas glissé). Pour atténuer cet effet, nous avons décidé de pondérer le calcul de la moyenne par le

glissement correspondant dans chaque sous-failles. Nous constatons que pour le séisme d'Illapel, la valeur estimée est plus cohérente avec les relations d'échelle mentionnées précédemment. Dans le cas du séisme d'Iquique, il y a encore un décalage significatif, qui pourrait alors être dû à la compacité de la rupture [Duputel et al., 2015].

Pour avoir une vision globale des relations d'échelle du travail de rupture, nous calculons l'énergie de rupture G pour un modèle de pulse de glissement auto-cicatrisant [self-healing pulse; Rice et al., 2005] pour les deux séismes, celui d'Iquique en 2014 et celui d'Illapel en 2015. Dans les deux cas, les distributions du travail de rupture semblent suivre la même relation d'échelle attendue pour l'énergie de rupture calculée pour des self-healing pulses.

Remerciements

Ces trois dernières années ont été remplies avec plein de défis et apprentissage, et je voudrais remercier ici toutes les personnes qui m'ont aidé à l'aboutissement de ce travail de thèse.

Je remercie les membres du jury: Quentin Bletery, Thomas Bodin, Olivier Lengliné, Hélène Lyon-Caen et Anne Socquet, pour avoir accepté ce travail de lecture. Ces commentaires ont beaucoup aidé pour l'amélioration de ce travail.

Je voudrais remercier particulièrement à mes deux directeurs de thèse Zacharie Duputel et Luis Rivera. Merci beaucoup pour s'être intéressés à mon profil, pour avoir compris ma situation et encore, avoir continué avec ce projet de thèse malgré le délai imprévu. Zach, je te remercie pour avoir toujours eu le temps pour m'expliquer mille et une fois, en présentiel ou en visio. Merci Luis pour avoir apporté ce côté latino qui m'a aidé à m'adapter rapidement, un jour j'écouterai toutes tes recommandations musicales.

Je remercie aussi à toutes les personnes qui m'ont aidé pendant ces trois ans de travail. Un grand merci à Romain Jolivet, et Sophie Lambotte, qui ont été partie de mon comité de suivi. De la même façon je remercie l'équipe de l'EOST, spécialement l'équipe sismo: Alessia, Christophe, Dimitri, Olivier, avec qui j'ai pu discuter de façon informel, suivant au café sismo. Mention d'honneur à Dilek, à qui j'ai fait souffrir avec mille ordre de missions et mes deux noms.

Une thèse sans café n'est pas possible, et pour ça je remercie aux gars des 40cts: Cédric, Clément, Frank, Hugo, Lucho, Lucille, Mérédith, Rémi, (désolé si je rate quelqu'un) avec qui j'ai vécu un déménagement, une épidémie, des fermetures des bâtiments, bref, des aventures. Merci beaucoup pour ces bières au terminal, wawa, O'Briens (paix à son âme).

L'arrivée à Strasbourg n'aurait pas été facile si j'aurais pas trouvé des gens si gentils et accueillants. Je vous remercie tellement: Benjamin, Cata, Damian, Didi, Guigui, Javi, Marta (sans h), Minghe, Nono, Quentin, Josi. Grâce à vous j'ai pu connaître des choses inimaginables. Même avec la distance, je garde précieusement tous les moments qu'on a vécu ensemble, ces cafés, promenades, et tapettes au Kung Fu. Vous avez changé ma vie pour toujours. J'aurai pour la vie une partie de vous et votre culture.

Être de l'autre côté de l'océan n'est pas une tâche facile, et je serai pas arrivé au bout de ce travail sans tout le soutien que j'ai eu de mes chères au Mexique. Mes oncles et tantes, Alejandro, Cris, Marcela, Malena, Miguel, Pedro, Raúl et Tere. Merci pour vos encouragements dès mes premiers pas.

Je remercie aussi à mes ami.e.s du Mexique: Ana, Armando, Charlie, Conrado, Itzel, Josué, Migue, Ray avec lesquels j'ai pu toujours discuter n'importe la distance ni l'heure (même à 2 heures du matin s'il y avait du match de football).

Ce n'est pas normal pouvoir choisir ta famille dans la vie, et même moins ta soeur. Gaby, je ne pourrai jamais te remercier pour tout ce que tu as fait pour moi, de prendre soin de Pancho, ou voir el Chapo seulement pour me distraire de l'hôpital. Je te remercierai toujours.

La vie est imprévisible, et on ne sait pas qu'est-ce qu'elle réserve, cependant, tout va bien se passer tant qu'on est avec les bonnes personnes. Je te serai toujours reconnaissant Bérénice pour m'avoir accompagné pendant les moments compliqués, même à distance. Je serai flatté à vie que tu m'as permis partager tous ces beaux instants.

La vie a décidé de nous séparer avant de commencer cette aventure. Ton rêve était de venir voir Paris, un rêve que j'ai réalisé pour toi. Un jour on se reverra, mais pendant ce temps-là, merci maman. Ce que je suis et serai est grâce à toi. J'espère que tu es fière de moi. Ce thèse est pour toi. Je t'aime et t'aimerai toujours.

Contents

Table of Contents	I
General Introduction	1
1 Source Inversion	7
1.1 Summary	7
1.2 How to characterize the seismic rupture?	7
1.3 Observations	8
1.3.1 Seismic Data	9
1.3.2 GNSS data	12
1.3.3 InSAR images	14
1.3.4 Tsunami Data	16
1.4 Forward problem	16
1.4.1 Point source representation	17
1.4.2 Extended source	19
1.5 Source parameterization	20
1.5.1 Point source parameterization	20
1.5.2 Source parameterization for an extended source - Static case	21
1.5.3 Source parameterization for an extended source - Kinematic case	23
1.6 Inversion schemes	26
1.6.1 Optimization approach by Tikhonov regularization	27
1.6.2 Bayesian approach	29
1.7 Retrieving dynamic parameters from kinematic slip models	39
2 Initiation phase of Earthquakes.	41
2.1 Summary	41
2.2 How do earthquakes begin?	41
2.3 Early work and numerical simulations of earthquake nucleation	43
2.4 Laboratory experiments	45
2.5 Foreshocks triggered by aseismic pre-slip?	47
2.6 Foreshocks as cascades of random failures?	51

CONTENTS

2.7	Co-existence of foreshock cascading and aseismic pre-slip	55
2.8	Seismic and aseismic fault slip during the initiation phase of the 2017 Mw=6.9 Valparaíso earthquake.	58
2.8.1	Abstract	58
2.8.2	Introduction	59
2.8.3	Pre-seismic Transient Displacements captured by GPS	61
2.8.4	Centroid Moment Tensor catalog	62
2.8.5	Uncertainty on predicted co-seismic displacements	65
2.8.6	Partitioning between seismic and aseismic fault slip	68
2.8.7	Discussion and conclusion	69
2.8.8	Acknowledgments	71
3	Revisiting the 2015 Mw=8.3 Illapel earthquake. From kinematic rupture inversion to rupture dynamics.	73
3.1	Abstract	74
3.2	Introduction	74
3.3	Data	76
3.4	Methodology	79
3.5	Results	84
3.6	Discussion	87
3.6.1	Impact of Shallow slip.	88
3.6.2	Encircling rupture pattern during the 2015 Illapel earthquake.	90
3.6.3	Breakdown work of the 2015 $M_W = 8.3$ Illapel earthquake	93
3.7	Conclusion	96
3.8	Acknowledgments	99
4	General conclusions	101
	Appendices	105
A	Supporting Information for Seismic and aseismic fault slip during the initiation phase of the 2017 Mw=6.9 Valparaíso earthquake	107
B	Supporting Information for Revisiting the 2015 Mw=8.3 Illapel earthquake. From kinematic rupture inversion to rupture dynamics.	131
	List of Figures	145
	List of Tables	162
	References	163

General Introduction

Earthquakes are one of the most destructive natural phenomena in the world. Their occurrence can cause several millions of euros in damages and human casualties. For instance, the 1985 $M_W = 8$ Michoacan earthquake caused approximately between three and four billion dollars losses and 10,000 casualties [Hall and Beck, 1986, Singh et al., 1988]. As a further example, the 2011 $M_W = 9.1$ Tohoku earthquake resulted in 19,747 casualties and the nuclear crisis of Fukushima nuclear center [Kazama and Noda, 2012]. For this reason, it is crucial to understand the mechanisms at their origin and how we can prevent future catastrophes.

With the validation of the continental drift theory in the 60s [Le Pichon, 1968, McKenzie and Parker, 1967], scientists could link earthquake origin to a geodynamic process. Efforts trying to explain earthquake mechanisms can be dated up to the early 1900s, with the elastic rebound theory done by Reid [1910]. Earthquakes are caused by the accumulation of potential energy (mainly elastic and gravitational energy) in the environment surrounding a locked fault. When the fault yield stress is reached, this stored energy is liberated in the form of seismic waves, fracture energy, and thermal energy (Figure 15). In general, earthquakes obey this principle, however, there are other phenomena that also interact in this cycle.

The second half of the XIXth century is marked by significant advances in the understanding of earthquake ruptures. For example, the first finite fault slip models for California earthquakes were developed by Trifunac [1974], Hartzell and Helmberger [1982], and Olson and Apsel [1982]. Simultaneously, the asperity model was proposed to explain earthquake observations [Aki, 1979, Das and Aki, 1977, Lay and Kanamori, 1981, Lay et al., 1982]. According to this conceptual model, faults are segmented with areas of high strength called asperities separated by weak stress barriers.

Assuming that such rupture segmentation is persistent, this model states that an asperity can break regularly with the quasiperiodic occurrence of a "characteristic

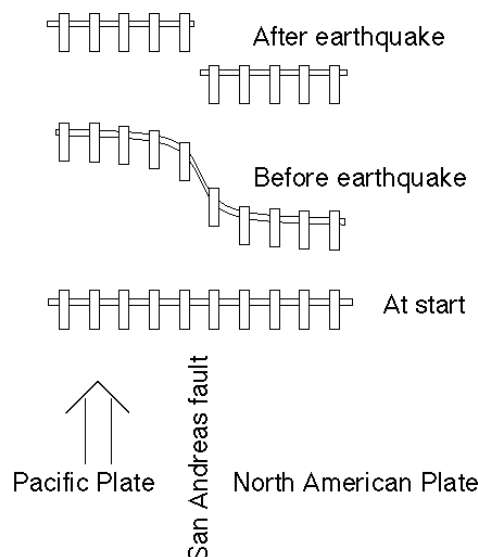


Figure 15: Example of Elastic Rebound theory for the San Andreas fault. In a first stage, stress is accumulated on the fault as a consequence of plates interaction. Then energy will be accumulated until reaching the yield stress. Finally, the fault will liberate this energy. Figure from USGS website <https://earthquake.usgs.gov/>.

earthquake" with a similar rupture extent and seismic moment. However, actual earthquake observations show that fault behavior is much more complex. If we consider a simple isolated fault system, three different behaviors can be described (Figure 16) [see Shimazaki and Nakata, 1980, Shearer, 2019]: (1) if these properties are invariant, we have a predictable cycle with the periodic occurrence of a characteristic earthquake. (2) If in this system, the static friction is invariant but the dynamic friction is not, we will be in a case where we can predict the time of recurrence. (3) If the dynamic friction is constant, but not the static friction, we will be able to estimate the slip, but not the recurrence time. In reality, the behavior is even more complex considering the interactions of multiple asperities [Kaneko et al., 2010] or long-range dynamic interactions [Cruz-Atienza et al., 2021, Obara and Kato, 2016, Zigone et al., 2012]. Such complexity leads researchers to the question of how feasible the earthquake predictability is and how can we characterize earthquake sources.

With the arrival of more advanced technology in the XXth century, new phenomena affecting fault behavior were discovered [Beroza and Ide, 2011].

For example, Dragert et al. [2001] discovered a new sort of event called slow slip events (SSE). SSEs are characterized by a slow displacement that lasts from days to months. In contrast with earthquakes, SSE releases energy in an aseismic way, i.e., there are no detectable seismic waves. In this regard, the occurrence of aseismic slip in earthquake initiation phases has been a matter of study for the last two

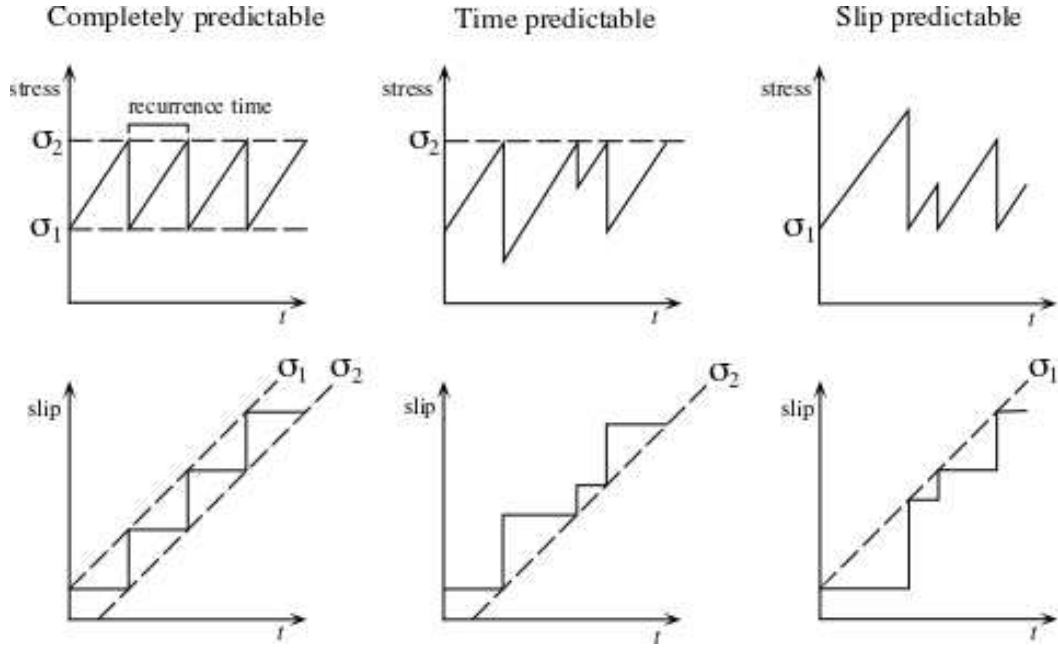


Figure 16: Simple models of recurring earthquakes parameterized by a yield stress level σ_2 (related to the static friction on the fault) and a post earthquake stress level σ_1 (related to the dynamic friction on the fault). This diagram is based on [Shimazaki and Nakata, 1980]. Figure from Shearer [2019].

decades [Das and Aki, 1977, Mignan, 2014].

Along with slow slip events, tectonic tremors, also called non-volcanic tremors were discovered [Obara, 2002]. These seismic events are known for non-having an impulsive phase and mostly come along with SSEs, depending on the geological context. Finally, it is worth mentioning also the existence of low-frequency earthquakes (LFEs) and very low-frequency earthquakes (VLFs), that are thought to constitute a large part of tectonic tremors [Ito et al., 2007, Shelly et al., 2006, 2007].

The discovery of SSEs and tectonic tremors leads scientists to a better understanding of earthquake physics and tectonic settings. We show a schematic representation of how these phenomena interact in subduction zones (Figure 17, from Lay [2015]). Domain A is where slow earthquakes (often referred to as tsunami earthquakes [Kanamori, 1972]) can occur. Domain B is the central region for megathrust earthquake development. Domain C is a transition region where seismic activity can still be present. Finally, domain D is characterized by the occurrence of SSEs and tectonic tremors. We can see that earthquakes are represented as red patches embedded in the fault region, surrounded by conditional stability regions (i.e., regions that sometimes fail seismically and sometimes slip aseismically depending on the stress conditions). Even though there are some similarities between this model and the asperity model, this model describes variability in terms of interface

frictional properties rather than strength variations as in the asperity model.

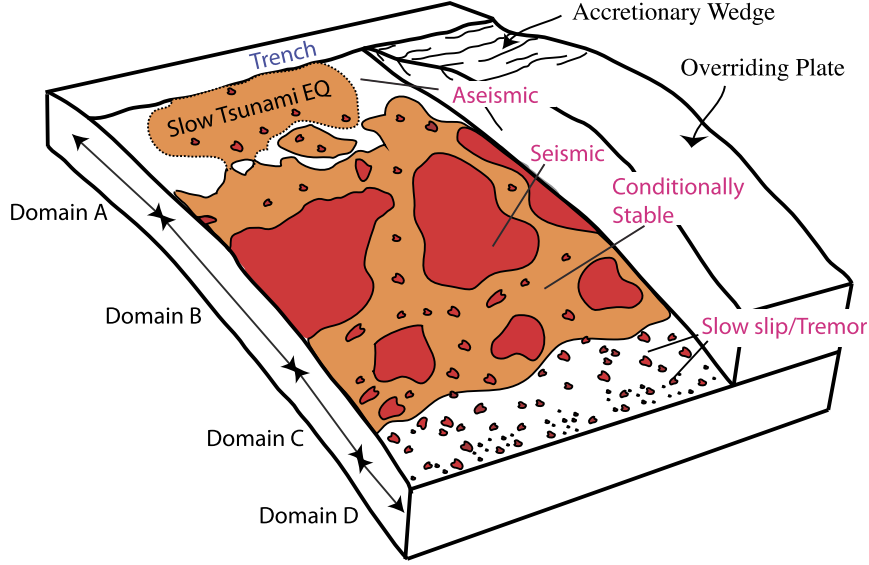


Figure 17: Schematic characterization of the megathrust frictional environment. Domain description is as follows: A: near-trench domain where tsunami earthquakes or anelastic deformation and stable sliding occur; B: central megathrust domain where large slip occurs with minor short-period seismic radiation; C: down-dip domain where moderate slip occurs with significant coherent short-period seismic radiation; and D: transitional domain, only present in some areas, typically with a young subducting plate, where SSEs, LFEs and tectonic tremors occur. Regions of unstable frictional sliding are red regions labeled “seismic”. Regions of aseismic stable or episodic sliding are white regions labeled “aseismic”. Orange areas are conditional stability [Scholz, 1998] regions, which displace aseismically except when accelerated by failure of adjacent seismic patches. Figure from Lay [2015].

The described models explain the earthquake occurrence by differences in frictional or strength properties. Although these properties were considered for a long time to be a permanent feature, the accumulation of observations over long periods shows that there might be long-term modifications in the fault behavior. For example, observations of the 2011 $M_W = 9.1$ Tohoku earthquake suggest that it was preceded by 15 years of progressive unlocking of the fault interface [Mavrommatis et al., 2014, Marill et al., 2021, Yokota and Koketsu, 2015].

Besides, another crucial aspect of earthquake source description is the imaging of the fault slip. Detailed characterization of fault slip is relevant since we can use it to increase our knowledge in seismology. For instance, we can develop fault slip-based scaling laws [Mai and Beroza, 2000, Manighetti et al., 2005, Strasser et al., 2010]. Besides, we can improve dynamic rupture models, which lead to a better understanding of earthquake rupture physics [Day et al., 1998, Causse et al., 2014, Heaton, 1990, Ide and Takeo, 1997]. In this regard, fault imaging results in a demanding task since we are dealing with an ill-posed problem inversion, for which

we can obtain different solutions using similar datasets. We can see in Figure 18 four different finite fault slip solutions for the 1999 $M_W = 7.6$ Izmit earthquake. Such non-uniqueness in the slip models can lead to distinct interpretations.

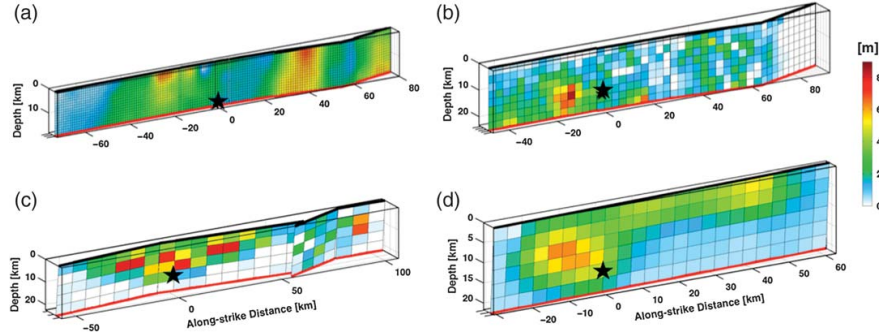


Figure 18: Selected finite-source rupture models for the 1999 $M_W = 7.6$ Izmit earthquake (Turkey), obtained using different inversion strategies and different datasets. Black stars mark the hypocenter. Colors indicate fault slip (in meters). Note the pronounced dissimilarities of the slip distributions for this event. The inversion results are from (a) Bouchon et al. [2002], (b) Sekiguchi and Iwata [2002], (c) Delouis et al. [2002], and (d) Yagi and Kikuchi [2000]. Figure from Mai et al. [2016].

The overall goal of this thesis is to conduct an extensive study of the source, covering different aspects of earthquake characterization. Firstly, we analyze the initiation phase of earthquakes, trying to glimpse details regarding the first stages of the rupture. Secondly, we focus on complex fault slip inversions, for which Bayesian tools have demonstrated to clarify some of the most complex patterns. This dissertation is organized as follows.

In chapter one, I detail the different inversion approaches used for obtaining co-seismic slip models. First, I present the different data sets that are used in inverse problems. Secondly, I describe the representation of earthquakes in point and extended sources. Then, I introduce the corresponding parameterization for point and extended sources. After, I describe the optimization-based inversion schemes used to obtain finite fault slip distributions. Finally, I present the Bayesian approach in inversion schemes. Additionally, I describe how kinematic models can be used to constrain rupture dynamics.

In chapter two, I first present the state-of-the-art regarding the initiation of earthquakes. I describe the different stages of earthquake ruptures and the current conceptual models that are under examination. Next, I present the application for the initiation phase of the 2017 $M_W = 6.9$ Valparaíso earthquake. We find that there are contributions of seismic and aseismic slip during the initiation phase of this earthquake. The results of this work have already been published and are included in this chapter.

In chapter three, we apply a Bayesian slip inversion approach described in chapter one to investigate the rupture process of the 2015 $M_W = 8.3$ Illapel earthquake. We introduce and compare a new methodology to account for prediction/epistemic uncertainty. By incorporating different datasets, we were able to characterize the complex rupture of this event. The results of this work will be soon submitted as a scientific research article to the journal Geophysical Journal International and are included in this chapter.

Finally, chapter four presents a general conclusion. We also discuss the impact our results could have on the current challenges of seismology, especially on the understanding of earthquake source physics.

Source Inversion

1.1 Summary

During my Ph.D., I applied different inversion techniques to obtain Moment Tensor (MT) solutions and slip models for large earthquakes in Chile. In this chapter, we will describe the observations, the forward model, and the inversion methods that can be used in source inversions. More precisely, we will describe the forward modeling for a point source and a finite-fault along with their parametrization. Subsequently, we will present two approaches for earthquake source inversions, the optimization, and Bayesian inversions schemes. For the Bayesian scheme, we describe some Bayesian samplers that are frequently used in earthquake studies. Finally, we discuss how dynamic parameters can be derived from kinematic slip models.

1.2 How to characterize the seismic rupture?

Seismology is a relatively new science that explores the interior of the Earth using indirect methodologies [Agnew et al., 2002]. These indirect measurements are conducted on the surface, so we don't have any in-situ measure of the phenomena. In seismology, for example, displacements or stress are difficult to measure directly for earthquakes at depth. Geophysics developed a broad range of inverse methods to solve such Earth-related problems [Menke, 2012]. Since earthquakes generally occur on faults for which only have indirect measurements, inversion theory turns out to be instrumental for earthquake studies. In the inverse theory, there are four

main elements that we describe below (see Figure 1.1).

The observations d_{obs} , are the measurement that we can assess on the Earth surface. In the case of earthquake studies, they mainly correspond to ground motion measurements (displacement, velocity or acceleration) but can also correspond to tsunami wave height (often derived from sea bottom pressure gauges).

The forward problem is the theory that explain the response of the medium given the model parameters. For example, it can be the theory describing the gravitational field for a given pair of masses. In seismology, we use the forward theory allowing us to predict the displacement field caused by a given earthquake (i.e., assuming a rupture geometry and slip distribution). The forward model is represented as $G(\mathbf{m})$, where \mathbf{m} are the model parameters to be used to explain the observations. The relation between \mathbf{m} and d_{obs} , (i.e., $d_{\text{obs}} = G(\mathbf{m})$) can be linear or non-linear.

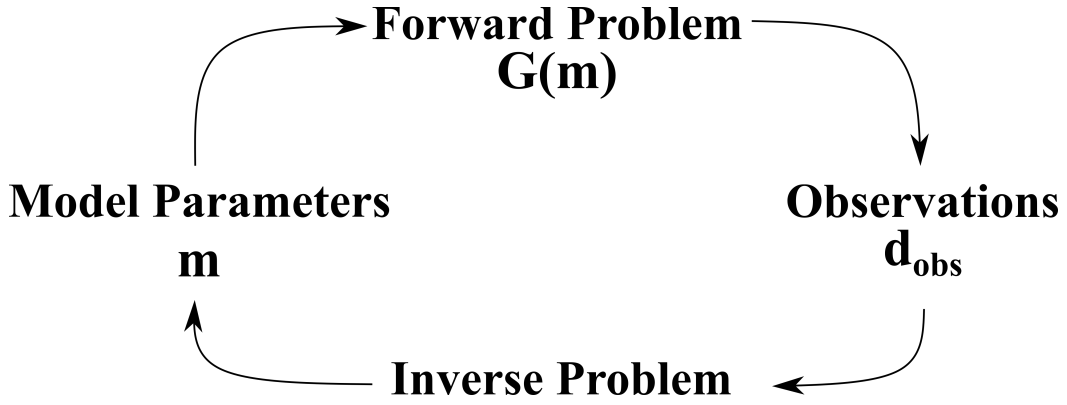


Figure 1.1: Scheme of inversion theory.

In geophysics, we often want to know the causes at the origin of an observed phenomena. With this purpose, we need to recover the model parameters \mathbf{m} that explain the observations d_{obs} . The underlying assumption is that we can find a series of parameters \mathbf{m}_{est} for which the following expression is true:

$$d_{\text{obs}} \approx G(\mathbf{m}_{\text{est}}) \quad (1.1)$$

The parameters \mathbf{m}_{est} can be estimated by different approaches, depending on the nonlinearity of the problem. Some of these methods are described in section 1.6.

1.3 Observations

By using observations available at the Earth surface, seismologists can explore the interior of the Earth. For example, tomographies unraveling the composition

of the Earth can be made using seismic records from earthquakes. Seismologists and geodesists usually classify data in two main categories: kinematic and static data. Kinematic data correspond to seismic data collected from accelerometers, seismometers, or High Rate Global Positioning System (HRGPS) stations. On the other hand, static data comprises diverse types of data, such as Global Navigation Satellite System (GNSS) displacements, Interferometric Synthetic Aperture Radar (InSAR) images, and tsunami waveform signals. The static data is only sensitive to earthquake final slip distributions, while kinematic data can capture features from the rupture history. Although tsunami data is usually sensitive to the final slip distribution, it can also provide information regarding the rupture history of very large earthquakes (i.e., with magnitudes $M_W > 8.5$).

1.3.1 Seismic Data

In seismology, we employ the temporal variation of the displacement field on the surface. This displacement field, generally represented as $u(x, t)$, is usually measured by seismometers that measure the ground velocity (the derivative of displacement). After instrument correction, such velocity records can be integrated to displacement waveforms. During this thesis, we also used strong-motion sensors that are usually accelerographs (i.e., measuring the ground acceleration).

The first seismometers were created at the end of the XIXth century [Rebeur-Paschwitz, 1895]. We have, for example, the torsion seismometer created by Wood & Anderson [Anderson and Wood, 1925]. These first seismometers were based on simple mechanical principles. For example, the first vertical seismometers were based on the inertia of a suspended mass connected to a spring. Figure 1.2 depicts a simple scheme of the operation of mechanical instruments. When an earthquake happens, the ground around the seismometer starts moving. Because the mass is connected to a spring, the displacement will be distinct from the surrounding ground displacement. The differential motion between the mass and the ground is measured using the voltage induced in a coil by the motion of a magnet. The behavior of the spring and the mass is well-known and is called the instrument response of the seismometer.

The signal recorded on the seismometer represents the temporal displacement signal convolved with the instrument response. In the angular frequency domain ω , the observed signal $S(\omega)$ corresponds to:

$$S(\omega) = I_D(\omega) U(\omega), \quad (1.2)$$

1.3. OBSERVATIONS

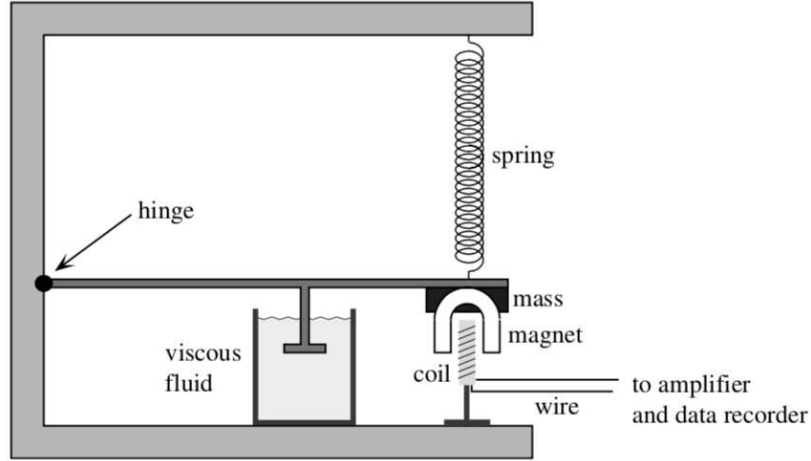


Figure 1.2: A simple inertial seismometer for measuring vertical motion. Movement of the suspended magnet induces a voltage in the coil; this signal is then amplified and recorded. Figure from Shearer [2019].

where $U(\omega)$ is the ground displacement, and $I_D(\omega)$ is the instrument response. Depending on the kind of instrument, the signal S can be approximately proportional to the ground velocity (seismometer) or to the ground acceleration (accelerometer). To work with the recorded signal, they need to be corrected for the instrumental response. The most common approach to correct is to deconvolute the instrumental response from the signal. Thus, to extract the ground displacement, we follow:

$$U(\omega) \sim F(\omega) \frac{S(\omega)}{I_D(\omega)}, \quad (1.3)$$

where $F(\omega)$ is a band-pass filter including the frequencies of interest applied to avoid any other effect due to the instrument. The response of the instrument must be a known function. In this manner, we can recover the actual ground motion and minimize any effect due to the instrument response. For example, the ideal seismometer would have a known wide velocity flat response through the entire frequency domain. The first mechanical instruments had a flat response in displacement at high frequencies (e.g. Wiechert, $T_0 \approx 10$ s) but the gain was limited. With the addition of a coil-magnet transducer (e.g. Galitzine) the gain was improved but the response became flat in velocity in a narrow frequency band (Figure 1.3). Thankfully, the range of frequencies with flat response in velocity has improved with the arrival of broadband seismometers. These new broadband seismometers operate as force-feedback systems. There are many other sources of noise in seismograms, such as the ambient noise induced by ocean-earth solid interactions and long-period noise induced by pressure variations.

Strong motions are instruments with low gain, often with a flat frequency response in

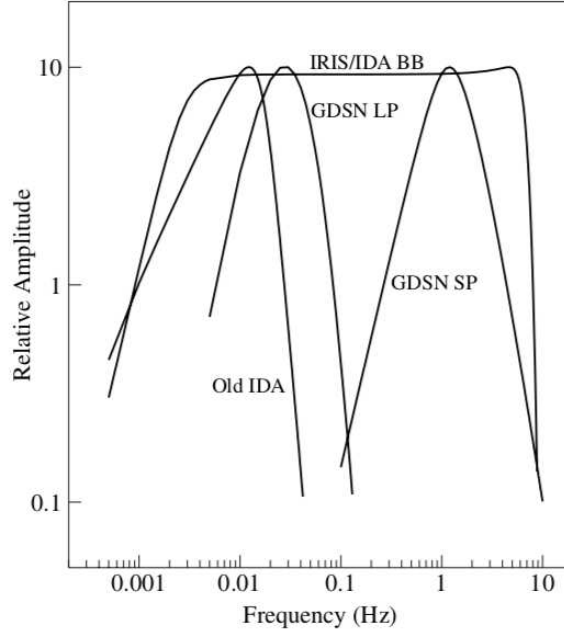


Figure 1.3: Velocity response functions for four different vertical-component instruments (old IDA station ALE, long and short-period channels for the GDSN station COL, and IRIS/IDA station ALE). Figure from Shearer [2019].

acceleration. Thanks to the low gain feature, these instruments don't easily saturate due to the large shaking in the vicinity of large earthquakes. Therefore, they are frequently used in earthquake source studies. In theory, we can integrate from acceleration to displacement. Firstly, to obtain the corresponding velocity, we would have to integrate the acceleration records as:

$$v(t) = \int A(t) dt + c \quad (1.4)$$

Theoretically, we consider the constant c should be equal to zero. However, in practice, there is a drift effect. This effect is due to various sources of instrumental variations, such as the transducer hysteresis of the measurement system or the gravity effect due to ground tilting. The impact of this drift has been largely studied by diverse authors [Boore and Bommer, 2005, Iwan et al., 1985]. Different techniques have been suggested to correct strong-motion records from spurious signals, including the drift shift [e.g., Bock et al., 2011, Chao et al., 2010, Graizer, 1979, Wang et al., 2011]. In Figure 1.4, we show the obtained seismogram from integrated acceleration. We notice a drifting effect, particularly in the second part of the signal. In this case, the effect was due to the large shake experienced by the recording instrument.

Seismic data is chosen depending on the aim of the study. For example, broadband data are often used at teleseismic distances (30-90 degrees) for diverse source

1.3. OBSERVATIONS

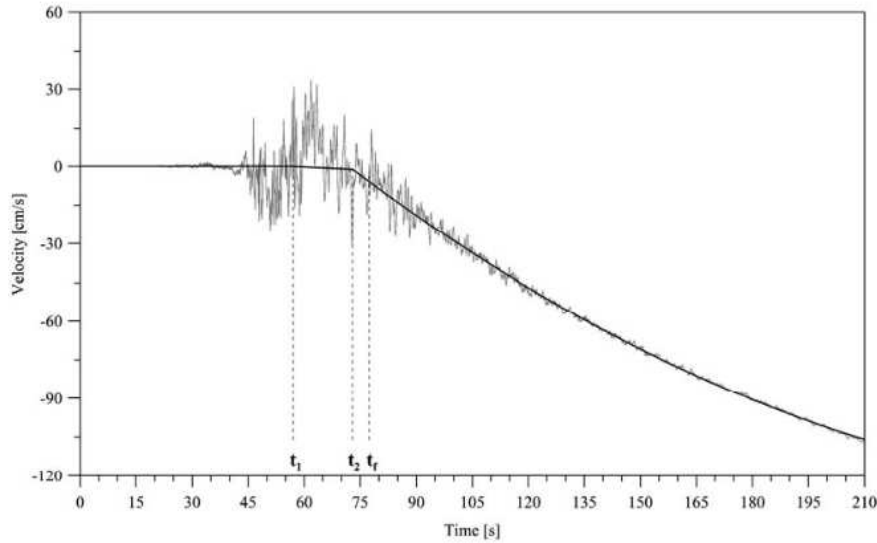


Figure 1.4: Example of velocitogram integrated from an accelerometer record at station 51JYC (31.96° N, 104.98° E) from the 2008 Wenchuan earthquake with inconstant baseline shift. The smooth line shows the nonlinear trend correction on velocity determined using the automatic scheme presented in Wang et al. [2011]. Figure from Wang et al. [2011].

studies (back projection, focal mechanism, etc). For finite fault studies, we usually employ near-field strong-motion records and/or broadband seismograms recorded at teleseismic to avoid saturation.

With the improvement of the sampling rate of GPS, geoscientists can now employ these instruments to sample the displacement on the ground with a high sampling rate. These new measurements called the High Rate Global Positioning System (HRGPS), has brought new opportunities to earthquake study [Bock and Melgar, 2016, Crowell et al., 2012, Geng et al., 2013, Melgar et al., 2015]. We recommend the following reading for further information about seismic data processing: Havskov and Alguacil [2004], Havskov and Ottemoller [2010].

1.3.2 GNSS data

Among geodetic data, we find the Global Navigation Satellite Systems (GNSS). Among GNSS, we can name the Global Positioning System (GPS) from the USA, the European system Galileo, and the Russian Global Navigation Satellite System (GLONASS). These measurements have been of growing importance in earthquake studies over the last 30 years. This technology started in the 70s decade with the launch of the first GPS satellite in 1978.

GNSS measurements rely on a system of reference from a satellite's constellation,

1.3. OBSERVATIONS

with which we can locate a point on the surface's Earth. This location is made by relative measurements of the phase of radiofrequency signals for each satellite. Then, a triangulation between satellites is conducted. For this reason, the resolution of GNSS largely depends on the number of satellites available at the observation time. Because the measurement depends on signals traveling through different mediums in a rotational Earth, corrections due to the atmosphere and rotation are necessary [Altamimi et al., 2016, Bock et al., 2000]. At present, two principal software packages are used to process GPS data: GAMIT, a software developed by MIT (<http://geoweb.mit.edu/gg/>), and GIPSY, developed by the Jet Propulsion Laboratory in Caltech (<https://gipsy-oasis.jpl.nasa.gov/>).

In seismology, we can employ permanent or campaign GNSS stations to study seismic events. When we use permanent stations, we measure the location of the corresponding station before and after the earthquake. Thus, we quantify the permanent static displacement produced by the seismic event [e.g., Matsu'ura et al., 2007, Moreno et al., 2009]. In Figure 1.5, we observe the daily displacement quantified in GPS stations in the Parkfield region. These time-series show clear coseismic offsets associated with earthquakes occurring in 2003 and 2004. It also shows post-seismic deformations following both events.

Survey GNSS data requires more careful interpretation since such measurements can incorporate displacement induced by a range of phenomena taking place in the region. Among these phenomena, we can mention interseismic and post-seismic displacements, as well as coseismic displacement caused by aftershocks [Klein et al., 2017, Twardzik et al., 2021].

As we discussed in the previous section, the last decade has seen a considerable development of High-Rate GPS (a GPS with a sampling rate ≥ 1 Hz). Such high sampling rate allows the treatment of the HRPGS displacements as seismograms and allows us to perform kinematic studies using HRGPS records. The general advantages are: (1) HRGPS provides direct measurements of ground displacement, we thus avoid integration issues (like for the acceleration signals), and (2) HRPGS signals don't saturate. Unfortunately, HRGPS observations are much noisier than seismological records, which prevent the use of such data for moderate sized or distant earthquakes. Moreover, HRGPS sampling rate is still relatively limited, which prevent the observation of high frequency waves.

1.3. OBSERVATIONS

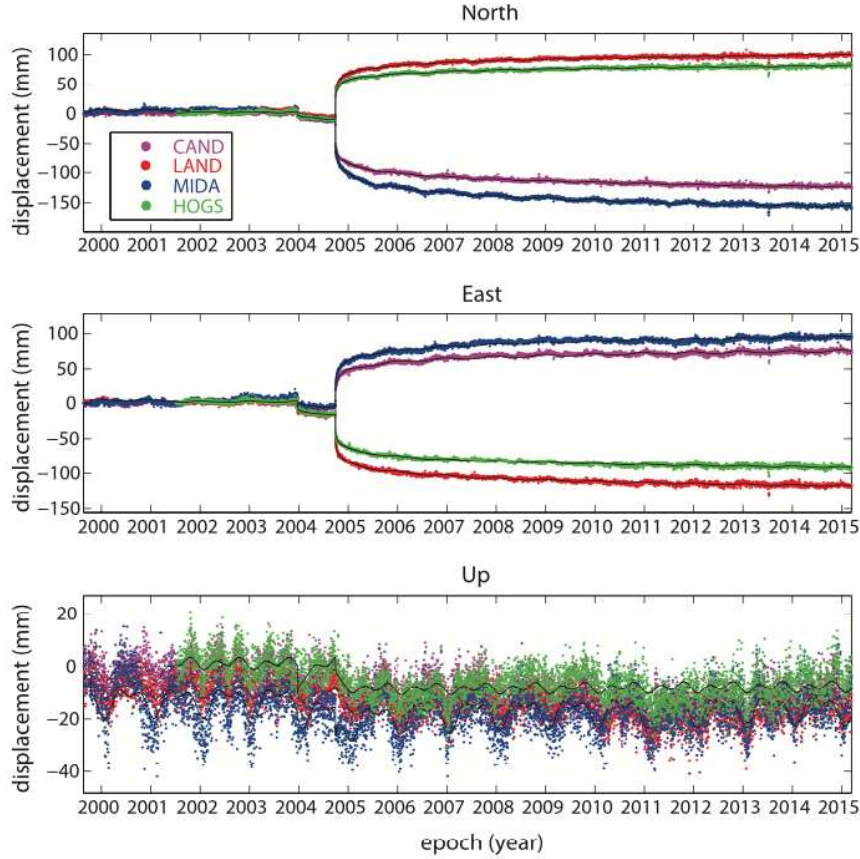


Figure 1.5: Detrended daily displacement time series of four continuous GPS (cGPS) stations spanning nearly 15 years in the Parkfield, California region, in north, east, and up components. The region experienced two earthquakes in this period (26 December 2003 $M_W = 6.6$ San Simeon and 28 September 2004 $M_W = 6.0$ Parkfield), which generated both coseismic and postseismic deformation. The stations span both sides of the San Andreas fault. Prepared by Lina Su. Figure from Bock and Melgar [2016].

1.3.3 InSAR images

Satellite data is also commonly employed to study earthquakes. We have, for example, the Synthetic-Aperture Radar (SAR) images that we can use to measure the ground deformation [Curlander and McDonough, 1991]. This technique is called Interferometric Synthetic-Aperture Radar (InSAR), and it is often used to quantify the coseismic displacement provoked by an earthquake. An extensive study of the InSAR methodology can be found in Jolivet [in French 2011] and Simons and Rosen [2007]. It is also worth mentioning the pioneering studies of Massonnet et al. [1993] and Zebker et al. [1994] that produced InSAR data to image the displacement caused by the 1992 $M_W = 7.3$ Landers earthquake.

The general principle of InSAR is as follows: We have a satellite with a known orbit

1.3. OBSERVATIONS

covering a region on the Earth with a fixed recurrent period. This satellite throws a series of electromagnetic pulses that are then reflected on the ground, back to the satellite. The phase difference between the received signals recorded sequentially in the same region reflects a change, for example, induced by the displacement of the ground between two consecutive passes. As the GNSS data, SAR images need corrections since they are affected by atmospheric effects and uncertainties in satellite orbits [Agram and Simons, 2015, Dalaison and Jolivet, 2020, Jolivet and Simons, 2018]. Because InSAR images depend on the recurrence time of the satellite, they are also affected by postseismic deformation and interseismic displacement.

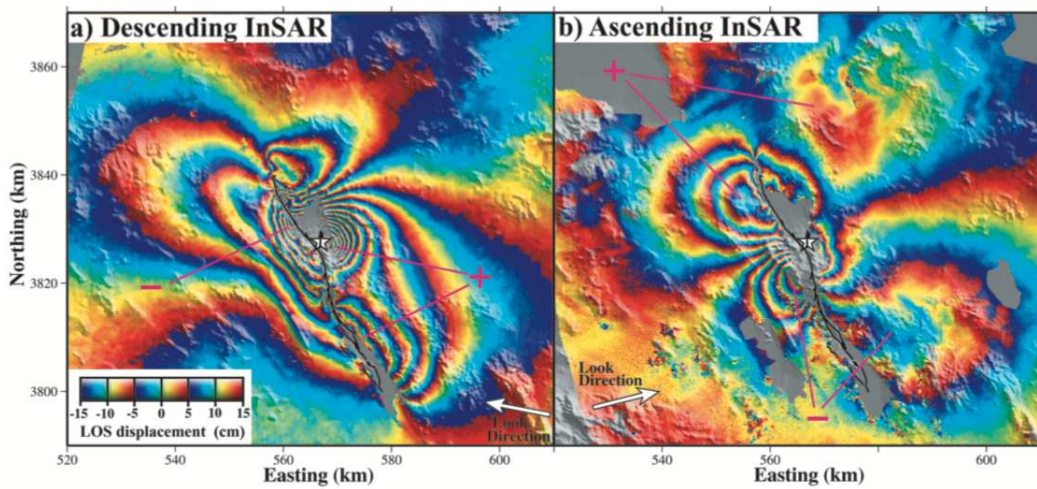


Figure 1.6: (a) Descending and (b) ascending interferograms showing the deformation of the Hector Mine earthquake. Each color cycle represents 10 cm of line-of-sight (LOS) displacement toward (yellow–red–blue) or away from (yellow–blue–red) the satellite. Arrows show the horizontal component of the look direction from the radar satellites. Purple + and - signs point to areas of positive and negative LOS displacement. The mapped fault trace is shown as thick line and the epicenter is denoted with a star. Coordinates are universal transverse Mercator (UTM) coordinates (zone 115) in kilometers. Figure from Jónsson et al. [2002].

In Figure 1.6, we show an example of InSAR displacements for the 1999 $M_W = 7.1$ Hector Mine, California earthquake, for which Jónsson et al. [2002] obtained a fault slip distribution. We observe two different images that correspond to the ascending and descending orbits.

As described above, satellites can record InSAR images in a recurrence period. This systematic measurement allows scientists to explore fault deformation evolution in time and space. For example, Rousset et al. [2016] detect an aseismic fault slip in the Anatolian fault from July 2013 to May 2014. This detection was made thanks to a series of approximately 205 InSAR images.

1.3.4 Tsunami Data

We have described data that are essentially obtained for inland regions, either in the form of GPS displacements, seismograms, or InSAR images. However, we can also use the ocean waves produced by earthquakes located under sea. At present, there are different equipment deployed in the sea to measure sea-level changes. One of this equipment is the Deep-ocean Assessment and Reporting of Tsunamis (DART) buoy network. The original network was installed by the National Oceanic and Atmospheric Administration in 2001. The DART's purpose is to detect tsunamis in the Pacific Ocean and also in the Indian and North-Atlantic Oceans, mainly [Meinig et al., 2005] (<https://www.ndbc.noaa.gov/dart/dart.shtml>).

Estimates of tsunami wave heights are crucial since megathrust earthquakes, such as the 2004 $M_W = 9.2$ Sumatra earthquake [Lay et al., 2005], have demonstrated to have devastating effects on society. For this reason, several works focusing on developing tsunami warnings have been developed [Allen and Greenslade, 2008, Melgar et al., 2016a, Ohta et al., 2012]. Aside from the improvement in early warning, tsunami data can also be used to study earthquake ruptures and create slip models. The first pioneer studies using tsunami data were conducted by Satake [1989] for earthquakes in the Japan trench. At present, using tsunami data is a common practice in finite fault inversions [Duputel et al., 2015, Gombert et al., 2018b].

1.4 Forward problem

In this section, we present the forward problem addressing the displacement fields produced by earthquake sources. More specifically, we will start describing the representation theorem and then continue with the displacement field generated by point and extended sources.

Earthquakes are usually generated in faults embedded in the crust (but can also be created by explosions). For this reason, natural seismic sources are represented as dislocations or discontinuities in the displacement field. We can also describe this dislocation with a set of body forces [Burridge and Knopoff, 1964]. To model seismic sources, we follow the notation and treatment of Aki and Richards [2002, chapter 3.]. Using the representation theorem, we consider an earthquake as a discontinuity in the displacement field $\Delta \mathbf{u}(\xi, \tau)$ occurring in space at any point ξ on the surface Σ , at a given rupture time τ . We can then describe the displacement

field $\mathbf{u}(\mathbf{x}, t)$ observed at the position \mathbf{x} and at time t as:

$$u_i(\mathbf{x}, t) = \int_0^T d\tau \int_{\Sigma} \Delta u_j(\xi, \tau) c_{j k p q}(\xi) \nu_k(\xi) G_{i p, q}(x, t; \xi, \tau) d\Sigma, \quad (1.5)$$

where G_{ip} is the Green function that describes the response in the component i at the receiver position and time (\mathbf{x}, t) due to a unit force applied in the direction p at position and time (ξ, τ) . The notation $(, q)$ symbolizes derivation with respect to the direction q . The properties of the medium at the surface are represented with the elastic coefficients tensor $c_{j k p q}$ and the normal vector to the discontinuity surface $\nu(\xi)$ at component k . The term T in the integral represents the total rupture duration of the earthquake.

1.4.1 Point source representation

Representing earthquakes as point sources is a common practice in seismology. We introduce the moment tensor, a concept that would help us create the point source representation. The moment tensor definition was originally proposed by Backus and Mulcahy [1976] to describe earthquake sources. For a detailed review of moment tensors, we recommend the work of Jost and Herrmann [1989]. In equation 1.5, we obtain the displacement field produced by a dislocation. We observe two integrals, one in time and one the fault surface. We can represent the integration in time by a convolution function as:

$$u_i(\mathbf{x}, t) = \int_{\Sigma} \Delta u_j c_{j k p q} \nu_k * G_{i p, q} d\Sigma. \quad (1.6)$$

From this expression, we can define the moment density tensor as:

$$m_{pq} = \Delta u_j c_{j k p q} \nu_k. \quad (1.7)$$

Each component of the moment density tensor represents a double force applied at each point of the dislocation surface [Aki and Richards, 2002]. In summary, we have three vector dipoles and three double couples with which we can represent any fault geometry by a linear combination (Figure 1.7). In terms of this symmetric tensor, which is time-dependent, the representation theorem describing the displacement field turns out to be:

$$u_i(\mathbf{x}, t) = \int_{\Sigma} m_{pq} * G_{i p, q} d\Sigma \quad (1.8)$$

We can consider the extended source in the surface Σ as a point source applied in

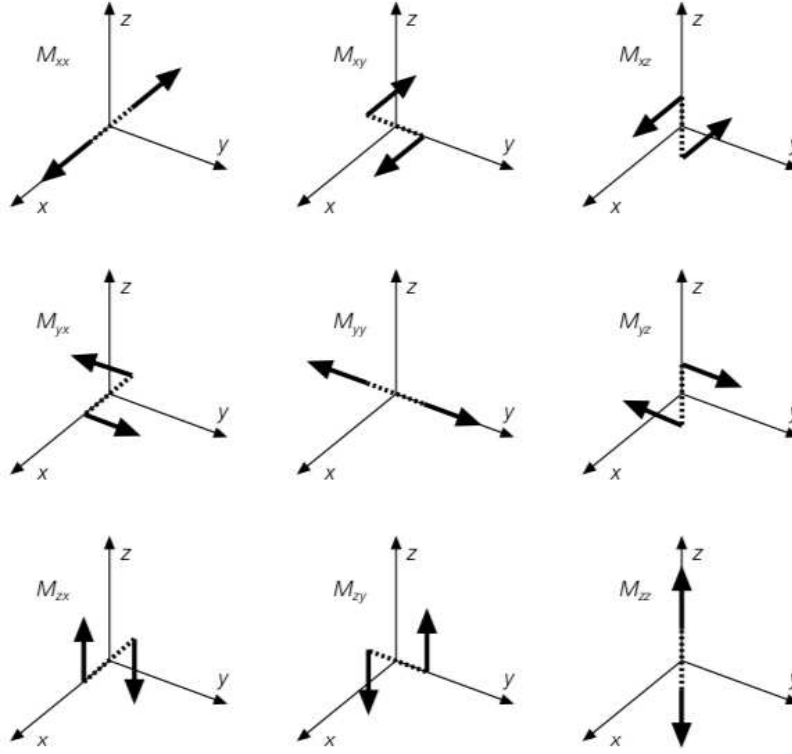


Figure 1.7: The nine force couples which are the components of the seismic moment tensor. Each consists of two opposite forces separated by a distance d (dashed line), so the net force is always zero. Figure from Stein and Wysession [2009].

the point ξ^0 . In this case, we define the moment tensor as:

$$M_{pq} = \int_{\Sigma} m_{pq} d\Sigma = \int_{\Sigma} \Delta u_j(\xi, \tau) c_{j k p q}(\xi) \nu_k(\xi) d\Sigma, \quad (1.9)$$

with a displacement field:

$$u_i(\mathbf{x}, t) = M_{pq} * G_{ip,q}. \quad (1.10)$$

In this manner, the characterization of seismic sources is achieved by finding the different moment tensor components at the location ξ^0 . The best point source location is called the Centroid location, and the corresponding moment tensor is the Centroid Moment Tensor (CMT) [Dziewonski et al., 1981]. If we consider that the earthquake mechanism doesn't change during the rupture, we can separate the moment tensor terms as:

$$M_{pq}(\tau) = M_{pq} S(\tau), \quad (1.11)$$

where $S(\tau)$ is a normalized function describing the evolution of the rupture, from its initiation to its final displacement. M_{pq} is the static seismic moment tensor. We can calculate the scalar seismic moment corresponding to the static seismic moment

1.4. FORWARD PROBLEM

tensor as [Silver and Jordan, 1982]:

$$M_0 = \frac{1}{\sqrt{2}}(\mathbf{M} : \mathbf{M})^{1/2} \quad (1.12)$$

In practice, M_0 is usually estimated as $M_0 = \mu \bar{u} A$, with μ representing the shear modulus, A the rupture area, and \bar{u} the average fault displacement.

We consider the elastodynamic Green function solution due to a Heaviside function and express the displacement field (equation 1.5) in function of the moment tensor as:

$$u_i(\mathbf{x}, t) = \int_0^T M_{pq} \dot{S}(\tau) H_{ip,q}(\mathbf{x}, t; \xi^0, \tau) d\tau, \quad (1.13)$$

where $H_{ip,q}(\mathbf{x}, t; \xi^0, \tau)$ is the response to a Heaviside function, and $\dot{S}(\tau)$ is the time-derivative of the function describing the evolution of the rupture. This time-derivative function is commonly called the moment rate function and is used to characterize seismic ruptures at regional or teleseismic distances [Vallée et al., 2011]. In practice, because of its simplicity, a triangular isosceles function centered at the centroid time is used as a source time function [Dziewonski et al., 1981, Ekström et al., 2012, Kanamori and Rivera, 2008]. Recent studies conducted by Meier et al. [2017] show that most earthquakes follow this shape and are indistinguishable even between intermediate and large earthquakes.

1.4.2 Extended source

If we have enough quality data, we can also characterize seismic sources by taking into account their finiteness. We have, for example, the pioneering work of Haskell [1964] to model the energy due to a finite fault earthquake. We change the notation of the representation theorem (equation 1.5) and again consider the elastodynamic Green function solution due to a Heaviside function:

$$u_n(\mathbf{x}, t) = \int_0^T d\tau \int_{\Sigma} \Delta \dot{u}_i(\xi, \tau) c_{ikpq}(\xi) \nu_k(\xi) H_{np,q}(\mathbf{x}, t; \xi, \tau) d\Sigma. \quad (1.14)$$

We can now consider that the spatio-temporal distribution of dislocations, $\Delta \dot{u}_i(\xi, \tau)$, can be represented using a finite number of basis function N_s [Ide, 2015] as:

$$\Delta \dot{u}_i(\xi, \tau) = \sum_{j=1}^{N_s} p^j \hat{u}_i^j(\tau) \phi^j(\xi) h^j(\xi, \tau), \quad (1.15)$$

$\Delta \dot{u}_i(\xi, \tau)$ is the i th-component of the slip vector on the fault. Here $\hat{u}_i^j(\tau)$ is the i th component of the unit vector representing the slip direction at time τ . This direction

1.5. SOURCE PARAMETERIZATION

is always parallel to the fault plane and generally a time-dependent function. $\phi^j(\xi)$ is a spatial basis function, and $h^j(\xi, \tau)$ is a function describing the temporal evolution respectively. The coefficient p^j has a physical dimension that is equal to a volume. Both $\phi^j(\xi)$ and $h^j(\xi, \tau)$ are normalized so the integral is unity:

$$\int \int_{\Sigma} \phi^j(\xi) d\Sigma = 1; \int_{-\infty}^{+\infty} h^j(\xi, \tau) d\tau = 1 \quad (1.16)$$

In practice, most of the finite fault studies use rectangular or triangular subfault divisions. We can assume that $\phi^j(\xi)$ corresponds to boxcar functions. In this manner, we have for the subfault j :

$$\phi^j(\xi) = \begin{cases} \frac{1}{\Sigma^j} & \text{if } \xi \in \Sigma^j \\ 0 & \text{otherwise} \end{cases} \quad (1.17)$$

where Σ^j corresponds to the surface of the j th-subfault in equation 1.15. In this case, p^j represents the seismic potency of the subfault, which is the product of the subfault area and the slip amount. Another common choice for $\phi^j(\xi)$ is to use linear or cubic spline functions.

1.5 Source parameterization

1.5.1 Point source parameterization

The point source representation is helpful for the rapid estimation of earthquake characteristics as the magnitude and focal mechanism. We have, for example, the moment tensor inversion schemes of Kikuchi and Kanamori [1991] or Utku [2011]. Similarly, we have the results of the global CMT project that systematically calculates centroid moment tensor solutions [Ekström et al., 2012].

We describe, as an example, the parameterization used in the W-phase centroid moment tensor (WCMT) solution [Duputel et al., 2012b]. We chose to explain this scheme since we use a modified version of the W-phase package in the next section. This solution is based on the W-phase, a signal detected at low frequencies between the P-wave and S-wave arrival (Figure 1.8). The W-phase can be interpreted as a superposition of the first, second and third overtones of spheroidal modes or Rayleigh waves [Kanamori, 1993, Kanamori and Rivera, 2008]. Nowadays, the W-phase CMT project runs in real-time, obtaining solutions for intermediate and large magnitude earthquakes in various operating centers [Duputel et al., 2012b, Hayes

et al., 2009].

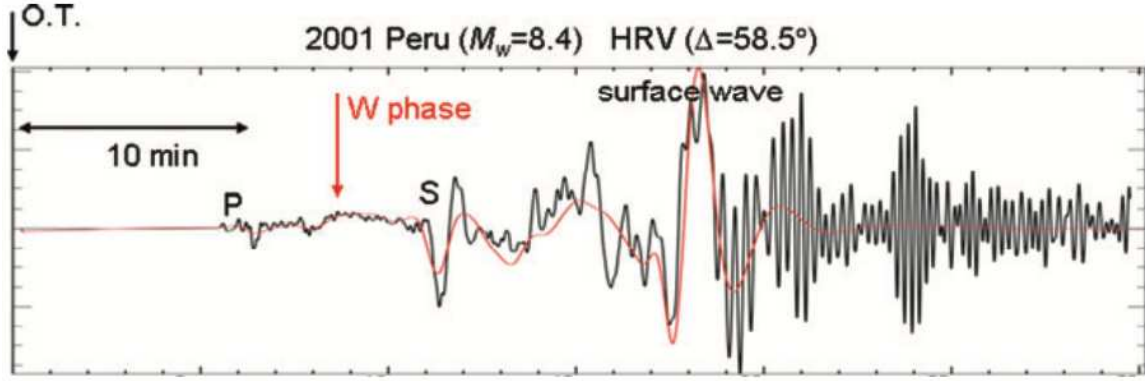


Figure 1.8: W phase from the 2001 Peruvian earthquake ($M_W = 8.4$) recorded at HRV, and the synthetic W phase computed by mode summation using the GCMT solution. Figure from Kanamori and Rivera [2008].

The WCMT inversion resolves for the moment tensor components, the coordinates of the centroid location, and the centroid time [Duputel et al., 2012b]. The moment tensor is described six independent components: $[M_{11}, M_{22}, M_{33}, M_{12}, M_{13}, M_{23}]$. We can also impose conditions to have a source without volumetric change:

$$\text{tr}(\mathbf{M}) = M_{11} + M_{22} + M_{33} = 0 \quad (1.18)$$

In spherical coordinates, the moment tensor components to invert are:

$$\mathbf{f} = [M_{rr}, M_{\theta\theta}, M_{\phi\phi}, M_{r\theta}, M_{r\phi}, M_{\theta\phi}]^t. \quad (1.19)$$

For the centroid location, we invert the 5 time-space coordinates:

$$\eta_c = [\theta_c, \phi_c, r_c, t_h, t_d]^t, \quad (1.20)$$

where θ_c is the colatitude, ϕ_c is the longitude, r_c the radius. The parameter t_h is the half duration (half-width of the proposed triangular moment rate function). The parameter t_d is the centroid delay (the temporal position of the center of the triangle, measured from the assumed origin time).

1.5.2 Source parameterization for an extended source - Static case

We now take into account the finiteness of the fault and obtain the final slip distribution due to a seismic rupture. In this regard, we have static data sets that are

1.5. SOURCE PARAMETERIZATION

only sensitive to the final slip distribution. To model these static data, we integrate equation 1.15 up to the final rupture time T . We obtain the final displacement as [Ide, 2015]:

$$\Delta u_i(\xi) = \sum_{j=1}^{N_s} p^j \hat{u}_i^j \phi^j(\xi), \quad (1.21)$$

where \hat{u}_i^j represents the rake direction of the final slip. This final slip distribution can be then expressed as a linear combination of two unit vectors on the fault plane:

$$\hat{u}_i^j = v_i^1 + v_i^2. \quad (1.22)$$

For example, we can use the strike-slip and dip-slip direction as unit vectors. If we substitute equation 1.22 into equation 1.21 and use the mentioned directions, we obtain:

$$\Delta u_i(\xi) = \sum_{j=1}^{N_s} (p^{j1} v_i^1 + p^{j2} v_i^2) \phi^j(\xi), \quad (1.23)$$

where p^{j1} and p^{j2} correspond to the coefficients of each unit vector, respectively. If we replace the previous equation into the representation theorem (equation 1.5), the displacement field can be expressed as:

$$u_i(\mathbf{x}) = \sum_{l=1}^{N_s} (p^{l1} v_j^1 + p^{l2} v_j^2) G_{ij}^l(\mathbf{x}) \quad (1.24)$$

With the Green function defined as:

$$G_{ij}^l(\mathbf{x}) = \int \int_{\Sigma} \phi^l(\xi) c_{j k p q}(\xi) \nu_k(\xi) G_{ip,q}(\mathbf{x}; \xi) d\Sigma(\xi) \quad (1.25)$$

If we use a sub fault parameterization, we have:

$$G_{ij}^l(\mathbf{x}) = \frac{1}{\Sigma^l} \int \int_{\Sigma^l} c_{j k p q}(\xi) \nu_k(\xi) G_{ip,q}(\mathbf{x}; \xi) d\Sigma(\xi) \quad (1.26)$$

where Σ^l corresponds to the subfault surface l for which $\phi^l(\xi) \neq 0$ (equation 1.17). We notice that we can characterize the slip distribution using the slip potency coefficients p^{l1} and p^{l2} . If we use this parameterization, the forward problem becomes linear, so the relation between \mathbf{d}_s and $\mathbf{G}(\mathbf{m})$ turns out to be:

$$\mathbf{d}_s = \mathbf{G}_s \mathbf{m}_s \quad (1.27)$$

where \mathbf{d}_s are the static data, \mathbf{G}_s the corresponding static Green function, and \mathbf{m}_s the slip potencies p^{l1} and p^{l2} for each subfault. The static Green functions correspond to

the analytical solution of the displacement field due to a dislocation [Okada, 1985, Steketee, 1958]. At present, there are different approaches developed to obtain the response of a displacement field in a layered medium [e.g., Zhu and Rivera, 2002] or 3D velocity models [Aagaard et al., 2013, e.g.].

1.5.3 Source parameterization for an extended source - Kinematic case

If we are interested in the temporal evolution of the rupture, we can use kinematic data that are sensitive to the slip history. On this subject, there are two main approaches used to study the rupture with kinematic data: the linear approach (Multi-time window method) and the nonlinear approach 1.9).

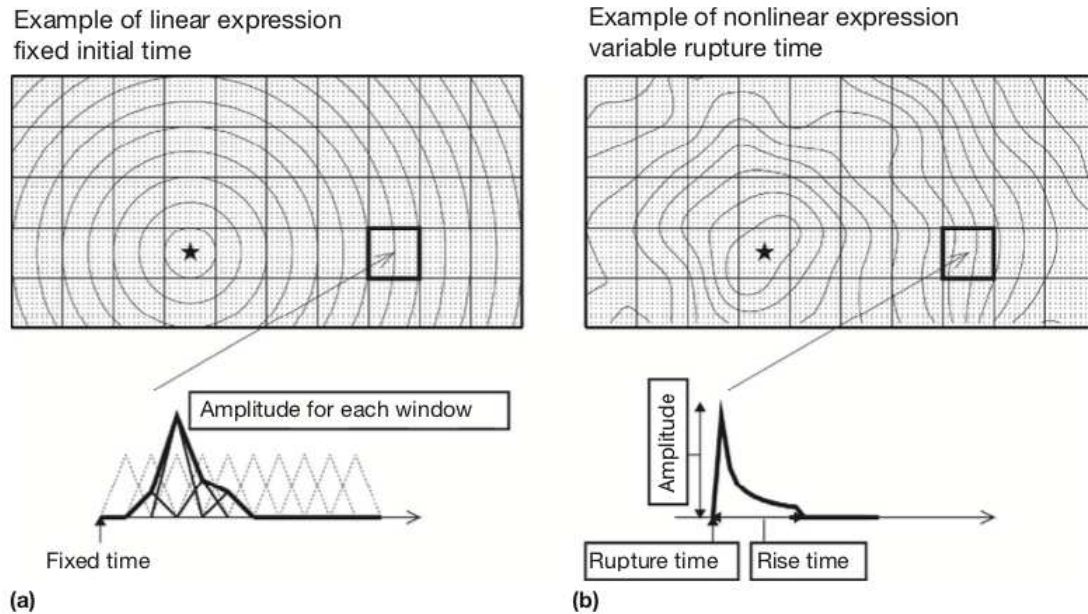


Figure 1.9: Schematic illustrations showing how to parameterize spatiotemporal slip distribution. The initial time of time function is shown by contours in each of the top figures. (a) Typical linear expression of the multi-time-window analysis. Unknown parameters are amplitude for each window. (b) An example of nonlinear expression, in which rupture time is also an unknown parameter. Figure from Ide [2015].

Linear approach - Multi-time window method

The multi-time window method is one of the most popular methods to study earthquakes. It was firstly proposed by Olson and Apsel [1982] and Hartzell and Helmberger [1982]. We show in Figure 1.9 (a) a schematic representation of this approach. Essentially, the method consists of the development of the function $\hat{u}_i^j(\tau)h^j(\xi, \tau)$

from equation 1.15 as a series of N_t coefficients q^k :

$$\hat{u}_i^j(\tau)h^j(\xi, \tau) = \sum_{k=1}^{N_t} q^k v_i^{jk} f(\tau - (k-1)\Delta\tau - \tau_0(\xi)), \quad (1.28)$$

where the unit vector v_i^{jk} indicates the direction of the slip vector for the j th spatial and k th temporal discrete unit in the spatiotemporal source volume. The function $f(\tau)$ is a temporal function that is zero for $\tau < 0$, with integration to infinity equal to unity. Commonly, we use a triangular function as $f(\tau)$ as shown in Figure 1.9 (a). We can see that for each index k , we have a triangular function with a delay $\Delta\tau$ that depends on k , and varies between the minimal rupture time $\tau = \tau_0(\xi)$ and a maximum rupture time $\tau = \tau_0(\xi) + (N_t - 1)\Delta\tau$. If we substitute the previous representation into equation 1.15, we obtain a representation in spatio-temporal basis functions for which we decompose the slip vector in two directions:

$$\Delta \dot{u}_i(\xi, \tau) = \sum_{j=1}^{N_s} \sum_{k=1}^{N_t} (p^{jk1} v_i^1 + p^{jk2} v_i^2) \phi^j(\xi) f(\tau - (k-1)\Delta\tau - \tau_0(\xi)), \quad (1.29)$$

where p^{jkl} is the seismic potency of the l th slip direction on the j th spatial and k th temporal discrete unit.

If we follow a similar approach as in the static case, we can substitute the equation 1.29 into the equation 1.5. Considering a boxcar function $\phi^j(\xi)$ for the j th subfault, and an initial rupture time $\tau_0(\xi) = \tau_0^j$, we obtain:

$$u_i(\mathbf{x}, t) = \sum_{l=1}^{N_s} \sum_{k=1}^{N_t} (p^{lk1} v_j^1 + p^{lk2} v_j^2) G_{ij}^{lk}(\mathbf{x}, t - (k-1)\Delta\tau - \tau_0^j) \quad (1.30)$$

with Green functions as:

$$G_{ij}^{lk}(\mathbf{x}, t) = \frac{1}{\Sigma^l} \int_0^T d\tau \int_{\Sigma^l} f(\tau) c_{j k p q}(\xi) \nu_k(\xi) H_{ip,q}(\mathbf{x}, t; \xi, \tau) d\Sigma(\xi). \quad (1.31)$$

As for the static case, we deal with a linear problem:

$$\mathbf{d}_k = \mathbf{G}_k \mathbf{m}_k \quad (1.32)$$

where \mathbf{d}_k are the kinematic data, \mathbf{G}_k the Green functions, i.e., the calculated waveforms for the spatio-temporal basis functions, and \mathbf{m}_k the coefficients p^{jkl} . As we discussed before, this parameterization is widely used since it permits the description of the kinematic source problem as a linear equations system. However, a disadvantage of this parameterization is that we need a large number of N_t functions

to model long earthquake ruptures, which increases the final number of parameters to invert. To overtake this issue, we can define a minimum rupture time for each subfault $\tau_0(\xi) = |\xi - \xi_0|/V_R^{max}$, where V_R^{max} is the maximum rupture velocity and ξ_0 the a priori hypocenter within the fault.

Nonlinear approach

In the multi-time window approach, we consider as known parameters the rupture time and the rupture velocity, being invariable between sub faults. However, such homogeneity is not necessarily true, so we parameterize the finite fault to take these variations into account. We observe in Figure 1.9 (b) how the different rupture velocities affect the evolution of the rupture and how the local source time function is distinct from the linear approach. We have in this approach the representation of $\Delta\dot{u}_i(\xi, \tau)$ as:

$$\Delta\dot{u}_i(\xi, \tau) = \sum_{j=1}^{N_s} \sum_{k=1}^{N_s} (p^{j1}v_i^1 + p^{j2}v_i^2)\phi^j(\xi)f(\tau - \tau^j, r^j), \quad (1.33)$$

where $f(\tau, r)$ is a function with null values for $\tau < 0$ and $\tau > r$, and with unity integral. τ^j correspond to the local initial rupture time, and r^j to the local rise time of the subfault j . The function $f(\tau, r)$, called in this approach moment rate function, is a known function and equal for all the sub faults, and it is not divided into temporal basis functions as for the multi-time window approach.

One important step of this technique is the selection of the moment rate function. The most common functions are the triangular and the boxcar function (Figure 1.10).. However, other more complex functions such as the Yoffe pulse or the Gaussian function are also used [Tinti et al., 2005b].

In this approach, we obtain a forward problem with a non-linear relation:

$$\mathbf{d}_k = \mathbf{G}_k(\mathbf{m}_k). \quad (1.34)$$

In this equation, \mathbf{d}_k represents the data. The function \mathbf{G}_k describes the predictions corresponding to the kinematic model \mathbf{m}_k . In contrast with the multi-time window approach, this parameterization is not lineal. The model parameters \mathbf{m}_k are the coefficients p^{jl} , the initial rupture time τ^j , and the rise time r^j . In practice, it is possible to model the rupture velocity V_R^j instead of the rupture time τ^j [e.g., Minson et al., 2013]. This procedure is conducted by mapping the hypocenter location and rupture velocity field into initial rupture times at each patch, implying the resolution

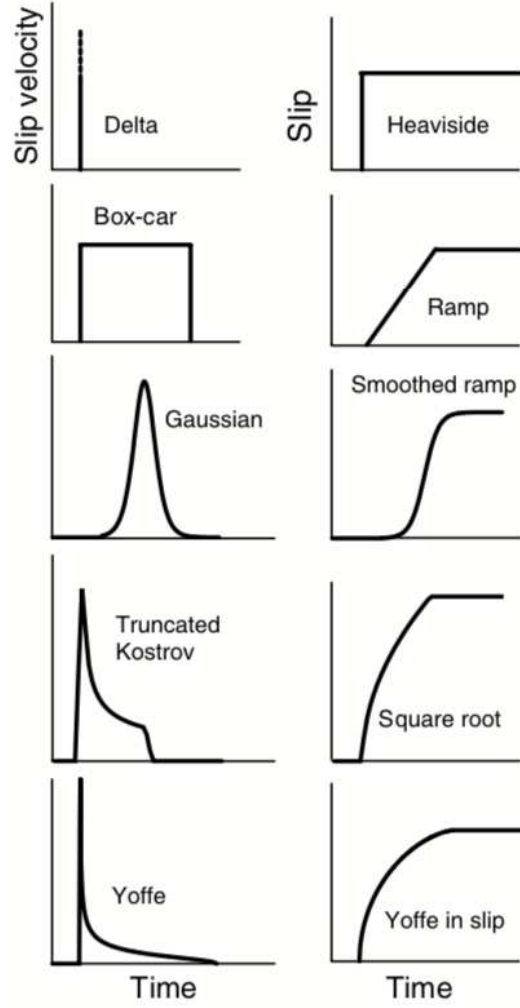


Figure 1.10: Slip-velocity functions of delta, boxcar, Gaussian, truncated Kostrov, and Yoffe are shown on the left. The corresponding slip functions of Heaviside, ramp, smoothed ramp, square root, and Yoffe in slip are shown on the right. Figure from Tinti et al. [2005b].

of the eikonal equation:

$$|\nabla \tau^j| = \frac{1}{V_R^j}, \quad (1.35)$$

where $\tau^j = 0$ in the hypocenter location.

1.6 Inversion schemes

Inversion schemes aim to infer the model \mathbf{m} that fits the observations given the forward problem and some constraints on the parameters. Let us define the residual vector $\mathbf{e} = \mathbf{d}_{\text{obs}} - \mathbf{G}(\mathbf{m})$ between the observations \mathbf{d}_{obs} and the predictions $\mathbf{G}(\mathbf{m})$ for a given source model \mathbf{m} . It is convenient to define a scalar quantity characterizing the overall magnitude of such residuals. A common approach is to use the L_2

norm of the residuals:

$$\chi(\mathbf{m}) = \|\mathbf{d}_{\text{obs}} - \mathbf{G}(\mathbf{m})\|_2^2. \quad (1.36)$$

$\chi(\mathbf{m})$ is proportional to the squared Euclidean length of the vector \mathbf{e} :

$$E = \sum_i e_i^2 = \mathbf{e}^T \mathbf{e}. \quad (1.37)$$

If we are in a linear Gaussian case, where $\mathbf{G}(\mathbf{m}) = \mathbf{G}\mathbf{m}$, the model $\tilde{\mathbf{m}}$ minimizing $\chi(\mathbf{m})$ (often referred to as the least-squares solution) is:

$$\tilde{\mathbf{m}} = (\mathbf{G}^t \mathbf{G})^{-1} \mathbf{G}^t \cdot \mathbf{d}_{\text{obs}}. \quad (1.38)$$

Although the least-squares solution is very convenient, in most cases, we face an ill-posed inverse problem, where $\mathbf{G}^t \mathbf{G}$ is a ill-conditioned matrix. In such situations, there are multiple solutions that can fit the observations equally well (there is no unique solution). A common practice to avoid such non-uniqueness of the problem, is to regularize the inversion. This can be made using the so called Tikhonov regularization scheme in an optimization approach. As recent application examples, we can cite the ELastostatic ADjoint INversion (ELADIN) method by Tago et al. [2021] and the work of Radiguet et al. [2011]. Another approach is to describe the whole solution space, that is the ensemble of models that can fit the observations given the a priori information (hereafter referred to as the Bayesian approach). Examples of Bayesian methods are the Transdimensional dimension algorithm [Dettmer et al., 2014] or the CATMIP algorithm [Minson et al., 2013].

1.6.1 Optimization approach by Tikhonov regularization

The Tikhonov regularization is a well-known approach to regularize ill-posed problems [in Russian Tikhonov, 1963]. Also known as ridge regression, the Tikhonov regularization has been employed in source studies since the early 80s. Examples of finite fault studies based on Tikhonov regularization are the finite fault studies conducted by Hartzell and Heaton [1983], Olson and Apsel [1982], and Segall and Harris [1987].

To deal with the non-uniqueness of the inverse problem, the Tikhonov regularization includes an additional regularization term to the misfit function in 1.36. The estimated parameters are then determined as:

$$\tilde{\mathbf{m}} = \text{argmin}(\|\mathbf{d}_{\text{obs}} - \mathbf{G}(\mathbf{m})\|_2^2 + \lambda^2 \|\mathbf{\Gamma} \mathbf{m}\|_2^2), \quad (1.39)$$

where Γ is the Tikhonov matrix, and λ is the damping parameter, which weights the regularization term. The matrix Γ can take diverse forms to impose different restrictions. Thus, for example, we can choose $\Gamma = \mathbf{I}$, which is called the zeroth-order Tikhonov regularization. Among all possible solutions that fit the data equally well, this regularization will favor the model with a minimum L_2 norm, implying a moment minimization in the case of slip inversions. Another option for Γ is to choose the Laplacian operator $\Gamma = \nabla^2$. This choice will favor smooth solutions, preventing rough slip changes. This regularization is also known as second-order Tikhonov regularization.

For the linear case $\mathbf{d} = \mathbf{G}\mathbf{m}$, we can assume a weighted matrix \mathbf{W} , so the equation will turn to $\mathbf{W}\mathbf{d} = \mathbf{W}\mathbf{G}\mathbf{m}$. We suppose that \mathbf{W} is diagonal, and we define the corresponding weight to each data. In this manner, the general solution of equation 1.39 becomes:

$$\tilde{\mathbf{m}} = (\mathbf{G}^t \mathbf{W}^2 \mathbf{G} + \lambda^2 \mathbf{\Gamma}^t \mathbf{\Gamma})^{-1} \mathbf{G}^t \mathbf{W}^2 \mathbf{d}_{\text{obs}}. \quad (1.40)$$

We focus now on the damping parameter λ . Its importance comes from the fact that it modulates the impact of the regularization term. We show in Figure 1.11 the differences between slip models when varying the λ parameter. We can see that the similarity with the reference model change for each λ . Such dependence turns out to be a weak point of this approach since the slip distribution, and therefore, the conclusions deduced from them, greatly count on λ . To avoid the over/under-estimation of λ , a common practice is to use the L-curve to estimate an appropriate value of λ [Hansen and O’Leary, 1993]. In this case, we will choose the λ value that is closer to the curve corner. However, the selection of this parameter remains arbitrary, affecting the resulted slip model [see Causse et al., 2010].

Despite the simplicity of the previous equation, it is rarely used since it can produce solutions with negative slips (i.e., in the direction opposite to the rupture rake angle). The existence of a negative slip is still under debate. For example, in the context of a subduction zone, it implies slip is occurring in the direction opposite to the long-term sliding of the megathrust interface. Although one might think of local stress changes inducing such phenomena, we do not expect to have large negative slip (which is often seen in solutions not enforcing positivity constraints). There are different techniques to impose bounded or positivity constraints using a Tikhonov regularization scheme, such as nonnegative least squares or the conjugate gradient method [Aster et al., 2018, Menke, 2012, Tarantola, 2005].

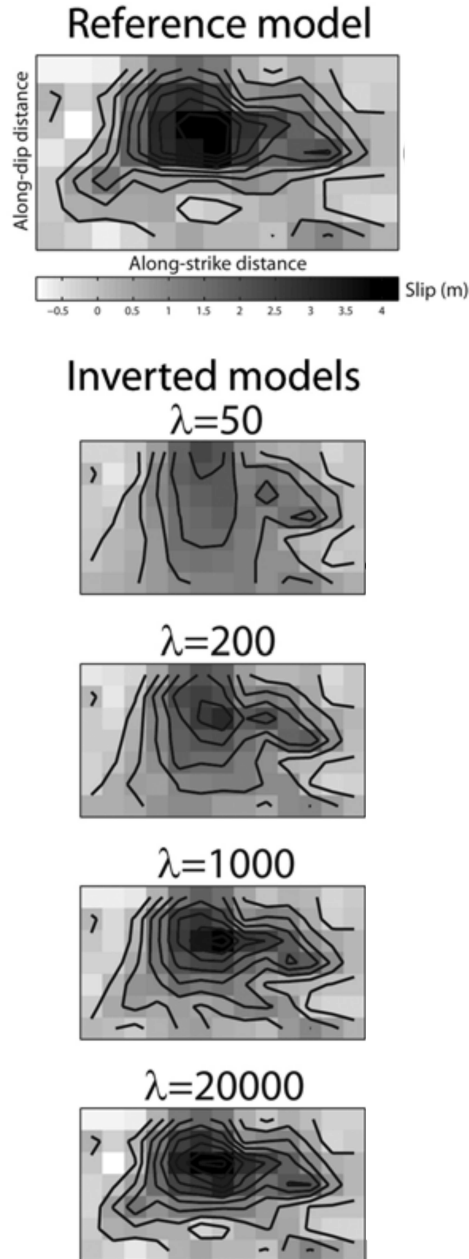


Figure 1.11: Reference k-2 static slip distribution and inverted models for different values of the smoothing parameter λ . The inversion process is performed by assuming that all the model and source parameters are known except the static slip. Mean slip equals 0.7 m. The space between the contour lines is 0.5 m. Figure from Causse et al. [2010].

1.6.2 Bayesian approach

Optimization techniques based on Tikhonov regularization are very convenient approaches to address slip inversion problems. However, as we have shown, it relies on nonphysical regularization that imposes restrictions to deal with the non-uniqueness of the inversion. In this manner, the Bayesian approach turns out to be

an interesting alternative as the solution is not made of a single model but rather an ensemble of plausible models given the observations and our *a priori* knowledge about the problem [Jackson and Matsu'Ura, 1985].

From the Bayes theorem, we can describe the *a posteriori* probability density function (PDF) of parameters $p(\mathbf{m}|\mathbf{d}_{\text{obs}})$, given the observations \mathbf{d}_{obs} as:

$$p(\mathbf{m}|\mathbf{d}_{\text{obs}}) = \frac{p(\mathbf{d}_{\text{obs}}|\mathbf{m})p(\mathbf{m})}{p(\mathbf{d}_{\text{obs}})} \quad (1.41)$$

where $p(\mathbf{m})$ is the *a priori* probability density function of parameters and $p(\mathbf{d}_{\text{obs}}|\mathbf{m})$ is the data likelihood function, describing the ability of the model parameters \mathbf{m} to explain the observations \mathbf{d}_{obs} . The denominator of the equation 1.41 is a normalization factor that can be defined as:

$$p(\mathbf{d}_{\text{obs}}) = \int p(\mathbf{d}_{\text{obs}}|\mathbf{m})p(\mathbf{m})d\mathbf{m}. \quad (1.42)$$

Contrary to the optimization approach, the solution of the inverse problem from a Bayesian perspective is the *a posteriori* probability distribution function $p(\mathbf{m}|\mathbf{d}_{\text{obs}})$. We now consider a generic data set, \mathbf{d}_{obs} , for which we can design a forward model $\mathbf{G}(\mathbf{m})$. We can define the forward model, including the uncertainties associated with our problem:

$$\mathbf{d}_{\text{obs}} = \mathbf{G}(\mathbf{m}) + \mathbf{e}_d + \mathbf{e}_p \quad (1.43)$$

where \mathbf{e}_d represents the uncertainty due to measurement errors and \mathbf{e}_p represents the uncertainty due to forward model uncertainty. The \mathbf{e}_p error can be related, for example, to inaccuracies in the Earth velocity model or the fault geometry. Both errors are modeled as Gaussian distributions since these distributions assume the least additional information, following the Principle of Maximum Entropy [Jaynes, 2003]. In this case, we can consider the likelihood function $p(\mathbf{d}_{\text{obs}}|\mathbf{m})$ as [Tarantola and Valette, 1982]:

$$\begin{aligned} p(\mathbf{d}_{\text{obs}}|\mathbf{m}) &= \mathcal{N}(\mathbf{d}_{\text{obs}}|\mathbf{G}(\mathbf{m}), \mathbf{C}_\chi) \\ &= \frac{1}{(2\pi)^{N/2}|\mathbf{C}_\chi|^{1/2}} \exp\left(-\frac{1}{2}(\mathbf{d}_{\text{obs}} - \mathbf{G}(\mathbf{m}))^T \mathbf{C}_\chi^{-1}(\mathbf{d}_{\text{obs}} - \mathbf{G}(\mathbf{m}))\right). \end{aligned} \quad (1.44)$$

In the previous equation, N is the total number of observations, and \mathbf{C}_χ is the covariance matrix defined as:

$$\mathbf{C}_\chi = \mathbf{C}_d + \mathbf{C}_p, \quad (1.45)$$

where \mathbf{C}_d and \mathbf{C}_p correspond to the observational and forward modeling uncertainty matrices, respectively (i.e., \mathbf{e}_d and \mathbf{e}_p). The term in the exponential function is

equivalent to the misfit function 1.36 when assuming covariance matrices to characterize uncertainties in the problem. The metric to characterize data residuals is therefore similar to what is used in optimization problems.

In the previous paragraphs, we described a general Bayesian inversion scheme that can be applied for linear or nonlinear problems. The C_d matrix is usually built by the corresponding measurement errors or using some estimates of the noise level (e.g., level of ambient noise before the earthquake for kinematic data). The C_p matrix is often neglected but in fact, it can often be comparable to or larger than C_d . Given its importance, different methodologies have been proposed to model uncertainties related to Earth model structure [Duputel et al., 2014] or fault geometry [Ragon et al., 2018]. As *a priori* probability distributions, we can use the known information about the earthquake such as the scalar seismic moment of the event [Fukuda and Johnson, 2008] or the overall orientation of slip on the fault Minson et al. [2013].

We consider now the case of linear forward models, with Gaussian prior PDF distribution:

$$p(\mathbf{m}) = \frac{1}{(2\pi)^{M/2} |C_m|^{1/2}} \exp \left(-\frac{1}{2} (\mathbf{m} - \mathbf{m}_{\text{prior}})^T C_m^{-1} (\mathbf{m} - \mathbf{m}_{\text{prior}}) \right), \quad (1.46)$$

where M is the number of parameters, $\mathbf{m}_{\text{prior}}$ the *a priori* expected mean value of the model parameters, and C_m is the *a priori* covariance matrix. In this specific case, with a linear forward model, the likelihood function in equation 1.44, and Gaussian *a priori* distributions, the *a posteriori* PDF takes the Gaussian form [Tarantola and Valette, 1982]:

$$p(\mathbf{m} | \mathbf{d}_{\text{obs}}) = \frac{1}{(2\pi)^{M/2} |\tilde{C}_m|^{1/2}} \exp \left(-\frac{1}{2} (\mathbf{m} - \tilde{\mathbf{m}})^T \tilde{C}_m^{-1} (\mathbf{m} - \tilde{\mathbf{m}}) \right). \quad (1.47)$$

with $\tilde{\mathbf{m}}$ being the average *a posteriori* model and \tilde{C}_m being the posterior covariance matrix (characterizing uncertainty on $\tilde{\mathbf{m}}$). We can estimate the *a posteriori* parameters as:

$$\begin{aligned} \tilde{\mathbf{m}} &= (\mathbf{G}^t C_\chi^{-1} \mathbf{G} + C_m^{-1})^{-1} (\mathbf{G}^t C_\chi^{-1} \mathbf{d}_{\text{obs}} + C_m^{-1} \mathbf{m}_{\text{prior}}) \\ \tilde{C}_m &= (\mathbf{G}^t C_\chi^{-1} \mathbf{G} + C_m^{-1})^{-1}. \end{aligned} \quad (1.48)$$

These expressions provide an analytical solution for the linear Gaussian case. If we compare it with the Tikhonov optimization approach, we notice some similarities. For example, the C_m^{-1} acts like a regularization term. If we consider $\mathbf{m}_{\text{prior}} = \mathbf{0}$, $C_\chi^{-1} = \mathbf{W}^2$, and $C_m^{-1} = \lambda^2 \Gamma^t \Gamma$, we obtain an equivalent expression to equation 1.40 (from the optimization approach).

One of the main disadvantages of the general Bayesian inversion scheme is the need to evaluate the complete *a posteriori* PDF distributions, which can be computationally expensive. This is not really a problem for linear Gaussian problem as such problems have an analytical solution (shown in equation 1.48). However, Gaussian priors can be impractical as it does not allow to impose bounded constraints on model parameters (e.g., slip positivity in a given direction). To solve non-Gaussian problems, a commonly used approach is to sample the posterior PDF. Such Bayesian sampling approaches consist in generating a population of model samples distributed according to $p(\mathbf{m}|\mathbf{d}_{\text{obs}})$, with a higher density where the models better explain the observations given the *a priori* information. Different methodologies have been proposed to overcome this issue and thus, obtain adequate and fast samplers. Despite the computation cost in terms of sampling, one advantage of this approach is that the inverse of the \mathbf{G} matrix is not needed. For this reason, the inversion can work without regularizing the inverse of \mathbf{G} (or $\mathbf{G}^t\mathbf{W}\mathbf{G}$ as in equation 1.40). We will briefly describe some Bayesian samplers that are used in seismology studies to obtain the *a posteriori* PDF distribution. We will also describe the Cascading Adaptive Metropolis in Parallel algorithm (CATMIP), a methodology applied in this work in chapter 3. For introduction readings of the Bayesian scheme, see Bishop [2006], Minson [2010], Sambridge and Mosegaard [2002].

Bayesian samplers - Rejection method

The rejection method (also known as the acceptance-rejection method) is one of the first sampling methods developed [Von Neumann, 1951]. For the rejection method, the goal is to draw samples from a target PDF $p(x)$. We start producing samples from a known distribution $g(x)$. Next, we assume that there is a known constant k such that $p(x) \leq k \cdot g(x)$ for all x . We can then draw samples from $p(x)$ following the algorithm summarized in Table 1.1. This algorithm starts by creating random samples from a known distribution. Then, the algorithm compares a normalized version of the sample's probability in the target distribution to a random variate. If the sample has a large probability in the target distribution, we are more likely to accept it. If the target PDF assigns a low probability to the sample, we are less likely to admit it. In this way, we arrive at having an ensemble of samples distributed proportionally to our target PDF.

Table 1.1: Rejection method

1.	Draw a candidate sample x from known distribution g
2.	Generate a sample u from the uniform distribution $U(0, 1)$
3.	If $u \leq \frac{p(x)}{k \cdot g(x)}$, accept x as a sample of p
4.	Return to step 1

Table 1.2: Metropolis algorithm

· For $i = 1, 2, \dots, N$	
1.	Draw $z \sim p'(y - x)$, where $p(x, y) = p'(y - x)$ and compute a candidate sample $y = x_{i-1} + z$
2.	Generate a sample u from the uniform distribution $U(0, 1)$
3.	Compute $\alpha(x, y) = \min\{\frac{p(y)}{k \cdot p(x_{i-1})}, 1\}$.
4.	If $u \leq \alpha$, $x_i = y$. Otherwise $x_i = x_{i-1}$.

Bayesian samplers - Metropolis algorithm

The Metropolis algorithm is perhaps the most employed Markov Chain Monte Carlo (MCMC) sampler [Chib and Greenberg, 1995, Metropolis et al., 1953]. A Markov chain is a sequence of random variables where the probability distribution of X^{n+1} depends solely on the previous value, X^n , and not on earlier values of random variables in the sequence [Aster et al., 2018, Meyn and Tweedie, 2012].

In this algorithm, we generate samples from a proposal distribution and then probabilistically decide whether or not to accept the candidate sample. The proposal PDF will depend only on the current state of the process, so the candidate sample will have a PDF of the form $p(x, y)$, where x is the current sample and y is the candidate sample. In the original algorithm, the proposal PDF has to be such that $p(x, y) = p(y, x)$, i.e., the probability of moving from x to y has to be the same the other way around. However, this requirement is not needed in alternative Metropolis-based algorithms such as the Metropolis-Hasting algorithm [Hastings, 1970].

In the Metropolis algorithm, we propose a PDF with a random sample x_0 , from which we will generate candidate samples following the procedure from Table 1.2. If the candidate sample has a higher probability (the PDF is larger than the previous PDF), it will be accepted. Contrary to the rejection method, if the candidate has a lower probability, it might be accepted depending on the value of the random variate u . This feature allows the algorithm to escape from local minima, exploring possible models from the solution space.

Several issues result from the local character of the method (i.e., the fact that each

model candidates y are generated in the vicinity of the previous sample x in Table 1.2). A poorly chosen proposal PDF $p(x, y)$ can easily result in a very small rejection rate (typically if $p(x, y)$ is tightly centered on x) or a very large rejection rate (typically if $p(x, y)$ generates model candidates far away from x). Such poor tuning can results in large correlation in the series of generated model samples. Another issue resulting from the local character of the method is the dependence of generated samples upon on the starting model (in particular if $p(x, y)$ is poorly designed). To mitigate this effect, a common approach is to remove all model samples generated during a "burn-in" period. There are other computing disadvantages, like the fact that the Markov chain is not parallelizable as the rejection method. However, several parallel adaptations have been built up to overcome these issues.

Bayesian samplers - Transitional Markov Chain Monte Carlo

The Transitional Markov Chain Monte Carlo (TMCMC) algorithm was proposed by Beck and Au [2002] and Ching and Chen [2007]. For an extensive revision, we recommend the work of Betz et al. [2016]. The idea behind this algorithm is to converge to the posterior PDF $p(\mathbf{m}|\mathbf{d}_{\text{obs}})$ by sampling a series of intermediate PDFs $f(\mathbf{m}|\mathbf{d}_{\text{obs}})_j$. For this purpose, we modify equation (1.41) to:

$$f(\mathbf{m}|\mathbf{d}_{\text{obs}})_j \propto p(\mathbf{m}) p(\mathbf{d}_{\text{obs}}|\mathbf{m})^{\beta_j}, \quad (1.49)$$

where $(j = 1, \dots, J)$ and β gradually varies from zero to one, i.e., $0 = \beta_0 < \beta_1 < \dots, < \beta_J = 1$. Thus, for $j = 0$ we have $\beta_0 = 0$, which implies that we are sampling from the *a priori* distribution $f(\mathbf{m}|\mathbf{d}_{\text{obs}}) \propto p(\mathbf{m})$. Finally, for $j = J$ we have $\beta_J = 1$, which means we are sampling the complete posterior PDF $p(\mathbf{m}|\mathbf{d}_{\text{obs}})$. The idea of this algorithm is that even though the shapes from $p(\mathbf{m})$ to $p(\mathbf{m}|\mathbf{d}_{\text{obs}})$ change dramatically, the change between two adjacent intermediate PDFs $f(\mathbf{m}|\mathbf{d}_{\text{obs}})_j$ is smooth. This approach is, in principle, very similar to the simulated annealing [Kirkpatrick et al., 1983], except that we stop at a temperature of 1 to sample the posterior PDF.

There are two main elements of this algorithm: a resampling process and the choice of the next β value from $f(\mathbf{m}|\mathbf{d}_{\text{obs}})_j$ to $f(\mathbf{m}|\mathbf{d}_{\text{obs}})_{j+1}$. If the increase of β is too large, the distribution will change too dramatically to ensure an appropriate sampling of the model space. On the other hand, if the increase of β is too small, the distribution will not change much and the sampling will not be efficient (computationally speaking). The selection of β is thus done dynamically, to ensure a constant gain of information between adjacent $f(\mathbf{m}|\mathbf{d}_{\text{obs}})_j$ (increasing β can be seen as increasing information

brought by the data in the problem). As shown by Ching and Chen [2007] this is equivalent to select β_{j+1} based on β_j such that the coefficient of variation COV (the ratio of the standard deviation to the mean) of $p(\mathbf{d}_{\text{obs}}|\mathbf{m})^{\beta_{j+1}-\beta_j}$ is equal to one.

Regarding the sampling process, the algorithm starts by sampling the prior distribution. So, for $j = 0$, we draw from the prior PDF N_s samples $\mathbf{m}_{(0,1)}, \dots, \mathbf{m}_{(0,N_s)}$. Next, we calculate the new β step using the coefficient of variation. For all the samples, $k = 1, \dots, N_s$, we compute the weighting coefficient $\omega_{(j,k)}$ (the probability of choosing a specific sample of $\beta_j, \mathbf{m}_{(j,k)}$):

$$\omega_{(j,k)} = \frac{p(\mathbf{m}_{(j,k)})p(\mathbf{d}_{\text{obs}}|\mathbf{m}_{(j,k)})^{\beta_{j+1}}}{p(\mathbf{m}_{(j,k)})p(\mathbf{d}_{\text{obs}}|\mathbf{m}_{(j,k)})^{\beta_j}} = p(\mathbf{d}_{\text{obs}}|\mathbf{m}_{(j,k)})^{\beta_{j+1}-\beta_j} \quad (1.50)$$

We compute the model sample covariance Σ_j . This covariance is used in the next step at $j = 1$ as the covariance of the Gaussian proposal PDF used in the Metropolis Chains (see below).

Then, we perform the resampling by randomly selecting samples $\mathbf{m}_{(j,k)}$ from the sample set. The probability of selecting a specific sample is given by the weighting coefficients $\omega_{(j,k)}$. During this random resampling, some samples will be duplicated while some others will not be selected (see Figure 1.12). Samples that are duplicated are then replaced with new samples that are generated using the Metropolis algorithm with a proposal PDF $N(\mathbf{m}, \alpha\Sigma_j)$ where α is an arbitrary coefficient to be tuned. Once this is done, we jump to the next value of β and continue in the same fashion until we reach $\beta = 1$. A summary of the algorithm is presented in Table 1.3).

This algorithm has two main advantages. First, the sampling is made from an equilibrium-like distribution, which permits to have a tolerable acceptance rate. Secondly, the proposal PDF is calculated from the current best candidates of the posterior distribution. For example, if two parameters trade-off with each other, the sampler will take large steps in the direction in which they co-vary and small steps in directions with low covariance. However, one of the main limitations of the TMCMC is that it is not parallelizable. Besides, there is a problem with a theoretical assumption in the TMCMC algorithm. Ching and Chen [2007] assume stationarity for all the PDFs $f(\mathbf{m}, \mathbf{d}_{\text{obs}})_j$, which implies ignoring the "burn-in" period of the MCMC sampling.

Bayesian samplers - CATMIP

We now describe the Cascading Adaptive Tempered Metropolis In Parallel (CATMIP) algorithm developed by Minson [2010] that we will use in chapter 3. CATMIP

Table 1.3: TMCMC algorithm

1.	Set $j = 0$. Generate N_s samples $\mathbf{m}_{0,1} \dots \mathbf{m}_{0,N_s}$ of the prior PDF $f_0 = p(\mathbf{m})$. <i>Selection of β step</i>
2.	Choose β_{j+1} such that the coefficient of variation = 1.
3.	Calculate the weighting coefficients and sample covariance Σ_j . <i>Resampling process</i>
4.	For $k = 1, \dots, N_s$ draw a sample $\bar{\mathbf{m}}^{(j-1)}$ from $\mathbf{m}_{j-1,1} \dots \mathbf{m}_{j-1,N_s}$ with probability $\omega(\mathbf{m}_{j-1,k})$. Use the Metropolis algorithm with $N(\mathbf{m}_{(j-1,k)}, \alpha \Sigma_j)$ as the proposal PDF to append a new sample to the chain of models which has $\mathbf{m}_{j-1,k}$ as its starting model.
5.	Repeat steps 2 to 4 until $\beta_J = 1$ is reached.

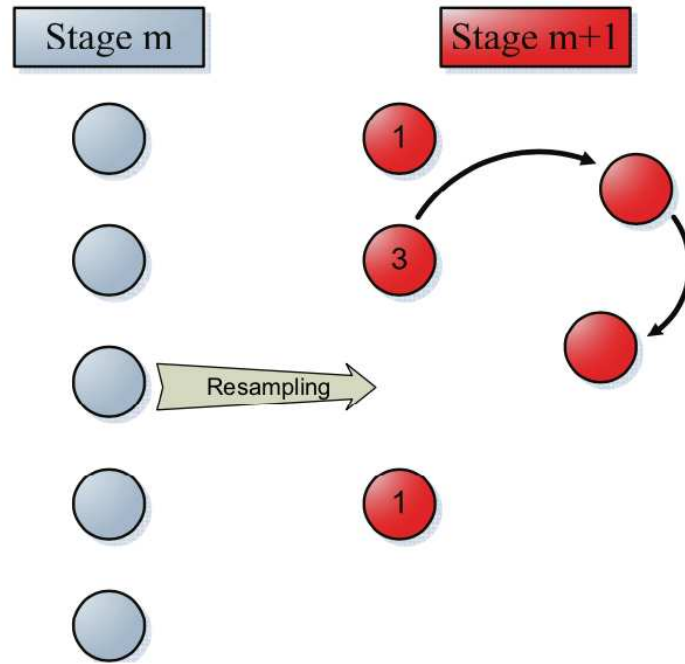


Figure 1.12: TMCMC algorithm schematic: This cartoon illustrates one complete cooling stage of the TMCMC algorithm. The five samples from β_m are resampled and then the Metropolis algorithm is run to replace the unique samples lost through resampling. Numbers indicate the frequency of each model after resampling. The five red samples comprise the posterior distribution for β_{m+1} . The algorithm is plotted with a 100% acceptance rate for simplicity. Figure from Minson [2010].

is in principle very similar to the TMCMC approach. Contrarily to TMCMC, CATMIP is based on multiple Metropolis chains that run in parallel and the resampling is done by duplicating/rejecting the last model samples of each chain, which allows a larger exploration in high-probability regions.

The algorithm also starts sampling the prior distribution and draw from the prior PDF N_s samples $\mathbf{m}_{(0,1)}, \dots, \mathbf{m}_{(0,N_s)}$ for β step $j = 0$. As for TMCMC, we calculate the new β step using the coefficient of variation. We also compute the model sam-

Table 1.4: CATMIP algorithm

1.	Set $j = 0$. Generate N_s samples $\mathbf{m}_0 = \{\mathbf{m}_{(0,1)} \dots \mathbf{m}_{(0,N_s)}\}$ of the prior $f_0 = p(\mathbf{m})$. <i>Selection of β step</i>
2.	Choose β_{j+1} such that the coefficient of variation = 1.
3.	Calculate the weighting coefficients and sample covariance Σ_j . <i>Resampling process</i>
4.	Draw N_s samples from \mathbf{m}_j with probability $\omega_{j,k}$. The set of resampled models is $\{\hat{\mathbf{m}}\}$.
5.	Use each resampled model $\hat{\mathbf{m}}$ as the seed for generating N_{steps} models from the Metropolis algorithm with proposal covariance $\alpha \Sigma_j$.
6.	Collect \mathbf{m}_{j+1} , the set of sampled Markov chains.
7.	Repeat steps 2 to 6 until $\beta_J = 1$ is reached.

ples covariance Σ_j that are used to design the proposal PDF used to sample the distribution at $j = 1$ (see description below). In an approach similar to TMCMC, we perform the resampling by randomly selecting samples $\mathbf{m}_{(j,k)}$ to create a new set $\{\hat{\mathbf{m}}\}$ (see Figure 1.13). The probability of selecting a specific sample is given by the weighting coefficients $\omega_{(j,k)}$. The difference with TMCMC is that, after resampling, the new samples in $\hat{\mathbf{m}}$ are used as seeds (i.e., initial models) to create parallel Markov chains of samples of fixed length N_{steps} (see Figure 1.13). Samples in each chain are generated using the Metropolis algorithm with a Gaussian proposal distribution of covariance $\alpha \Sigma_j$. This exploration is embarrassingly parallel as we are dealing with parallel Markov chains. When the Markov chains arrive at the chain length limit, the final models from all chains are collected to make $\mathbf{m}_{(j+1,k)}$. The choice of the factor α is adapted to the acceptance rate (i.e., the ratio of accepted samples) using acceptance and rejection weights [see Minson et al., 2013]. Nowadays, the Altar code (<https://altar.readthedocs.io>), an implementation of CATMIP running on CPUs and GPUs, also proposes to use the adaptative metropolis algorithm. In both cases, the idea is to increase the random walk steps when the acceptance rate is too large and to decrease the random walk steps when the acceptance rate is too small. The overview of the CATMIP algorithm is given in Table 1.4.

An additional feature of the algorithm is cascading. This allows us to split the inverse problem and solve it in several sequential parts. For example, in slip inversions, we can first extract final slip distributions using the static data. Then, we can use the static slip model samples as starting points to resolve the full kinematic slip inversion. In this way, the complete slip inversion problem is already constrained to samples that are consistent with the static case.

Let us consider a case where we have two data sets: \mathbf{D}_1 and \mathbf{D}_2 . We also divide

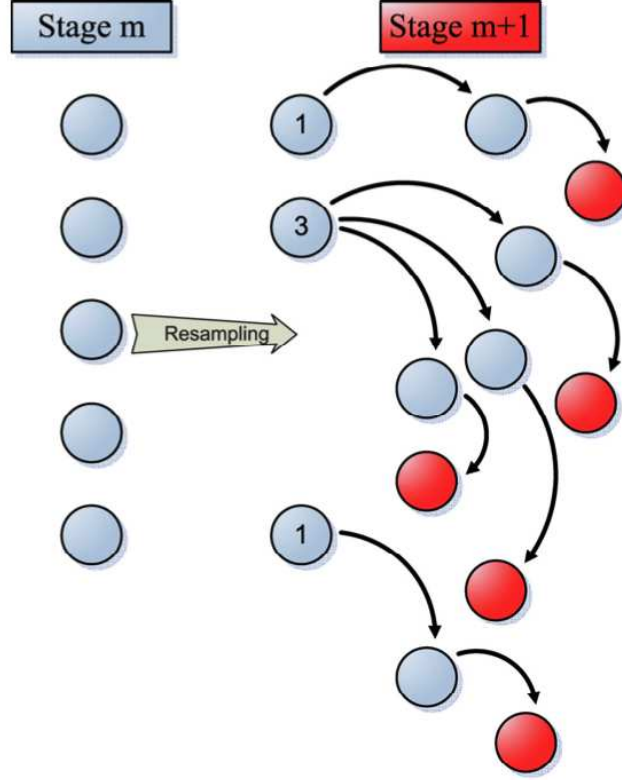


Figure 1.13: CATMIP algorithm schematic. This cartoon illustrates one complete cooling stage of the CATMIP algorithm. The five samples from β_m are resampled and then an instance of the Metropolis algorithm is run for each of the resulting samples. Numbers indicate the frequency of each model after resampling. The five red samples comprise the posterior distribution for β_{m+1} . The algorithm is plotted with very short Markov chains and a 100 per cent acceptance rate for simplicity. In applications, the Markov chains would be much longer and the acceptance rate much lower. Figure from Minson et al. [2013].

the parameters of the problem into two $\mathbf{m} = (\mathbf{m}_1, \mathbf{m}_2)$, where $\mathbf{m}_1, \mathbf{m}_2$ are taken as independent *a priori*. Let's suppose that the data likelihood for \mathbf{D}_1 depends only on model parameters \mathbf{m}_1 while data likelihood for \mathbf{D}_2 depends on both \mathbf{m}_1 and \mathbf{m}_2 . In our case, static data (\mathbf{D}_1) is only sensitive to the final slip distribution (\mathbf{m}_1), while kinematic data (\mathbf{D}_2) is also sensitive to the rupture evolution. The corresponding posterior distribution takes the form of:

$$\begin{aligned}
 p(\mathbf{m}|\mathbf{D}) &\propto p(\mathbf{m})p(\mathbf{D}|\mathbf{m}) \\
 &= p(\mathbf{m}_1)p(\mathbf{m}_2)p(\mathbf{D}_1|\mathbf{m}_1)p(\mathbf{D}_2|\mathbf{m}_1, \mathbf{m}_2) \\
 &= [p(\mathbf{m}_1)p(\mathbf{D}_1|\mathbf{m}_1)]p(\mathbf{m}_2)p(\mathbf{D}_2|\mathbf{m}_1, \mathbf{m}_2) \\
 &\propto p(\mathbf{m}_1|\mathbf{D}_1)p(\mathbf{m}_2)p(\mathbf{D}_2|\mathbf{m}_1, \mathbf{m}_2)
 \end{aligned} \tag{1.51}$$

In the framework of transitioning schemes, we can incorporate 1.51 in terms of

transitional distributions in equation 1.49:

$$f(\mathbf{m}|\mathbf{D}, \beta_j, \gamma_n) \propto p(\mathbf{m}_1)p(\mathbf{m}_2)p(\mathbf{D}_1|\mathbf{m}_1)^{\beta_j}p(\mathbf{D}_1|\mathbf{m}_1, \mathbf{m}_2)^{\gamma_n}. \quad (1.52)$$

Thus, we can sample the PDF $p(\mathbf{m}|\mathbf{D})$ by using the algorithm developed in Table 1.4 in two steps:

$$\begin{aligned} (1) \quad & f(\mathbf{m}_1|\mathbf{D}_1, \beta_j) \propto p(\mathbf{m}_1) p(\mathbf{D}_1|\mathbf{m}_1)^{\beta_j} \\ & 0 \leq \beta_j \leq 1 \\ (2) \quad & f(\mathbf{m}|\mathbf{D}, \gamma_n) \propto p(\mathbf{m}_1) p(\mathbf{D}_1|\mathbf{m}_1) p(\mathbf{m}_2) p(\mathbf{D}_2|\mathbf{m}_1, \mathbf{m}_2)^{\gamma_n} \\ & 0 \leq \gamma_n \leq 1. \end{aligned} \quad (1.53)$$

Even though we have to run the algorithm twice, in practice, obtaining $f(\mathbf{m}_1|\mathbf{D}_1, \beta_j)$ from the data set \mathbf{D}_1 and then $f(\mathbf{m}|\mathbf{D}, \gamma_n)$ is faster than running the full inverse problem directly.

1.7 Retrieving dynamic parameters from kinematic slip models

We can use kinematic slip models to characterize the dynamic parameters of the source. Since the slip distribution is directly linked to spatiotemporal stress distribution, a common approach is to use it as a boundary condition in stress evolution computations [Bouchon, 1997, Ide and Takeo, 1997]. In such a way, we end with a slip–stress relation at each point on the fault plane. For example, in Figure 1.14 center, we show the slip distribution built by Ide and Takeo [1997]. We can see at the top and the bottom the corresponding stress evolution within the fault.

It is worth mentioning that the slip–stress relation is based on the slip-weakening model, as theoretically proposed by Ida [1972] and Andrews [1976]. Thus, besides the stress evolution, we can estimate dynamic parameters related to the slip-weakening model, such as the critical slip weakening distance D_c and the fracture energy G_c . One example of earthquake description is the work of Guatteri and Spudich [1998] and Guatteri and Spudich [2000]. They showed that the estimation of G_c is more stable than that of D_c since G_c is controlled by the slip rate and thus less affected by the limited resolution. Similarly, Tinti et al. [2005a] estimate the breakdown energy for a series of earthquakes using kinematic slip distributions.

1.7. RETRIEVING DYNAMIC PARAMETERS FROM KINEMATIC SLIP MODELS

Regarding the stress evolution computation, it can be executed using numerical methods. For example, Aochi et al. [2000] compute the stress evolution using a boundary integral equation method (BIEM), following the methodology from Fukuyama and Madariaga [1998] for a planar fault in a 3D Elastic medium.

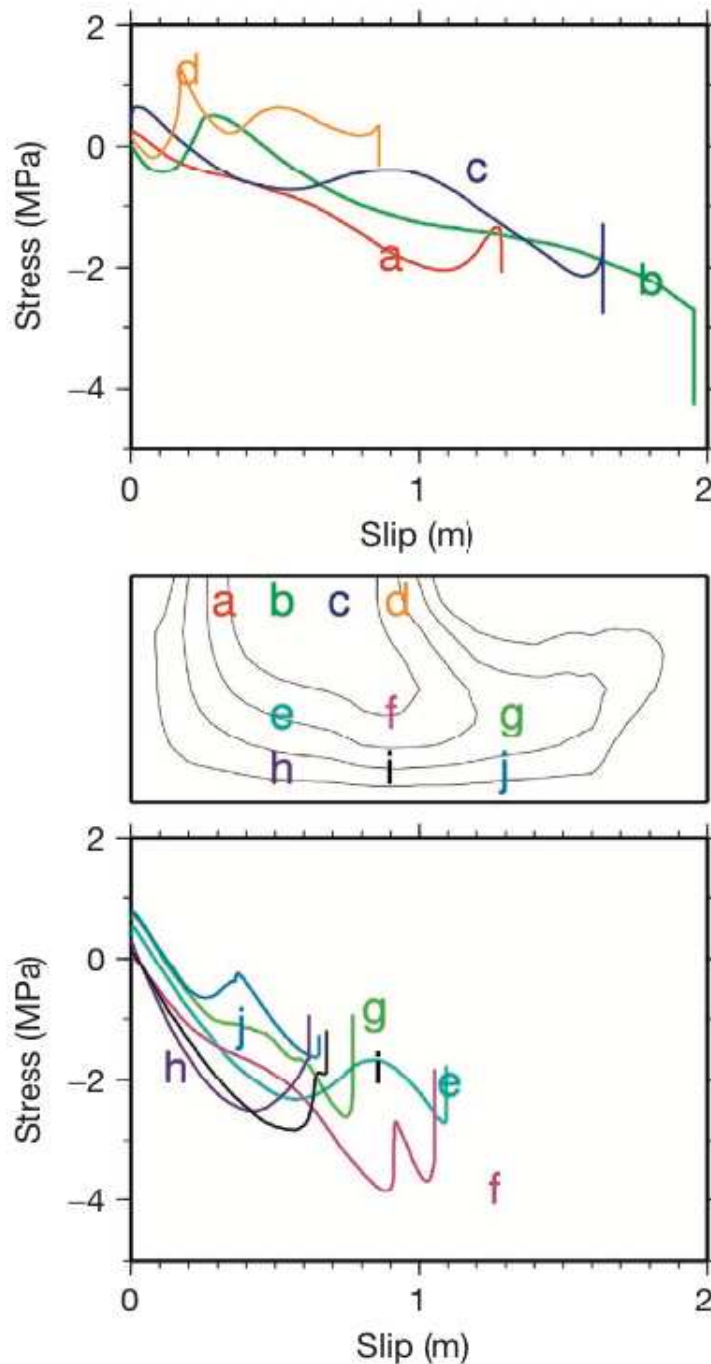


Figure 1.14: The relation between slip and stress on the fault plane, determined for the 1995 Kobe earthquake [Ide and Takeo, 1997]. Each trace is the function calculated at the corresponding location in the middle figure that shows final slip distribution by contours. Figure from Ide [2015].

Initiation phase of Earthquakes.

2.1 Summary

In this chapter, we discuss state-of-the-art models that seek to explain the initiation phase of earthquakes. We start by introducing laboratory and numerical experiments that examine the nucleation phase of seismic ruptures. Next, we investigate in detail the foreshock cascade model and the aseismic preslip triggering model. Then, we continue by describing the foreshocks and the geodetic preslip observations supporting each model. Finally, we investigate the initiation phase of the 2017 $M_W = 6.9$ Valparaíso earthquake by combining GNSS and seismic observations. We take into account the uncertainties related to earthquake location for the largest foreshock of the sequence. We find that only half of the observed GPS displacement can be explained by seismic contribution, suggesting the existence of an aseismic slip during the initiation phase of this earthquake. The results of this work have already been published and are included in this chapter.

2.2 How do earthquakes begin?

To understand how earthquakes begin, we have to go back to the first proposed theories trying to explain earthquake occurrence in the 70s decade. With the arrival of new geophysical observations and the advent of plate tectonics theory, geoscientists could compare seismic fault slip estimated for earthquakes against the convergence rate in subduction zones. From this comparison, we have among the first

2.2. HOW DO EARTHQUAKES BEGIN?

studies suggesting the existence of aseismic slip on faults the work of Kanamori [1977]. From this outcome, one question that arises is what is the interaction between aseismic slip on faults and earthquakes? Does this aseismic slip enhance the rupture beginning?

To answer these questions, the asperity model was proposed by Lay and Kanamori [1981] and Lay et al. [1982]. As explained in the General Introduction, this model aims to explain the slip behavior with the existence of heterogeneities within the fault. These heterogeneities can be seen as zones with high, intermediate, or low stress. In this way, if the rupture propagates through a region where the stress is high relative to the surroundings, the earthquake will break this region called "asperity", having, as a result, a relatively large slip. In Figure 2.1 we show the original asperity models proposed by Lay and Kanamori [1981], to explain some slip models and the influence of stress heterogeneities within the fault.

On the other hand, we have the barrier model suggested by Das and Aki [1977] and Aki [1979]. In this model, a barrier is a region that can stop the rupture but can also be broken. If the barrier area is large enough, the propagation of the rupture tip will be stopped [Husseini et al., 1975]. However, if the region is small compared with the crack tip, there can be three different scenarios:

- The barrier will break if the tectonic stress is relatively high.
- If the tectonic stress is relatively low, the rupture will proceed beyond the barrier, leaving behind an unbroken barrier.
- If the tectonic stress is intermediate compared with the stress within the barrier, at the beginning the barrier will not cede, but it will eventually break due to the increase of dynamic stress.

In this regard, Aki [1979] proposes to map barriers within the fault using aftershocks sequences.

As we have shown so far, these models illustrate the general features of earthquake rupture. However, these models treat each event as time semi-independent from each other and not as part of the same processes. In other words, the first theoretical models explained each phenomenon, but not all together.

2.3. EARLY WORK AND NUMERICAL SIMULATIONS OF EARTHQUAKE NUCLEATION

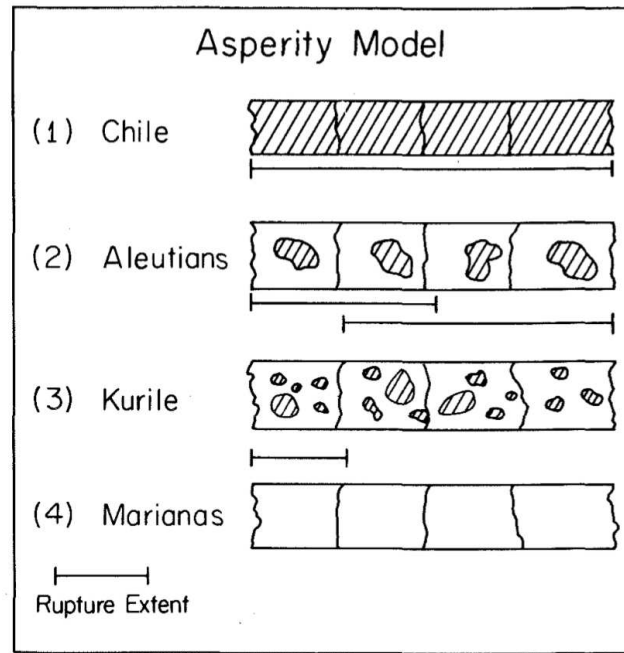


Figure 2.1: An asperity model indicating the different nature of stress distribution in each subduction zone category. The hatched areas indicate the zones of strong coupling. Figure from Lay and Kanamori [1981].

2.3 Early work and numerical simulations of earthquake nucleation

Das and Scholz [1981] performed one of the first studies to model the entire source cycle. In their model, the authors consider an earthquake as a shear crack, which propagation follows an experimental-derived law. This experimental law depends on the stress intensity factor at the crack tip, k and its relationship with crack parameters, the modulus of cohesion K_c in the presence of corrodent (such as water), and the stress-corrosion limit K_0 .

One of the most important statements of this theory is that an earthquake needs to be preceded by a nucleation phase in which a preseismic slip is necessary. Such nucleation phase can potentially explain the occurrence of foreshocks depending on the amplitude of k relative to K_c . If a region is embedded in the nucleation zone and $k \geq K_c$, this zone will experiment the occurrence of foreshocks until the mainshock event. Such theory suggest: (1) given the acceleration nature of the nucleation phase, the probability for foreshocks to happen increases as we approach the mainshock, and (2) the occurrence of foreshocks does not necessarily occur depending on the nucleation zone size and preslip amplitude.

Regarding geophysical observations, Ellsworth and Beroza [1995] analyzed the ini-

2.3. EARLY WORK AND NUMERICAL SIMULATIONS OF EARTHQUAKE NUCLEATION

tiation phase of about 30 earthquakes, with magnitudes from $M_W = 2.6$ to $M_W = 8.1$. The results of this study lead to the definition of two conceptual models to explain the occurrence of foreshocks during the initiation phase: the foreshock slow cascade model and the preslip model.

In the slow cascade model (Figure 2.2 (a)), stress changes induced by foreshocks contribute to a slow cascade of random failures, leading eventually to the mainshock. According to this model, foreshocks act as stochastic events that continue until the mainshock event. This behavior implies that it will be nearly impossible to predict the future occurrence of an earthquake.

In the preslip model (Figure 2.2 (b)), earthquakes are preceded by an aseismic preslip that slides over a region. During this nucleation phase, the aseismic slip gradually accelerates until the occurrence of the mainshock event. According to this model, aseismic preslip drives the triggering of foreshocks, suggesting the possibility to forecast some earthquakes.

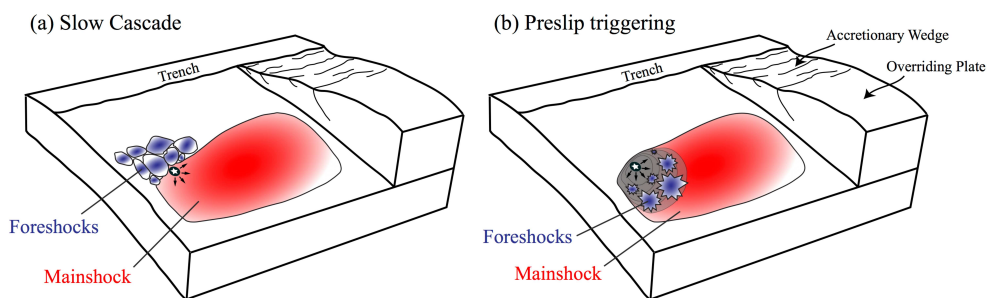


Figure 2.2: Schematic depiction of two possible mechanisms for foreshock generation. (a) Foreshocks triggered by previous foreshocks finally trigger the mainshock in a cascade of failures. (b) Foreshocks occur within the nucleation zone as asperities are loaded by the aseismic nucleation. The mainshock rupture is in Red and Foreshocks are in Blue. Figure courtesy of Z. Duputel.

Thanks to the development of rock friction laws, like the rate-and-state law [Marone, 1998, Scholz, 1998], earthquake rupture numerical models with rock-based friction laws were finally created [Cochard and Madariaga, 1996, Rice and Ben-Zion, 1996]. More recently, researchers have continued developing numerical models involving more physical mediums, i.e., 2D and 3D models, to unveil the nucleation phase complexity [e.g., Ampuero and Rubin, 2008, Lapusta and Rice, 2003, Rubin and Ampuero, 2005]. For example, Lapusta and Liu [2009] developed a 3D methodology to simulate the rupture evolution of a vertical planar strike-slip fault. Their simulation is capable of recreating seismic and aseismic slip on the fault.

We now present the experimental studies related to the initiation phase. Most of these studies relied on laboratory earthquakes, either modeled with rocks or

laboratory-made faults.

2.4 Laboratory experiments

At the same time that numerical models were being developed to understand the seismic rupture, the first experimental works were developed [Scholz, 1968, Scholz et al., 1969]. In this regard, Dieterich [1978] proposes a time-dependent friction theory using different experimental observations. In their work, authors suggest that there could be a creeping before the main slip event.

On the other hand, Ohnaka and Shen [1999] designed a series of laboratory experiments to elucidate characteristics of the nucleation and dynamic stages of earthquake ruptures. One of the main conclusions of this work, is that the nucleation stage consists of two phases: phase I, an initial quasi-static phase, and phase II, a subsequent accelerating phase (Figure 2.3). In phase I, the rupture evolves steadily. In phase II, the rupture growth accelerates. Using the results of Ohnaka and Shen [1999], Ohnaka [2000] introduces a scaling relationship for earthquake size and its nucleation zone.

We focus now on the work of Latour et al. [2013]. In their work, they use a laboratory-made fault using polycarbonate as a rock-analog material, for which they impose stress conditions trying to simulate subduction regimes (Figure 2.4). They used high-speed photoelasticity and high-frequency acoustic monitoring to track the slip on the fault.

The outcomes from this work support the previous conclusion of Ohnaka and Shen [1999] regarding the existence of two stages in the nucleation phase, an initial quasi-static and an accelerating phase. However, there is a crucial difference in phase I. Rather than having a steadily constant velocity growth, Latour et al. [2013] observe an exponential velocity growth. In addition, Kaneko et al. [2016] compare the results of Latour et al. [2013] with numerical modeling, showing that rate-and-state friction laws and elastic continuum can reproduce the behaviors of rupture nucleation seen in laboratory experiments.

Despite the observation of nucleation phases in both numerical and laboratory studies, the origin of foreshock sequences and the detectability of earthquake nucleation is still under debate. The origin of foreshocks turns out to be crucial to understand the physics during the initiation of earthquakes. In the following sections, we describe the observations supporting each model. Finally, we discuss studies that suggest the coexistence of both models.

2.4. LABORATORY EXPERIMENTS

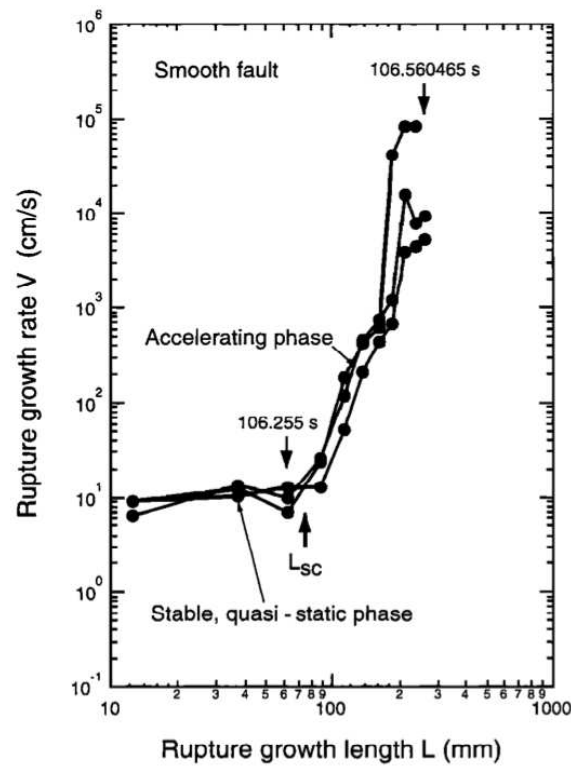


Figure 2.3: Plots of the logarithm of the rupture growth rate V against the logarithm of the rupture growth length L during the nucleation for events on the smooth fault. L_{sc} denotes the critical length beyond which the rupture grows at accelerating speeds, and the times $t_1 = 106.255$ and $t_2 = 106.560465$. Figure from Ohnaka and Shen [1999].

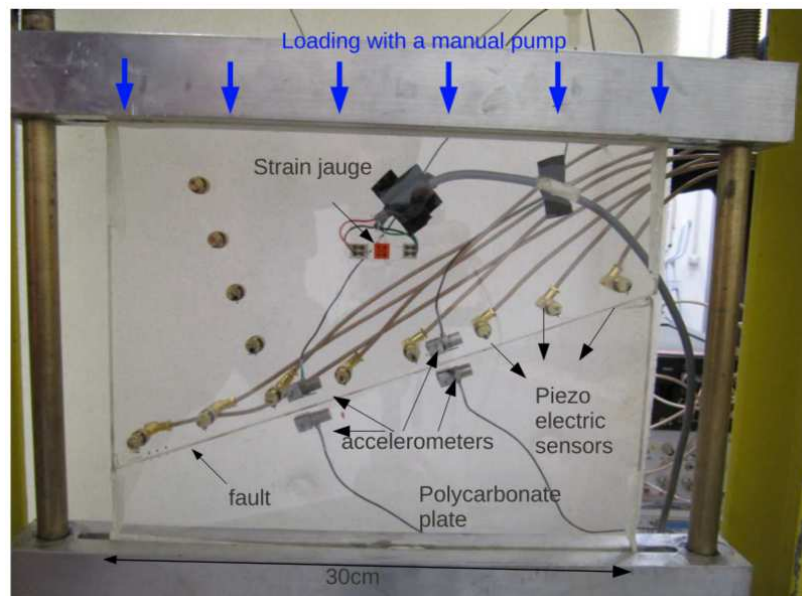


Figure 2.4: Photograph of the polycarbonate plate with the acoustic array, in the loading apparatus. Figure from Latour et al. [2013].

2.5. FORESHOCKS TRIGGERED BY ASEISMIC PRE-SLIP?

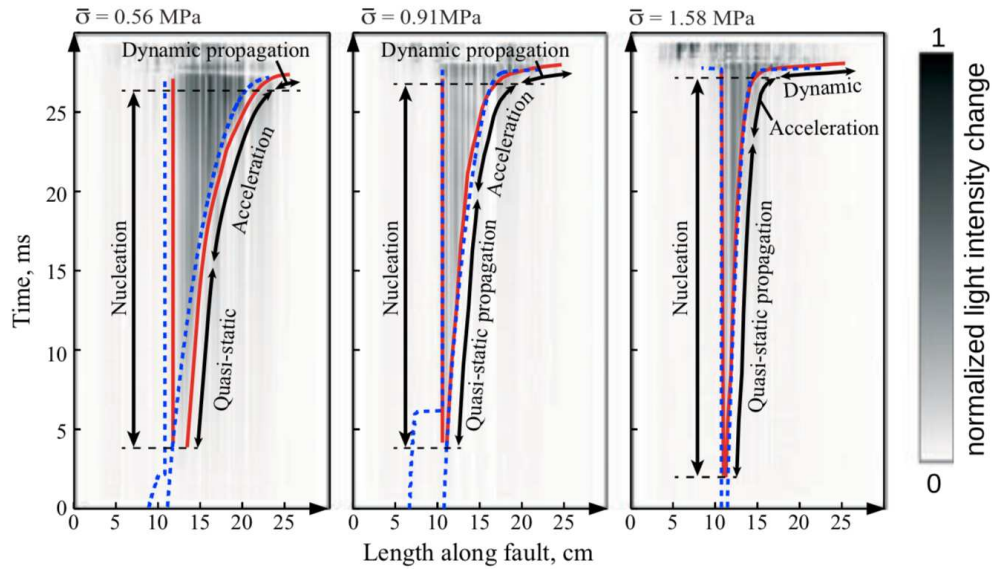


Figure 2.5: Examples of videograms showing three spontaneous laboratory earthquakes at increasingly higher normal prestresses – Gray scale indicates the light intensity change since time $t = 0$. Red curves highlight the position of rupture tips as a function of time (from Latour et al. [2013]). Blue dashed lines are the predicted position of rupture fronts in numerical simulations conducted by Kaneko et al. [2016]. Rupture nucleation can be decomposed into a quasi-static phase followed by an acceleration phase before dynamic (seismic) rupture propagation. Notice that the characteristics of rupture nucleation depend on the level of imposed normal stress (indicated on top of each subplot). Figure modified from Kaneko et al. [2016], courtesy of Z. Duputel.

2.5 Foreshocks triggered by aseismic pre-slip?

Dodge et al. [1996] is one of the first study introducing the preslip triggering model to explain the occurrence of foreshock sequences. In this study, six earthquake sequences in the California region were studied. This region is one of the best-instrumented zones all around the world, with more than 500 permanent stations nowadays (<https://scedc.caltech.edu/about/dchistory.html>). After analyzing six foreshock sequences in California, they concluded that foreshocks production could not be caused by this transfer but by an aseismic preslip.

Assuming that foreshocks are triggered by aseismic preslip, one way to detect extended nucleation phases is to look for significant increases in seismicity rates before large earthquakes. On this subject, Bouchon et al. [2013] analyze foreshock-mainshock sequences in Japan and the west coast of North America. They found that the interplate earthquakes are preceded by more pronounced increases in foreshock seismic activity than intraplate events. In Figure 2.6, we can see the normalized stacks of the cumulative seismic moments. On average, we observe that for a

2.5. FORESHOCKS TRIGGERED BY ASEISMIC PRE-SLIP?

24-hour stack, there is an overall increase in seismic activity between three and one day before the mainshock, suggesting an aseismic pre-slip occurring over that time-scale on average. As noted in section 2.6, such an increase of seismicity rate could in fact be explained by the natural clustering of earthquakes (i.e., the cascading of foreshocks).

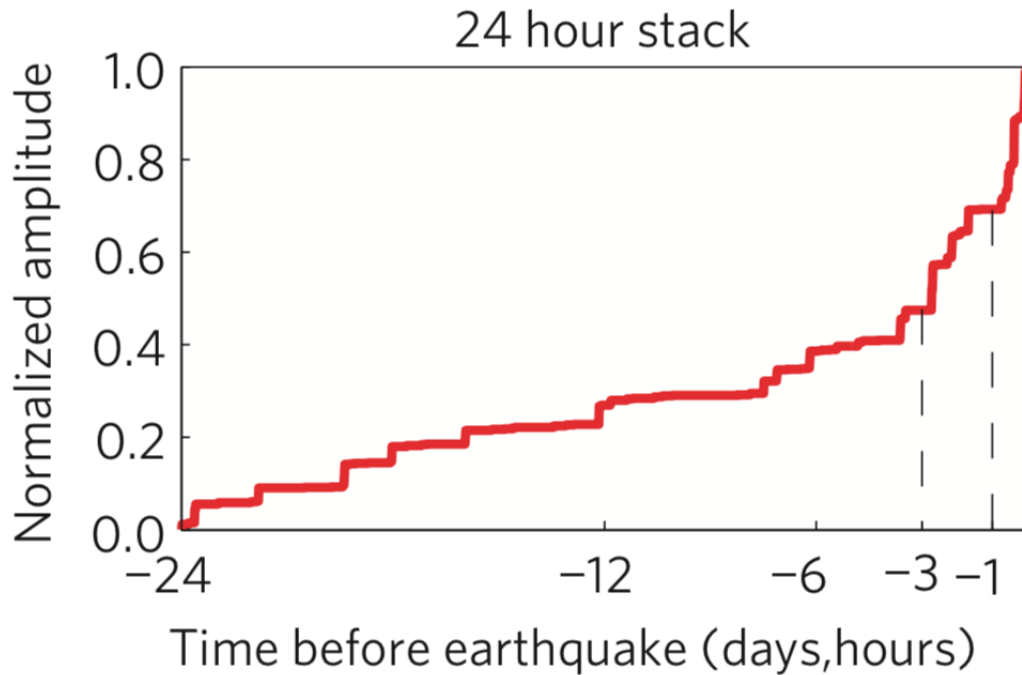


Figure 2.6: Normalized stacks of the cumulative seismic moments of all the inter-plate sequences. Each sequence carries the same weight. Figure from Bouchon et al. [2013].

Another way to use seismology information to characterize the initiation phase of earthquakes is by searching for repeating earthquakes. By definition, a repeating earthquake is a family of events that generate very similar waveforms [Nadeau et al., 1995]. The fact that these events have very similar waveforms is interpreted as the repetitive rupture of a single asperity on the fault. Assuming that the rupture of this asperity is triggered by surrounding fault creep, such repetitive events can be used to assess variation of aseismic slip rate. For example, Bouchon et al. [2011] detected numerous earthquakes with the same waveform signal 44 minutes before the occurrence of the 1999 $M_W = 7.6$ Izmit earthquake, showing a phase of slow slip occurring prior to the mainshock.

Similarly, several studies have been made in the Japan region to analyze earthquake sequences [Igarashi et al., 2003, Uchida et al., 2016]. For the 2011 $M_W = 9.0$ Tohoku earthquake sequence, we have the work of Uchida and Matsuzawa [2013] and Mavrommatis et al. [2015], that show an acceleration of aseismic slip preceding

2.5. FORESHOCKS TRIGGERED BY ASEISMIC PRE-SLIP?

the mainshock estimated from repeating earthquakes.

The repeating earthquakes can also be found in intraplate context. Tape et al. [2013] investigated the nucleation phase of the 2012 $M_W = 3.9$ Nenana earthquake, which originated in a strike-slip fault located in central Alaska. This earthquake was triggered by the 2012 $M_W = 8.2$ Sumatra earthquake, whose surface waves act like an aseismic pre-slip perturbing the fault.

With the advances in Global Navigation Satellite Systems (GNSS), the study of ground displacements has taken an important role in unveiling the occurrence of aseismic slips. In this sense, the 2011 $M_W = 9.0$ was one of the first earthquakes for which there is good GPS coverage and a dense seismic network. On one side, Kato et al. [2012] employed repeating earthquakes to retrieve the evolution of a slow slip starting one month before the mainshock event. On the other hand, by using the Japanese GPS network, an aseismic slip preceding the mainshock was traced back up to 14 years before the mainshock [Marill et al., 2021, Mavrommatis et al., 2015, Miyazaki et al., 2011, Ozawa et al., 2012, Yokota and Koketsu, 2015].

In this regard, the 2014 $M_W = 8.1$ Iquique earthquake brings a unique opportunity to evaluate all the different techniques. Indeed, this earthquake is one of the few sequences for which one may combine seismic and GNSS observations to analyze the initiation phase of the mainshock. The $M_W = 8.1$ Iquique earthquake took place in northern Chile on April 1st, 2014, having a foreshocks sequence with a largest magnitude of $M_W = 6.7$ on March 16th, 2014 [Brodsky and Lay, 2014, Lay et al., 2014]. Interestingly, Ruiz et al. [2014] observe a transient signal in the GPS displacement time series preceding the mainshock (Figure 2.7). Their analysis suggests that foreshock-induced displacement could only explain 20% of the observed displacement and that the rest of the observed transient correspond to aseismic preslip before the mainshock. This conclusion is also supported by repeating earthquake studies that suggest an aseismic slip occurring prior to the main event, with a moment magnitude around $M_W \approx 6.7$ [Kato and Nakagawa, 2014, Kato et al., 2016, Meng et al., 2015]. In this respect, Socquet et al. [2017] detected a slow slip event starting eight months before the mainshock of the Iquique sequence, triggering at the same time an increase in seismic activity and a decrease in the b value. These results suggest a progressive expansion of failures into the conditionally stable areas surrounding small seismic asperities, which eventually, lead to the main rupture nucleation.

On the contrary, Schurr et al. [2014] show that the transient displacement can be explained only using the cumulated coseismic slip produced by the entire foreshock sequence. This conclusion contradicts the findings of Ruiz et al. [2014], enhancing

2.5. FORESHOCKS TRIGGERED BY ASEISMIC PRE-SLIP?

the debate about foreshocks' role in the initiation phase. To compare both foreshocks models, Bedford et al. [2015] analyze the continuous GPS data before the 2014 $M_w = 8.1$ Iquique earthquake. They found that most of the transient GPS displacement can be interpreted as foreshocks coseismic displacements. However, there are two episodes between 18–21 and 25–31 March where the foreshock coseismic displacements cannot describe the observed displacements. This displacement could be explained either as induced by foreshocks afterslip or an aseismic preslip.

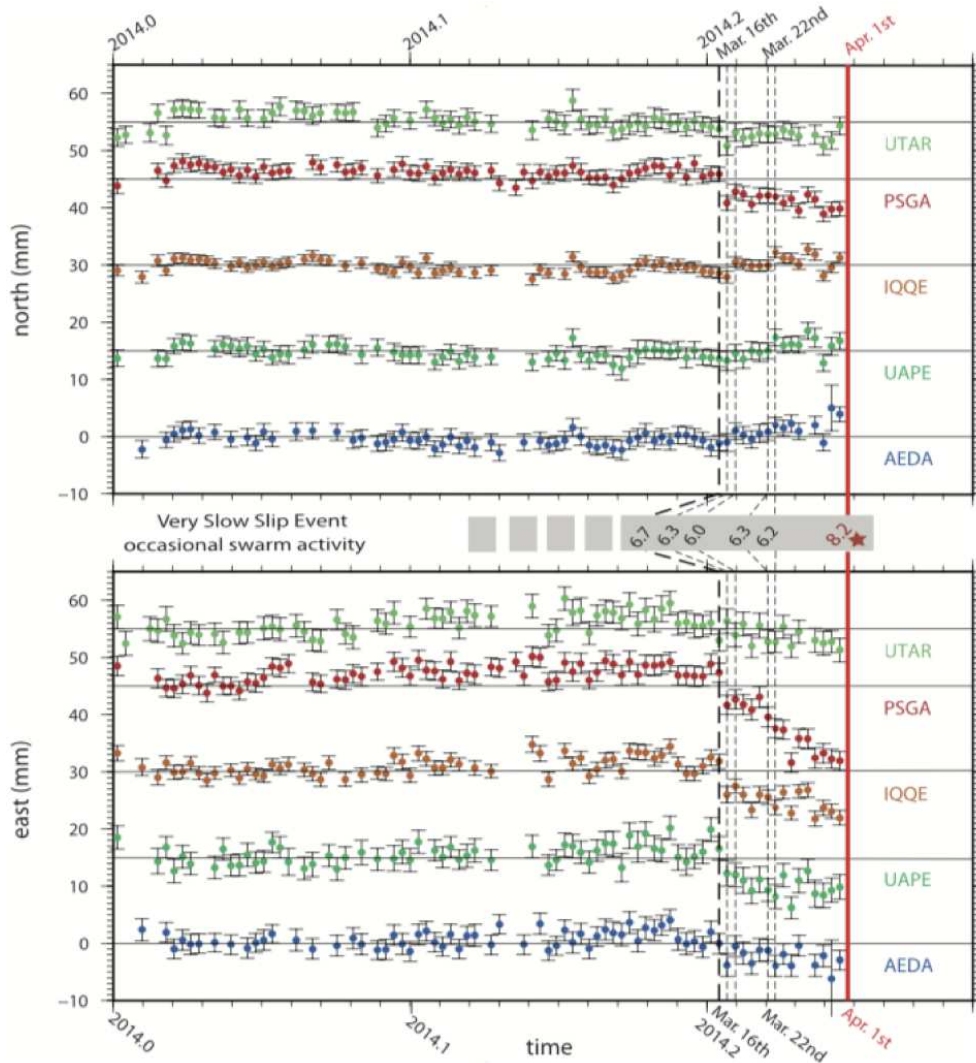


Figure 2.7: Motion of coastal GPS stations preceding the Iquique earthquake. (A) North and (B) east components relative to a linear evolution model with seasonal variations estimated since 2012. The thick red line denotes the origin time of the mainshock, whereas the black dotted lines show the occurrence times of the $M_w > 6$ foreshocks. Error bars indicate 1σ formal uncertainty. Figure from Ruiz et al. [2014].

By taking into account the uncertainty in earthquake locations, Herman et al. [2016] attempted to assess the seismic and aseismic slip during the initiation phase of

2.6. FORESHOCKS AS CASCADES OF RANDOM FAILURES?

the 2014 $M_W = 8.1$ Iquique earthquake. They found that starting with the largest foreshock of $M_W = 6.7$, the three largest foreshocks occurred in regions where the Coulomb stress has had changed due to preceding events, indicating that these events were brought to failure by prior seismicity. At the same time, they found, as previously reported, that an aseismic slip could probably take place in the region during the initiation phase. These results suggest that both foreshocks' models could be happening and interacting simultaneously within the fault.

2.6 Foreshocks as cascades of random failures?

The detection of foreshocks can be traced back to the 1970s with the work of Jones and Molnar [1976], where foreshocks are cited as one of the reasons for the success in predicting the 1975 $M_S = 7.3$ Haicheng earthquake. In their study, Jones and Molnar [1976] observe an increase of the foreshock seismicity rate before the mainshock.

With the densification of seismological networks, and the development of new detection methods, foreshock sequences detection increases globally. Several studies point out the difference between the rate of foreshocks and how this rate increases close to the mainshock beginning [Abercrombie and Mori, 1996, Bowman and King, 2001, Ellsworth and Beroza, 1995, Jaumé and Sykes, 1999, Knopoff et al., 1996, Reasenber, 1999].

One crucial aspect to consider in foreshock occurrence is the statistical significance of the foreshocks rate. In this regard, Helmstetter and Sornette [2003] propose to use the Epidemic-Type Aftershock (ETAS) model, a model previously introduced by Kagan and Knopoff [1981, 1987], Ogata [1988], to study changes in the foreshocks rate. The Epidemic-Type Aftershock (ETAS) model is a statistical model that tries to mimic earthquake catalogs, including several mainshock-aftershock sequences [Zhuang et al., 2012]. In general terms, the temporal ETAS model can be represented as follows:

$$\lambda(t) = \mu + \sum_{i|t_i < t} A \exp^{\alpha(M_i - M_c)} (t - t_i + c)^{-p}, \quad (2.1)$$

where $\lambda(t)$ is the temporal conditional intensity, μ is the time-independent background seismicity rate, and M_c is the magnitude of completeness. The sum represents the expected aftershock rate at a given time that is triggered by the previous seismicity. The parameters A and α describe the overall regional aftershock productivity and the magnitude dependence on the number of triggered events, respec-

2.6. FORESHOCKS AS CASCADES OF RANDOM FAILURES?

tively. Finally, c and p are the parameters of the Omori-Utsu law [Utsu, 1957, Utsu et al., 1995] describing the time-decay of the aftershock seismicity rate following a mainshock.

In their work, Helmstetter and Sornette [2003] suggest that the difference between foreshock, aftershock, and mainshock definition is rather empirical than physically-based. In particular, they argue that there is no statistical difference between foreshock, mainshock, and aftershock behaviors. They investigated the catalog of the Southern California Data Center (SCEC) between 1932-2000, with more than 22000 earthquakes. Their results suggest that most of the foreshock sequences can be explained by the natural clustering of earthquakes (i.e., mainshock-aftershock sequences), thus, supporting the foreshock cascade model. Besides, they suggest that seismic activity before a mainshock is independent of its magnitude.

Since the work of Helmstetter and Sornette [2003], the ETAS model has been used to explore foreshock seismicity rates to investigate anomalous seismicity rates during earthquake initiation phases [Marsan and Enescu, 2012, Marzocchi and Zhuang, 2011, McGuire et al., 2005].

Thanks to the new and more accurate location techniques, in the last twenty years there has been an improvement in earthquake location and completeness of catalogs [Gibbons and Ringdal, 2006, Ross et al., 2019]. One example of this improvement is the work of Ellsworth and Bulut [2018]. In this study, the authors analyze the foreshock sequence preceding the 1999 $M_W = 7.6$ Izmit earthquake. For this purpose, they relocated the sequence using the double-difference method and performed cluster analysis and template matching. Using these relocated foreshocks, they calculated the stress change due to each foreshock. In Figure 2.8, we observe distribution of foreshocks along the fault. As we can see, the region of stress change fall in the new hypocenter location. These results support the idea that foreshocks trigger each other in a cascade of failures until reaching the instability that will lead to the mainshock. These conclusions are in disagreement with the analysis of Bouchon et al. [2011], previously describe in the previous section.

It is also worth noting the work of Ross et al. [2019] that improved the South California catalog from 2000 to 2017. In their work, they used the template matching method to detect new events. They designate their catalog as the quake template matching (QTM) catalog, with nearly 1.81 million earthquakes. We show in Figure 2.9 the obtained event density for the southern California region.

By using the QTM catalog, Trugman and Ross [2019] investigate the foreshock activity sequences in the region of southern California. They use 46 mainshocks that

2.6. FORESHOCKS AS CASCADES OF RANDOM FAILURES?

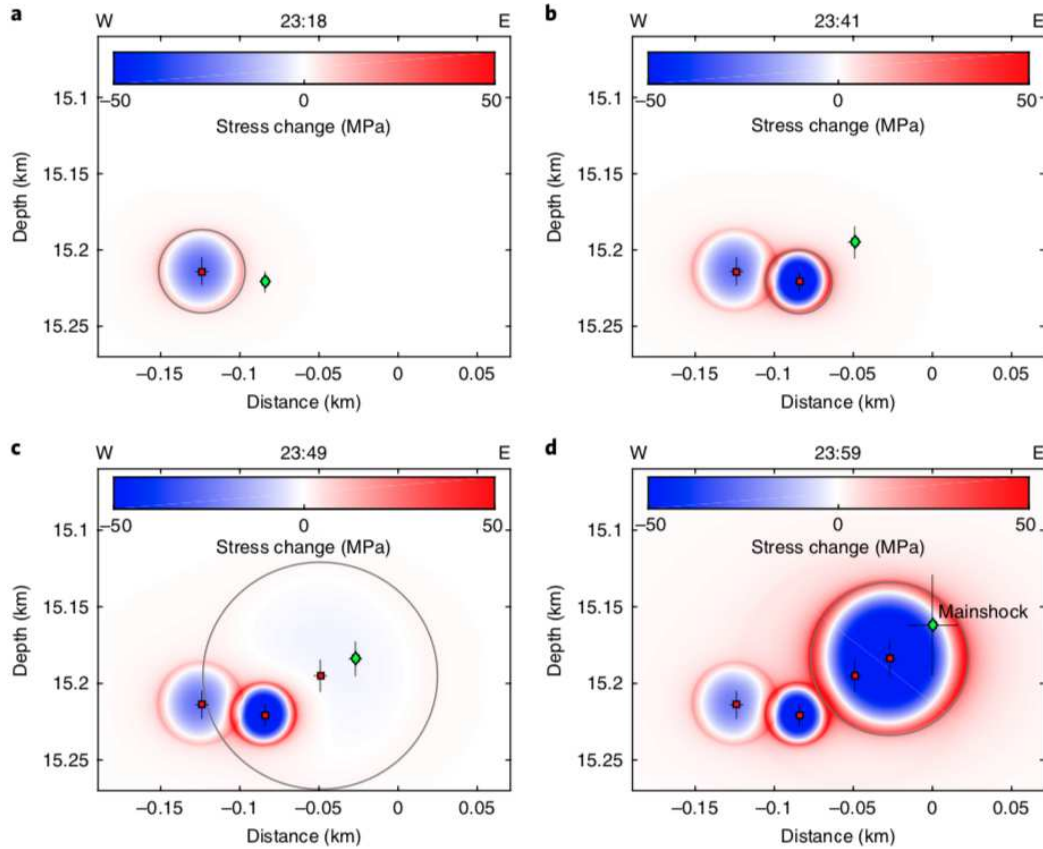


Figure 2.8: East–west cross sections of the evolving shear stress changes on the fault plane during the foreshock sequence to the 1999 Izmit earthquake. a–d, Each frame corresponds to the origin time of one of the four largest foreshocks and adds the stress change from that event. Stress change based on a previously reported source model [Madariaga and Ruiz, 2016]. Red squares and error-bars show hypocentroids and 2σ location uncertainty of events occurring through the time indicated in the figure heading. Green diamonds denote the hypocentroid of the next foreshock in the sequence (a–c) and the mainshock hypocentre (d). Figure from Ellsworth and Bulut [2018].

were selected for being spatial and time-isolated. To analyze the seismicity rate, they used a Poisson distribution-based method, the interevent time method [Hainzl et al., 2006]. One crucial assumption from this method is that it doesn’t account for triggered event interactions as the ETAS model. The results suggest that 72 percent of these mainshocks are preceded by foreshock activity that is significantly elevated compared to the local background seismicity rate. Besides, such occurrence suggests that foreshocks in nature are more prevalent than previously thought. This conclusion enhances the preslip model. However, as we point out, the used Poisson distribution-based method does not take into account the interaction of events.

Following this study, van den Ende and Ampuero [2020] also analyze the QTM catalog but using a Gamma distribution model. In this manner, they found that only 15

2.6. FORESHOCKS AS CASCADES OF RANDOM FAILURES?

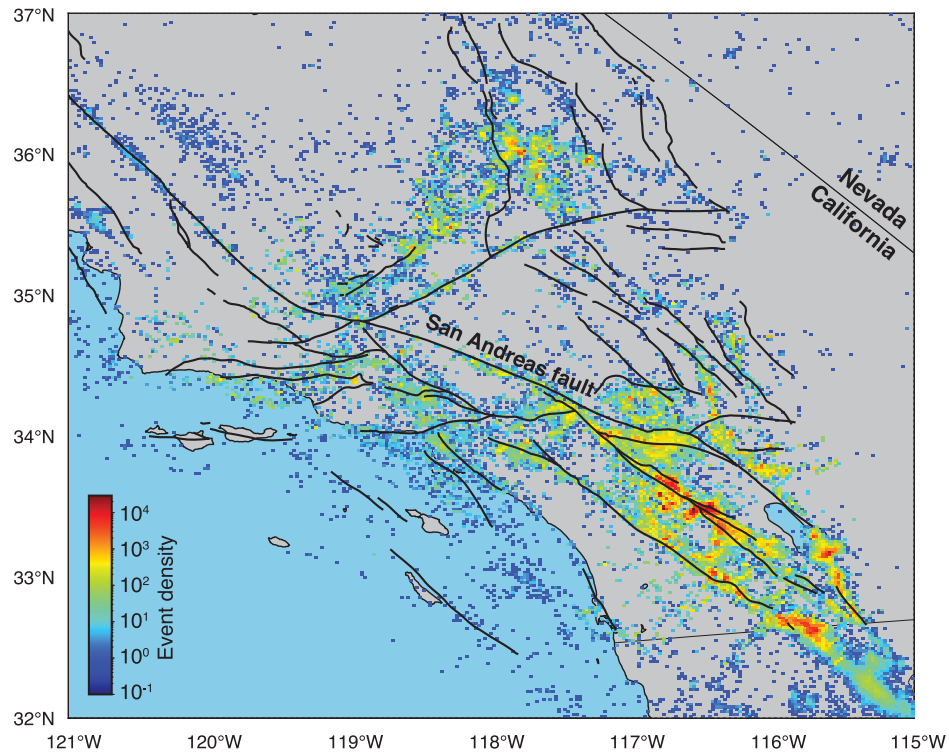


Figure 2.9: Map of earthquake density in the QTM catalog (bins: 2 km by 2 km). Figure from Ross et al. [2019]

of 46 mainshocks (33 %). However, taking into account temporal fluctuation in the catalog, only 18 % of the foreshock sequence seismicity rates remain unexplained, hence, linked to initiation processes.

Finally, Moutote et al. [2021] use the ETAS model to analyze the same foreshocks sequences. The ETAS model can fully represent earthquake clustering contrarily to Poisson or Gamma distributions that do not account for earthquake interactions. By taking into account earthquake interactions, 18 % of foreshock sequence rates could not be explained by their ETAS model. This result suggests that anomalous seismicity rates are less common than what was originally suggested by Trugman and Ross [2019]. This study suggests that most foreshock sequences can be explained by foreshock cascades. Nevertheless, the number of unexplained sequences remain significant for which it would be interesting to search for the existence of preslip (i.e., using near-fault observations)

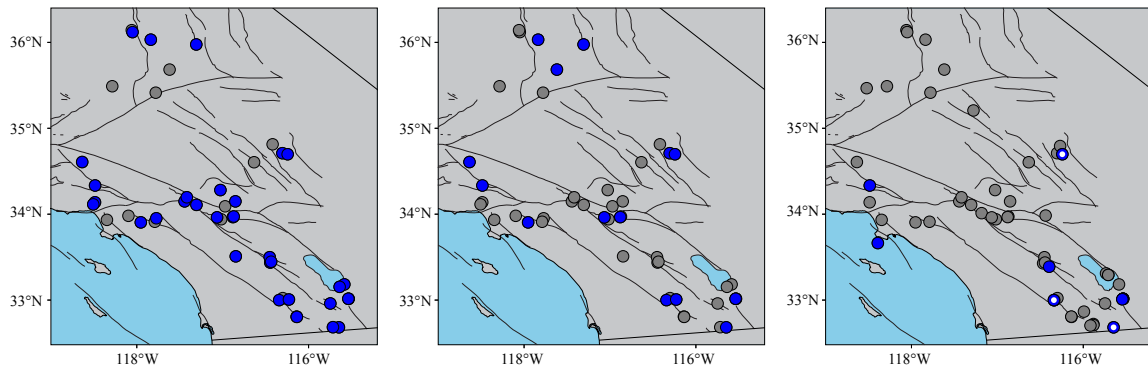


Figure 2.10: Anomalous foreshock-mainshock sequences. Left) Poisson distribution model from Trugman and Ross [2019]. Center) Gamma distribution model Differences between models from van den Ende and Ampuero [2020]. Right) ETAS model from Moutote et al. [2021]. Figure courtesy of Z. Duputel and L. Moutote.

2.7 Co-existence of foreshock cascading and aseismic pre-slip

As we have shown, previous studies lead to different conclusions regarding the origin of observed foreshock sequences. The outcomes of each study depend on several assumptions, so the role of foreshocks in the earthquake initiation phase is still under debate.

For example, observations during the 2014 $M_W = 8.1$ Iquique earthquake tend to suggest that both foreshock cascading and preslip triggering could possibly co-exist in nature. We can have, for instance, an aseismic slip triggering foreshock cascades (possibly mediated by afterslip). Therefore, we can think that the earthquake initiation consist in the co-existence of foreshock triggered by aseismic slip and events triggered by earthquake interactions (i.e., static or dynamic stress-transfer). Such co-existence is clear for the Iquique earthquake. We can see in the *Centro Sismológico Nacional* (CSN) catalog that large foreshocks actually triggered a sequence of aftershocks. At the same time, analysis of Herman et al. [2016] and Socquet et al. [2017] show that there is still transient displacements that cannot be fully explained by foreshocks co-seismic offsets (hence suggesting aseismic preslip).

In this regard, Mignan [2014] conducted a meta-analysis of foreshocks role studies, where he observes that the conclusion about the origin of foreshock sequences depends substantially on the employed approach. Studies suggesting an aseismic preslip triggering model are mostly based on the analysis of individual foreshock sequences. On the other hand, the foreshock cascade model is mostly supported by

2.7. CO-EXISTENCE OF FORESHOCK CASCADING AND ASEISMIC PRE-SLIP

studies stacking many datasets together. Similarly, we recognize that the foreshock cascade model conclusion is 100% based on statistical methods, i.e., methods using large datasets or catalogs. Meanwhile, the aseismic preslip triggering has been obtained by different methods, statistical, heuristic (where foreshocks observations are difficult to explain by earthquake triggering), and physical (i.e., static stress transfer theory).

In this respect, McLaskey [2019] conducted a series of experiments on a 3 meters rock sample. The fact of having a larger experiment setting contributes to taking into account the complexity of the earthquake initiation process. The nucleation length L_c calculated in this experiment follows the same scaling relationships previously reported by Ohnaka and Shen [1999] and Latour et al. [2013]. The results from this study suggest a rate-dependent “cascade up” model for earthquake initiation, which can successfully recreate the foreshocks cascade’s behavior with the presence of an aseismic slip (Figure 2.11), which supports the idea of the coexistence of models.

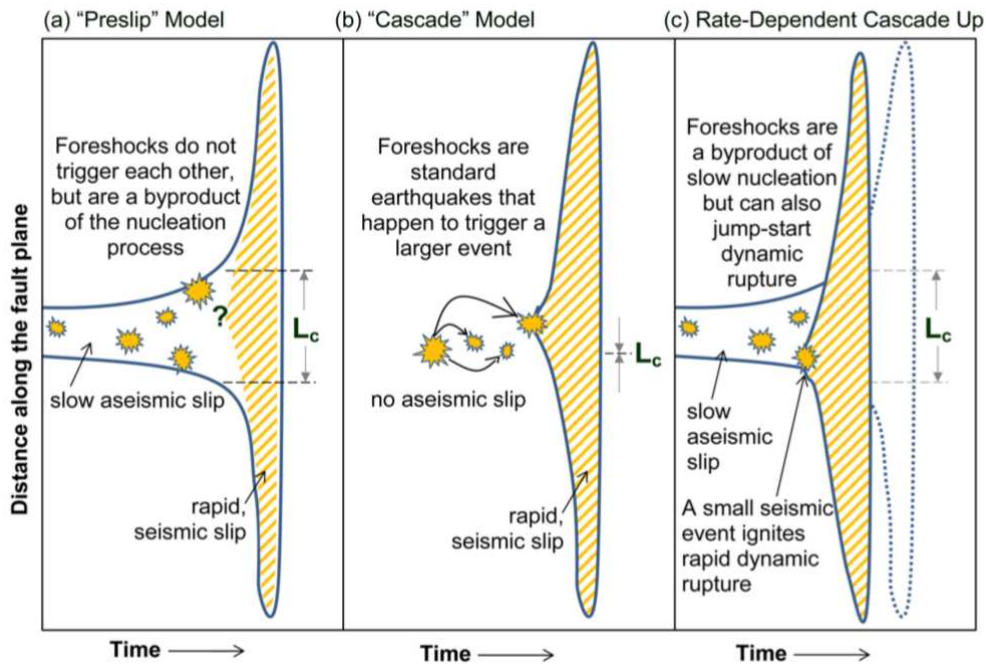


Figure 2.11: Three earthquake initiation models, their relationship to L_c , and their implications for foreshocks. The preslip model (a) and cascade model (b) illustrate endmember behavior where L_c is large (>10 km) or small (<1 m). (c) The laboratory observations suggest a rate-dependent cascade up model, which contains attributes of both end members. Figure from McLaskey [2019].

Beyond the fact that many studies are based on incomplete seismicity catalogs, one limitation of past studies is the fact that they often do not combine multiple observations. As a matter of fact, many studies investigate seismicity catalogs alone, without including geodetic observations. This is clearly due to the lack of near-

2.7. CO-EXISTENCE OF FORESHOCK CASCADING AND ASEISMIC PRE-SLIP

fault observations for many foreshock sequences that prevent such joint analysis. Studying sequences for which a joint analysis is possible is therefore important to decipher the behavior of faults during the preparation of large earthquakes.

The following study was done in collaboration with Agnès Chounet, Zacharie Duputel, Jorge Jara, Cédric Twardzik, and Romain Jolivet. We focus on the initiation phase of the 2017 $M_W = 6.9$ Valparaíso earthquake. In this study, I analyzed and compared geodetic and seismic observations, and wrote the manuscript. AC developed and adapted the CMT inversion algorithm and obtained the CMT catalog. ZD conceived and led the study, and performed the slip inversions. CT and JJ processed the GPS data. RJ developed the CSI code used to gather GPS data and static Green's functions for a given fault geometry. The results of this work have already been published in Geophysical Research Letters and can be cited as:

Caballero, E., Chounet, A., Duputel, Z., Jara, J., Twardzik, C., & Jolivet, R. (2021). Seismic and aseismic fault slip during the initiation phase of the 2017 $M_W = 6.9$ Valparaíso earthquake. Geophysical Research Letters, 48, e2020GL091916. <https://doi.org/10.1029/2020GL091916>.

2.8 Seismic and aseismic fault slip during the initiation phase of the 2017 $M_W=6.9$ Valparaiso earthquake.

2.8.1 Abstract

Transient deformation associated with foreshocks activity has been observed before large earthquakes, suggesting the occurrence of a detectable pre-seismic slow slip during the initiation phase. A critical issue consists in discriminating the relative contributions from seismic and aseismic fault slip during the preparation phase of large earthquakes. We focus on the April-May 2017 Valparaíso earthquake sequence, which involved a $M_W = 6.9$ earthquake preceded by intense foreshock activity. To assess the relative contribution of seismic and aseismic slip, we compare surface displacement predicted from foreshocks source models with transient motion measured prior to the mainshock. The comparison between observed and predicted displacements shows that only half of the total displacement can be explained by the contribution of foreshocks. This result suggests the presence of aseismic preslip during an initiation phase preceding the mainshock.

Plain Language Summary

Several studies suggest that some large earthquakes are preceded by aseismic fault slip. Such preslip could explain foreshock activity and transient displacements observed before some large earthquakes. However, a large portion of observed pre-seismic deformations could be associated with the displacement field caused by each individual foreshock earthquakes. This study focuses on the 2017 $M_W = 6.9$ Valparaíso (Chile) earthquake that was preceded by a noticeable GPS displacement and numerous foreshocks. By combining geodetic and seismic observations, our results show that only half of pre-seismic displacement can actually be explained by the contribution of foreshocks. This confirms that the Valparaíso earthquake was preceded by detectable aseismic fault slip accelerating into the main dynamic rupture.

2.8.2 Introduction

Experimental and theoretical studies suggest that earthquakes begin with aseismic slow slip accelerating into a dynamic, catastrophic rupture [Das and Scholz, 1981, Kaneko et al., 2016, Latour et al., 2013, Ohnaka, 2000]. Laboratory-derived rate-and-state models depict different evolution of preslip within nucleation zones of various sizes [Ampuero and Rubin, 2008, Kaneko and Ampuero, 2011]. With technological advances such as high-speed photoelastic techniques, the progressive acceleration from slow stable slip to fast dynamic slip can be accurately monitored in laboratory conditions [e.g., Latour et al., 2013]. Despite these advances, the detectability of such nucleation phases on natural faults is still an open question. In addition to the nucleation itself, observations of the precursory phase leading to an earthquake indicate that earthquakes are often preceded by foreshocks that could potentially be triggered by aseismic preslip [Bouchon et al., 2011, 2013, Kato et al., 2012]. Nonetheless, the role of foreshocks during this precursory phase remains unclear. At present, two end-member conceptual models compete in explaining the occurrence of foreshocks. In the first model, foreshock stress changes contribute to a slow cascade of random failures, leading eventually to the mainshock [Ellsworth and Bulut, 2018, Helmstetter and Sornette, 2003, Marsan and Enescu, 2012]. The second model proposes that foreshocks are triggered by aseismic slip corresponding to the nucleation process of the mainshock [Bouchon et al., 2011, Dodge et al., 1996].

The continued development of geophysical networks in active tectonic regions provides new opportunities to better capture the genesis of earthquakes. Geodetic observations provide strong evidences of pre-seismic transient deformations at various time-scales [Ito et al., 2013, Mavrommatis et al., 2014, Ozawa et al., 2012, Socquet et al., 2017, Yokota and Koketsu, 2015]. However, the interpretation of such observations is often difficult. This is particularly evident for the 2014 $M_W = 8.4$ Iquique (Chile) earthquake, which was preceded by an active foreshock sequence that started 8 months before the mainshock [Kato and Nakagawa, 2014]. This foreshock sequence was accompanied by clear GPS transient displacements, corresponding at least to some extent to aseismic fault slip preceding the mainshock [Ruiz et al., 2014, Socquet et al., 2017]. The aseismic behavior of the observed pre-seismic transient is however debated as it might largely correspond to the cumulative co-seismic displacement of the foreshocks and associated afterslip [Bedford et al., 2015, Schurr et al., 2014]. A reliable estimate of the relative contribution of seismic and aseismic deformations during nucleation is essential to better capture fault processes at the onset of earthquakes [Herman et al., 2016].

2.8. SEISMIC AND ASEISMIC FAULT SLIP DURING THE INITIATION PHASE OF THE 2017 MW=6.9 VALPARAISO EARTHQUAKE.

On 24 April 2017, a $M_W = 6.9$ earthquake occurred offshore Valparaíso in the central segment of the Chilean megathrust (33.089°S, 72.116°W, 21:38:28 UTC; Centro Sismológico Nacional, CSN). This event is relatively moderate given that this region of the Chilean subduction experienced earthquakes of magnitudes $M_W > 8$ [Comte et al., 1986, Dura et al., 2015]. This earthquake, however, caught the attention of seismologists because it was preceded by a vigorous foreshock activity in the ~ 2 days preceding the mainshock. This precursory activity has also been captured by GPS stations indicating a pre-seismic trenchward motion over a similar time-scale [Ruiz et al., 2017, 2018]. A preliminary analysis of seismological and geodetic observations suggests that 80% of pre-seismic GPS displacement is due to aseismic fault slip preceding the mainshock [Ruiz et al., 2017]. This first order estimate is obtained by comparing inverted preslip with the seismic moment of foreshocks assuming they are all located on the subduction interface. This assumption is questionable as seismicity catalogs depict a significant dispersion of earthquake locations around the plate interface [Ruiz et al., 2017, 2018], most events being located at depths larger than the slab 1.0 model [Hayes et al., 2012]. Such dispersion, probably related to depth uncertainty, implies a significant non-random bias in seismic moment for dip-slip earthquakes. For example, if an earthquake at 20 km depth is mislocated at 25 km, the moment is underestimated by nearly 20% using long-period teleseismic records [Tsai et al., 2011]. Such mis-estimation of seismic moment may lead to non-negligible errors in the contribution of foreshocks to observed pre-seismic deformations.

The primary goal of this study is to assess the relative contribution of seismic and aseismic slip during the few days preceding the 2017 Valparaíso earthquake. Estimating the seismic contribution to observed geodetic displacement is difficult as we deal with moderate-sized foreshocks ($M_W < 6$) for which a co-seismic offset is not clearly visible on GPS time-series. The seismic contribution to the observed displacement can be estimated by modeling the source of foreshocks from seismic data. However, this process should be done carefully as source models and the corresponding predictions can be affected by significant uncertainties. In this work, we obtain a moment-tensor catalog and predict the corresponding co-seismic offsets at GPS stations accounting for observational and modeling uncertainties. In particular, we account for prediction uncertainties associated with inaccuracies in the Earth model. We find that about half of the observed GPS pre-seismic displacement is aseismic and is caused by preslip in the vicinity of the impending mainshock hypocenter. Such pre-seismic deformation is unlikely to be explained by afterslip induced by preceding foreshocks. This suggests that aseismic preslip played an important role in the 2017 Valparaíso sequence.

2.8. SEISMIC AND ASEISMIC FAULT SLIP DURING THE INITIATION PHASE OF THE 2017 MW=6.9 VALPARAISO EARTHQUAKE.

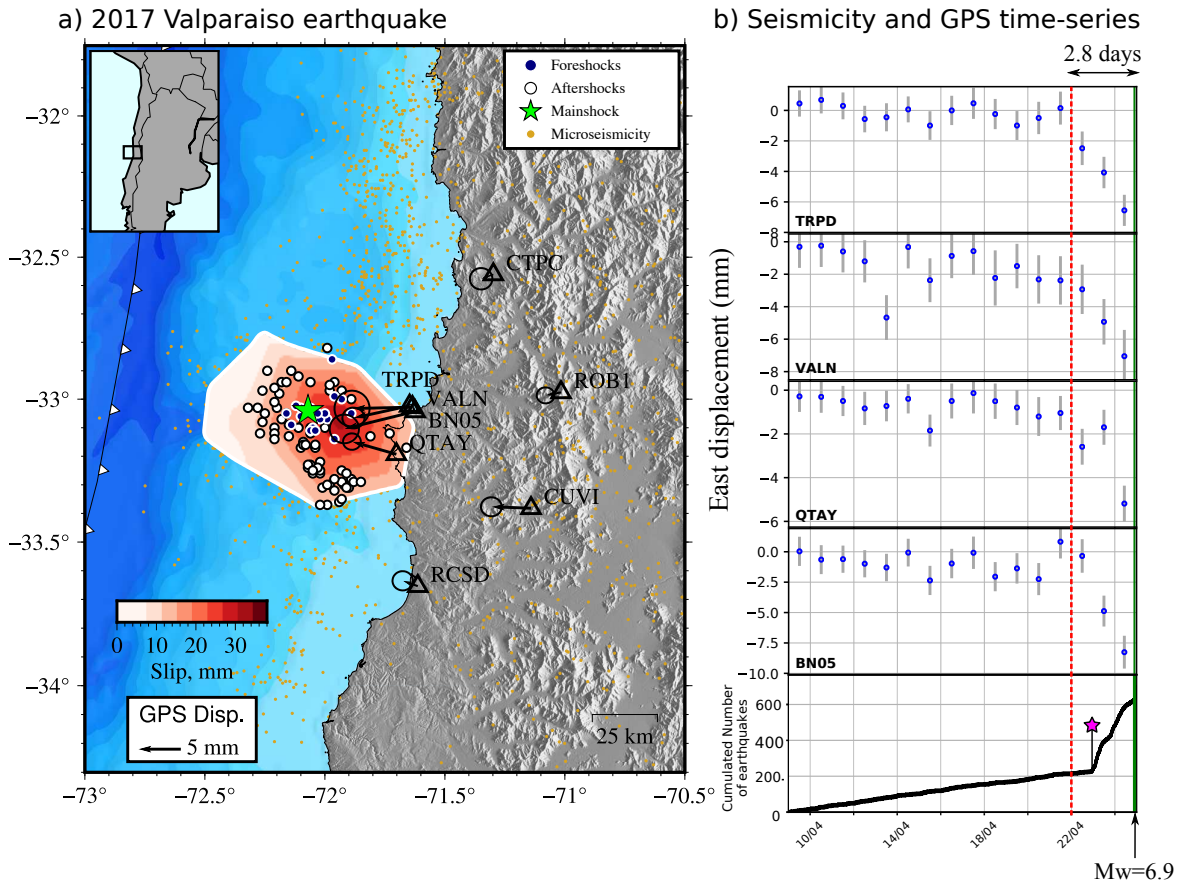


Figure 2.12: The 2017 Valparaíso earthquake sequence. (a) Earthquake locations including foreshocks (blue circles), mainshock (green star), and aftershocks (white circles). The red colormap indicates the preslip distribution resulting from the inversion of GPS data (see section 2.8.6). The black arrows show the cumulative observed GPS surface displacements (up to one hour before the mainshock). Orange dots indicate the seismicity distribution from 2017/01/01 until 2017/10/05 according to the microseismicity catalog obtained by S. Ruiz et al. (2017). (b) GPS Time-series in the vicinity of Valparaíso. The vertical red dashed line indicates approximate onset of the transient displacement visible on the timeseries. The cumulative number of earthquakes from S. Ruiz et al. (2017) is shown at the bottom of the figure. The purple star represents the largest $M_W = 6.0$ foreshock.

2.8.3 Pre-seismic Transient Displacements captured by GPS

We process GPS data of 68 stations in South America from several networks (CSN, LIA Montessus de Ballore, Ministerio de Bienes Nacionales, RAMSAC, RBMC-IP, IGS, IGM Bolivia, see supplementary information S1 for references). Processing is done using a differential approach [Herring et al., 2018] including tropospheric delays and horizontal gradients. The results are computed in the ITRF 2014 reference frame [Altamimi et al., 2016] and converted in a fixed South-America frame [Nocquet et al., 2014]. We use daily solutions except for the last position before the mainshock, which is obtained from data up to one hour before the event. We

2.8. SEISMIC AND ASEISMIC FAULT SLIP DURING THE INITIATION PHASE OF THE 2017 MW=6.9 VALPARAISO EARTHQUAKE.

remove a trend corresponding to interseismic motion from the time-series by fitting a linear regression in a 4 months time-window before the mainshock. Finally, we subtract the first sample of the time-series (i.e., which we consider as displacement zero) and obtain the corresponding offsets.

Figure 2.12-b and S3 show the resulting horizontal displacements for stations in the vicinity of the study area. There is a clear westward motion starting about 3 days before the mainshock and reaching ~ 8 mm close to the coast. Figure 2.12-b compares GPS time-series with the cumulative number of earthquakes in the micro-seismicity catalog obtained by Ruiz et al. [2017]. Interestingly, the pre-seismic GPS transient starts before a noticeable increase in seismicity. In Figure 2.12-b, we can see that the slope of cumulative seismicity rate does not change significantly at the beginning of the transient. The increase in seismicity rate is delayed by about 24 hours and only starts with a $M_W = 6.0$ foreshock on April 23 (purple star in Figure 2.12-b). This suggests that aseismic preslip initiated on the fault before the increase in foreshock activity.

2.8.4 Centroid Moment Tensor catalog

To constrain the contribution of foreshocks to the observed GPS displacement, we estimate Centroid Moment Tensor (CMT) parameters for moderate to large earthquakes during the Valparaíso earthquake sequence (from 2017/04/05 up to 2017/05/30). We use records from broadband seismic stations located within 12° from the mainshock hypocenter. These stations are mostly included in the C and C1 regional networks maintained by the Centro Sismológico Nacional (CSN) of the Universidad de Chile [Universidad de Chile, 2012]. We also use stations operated by GEOSCOPE, and IRIS/USGS network [Institut de Physique du Globe de Paris and Ecole et Observatoire des Sciences de la Terre de Strasbourg (EOST), 1982, Albuquerque Seismological Laboratory (ASL)/USGS, 1993, 1988].

We use a modified version of the W-phase algorithm adapted to regional distances and the magnitude range of the Valparaíso sequence [Kanamori and Rivera, 2008, Zhao et al., 2017]. Estimated parameters are the deviatoric moment tensor, the centroid location, the centroid time, and the half-duration of an isosceles triangular moment rate function. The inversion is performed by fitting full waveforms in a 180 s time-window starting at the P-wave. We filter data between 12 s and 100 s using different pass-bands for different magnitude events (see Table S1 in the online supplementary). We compute Green's functions for the source inversion in a 1D layered structure extracted from the 3D Earth model of Ruiz et al. [2017] in the area

2.8. SEISMIC AND ASEISMIC FAULT SLIP DURING THE INITIATION PHASE OF THE 2017 MW=6.9 VALPARAISO EARTHQUAKE.

of Valparaíso (Figure S4).

The resulting CMT catalog is shown in Figure 2.13 and in table S2. Most earthquakes (more than 90% of the total catalog) have thrust mechanisms. Interestingly, foreshocks are mostly concentrated close to the mainshock hypocenter (see Figure 2.12 and Figure 2.13-a). On the other hand, aftershocks show a different behavior, surrounding the region where foreshocks have previously occurred.

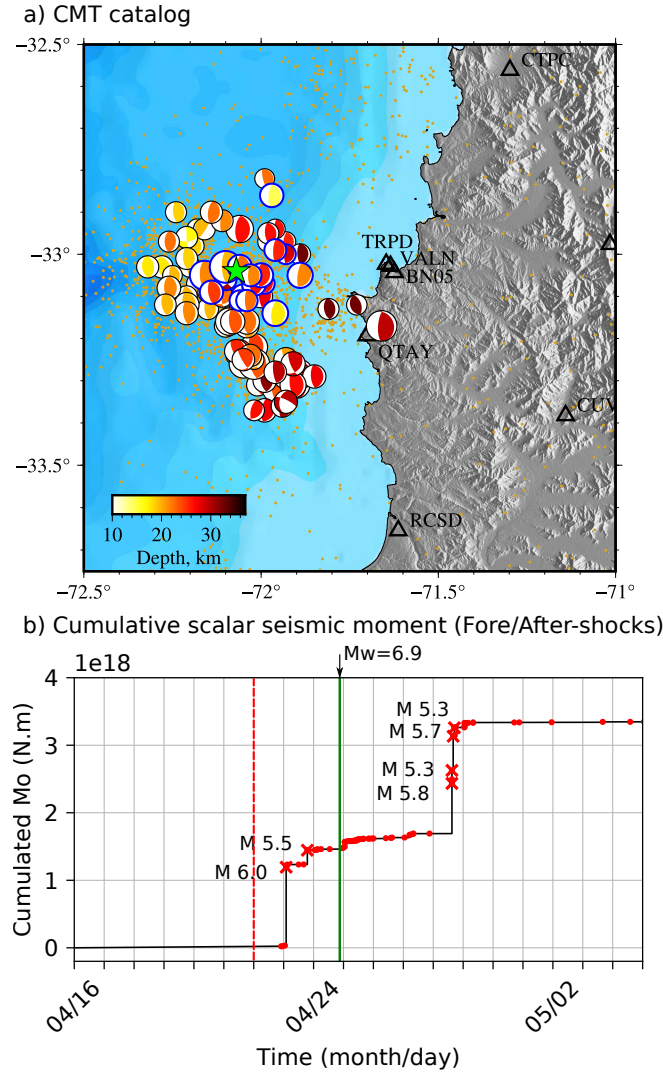


Figure 2.13: CMT solutions of the 2017 Valparaíso earthquake sequence and cumulative moment (a) CMT solutions of the 2017 Valparaíso earthquake sequence. Focal mechanisms are contoured in blue and black for foreshocks and aftershocks respectively. The size of beach balls scales with the moment magnitude. Color of the compressive quadrants represents the event depth. (b) Cumulative scalar seismic moment of the 2017 Valparaíso sequence. The mainshock scalar moment is not included in this figure. The red dashed line outlines the approximate onset of transient displacements visible on GPS time-series. The green line indicates the origin time.

The cumulative scalar seismic moment released by foreshocks before the main-

2.8. SEISMIC AND ASEISMIC FAULT SLIP DURING THE INITIATION PHASE OF THE 2017 MW=6.9 VALPARAISO EARTHQUAKE.

shock is largely dominated by two events with $M_W \geq 5.5$ (cf., Figure 2.13-b). These foreshocks of magnitude $M_W = 6.0$ and $M_W = 5.5$ occurred respectively 43 hours and 26 hours before the mainshock. As our CMT catalog only consists of $M_W \geq 3.8$ earthquakes, the contribution of microseismicity is not included in our estimates of cumulative seismic moment before the mainshock. Even though the individual contribution of these small earthquakes to the observed displacement is negligible, their large number may contribute to surface displacement. To assess the contribution of small earthquakes, we consider the frequency-magnitude distribution of our CMT catalog assuming a completeness magnitude of $M_c = 3.9$ (Figure S5). We compare our catalog with previous moment tensor catalogs of the same sequence [Ruiz et al., 2017, 2018], which are qualitatively consistent with our estimates (Figure S5). We then compute the Gutenberg-Richter (GR) law using the methodology proposed by Aki [1965] for the whole sequence, and the foreshocks sequence. Even though the GR laws show some discrepancies, they are in good agreement considering the uncertainties on our estimates (Figure S5). The foreshocks GR law is then extrapolated to lower magnitudes, and the cumulative moment of magnitudes below the magnitude of completeness is included to correct for the influence of small, hence not detected earthquakes. Our CMT catalog suggests a cumulative moment $M_0 = 1.474 \times 10^{18}$ N·m. The cumulative seismic moment of foreshocks with magnitudes below completeness is $M_0 = 4.966 \times 10^{15}$ N·m (i.e., $M_w = 4.4$). The contribution of microearthquakes is therefore negligible compared to seismic events.

To evaluate the contribution of foreshocks to observed surface displacements, we calculate synthetic static displacements using our CMT catalog and the same 1D velocity model employed to obtain our CMT solutions. Synthetics are computed using the CSI package (<http://www.geologie.ens.fr/~joliviet/csi>) incorporating the approach of Zhu and Rivera [2002] to compute static displacement in a layered model. Results on Figure S6 indicate that the largest foreshock ($M_W = 6.0$) largely dominates the co-seismic contribution to the observed GPS transient while $M_W < 6.0$ events in our catalog generate relatively small surface displacement. Assuming that microearthquakes are located in the vicinity of $M_W \geq 3.8$ foreshocks, they should also have a negligible contribution to the observed surface displacement (given their small cumulative scalar moment). As the $M_W = 6.0$ foreshock plays an important role in the sequence, we assess uncertainties associated with the corresponding CMT parameters.

2.8.5 Uncertainty on predicted co-seismic displacements

Synthetic co-seismic surface displacements are sensitive to uncertain earthquake source parameters. For large magnitude foreshocks, uncertainties on centroid location and moment tensor affect our estimates of the co-seismic contribution to the transient displacement observed before the mainshock. Source parameters uncertainties can either result from observational errors, or from errors in the forward model (prediction/theoretical errors). For example, there might be inaccuracies in the velocity model, which is known to induce non-negligible errors in CMT solutions [Duputel et al., 2012a, 2014, Morales-Yañez et al., 2020]. The point source assumption is another source of uncertainty in the forward model. As for the observations, temporally and spatially variable noise level at seismic stations is a major source of uncertainty.

In order to assess uncertainties associated with the CMT solution of the largest $M_W = 6.0$ foreshock, we perform a new CMT inversion within a Bayesian framework, following Duputel et al. [2012a, 2014]. Each source of uncertainty considered here is integrated in the problem as a covariance matrix. The covariance matrix C_d , associated with observational errors, is derived after a first CMT inversion. From this inversion, an average correlation function is derived from residuals between synthetic and observed waveforms at each station. This allows us to estimate the correlation between neighbor data samples, and include it into C_d . The standard deviation for each channel is fixed to 4 times the corresponding average absolute residuals. This empirical procedure provides a conservative estimate of observational uncertainty associated with each waveform.

Forward modeling uncertainties are represented by the matrix C_p , which assesses the influence of inaccuracies in the Earth model. We use the same velocity model as in section 2.8.4 assuming log-normal uncertainties on elastic parameters as shown in Figure S4. Uncertainty in each layer is estimated by assessing the spatial variability of the 3D Earth model of Ruiz et al. [2017] in the epicentral region and by comparison with other regional models [e.g., Ruiz et al., 2018]. To evaluate the corresponding variability in the predictions, we employ the first-order perturbation approach described in Duputel et al. [2014], assuming that prediction error is linearly related with uncertainty on the elastic parameters. A test is described in supplementary information S2 and Figures S7-S8 to assess the validity of this approach.

The posterior ensemble of plausible source locations and moment tensors is appraised using a strategy similar to Sambridge [1999]. At a fixed point-source location in time and space, the posterior distribution of moment tensor parameters is

2.8. SEISMIC AND ASEISMIC FAULT SLIP DURING THE INITIATION PHASE OF THE 2017 MW=6.9 VALPARAISO EARTHQUAKE.

Gaussian and can be written as [Tarantola and Valette, 1982]:

$$p(\mathbf{m}|\mathbf{d}_{obs}, \mathbf{x}) = N(\tilde{\mathbf{m}}, \tilde{\mathbf{C}}_m) \quad (2.2)$$

where \mathbf{m} are the moment tensor parameters, \mathbf{d}_{obs} is the data vector containing the concatenated observed waveforms and \mathbf{x} is the point source location. The right-hand member of this equation is a Gaussian distribution of mean $\tilde{\mathbf{m}}$ and covariance $\tilde{\mathbf{C}}_m$. The posterior mean $\tilde{\mathbf{m}}$ is the maximum *a posteriori* moment tensor given by:

$$\tilde{\mathbf{m}} = (\mathbf{G}^t \mathbf{C}_\chi^{-1} \mathbf{G})^{-1} \mathbf{G}^t \mathbf{C}_\chi^{-1} \mathbf{d}_{obs}, \quad (2.3)$$

where \mathbf{G} is the Green's function matrix while $\mathbf{C}_\chi = \mathbf{C}_d + \mathbf{C}_p$ is the covariance matrix reflecting observational (\mathbf{C}_d) and prediction uncertainties (\mathbf{C}_p). The posterior covariance matrix is given by:

$$\tilde{\mathbf{C}}_m = (\mathbf{G}^t \mathbf{C}_\chi^{-1} \mathbf{G})^{-1} \quad (2.4)$$

To get the joint posterior distribution on moment tensor \mathbf{m} and source location \mathbf{x} , we first calculate $\tilde{\mathbf{m}}$ and $\tilde{\mathbf{C}}_m$ on a 3D grid of possible point-source locations around the hypocenter. Starting from the initial location \mathbf{x}_c determined in section 2.8.4 (corresponding a moment tensor \mathbf{m}_c), we then employ an hybrid metropolis algorithm by repeating the following iterations until a sufficiently large number of model samples is generated:

1. Randomly generate a candidate point-source location $\mathbf{x}^* = \mathbf{x}_c + \delta\mathbf{x}$ where $\delta\mathbf{x}$ is a small perturbation randomly generated from a Gaussian distribution with a standard deviation of 0.1° in latitude/longitude and $\sigma=0.1$ km in depth.
2. Extract $\tilde{\mathbf{m}}$ and $\tilde{\mathbf{C}}_m$ from the grid point closest to \mathbf{x}^* and generate a random model \mathbf{m}^* from $p(\mathbf{m}|\mathbf{d}_{obs}, \mathbf{x}^*)$ in eq. (2.2).
3. Accept or reject \mathbf{m}^* and \mathbf{x}^* using a standard Metropolis approach:
 - Draw a random number $\alpha \sim U(0, 1)$
 - Accept \mathbf{m}^* and \mathbf{x}^* if $\alpha < \min\left(1, \frac{p(\mathbf{m}|\mathbf{d}_{obs}, \mathbf{x}^*)}{p(\mathbf{m}_c|\mathbf{d}_{obs}, \mathbf{x}_c)}\right)$.
 - Otherwise duplicate \mathbf{m}_c and \mathbf{x}_c

Figure 2.14 shows 4500 model samples generated using the approach described above. The posterior distribution shows a location uncertainty of about 10 km. We observe a good fit between observed and synthetic seismograms (Figure S9). However, we also notice a trade-off between longitude and depth, which probably results

2.8. SEISMIC AND ASEISMIC FAULT SLIP DURING THE INITIATION PHASE OF THE 2017 MW=6.9 VALPARAISO EARTHQUAKE.

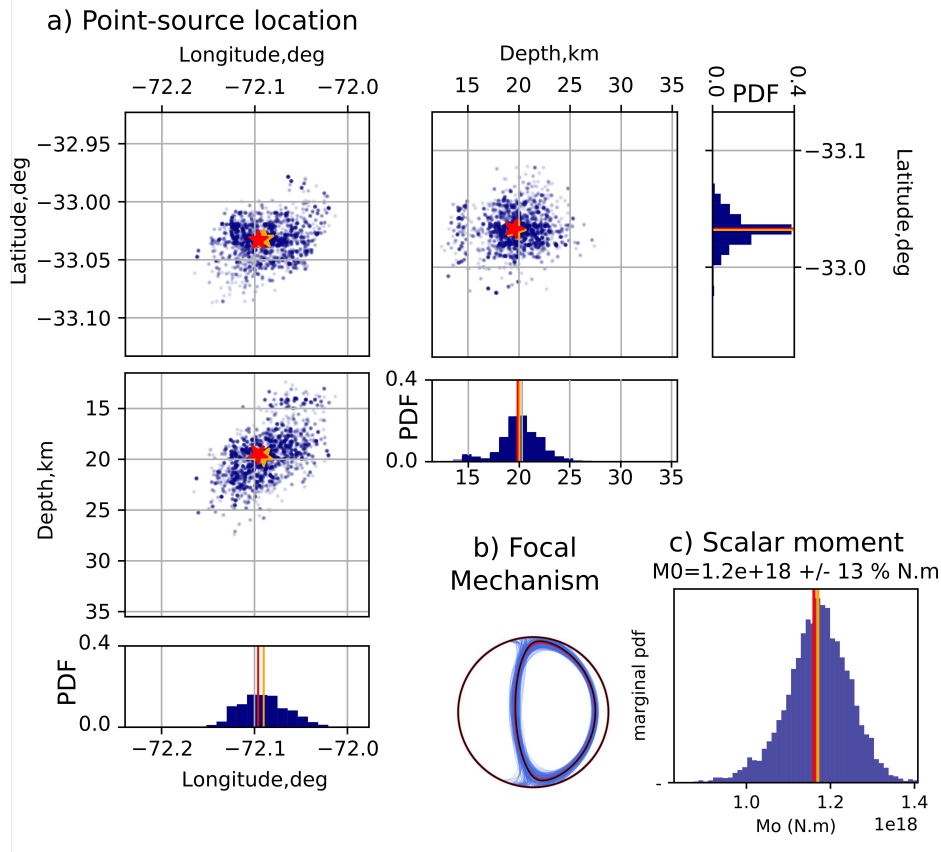


Figure 2.14: Bayesian point-source model for the $M_W=6.0$ foreshock on 2017-04-23. Blue circles and lines in the figure represent model samples randomly drawn from the posterior distribution. a) Samples from the posterior PDF depicting uncertainties in the point source location. The red and orange stars are the initial solution (i.e. starting model) and the posterior mean model respectively. b) Focal mechanism uncertainty. c) Marginal posterior PDF of the scalar seismic moment. The red and orange lines are the initial and the posterior mean model.

from the distribution of stations used for inversion (Figure S10). To evaluate the uncertainty on the predicted co-seismic displacement, we simulate static displacement for each model samples shown in Figure 2.14. The resulting stochastic co-seismic displacements are shown in Gray in Figure 2.15a for GPS stations that are closest to the mainshock epicenter. This shows prediction uncertainties ranging from 0.25 to 0.4 mm on the east component of displacement. Despite these uncertainties, the predicted cumulative co-seismic offsets are still significantly smaller than the observed pre-seismic displacements (~ 6 to 8 mm of the east component for the closest stations).

2.8.6 Partitioning between seismic and aseismic fault slip

In Figure 2.15, we compare the total cumulative foreshock co-seismic offset with the observed pre-seismic GPS displacement. Predicted co-seismic displacements include the contribution of microearthquakes below the magnitude of completeness, assuming a total scalar moment derived from our GR analysis with a location and mechanism similar to the $M_W = 6.0$ foreshock. As discussed earlier, only the largest foreshock $M_W = 6.0$ is significantly contributing to co-seismic displacements (see Figure 2.15a and S6). The contribution of earthquakes smaller than $M_W = 6.0$ has a minimal impact on the final result.

To get a total budget of seismic and aseismic displacement before the mainshock, Figure 2.15b compares GPS data 1 hour before the mainshock with the corresponding cumulative foreshock displacement. Observed displacement are on average between 4 and 6 mm larger than co-seismic offsets. Such differences cannot be explained by uncertainties on the observations and the predictions. These results clearly suggest that a significant portion of the observed pre-seismic deformation is actually aseismic and cannot be caused by foreshocks. We estimate that about $51 \pm 11\%$ of the displacement measured at the GPS stations originates from aseismic slip on the megathrust. As shown in Figure 2.15c, the portion of aseismic deformation is quite consistent between stations suggesting that a common source located in the vicinity of the foreshocks could explain those results.

To further explore this hypothesis, we then conduct two inversions: a first slip inversion of the total GPS pre-seismic displacement and another inversion after removing the contribution of foreshocks (i.e., aseismic displacement only). To build a fault geometry, we use the CSI package to mesh the *Slab 2.0* model with triangles of variable sizes as shown in Figure 2.15e-f. We invert for slip values at the triangular nodes using AlTar, a Markov chain Monte Carlo sampler based on the algorithm described by Minson et al. [2013]. Continuous fault slip distribution is represented as a linear interpolation of the slip values at the triangular nodes. Green's functions are computed in the same stratified elastic model used for our CMT catalog (Figure S4). Given the limited amount of available observations, we enforce a positive Laplacian prior distribution with a scale parameter of 1 m. Such sparsity-inducing prior will favor "simple" models with slip only where it is requested by the data. Results in Figure 2.15e-f shows that GPS observations can be explained by slip in the vicinity of the mainshock hypocenter. Aseismic slip distribution appears to be somewhat more spread out, which may be an effect of the larger uncertainty associated with GPS data after removing the contribution of foreshocks (as the co-seismic prediction uncertainty propagates in the corrected GPS data).

2.8.7 Discussion and conclusion

We investigate the seismic and aseismic motions during the preparation phase of the 2017 $M_w = 6.9$ Valparaíso earthquake. We first evaluate the contribution of foreshock-induced displacement to pre-seismic GPS observations. Co-seismic offsets are largely dominated by a $M_W = 6.0$ foreshock that occurred ~ 43 hours before the mainshock. As pointed out in section 2.8.3, the transient GPS signal starts before the increase in seismicity rate. More specifically, we can see in Figure 2.15a that the observed displacement on April 22 mainly corresponds to aseismic slip as no significant foreshock occurs on that day. On the other hand, the position on April 23 results from a combination of seismic and aseismic fault slip. The detailed evolution of the partitioning between seismic and aseismic slip is difficult to interpret using daily GPS time-series in which each position corresponds to an average over 24 hours. This analysis is also subject to large observational and prediction uncertainties. For these reasons, we focus on the overall partitioning between seismic and aseismic slip during the preparation phase of the Valparaíso earthquake.

Our analysis shows that a significant part of pre-seismic GPS observations are not explained by foreshock-induced displacement even when accounting for prediction and observation uncertainties. We estimate that $\sim 50 \pm 11\%$ of GPS displacements is likely caused by aseismic slip, a ratio that is fairly consistent for different stations in the vicinity of the Valparaíso sequence (Figure 2.15c). To check whether such pre-seismic motion could be explained by slip on the plate interface, we conduct a slip inversion after correcting GPS data from foreshock-induced displacement (cf., Figure 2.15f). The distribution of aseismic preslip spreads toward the west of Valparaíso city with an extension of about 50×90 km and a scalar moment of $M_0 = 3.08 \times 10^{18}$ N.m (i.e., $M_w = 6.26$). This aseismic motion represents about 50% of the moment calculated for the slip model derived from uncorrected GPS data ($M_0 = 5.67 \times 10^{18}$ N.m, Figure 2.15e). Given the cumulative moment of foreshocks ($M_0 = 1.48 \times 10^{18}$ N.m), we estimate that nearly 70% of the scalar moment released during the preparation phase of the Valparaíso mainshock is aseismic, which is roughly in agreement with estimates from Ruiz et al. [2017]. The smaller portion of aseismic moment derived from the comparison of slip models in Figure 2.15e-f likely results from the simplistic assumption in Figure 2.15e that all foreshocks are located on the plate interface.

Even if our analysis demonstrates the existence of aseismic slip prior to the Valparaíso mainshock, such aseismic motion may include afterslip from preceding bursts of seismicity. This has been suggested for pre-seismic displacement observed before the 2014 $M_W = 8.1$ Iquique earthquake, which could potentially be

2.8. SEISMIC AND ASEISMIC FAULT SLIP DURING THE INITIATION PHASE OF THE 2017 MW=6.9 VALPARAISO EARTHQUAKE.

explained by afterslip induced by foreshock seismicity [Bedford et al., 2015]. Testing such possibility for the 2017 Valparaíso sequence is difficult as we cannot easily isolate the afterslip signal from GPS time-series, which likely incorporate other contributions including preslip of the impending mainshock. To assess the contribution of afterslip, we employ two approaches. In a first approach, we use the mainshock post-seismic GPS signals as a proxy for the afterslip induced by foreshocks. The mainshock post-seismic time-series are normalized by the co-seismic offset of each station to evaluate the relative proportion of post-seismic displacement as a function of time. This suggests that about 10% of the co-seismic moment after 43 hours corresponds to post-seismic deformations (see Figure 2.15d and Figure S11). This result is consistent with values reported for earthquakes with similar or larger magnitudes [Chlieh et al., 2007, D'agostino et al., 2012, Lin et al., 2013]. If we assume a similar behavior for the foreshocks, the post-seismic signal caused by foreshocks is below measurement uncertainties (approximately 0.7 mm for an uncertainty of 1.1 mm in GPS signals) and can therefore be neglected. In a second approach, we make the more conservative assumption that afterslip caused by foreshocks is totally released before the mainshock. Following the empirical scaling relationship $M_{0(postseismic)}/M_{0(coseismic)} = 0.36 + / - 0.2$ proposed by Alwahedi and Hawthorne [2019], the aseismic displacement not related to foreshocks is reduced to about $37\% + / - 13\%$ of the total pre-seismic GPS observations (Figure S12). The total observed displacement is therefore unlikely to be explained by the contribution of foreshocks even when adding the associated afterslip. Such evaluation should be taken with caution due to the non-linear nature of the relationship between slip rate and co-seismic stress change for afterslip [e.g., Perfettini and Avouac, 2004, Perfettini et al., 2010].

Diverse numerical and experimental studies bring up the potential importance of aseismic preslip in the triggering of foreshocks [e.g., Kaneko et al., 2016, McLaskey and Kilgore, 2013]. If such observations apply on natural faults, foreshock locations could potentially inform us about the overall spatial extent of the nucleation zone prior to an earthquake. This idea is in fairly good agreement with our results suggesting a first-order correlation between preslip distribution and the location of foreshocks (Figure 2.12 and Figure 2.15). Even if preslip appears to be an important mechanism in the triggering of foreshocks, part of the foreshock activity likely results from cascading phenomena due to stress changes of neighboring events. In addition, we still need to understand why most earthquakes are not preceded by foreshock activity and even less with observable pre-seismic motion. This lack of systematic precursory activity might partly be due to an observational gap due to the incompleteness of current seismicity catalog [as suggested by Mignan, 2014] or

the lack of near fault geodetic observations prior to large earthquakes. The analysis of an highly complete earthquake catalog in Southern California showed that 72% of $M_W \geq 4$ earthquakes in the region are preceded by an elevated seismic activity compared with the background seismicity rate [Trugman and Ross, 2019], suggesting that foreshock activity is more ubiquitous than previously thought. However, a recent reanalysis of the same catalog suggested that a much smaller portion of these foreshock sequences were really anomalous and could not be attributed to temporal fluctuations in background seismicity rate [van den Ende and Ampuero, 2020]. Although anomalous foreshock sequences currently appears to be the exceptional, the improvement of near-fault geodetic and seismological observational capabilities are essential to bridge the gap between natural fault observations and laboratory experiments, where foreshocks are commonly observed.

2.8.8 Acknowledgments

We thank J. Ruiz, S. Ruiz, L. Rivera and J. C. Baez for helpful discussion. This project has received funding from the European Research Council (ERC, under the European Union’s Horizon 2020 research and innovation programme under grant agreement No. 805256 and grant agreement No 758210) and from Agence Nationale de la Recherche (project ANR-17-ERC3-0010). This research was also supported by the Mexican National Council for Science and Technology (CONACYT), scholarship 2018-000003-01EXTF-00012. RJ acknowledges funding from the Institut Universitaire de France. The seismological data used in this study were acquired by CSN, GEOSCOPE and IRIS/USGS are freely accessible through the IRIS DMC (<https://service.iris.edu/>). The authors thank to Instituto Geográfico Militar of Bolivia (<http://www.igmbolivia.gob.bo>), The International GNSS (<http://www.igs.org>), Instituto Brasileiro de Geografia e Estatística (<http://www.ibge.gov.br>), Instituto Geográfico Nacional de Argentina (<http://www.ign.gob.ar>), Laboratoire International Associé “Montessus de Ballore” (<http://www.lia-mb.net>), Ministerio de Bienes Nacionales de Chile (www.bienesnacionales.cl) and the Centro Sismológico Nacional de Chile (<http://www.csn.uchile.cl>) for making the raw GNSS data available. GNSS data are available via the URLs listed above. We thank an anonymous reviewer, Piero Poli, and Editor Germán Prieto for their valuable comments which improved this manuscript.

2.8. SEISMIC AND ASEISMIC FAULT SLIP DURING THE INITIATION PHASE OF THE 2017 MW=6.9 VALPARAISO EARTHQUAKE.

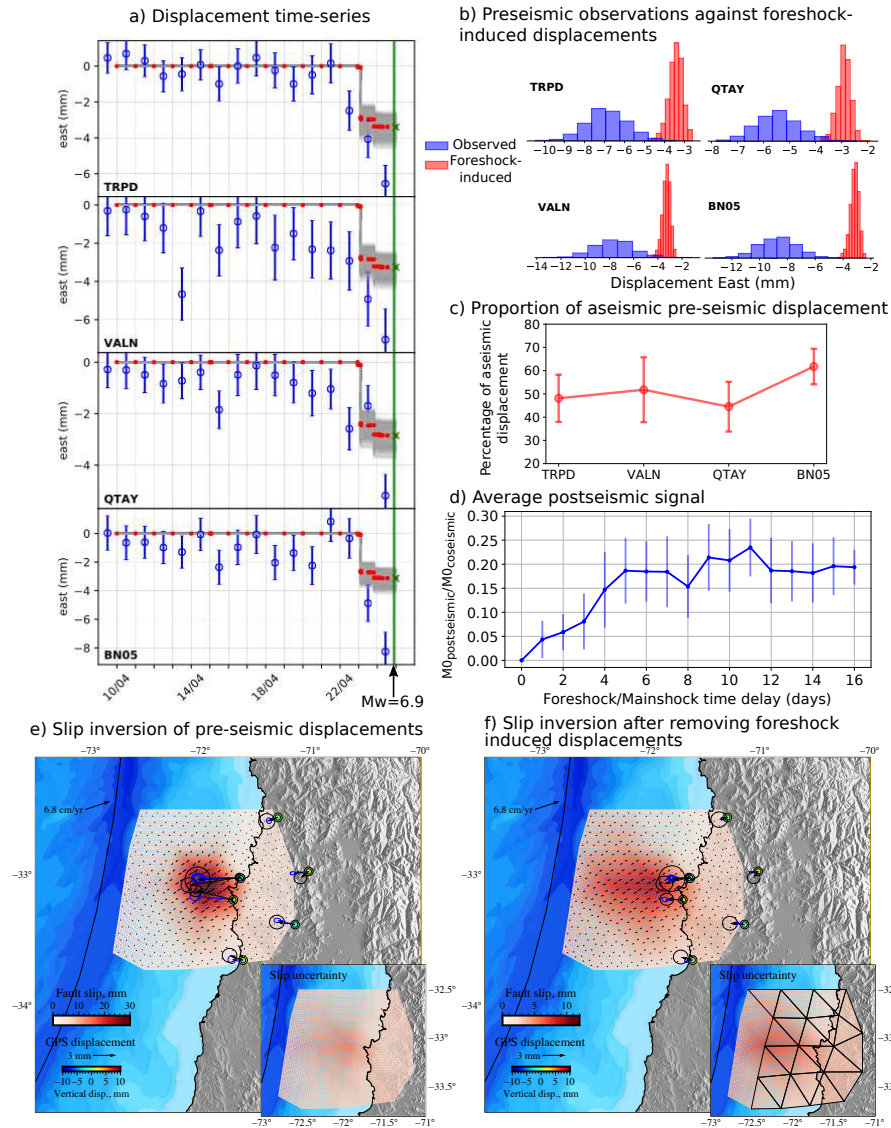


Figure 2.15: Slip during the Valparaíso foreshock sequence. a) Time series of GNSS data (blue) and stochastic foreshock-induced co-seismic displacement (gray). Red dots represent the average of stochastic co-seismic offsets. Green cross corresponds to the total foreshock displacement, including the contribution of earthquakes below the magnitude of completeness. b) Distributions of observed pre-seismic displacement and predicted cumulative co-seismic offsets caused by foreshocks. Blue histograms represent observations assuming Gaussian uncertainties from standard errors estimated at each station. Red histograms correspond to the posterior distribution of cumulative foreshock-induced co-seismic displacement. c) Percentage of aseismic displacement for each station. d) Average postseismic signal measured on stations TRPD, VALN, BN05 and QTAY (see Figure S11). e) Slip inversion of pre-seismic GPS data. f) Slip inversion of GPS data after removing foreshock-induced displacement. Black and blue arrows are observed and predicted horizontal GPS displacements along with their 1- σ ellipses (representing observational and prediction uncertainties, respectively). Colored circles are observed (outer circles) and predicted (inner circles) vertical displacements from GPS and tide gauges, respectively.

Revisiting the 2015 $M_w=8.3$ Illapel earthquake. From kinematic rupture inversion to rupture dynamics.

In this chapter we perform a Bayesian slip inversion approach described in chapter one to investigate the rupture process of the 2015 $M_W = 8.3$ Illapel earthquake. We introduce and compare a new methodology to account for prediction/epistemic uncertainty. By incorporating different datasets, we were able to characterize the complex rupture of this event.

The following study was done in collaboration with Zacharie Duputel, Cedric Twardzik, Junle Jiang, Hideo Aochi, Cunren Liang, Lijun Zhu, Romain Jolivet, Eric Fielding, Mark Simons and Luis Rivera. At of July 2022, it is in preparation to be submitted to Geophysical Journal International. In this study, I processed the seismic data, performed the joint inversion, analyzed the results, and wrote the manuscript. ZD conceived and led the study. CT obtained the corrections for the GPS data. HA wrote the code to obtain the stress evolution. JJ processed the tsunami data and Green's functions. RJ and ZD developed the CSI code used to gather data and Green's functions for a given fault geometry. EF and CL processed the InSAR data. LZ, ZD, RJ, JJ and MS developed the code AITar that we use to perform the joint inversion.

3.1 Abstract

The 2015 $M_W = 8.3$ Illapel earthquake is the largest mega-thrust earthquake that has been recorded along the Chilean subduction zone since the 2010 $M_W = 8.8$ Maule earthquake. Previous studies indicate a rupture propagation from the hypocenter to shallower parts of the fault, with a maximum slip varying from 10 to 16 meters. The amount of shallow slip differs dramatically between rupture models with some results showing almost no slip at the trench and other models with significant slip at shallow depth. In this work, we revisit this event by combining a comprehensive data set including continuous and survey GPS corrected for post-seismic and after-shock signals, ascending and descending InSAR images of the Sentinel-1A satellite, tsunami data along with high-rate GPS, and doubly integrated strong-motion waveforms. We follow a Bayesian approach, in which we obtain an ensemble of models. The kinematic inversion is done using the cascading capability of the AITar algorithm, allowing us to first get a static solution before integrating seismic data in a joint model. We propose a new technique to calculate the forward problem uncertainties matrix C_p using the second-order approach. We compare this new approach with other current computations techniques. Results suggest that we can retrieve the main features of complex ruptures such as the Illapel event with the new 2nd order approach. Kinematic models show a rupture with two main slip patches, with an important shallow slip contribution. Rupture times suggest that an encircling effect occurs when rupture propagates between the two main slip patches, westward of the hypocenter. Encircling effects have been previously suggested by previous back-projection results. To gain insight into rupture dynamics, we use kinematic models to compute the stress evolution on the fault as a function of time. We compute the breakdown work density from the stress evolution and compare the resulting probability density estimates with similar calculations done for other earthquakes.

3.2 Introduction

Chile is one of the seismically most active regions on Earth, where the Nazca plate subducts under the South American plate with a convergence rate of approximately 67 mm/yr [Angermann et al., 1999, Vigny et al., 2009]. This large plate convergence rate is accompanied with the occurrence of large mega-thrust earthquakes, such as the 1943 $M_W = 7.9 - 8.3$ Illapel event, the 1960 $M_W = 9.5$ Valdivia earthquake, the 2010 $M_W = 8.8$ Maule earthquake, and the 2014 $M_W = 8.1$ Iquique earthquake

3.2. INTRODUCTION

[Lomnitz, 2004, Ruiz and Madariaga, 2018]. One of the recent large mega-thrust earthquakes in Chile is the 2015 $M_W = 8.3$ Illapel earthquake. It occurred off the west coast of the Coquimbo region on September 16th, 2015, at 22:54:31 UTC, with a reported magnitude of $M_W = 8.3$ (Centro Sismológico Nacional, CSN), triggering a tsunami that reached the west Pacific coasts [Li et al., 2016, Ruiz and Madariaga, 2018]. The same area was previously hit by an earthquake of similar magnitude in 1943 [Beck et al., 1998].

Different groups have published numerous kinematic slip rupture models for the 2015 $M_W = 8.3$ Illapel earthquake. As discussed by Satake and Heidarzadeh [2017], even though all of these models share some general features, some properties of the rupture are still under debate. For example, the amount of shallow slip differs dramatically between rupture models, with some models showing almost no slip at the trench contrarily to other results. Several models suggest a relatively simple rupture with one single main slip patch, mainly located at the north-west of the hypocenter with various amount of shallow slip [An and Meng, 2017, Heidarzadeh et al., 2016, Li et al., 2016, Ruiz et al., 2016, Tilmann et al., 2016]. For example, An and Meng [2017] suggest the absence of shallow slip, while other works indicate that shallow slip is necessary to explain tsunami records [Lay et al., 2016, Li et al., 2016, Tilmann et al., 2016]. In fact, Tilmann et al. [2016] suggested that the difference between the 1943 Illapel event and the 2015 event is the shallow rupture experienced during the 2015 event.

The degree of rupture complexity also varies among previously published results. In contrast with the relatively simple rupture processes suggested by the aforementioned results, other studies suggest a more complex rupture scenario with at least two main slip asperities [Melgar et al., 2016b, Lee et al., 2016]. While the relatively compact model of Melgar et al. [2016b] is consistent with tsunami observations, Lay et al. [2016] show that the model of Lee et al. [2016] involving a broad area of shallow slip rupturing multiple times cannot reproduce tsunami data. Several back-projections studies confirm the complexity of the 2015 Illapel rupture [Melgar et al., 2016b, Okuwaki et al., 2016, Yin et al., 2016]. A common result among back-projection studies is that the Illapel earthquake presents a northwestward migration. For example, An et al. [2017] shows a complex frequency dependent rupture propagation with several branches. The back-projected low-frequency (LF) sources migrate mainly to the west, while the high-frequency (HF) sources start going north-eastward after turning towards the northwest. On the other hand, Meng et al. [2018] results show a rupture that splits into two different branches separated along dip. The analysis of these multiple rupture branches suggests an encircling rupture that seems to be aligned with regions experiencing a high slip rate and large shallow

slip. Unfortunately, such a complex pattern hasn't been confirmed with previous kinematic slip inversion models. This could be due to the fact that such encircling rupture effects is only visible when analyzing the high-frequency wavefield. In addition, such encircling pattern likely involve abrupt changes in rupture velocities, while most slip inversions consider fixed rupture velocities.

In this work, we revisit the 2015 $M_W = 8.3$ Illapel earthquake by combining a comprehensive data set including permanent and survey GPS stations corrected for post-seismic and aftershock signals, ascending and descending Sentinel 1A InSAR images along with high-rate GPS and doubly integrated strong-motion waveforms. We follow a Bayesian approach using the AITar code, which allows us to obtain the posterior probability distribution of slip models rather than a single optimum solution. Moreover, we do not impose any smoothing or empirical regularizations, which could potentially smooth out rupture complexities. We also employ a non-linear parameterization enabling significant variation of rupture velocity during the rupture process. We also analyze the impact that prediction error covariance matrices have on coseismic slip inversions results. To further investigate the dynamics of the 2015 Illapel rupture process, we also employ our posterior probability distributions to measure the fracture energy and the associated uncertainty. The resulting estimates are compared to the $M_W = 8.2$ Iquique earthquake and with existing scaling relationships

3.3 Data

We investigate the complex rupture of the 2015 $M_W = 8.3$ Illapel earthquake using multiple datasets that are shown in Figure 3.1. This database includes GPS offsets, Interferometric Synthetic Aperture Radar (InSAR) images, tsunami data along with high-rate GPS and strong motion waveforms.

InSAR images are obtained from the Sentinel 1A satellite with ascending and descending orbits (see supplementary information). We use 14 tsunami stations: 6 DART buoys and 6 coast gauges focusing mainly on first arrivals and open sea sites to minimize coastal effects (see supplementary information). We use daily and survey GPS data provided by Klein et al. [2017]. Both datasets are affected by co-seismic offsets induced by $M_W = 7.1$ and $M_W = 6.8$ aftershocks occurring respectively 23 min and 5 hours after the mainshock. Survey GPS data also includes several weeks of post-seismic displacement. Details of GPS data processing can be found in Klein et al. [2017]. To correct both daily and campaign GPS data from aftershocks and post-seismic deformation, we use high-rate post-seismic

3.3. DATA

time-series from Twardzik et al. [2021]. These measurements are interpolated using cubic splines and removed from co-seismic GPS offsets. We estimate uncertainty of the corrected data by conducting the aforementioned correction stochastically (using Gaussian realizations given uncertainties on daily, survey and post-seismic GPS datasets). We scale the resulting standard deviations to ensure a unit reduced χ^2 . This results in a scaling factor of 10 for the East component and a scaling factor of 5 for the West and Up components. While this approach is empirical, it allows us to avoid any overfitting of the GPS observations while keeping a relative weighting between stations based on the variability of the corrected observations.

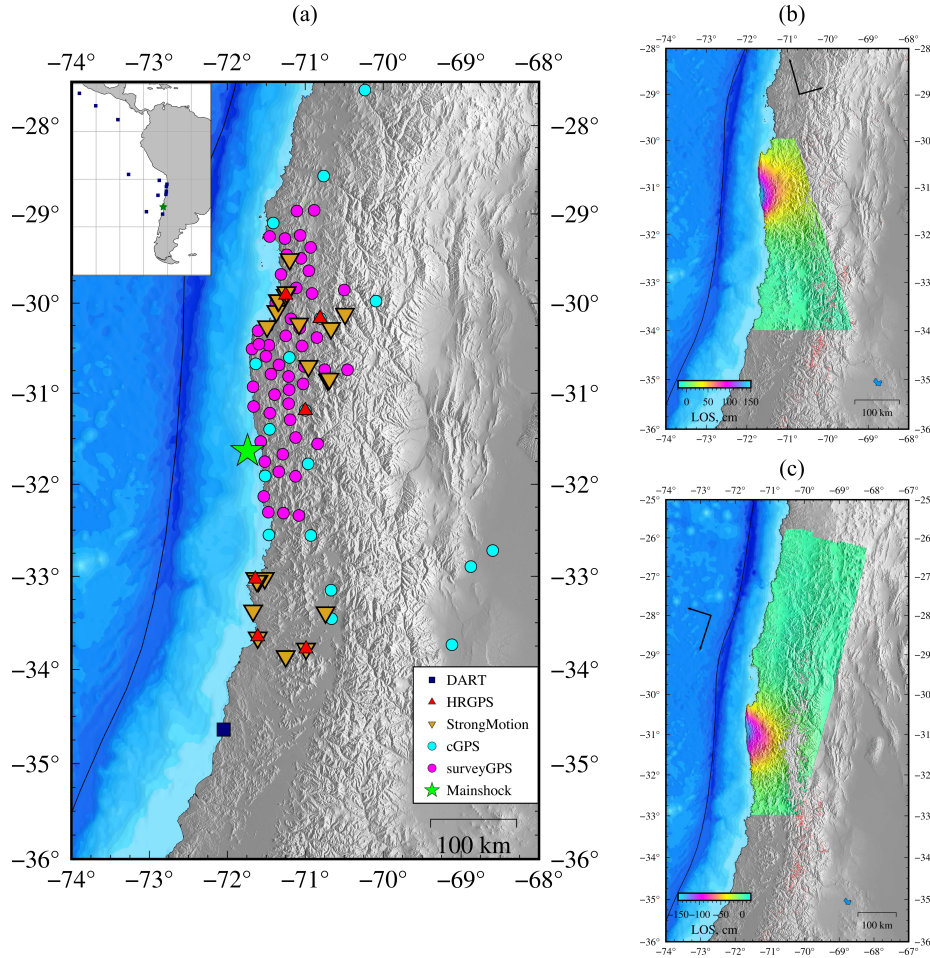


Figure 3.1: General overview of the studied region with data sets used in this study (a). Green star represents the hypocenter obtained by the Chilean Seismological Center (CSN). Ascending (b) and descending (c) Sentinel 1-A InSAR images.

For the kinematic data set, we use records from High Rate GPS (HRGPS) stations and strong motion data located within 5 degrees from the mainshock hypocenter. These stations are part of the Chilean Seismological Service (CSN) of the Universidad de Chile [Universidad de Chile, 2012]. In total, we have 96 strong motion waveforms that we double integrate into displacement time series. The integration of ac-

3.3. DATA

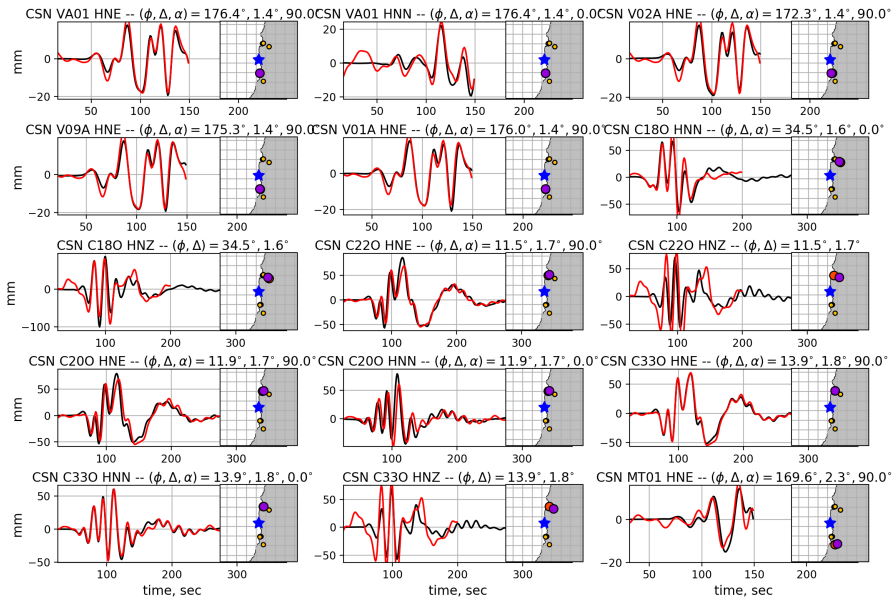


Figure 3.2: Comparison between displacements corrected from ground motion records and HRGPS displacements. Red and black waveforms represent HRGPS and strong motion respectively. On the maps, the blue star represents the CSN hypocenter while circles indicate station location (orange for the strong motion station depicted, yellow for the ensemble of strong motion stations, and purple for HRGPS stations). Variation in waveforms is mostly due to differences in colocation.

celeration data is a delicate operation as it often results in large drifts in velocity and displacement waveforms. To obtain displacement records, after removing any linear trend in accelerograms, we therefore remove an additional velocity drift at the end of the waveforms. This additional coda correction is done by using a quadratic function to fit to displacement waveforms from the time when 90% of the acceleration energy is reached. Visual inspection of the corrected displacement records is then done to ensure the good quality of the data. To further check the corrected records, we compare the obtained strong motion displacements with HRGPS displacements (Figure 3.2 and Figure S1). In total, we were able to recover 43 displacement components from strong motion with high-quality displacement waveforms.

To calculate synthetic static displacements, we use the Classic Slip Inversion (CSI) package (<https://github.com/jolivetr/csi>), following the approach of Zhu and Rivera [2002] for an Earth layered model. We calculate Green's Functions using the one-dimensional velocity model built by Duputel et al. [2015] (see Figure 3.3). For the kinematic Green's Functions, we use the wavenumber integration module for a layered model of the CPS seismology package (<http://www.eas.slu.edu/eqc/eqccps.html>) from [Herrmann, 2013]. We filter both the kinematic Green function and data between [0.01, 0.06667] Hz.

3.4 Methodology

To perform the joint inversion, we follow a Bayesian approach in which we obtain an ensemble of models and not a unique solution. The inversion is done using the cascading capability of the AlTar code (<https://altar.readthedocs.io>), allowing us to first get a static solution before integrating waveform data in a joint model. This code is based on the Cascading Adaptative Metropolis In Parallel (CATMIP) algorithm proposed by Minson et al. [2013] that we will describe below. The AlTar package has been successfully employed for different problems. Jolivet et al. [2015] and Jolivet et al. [2020] estimated the interseismic coupling of the San Andreas fault and the Northern Chile subduction interface. Studies of individual earthquakes have been carried out by Duputel et al. [2015], Bletery et al. [2016], and Gombert et al. [2018a], among others. Finally, Jiang and Simons [2016] imaged the seafloor deformation during the 2011 Tohoku Earthquake.

Starting from the Bayes theorem, we can obtain the *a posteriori* probability density function (PDF) of the parameters \mathbf{m} , given the observations \mathbf{d}_{obs} as:

$$p(\mathbf{m}|\mathbf{d}_{\text{obs}}) = \kappa p(\mathbf{m}) p(\mathbf{d}_{\text{obs}}|\mathbf{m}), \quad (3.1)$$

where $p(\mathbf{m})$ is the *a priori* probability density function of parameters, $p(\mathbf{d}_{\text{obs}}|\mathbf{m})$ is the data likelihood function and κ a normalization factor. The likelihood function can be defined as:

$$p(\mathbf{d}_{\text{obs}}|\mathbf{m}) = \exp\left(-\frac{1}{2}(\mathbf{d}_{\text{obs}} - \mathbf{g}(\mathbf{m}))^T \mathbf{C}_{\chi}^{-1}(\mathbf{d}_{\text{obs}} - \mathbf{g}(\mathbf{m}))\right). \quad (3.2)$$

\mathbf{C}_{χ} is the sum of \mathbf{C}_{d} and \mathbf{C}_{p} , which correspond to the observational and forward modeling uncertainties, respectively. In the case of the CATMIP algorithm, we sample the *a posteriori* PDF using a series of transitional intermediate PDF. The transitional PDFs are controlled by the parameter β , which acts as a tempering parameter. By incorporating the beta parameter into equation 3.1, we obtain:

$$f(\mathbf{m}|\mathbf{d}_{\text{obs}}, \beta_k) \propto p(\mathbf{m}) p(\mathbf{d}_{\text{obs}}|\mathbf{m})^{\beta_k}, \quad (3.3)$$

where $(k = 1, \dots, M)$ and β varies from zero to one, i.e., $0 = \beta_0 < \beta_1, \dots, \beta_M = 1$.

These transitional steps will converge to the solution by smoothly informing the system. Given the number of parameters, we also use the cascading capability of the AlTar code. Cascading allows to firstly solve the static problem and then use this solution as initial samples in the joint inversion. Extensive details of the algorithm can

3.4. METHODOLOGY

be found in Minson et al. [2013]. As mentioned before, the C_x matrix incorporates different uncertainty assessments. The observational uncertainty is commonly related to errors in measurements. The details of observational uncertainty estimates can be found in the supplementary information.

The forward modeling uncertainties are associated with imperfect modelling that can be caused by different factors, such as imperfect Earth models or fault geometries [Beresnev, 2003, Ide, 2015, Wald and Graves, 2001, Williams and Wallace, 2015]. Several studies have highlighted the importance of considering forward modeling uncertainties in slip inversions [Duputel et al., 2012a, 2014, Hallo and Gallovič, 2016, Ragon et al., 2018, Yagi and Fukahata, 2011]. For example, Duputel et al. [2014] study the uncertainties linked to inaccuracies in the Earth structure model. On the other side, Ragon et al. [2018] analyze uncertainties associated with inaccuracies in fault geometries. Also, Razafindrakoto and Mai [2014] assess the influence of the employed source time function and elastic structure on earthquake slip imaging.

In the present study, we focus on accounting uncertainties due to Earth structure modeling. Specifically, we evaluate the impact of inaccuracies in the 1D velocity model employed to compute static and kinematic predictions. Uncertainties in the elastic parameters Ψ is assumed to follow a log-normal distribution:

$$p(\log \Psi) = \frac{1}{\sqrt{(2\pi)^N |\mathbf{C}_\Psi|}} \exp \left(-\frac{1}{2} (\log \Psi - \log \bar{\Psi})^T \mathbf{C}_\Psi (\log \Psi - \log \bar{\Psi}) \right), \quad (3.4)$$

where \mathbf{C}_Ψ is the covariance characterizing uncertainty around $\log \bar{\Psi}$ (the logarithm of the elastic parameters used to compute the predictions shown in Figure 3.3). This choice of a log-normal distribution is motivated by the fact that (1) the elastic parameters are strictly positive and (2) Ψ values are derived from tomography techniques based on relative model perturbations ($\delta \log \Psi$; [e.g., Tromp et al., 2005]). The uncertainty on the Earth model considered in the present study is shown in Figure 3.3. The level of uncertainty is measured by comparing different models from the region [following Duputel et al., 2015].

We follow three different schemes to map Earth model uncertainty into prediction uncertainty. The first straightforward approach is to empirically calculate the prediction uncertainty covariance matrix \mathbf{C}_p using predictions computed for a large number of random Earth models Ψ_i , ($i = 1, \dots, n$) drawn from $p(\log \Psi)$:

$$\mathbf{C}_p = \frac{1}{n-1} \sum_{i=1}^n (\mathbf{g}(\Psi_i, \mathbf{m}) - \mathbf{g}(\bar{\Psi}, \mathbf{m})) (\mathbf{g}(\Psi_i, \mathbf{m}) - \mathbf{g}(\bar{\Psi}, \mathbf{m}))^T, \quad (3.5)$$

3.4. METHODOLOGY

where $g(\Psi_i, \mathbf{m})$ is the prediction for the Earth model Ψ_i and the source model \mathbf{m} . In our case, we use a preliminary source model \mathbf{m} derived from a first preliminary slip inversion. $g(\bar{\Psi}, \mathbf{m})$ is the prediction response for the average Earth model. This empirical approach is computationally expensive because it needs the calculation of predictions for each randomly generated Earth model. To evaluate the number of models \mathbf{n} necessary to calculate an accurate empirical C_p matrix, we compare empirical C_p matrices calculated for an increasing number of random Earth models. We observe that the empirical C_p matrix is converging using 195 random Earth samples (Figure S2), corresponding to relatively smooth histograms in Figure 3.3.

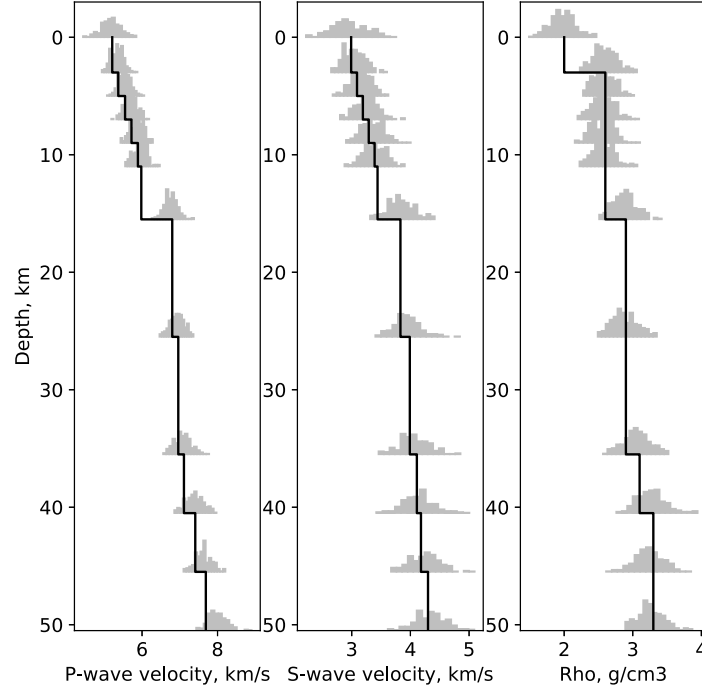


Figure 3.3: Model variability of the P-wave, S-wave, and density as a function of depth in the Illapel region. The black line represents the velocity layered model used for Green's Function (GF) calculation. Grey histograms are the probability density function for each parameter as a function of depth.

To test a computationally less expensive approach, we also follow the first-order approximation approach proposed by Duputel et al. [2014]. Assuming that we can approximate our forward model $g(\Psi, \mathbf{m})$ by linearized perturbations, for an *a priori* Earth model we have then:

$$g(\Psi, \mathbf{m}) \approx g(\tilde{\Psi}, \mathbf{m}) + \mathbf{K}_{\Psi}(\tilde{\Psi}, \mathbf{m}) \cdot (\Psi - \tilde{\Psi}), \quad (3.6)$$

where \mathbf{K} is the sensitivity kernels of the prediction with respect to elastic parameters

3.4. METHODOLOGY

used to compute forward predictions:

$$(\mathbf{K}_\Psi)_{ij}(\tilde{\Psi}, \mathbf{m}) = \frac{\partial g_i}{\partial \Psi_j}(\tilde{\Psi}, \mathbf{m}). \quad (3.7)$$

We use then \mathbf{K} to estimate \mathbf{C}_p as:

$$\mathbf{C}_p = \mathbf{K}_\Psi \cdot \mathbf{C}_\Psi \cdot \mathbf{K}_\Psi^T, \quad (3.8)$$

where \mathbf{C}_Ψ is the same log-normal covariance that we use for perturbing the random models of the empirical \mathbf{C}_p . While this approach looks appropriate for static data, it could be problematic for kinematic data as the link between Earth model perturbations and waveform predictions is probably not linear. Indeed, changes in the velocity model induce both time-shifts and amplitude variations in the predicted waveforms.

Therefore, we also explore the possibility of using a 2nd order perturbation approach previously introduced by Caballero et al. [2021] for point source inversions. In this approach, we can estimate a covariance matrix using a second order approximation of the forward model as:

$$g(\Psi, \mathbf{m}) \approx g(\tilde{\Psi}, \mathbf{m}) + \mathbf{K}_\Psi(\tilde{\Psi}, \mathbf{m}) \cdot (\Psi - \tilde{\Psi}) + \frac{1}{2} (\Psi - \tilde{\Psi}) \cdot \mathbf{H}_\Psi(\tilde{\Psi}, \mathbf{m}) \cdot (\Psi - \tilde{\Psi}), \quad (3.9)$$

where \mathbf{H}_Ψ is the second order derivative with respect to the elastic parameters:

$$(\mathbf{H}_\Psi)_{ijk}(\tilde{\Psi}, \mathbf{m}) = \frac{\partial^2 g_i}{\partial \Psi_k \partial \Psi_j}(\tilde{\Psi}, \mathbf{m}). \quad (3.10)$$

From equation 3.9, we can then calculate the matrix \mathbf{C}_p creating a large number of models and following the equation 3.5.

The derivatives in equation 3.9 are computed numerically using finite differences. We summarize the difference in computational cost between approaches in table 3.1. The computational cost of each approach in terms of forward model evaluation is summarized in Table 3.1. In this study, the empirical approach necessitated about 200 forward model evaluations, which is much less than what is necessary when using a 2nd order approach. However, the computational cost is significantly reduced when considering 1st order derivatives or 2nd order derivatives without cross-terms. In the following, we will only consider the empirical, first order and 2nd order without cross-terms approaches.

In Figure 3.4 and Figure S3, we compare the diagonal of the \mathbf{C}_p matrix for HRGPS and strong motion stations. The 1st and 2nd order matrices seem to capture the

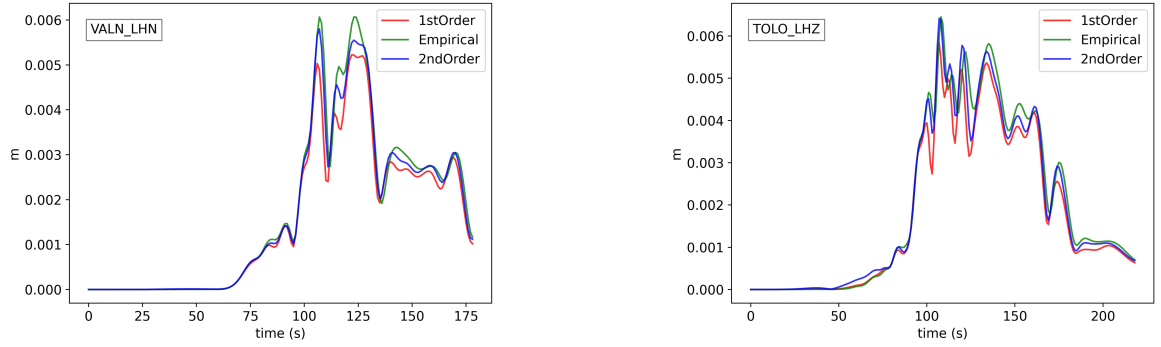
3.4. METHODOLOGY

Table 3.1: Approaches to calculate C_p (for 36 parameters)

Approach.	Number of forward model evaluations
Without C_p	0
Empirical	195 (in this study)
1st order Forward Derivatives	37
1st order Centered Derivatives	72
2nd order without cross-terms	73
2nd order	1333

main features of the empirical C_p matrix. However, there are differences that could play an important role in complex inversion problems. For this reason, in the next section, we explore the impact of the C_p matrix on the coseismic models of the 2015 $M_W = 8.3$ Illapel earthquake.

(a) HRGPS



(b) Strong motion

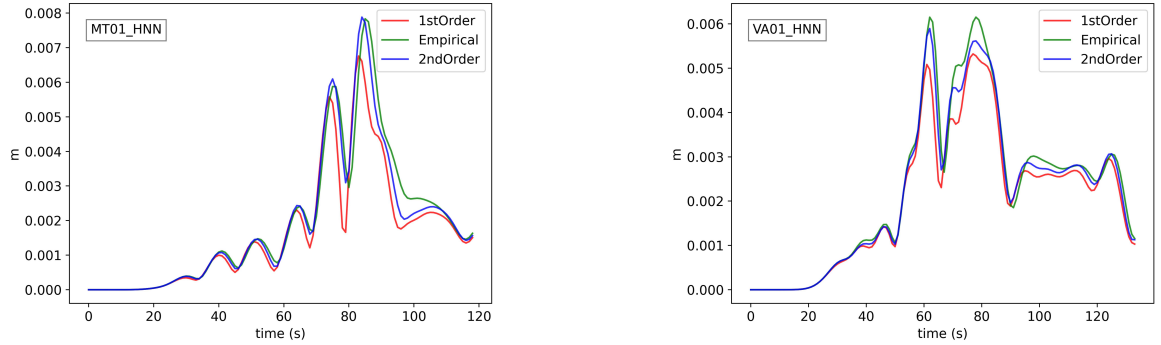


Figure 3.4: Covariance matrix comparison for HRGPS records (a) and Strong Motion stations (b). The green line represents the diagonal of the empirical covariance matrix (i.e., the matrix created from an ensemble of models). The red and blue line represents the diagonal of the matrix calculated using the 1st and 2nd order approximation approach.

To represent the 2015 $M_W = 8.3$ Illapel earthquake fault, we design a curved fault geometry matching local seismicity and focal mechanisms. The fault surface is divided into 10 down-dip and 17 along-strike patches (170 in total) with 18km side-

3.5. RESULTS

length. We invert for along-strike slip, down-dip slip, rise time, rupture velocity from each subfault, and hypocenter location (along-strike and down-dip distance). The *a priori* distributions are shown in Figure S4. We use the hypocenter of the CSN as *a priori* since it was obtained using regional data. For InSAR images, we include a nuisance parameter to correct each image from a constant offset, i.e., two nuisance parameters in total. We add translation parameters for the GPS data sets, i.e., three parameters for each set.

Since we are working with different data sets, we want to know how sensitive they are to slip on the fault. Thus, we carry out a sensitivity analysis for each data set. We follow the approach similar to Duputel et al. [2015]. The sensitivity of each data set is calculated as:

$$\mathbf{S}(D) = \text{diag}(\mathbf{G}^t(D) \cdot \mathbf{C}_\chi^{-1}(D) \cdot \mathbf{G}(D)), \quad (3.11)$$

where \mathbf{G} is the corresponding Green functions (in the down-dip direction), and \mathbf{C}_χ is the covariance matrix described above for a given data set D . For a given subfault, this measure is equivalent to computing the L_2 norm of the predictions due to one-meter dip-slip in the considered patch. The corresponding sensitivities are shown in Figure S5. We can see that tsunami data are sensitive mainly to the shallow region of the fault. In contrast, InSAR and GPs data better image the inshore fault region. The kinematic data is globally sensitive to slip over the entire fault. Finally, if we use the whole data set, we have an overall good sensitivity over the entire fault.

3.5 Results

Following the cascading approach of the AI-Tar code, we first perform an inversion of the final slip using static data (that is, InSAR, GPS and tsunami data). We thus generate a posterior ensemble of slip models for which the posterior mean and uncertainty is shown in Figure 3.5. This model presents two main slip patches that extend up-dip to the trench. The peak slip is around 23.93 ± 5.4 meters, while the mean fault slip is about 3.34 ± 0.12 meters. Even if tsunami data is employed, slip uncertainty is larger in the shallow part of the fault, due to the lack of data coverage in that area.

We then use the *a posteriori* PDF of the static slip model as seeds to make three different joint inversions: one using an empirical \mathbf{C}_p matrix and two others using a \mathbf{C}_p matrix calculated using the first and second order perturbation approach. The final slip distribution obtained using these different approaches are shown in Figure

3.5. RESULTS

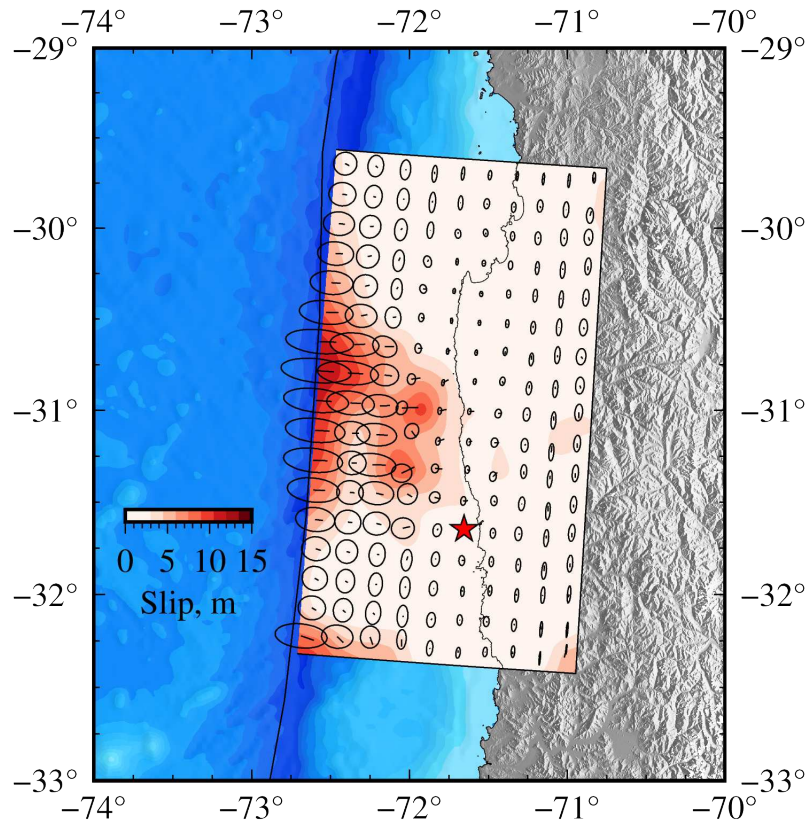


Figure 3.5: Posterior mean coseismic slip model for the static data set. Arrows represent the slip directions and the ellipses its corresponding uncertainty.

3.6. We also compare the posterior distributions of dip-slip in the online supplement (Figure S6). The posterior mean coseismic models are relatively similar, showing two, possibly three main slip patches. The three solutions exhibit two clear slip zones, one northwestward to the hypocenter and the other at shallow depths close to the trench. The deeper slip patch is well constrained for the three solutions, with a mean slip of $6 \sim 7$ meters for this region. The solution based on 1st order C_p show slip patch that is quite compact at shallow depth, while shallow slip is more broadly distributed when considering 2nd order or empirical C_p matrices. This results into a larger peak slip value for the 1st order C_p solution (21.07 ± 2.03 m), while empirical C_p (17.35 ± 1.96 m) and 2nd order C_p (18.52 ± 2.74 m) display smaller peak slips.

Figure 3.7 compares rupture times between solutions (taking the solution based on empirical C_p as reference). Both the first order and second order C_p matrices result in rupture times that are similar to the empirical covariance matrix. However, the second order approach presents an overall smaller dispersion ($\sigma = 4.75$ s) compared with the first order approach ($\sigma = 5.97$ s).

Details of the solution obtained using a 2nd order C_p is shown in Figure 3.8. Similar

3.5. RESULTS

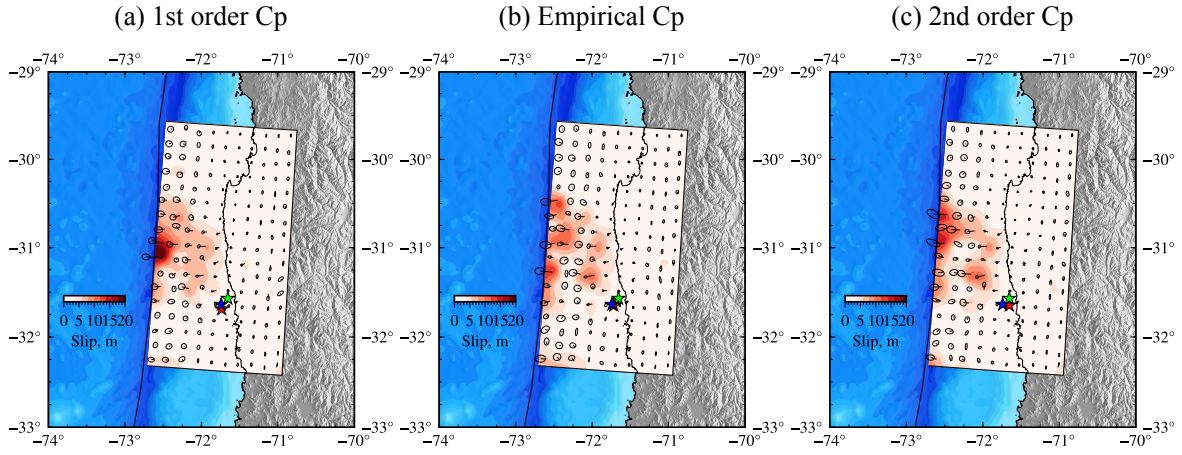


Figure 3.6: Comparison of co-seismic slip distributions obtained using different prediction error covariances C_p . Red colors are the final slip distributions. Arrows represent the slip directions with their corresponding uncertainty. The red star is the inverted hypocenter location (empirical, 1st, and 2nd order approximation, respectively). The blue star is the CSN hypocenter, and the green star is the USGS hypocenter.

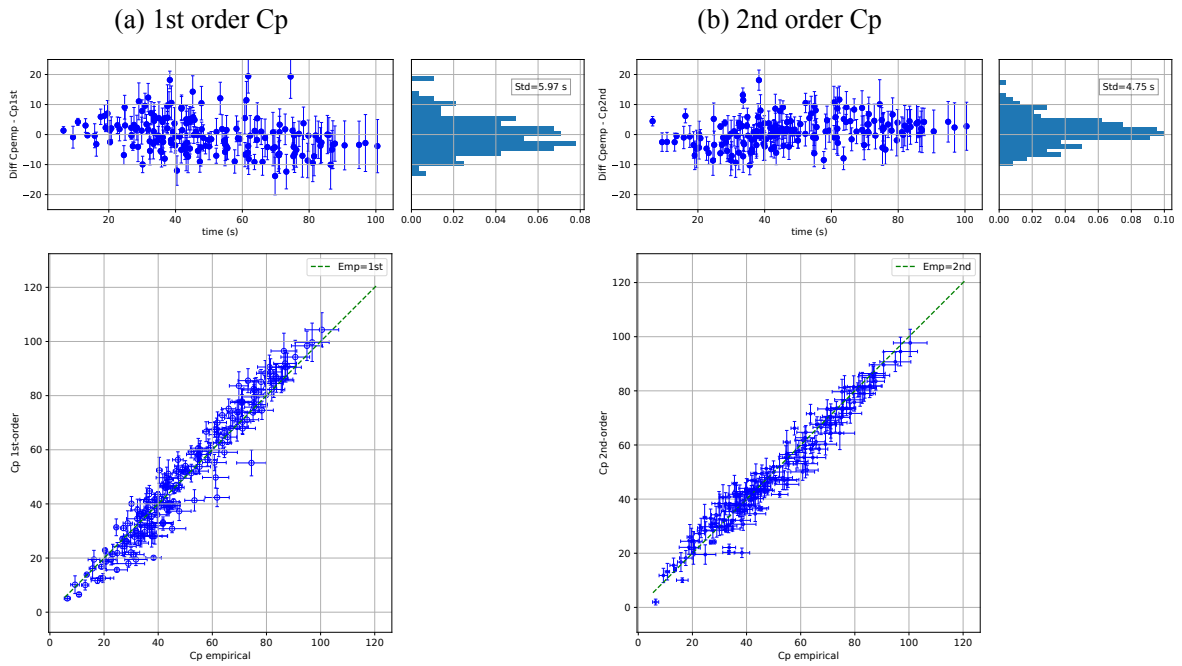


Figure 3.7: Rupture times comparison between different C_p inversion solutions. Comparison between the empirical covariance matrix and the first order (a) and 2nd order (b) approaches.

figures are presented for the 1st order and empirical C_p in supplementary Figures S7 and S8. Stochastic rupture propagation fronts in Figure 3.8 (a) suggest a complex rupture pattern. It slowly grows close to the hypocenter, and then propagates northwestward to a shallower area of the subduction interface. The patches with larger slips display a rupture speed varying from 2 to 4 km/s. Stochastic moment

3.6. DISCUSSION

rate functions in Figure 3.8 (b) indicate an overall rupture duration of 120 seconds approximately. The average scalar seismic moment is $M_0 = 3.20 \times 10^{21} \text{N} \cdot \text{m}$, i. e., a moment magnitude of $M_W = 8.27$. We can notice two energy peaks, a small one at 25 seconds, and another one at 50 seconds. As it has been reported before [Gombert et al., 2018b], we observe an anti-correlation of rise-time and initial rupture times (Figure S9). This likely results from the fact that observations are more sensitive to the slip pulse centroid time than its initial rupture time. We therefore also analyze the posterior distribution of centroid times in Figure 3.8 (c). The distribution of centroid times clearly shows the complexity of the rupture propagation, especially at the north-west of the hypocenter. The centroid time propagation is not homogeneous, displaying a complex pattern, especially to the west of the hypocenter.

We use the posterior coseismic model to calculate synthetic displacements and compare them with GPS observations (Figure 3.9 (a)). Both permanent stations and campaign survey stations show an acceptable fit, including the vertical components. Stochastic predictions of tsunami waveforms display a good agreement with tsunami observations (Figure 3.9 (b)). In particular, we see that later arrivals are often well fitted even if they are not inverted for. Some tide gauges stations present a slight time-shift between observed and predicted waveforms. This shift could be explained by local site effects, which are hard to model. Figure 3.10 shows that InSAR data is also well predicted by our posterior coseismic model. The InSAR residuals are smaller than 10% of LOS displacements with spatial distributions that do not seem to be strongly correlated with the co-seismic displacement pattern. Kinematic data show a directivity effect with larger amplitudes toward the north that is well reproduced by the model (Figures 3.11, and S10). We can see that stochastic waveforms reproduce most of the complex features visible in the HRGPS and strong motion records.

3.6 Discussion

In the next subsections, we will examine individually different aspects of the Illapel earthquake rupture. We first assess the reliability of our model close to the trench by exploring the importance of shallow slip to fit tsunami records. We then investigate complex encircling rupture patterns visible in our solutions. Finally, we use our posterior ensemble of slip models to assess fracture energy in comparison with existing scaling laws.

3.6. DISCUSSION

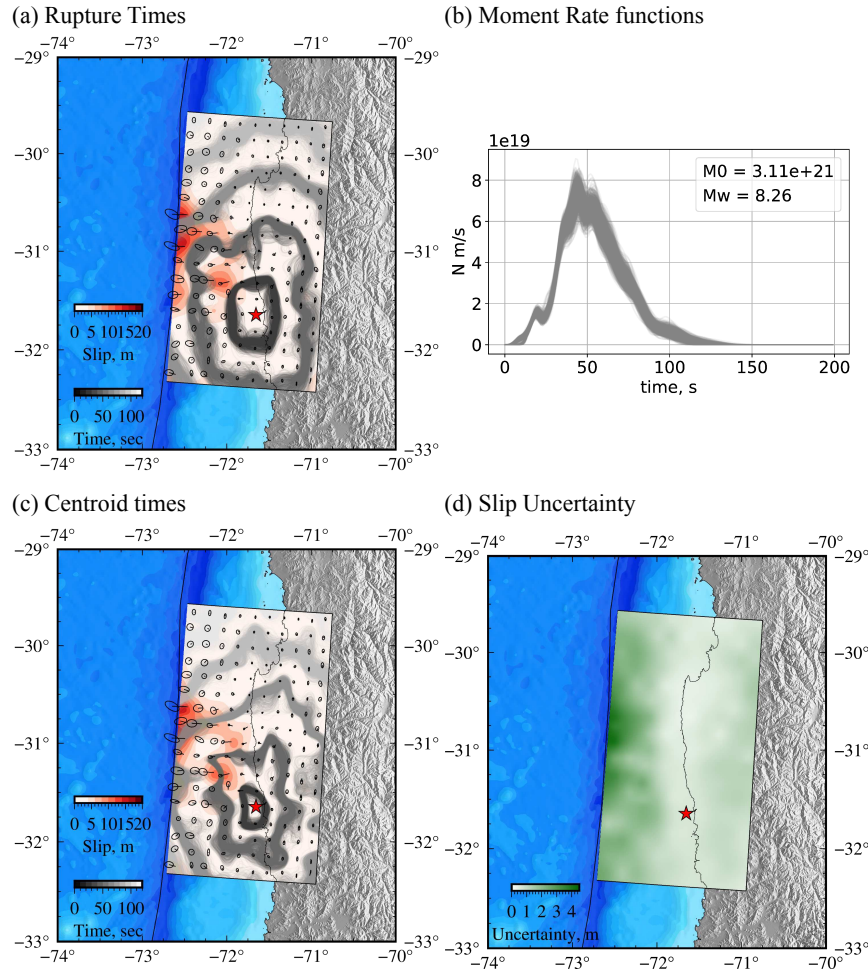


Figure 3.8: Impact of using a 2nd order approximation C_p in slip inversion. (a) Posterior mean coseismic slip model, arrows represent the slip directions and the ellipses its corresponding uncertainty. Contours show stochastic rupture fronts samples from the *a posteriori* distribution. (b) Stochastic moment rate functions. (c) Posterior mean coseismic slip model with contours that represent stochastic centroid time fronts samples from the *a posteriori* distribution. (d) Uncertainty of the ensemble of coseismic slip models. The red star in the figures represents the inverted hypocenter location.

3.6.1 Impact of Shallow slip.

At present, there is no general agreement regarding the amount of shallow slip during the Illapel earthquake, since some studies indicate the absence of shallow slip [An and Meng, 2017], while others demonstrate that shallow slip is necessary to explain tsunami observations [Lay et al., 2016]. To explore the contribution of shallow slip on the inversion, we perform a static slip inversion imposing the shallow slip to be very small. Results in Figure 3.12 are obtained by using a narrow gaussian centered on zero for the along-dip component of slip (considering a standard deviation of 0.5m). If we compare the resulting solution in Figure 3.12 with the previous pos-

3.6. DISCUSSION

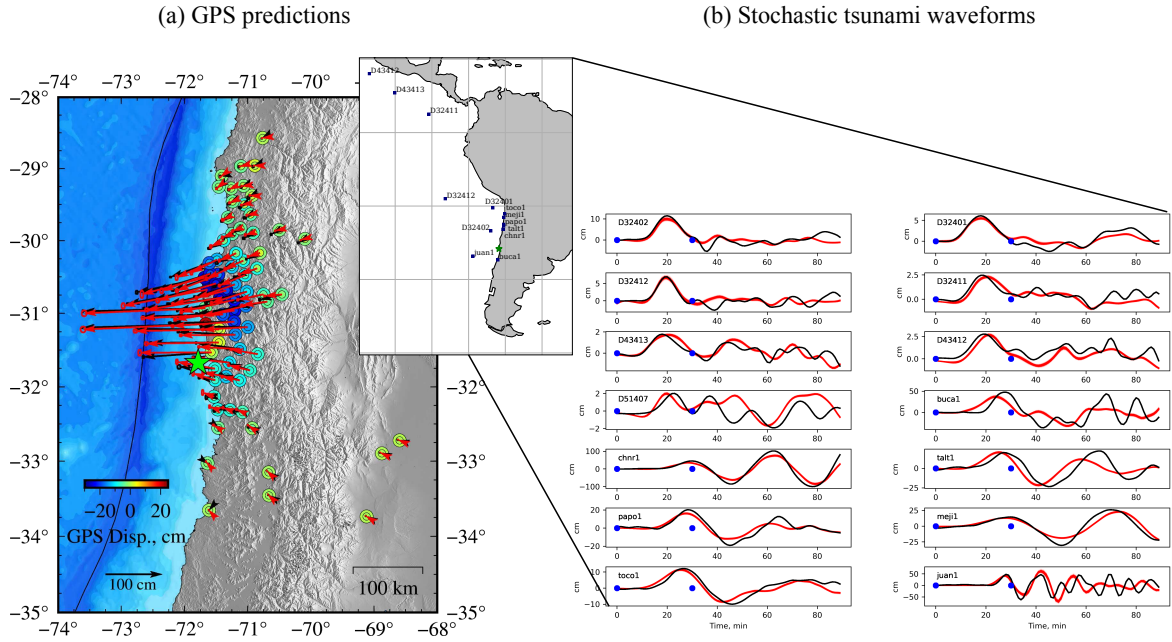


Figure 3.9: (a) Observed displacement GPS (black arrows) and predictions for the posterior mean model (red arrows) using a 2nd order approximation C_p . The colormap indicates vertical component displacements for observed (outer circle) and synthetic (inner circle) data. (b) Comparisons between tsunami observations (black) and stochastic predictions (red) using a 2nd order approximation C_p . The tsunami waveform signal used in the inversion is shown between blue dots. The map corresponds to each tsunami station.

terior coseismic models in Figure 3.5 and Figure 3.8, we can still find the downdip slip patch close to the hypocenter. However, the shallow part of the model is significantly different due to the new prior. The comparison of model performance for both solutions is shown in Figure 3.12 (b). We can see that the solution without shallow slip cannot fit the tsunami waveforms as well as our initial model. The existence of large shallow slips supports the fact that the 2015 event is not a simple repeat of the earthquake that affected the region in 1943 [Tilman et al., 2016]. This is consistent with historical reports indicating that the tsunami generated in 1943 was much smaller than what was observed in 2015. In addition, the differences in the duration of teleseismic body-wave arrivals for both events suggest that the 1943 rupture did not involve shallow slip [Tilman et al., 2016]. The reason why the 2015 event involve shallow slip contrarily to the 1943 event is unclear. One possibility is that shallow slip deficit was larger in 2015 than in 1943. This is consistent with coupling models from Metois et al. [2016] showing that the fault is not creeping at plate rate at shallow depth. However, this remains speculative as fault coupling close to the trench is poorly resolved by land-based geodetic data and could potentially be biased when ignoring stress shadowing effects [Lindsey et al., 2021].

3.6. DISCUSSION

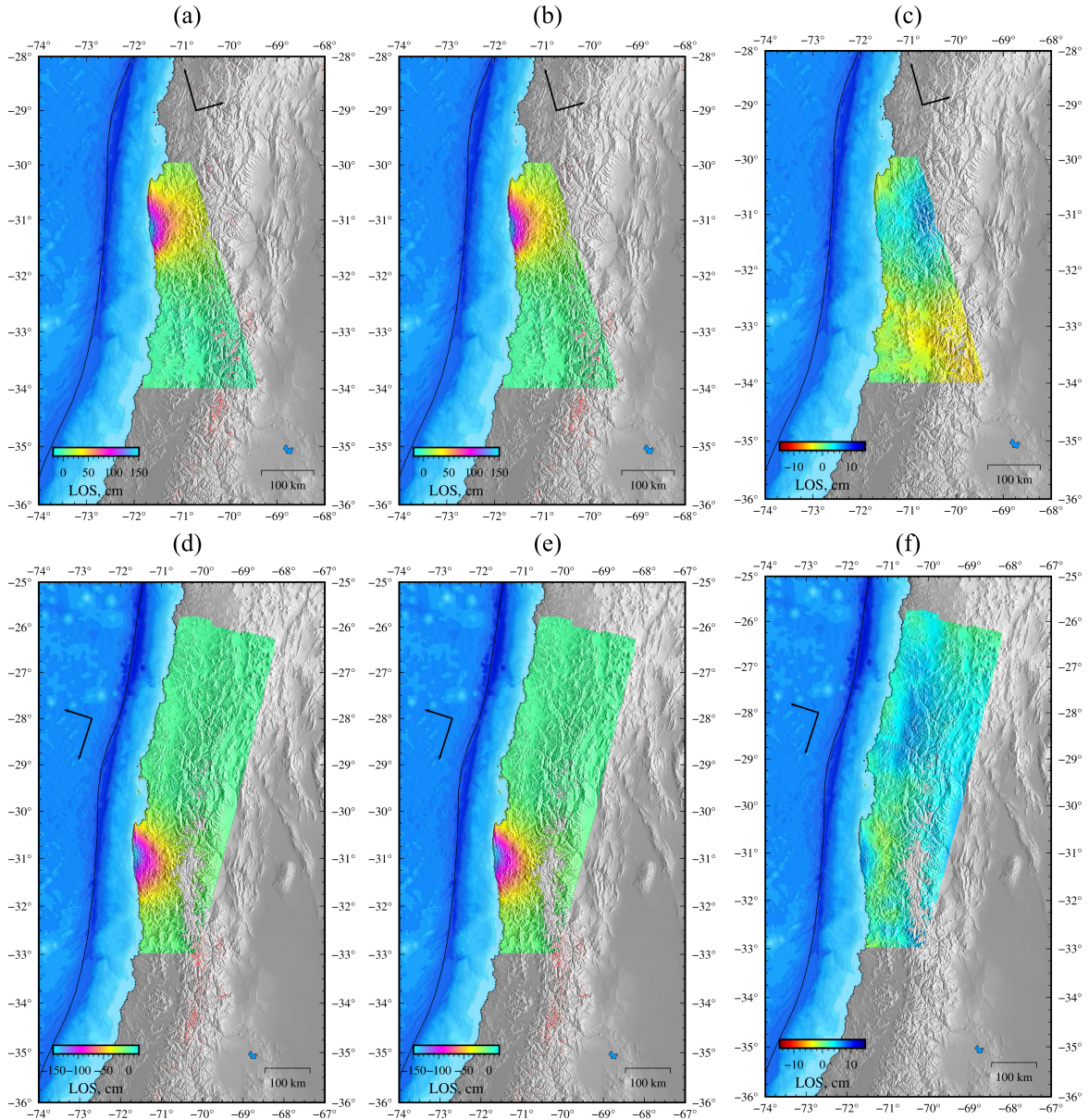


Figure 3.10: InSAR images misfit using the posterior coseismic model using the 2nd order C_p matrix solution. Observed ascending (a) and descending (d) Sentinel 1-A images. We show the corresponding synthetic displacement for ascending (b) and descending (c) images and the respective residual, ((c) for ascending, and (f) for descending images).

3.6.2 Encircling rupture pattern during the 2015 Illapel earthquake.

Back-projection results from Meng et al. [2018] show an encircling rupture during the 2015 Illapel earthquake. However, this encircling effect hasn't been reported by any previous kinematic slip inversion model. Results in Figures 3.8 (a) and (c) show a possible encircling behavior northwestward from the hypocenter location. We use

3.6. DISCUSSION

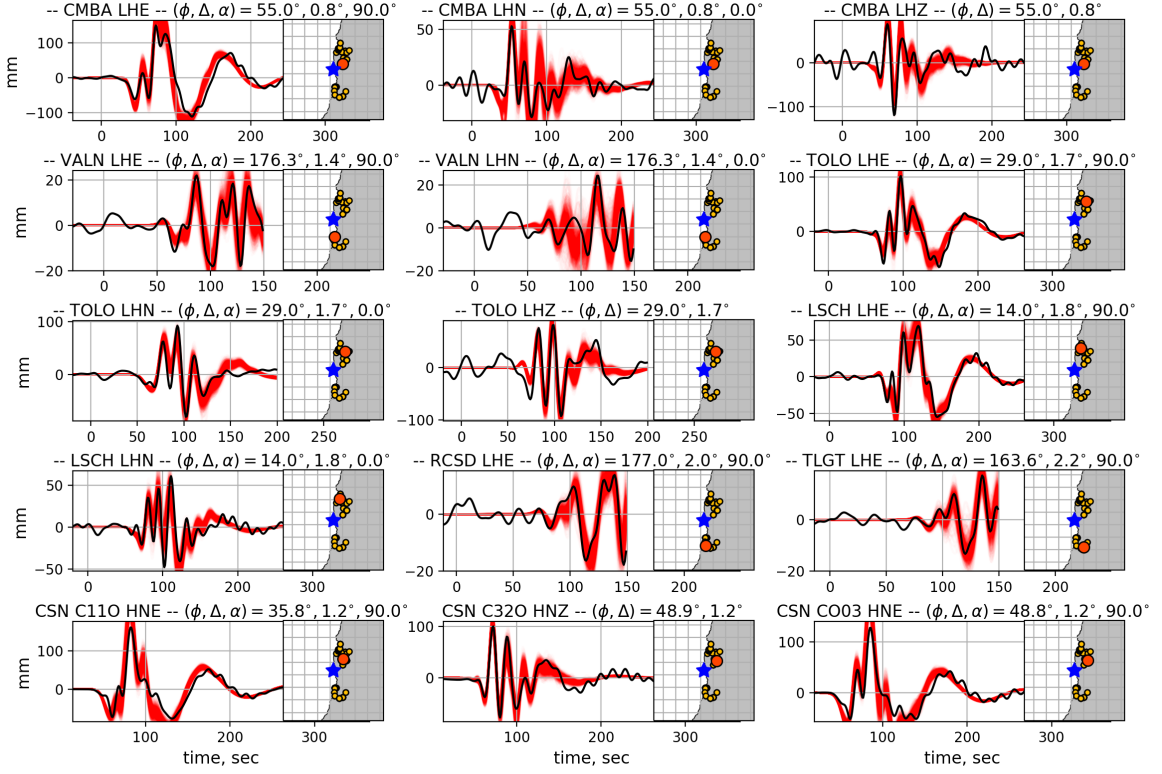


Figure 3.11: Examples of comparisons between data (black) and stochastic predictions (red) for HRGPS and Strong Motion stations using a 2nd order approximation C_p . On the maps, the blue star represents the hypocenter while circles indicate station location (orange for the station depicted and yellow for the other stations)

the posterior coseismic mean model to investigate the slip and slip rate evolution. Snapshots are shown in Figure 3.13. The rupture slowly grows propagating to the north-west during 35 seconds. Around 40 seconds, the rupture splits in three slip-rate pulses depicting a first encircling pattern west of the hypocenter (cf., slip rate snapshots between 40 and 50 seconds) and another encircling pattern to the northwest (cf., slip rate snapshots between 45 and 60 seconds). These encircling slip pulse contour fault areas with small slip amplitudes (cf., final slip distribution in Figures 3.8 and 3.13). Both slip branches finally join together generating a large slip-rate pulse around 60 sec continuing at shallow depth toward the north until the end of the rupture.

If we compare it with previous studies, we find that the general northwestward migration pattern is quite similar to the results published by Melgar et al. [2016b]. The encircling slip pulses visible in our solution between 40 and 60 seconds are consistent with previous back-projection results that suggest such complexities in the rupture. Ruiz et al. [2016] back-projection results show an early stage bilateral rupture that later merged and propagated up-dip. Meng et al. [2018] report two episodes

3.6. DISCUSSION

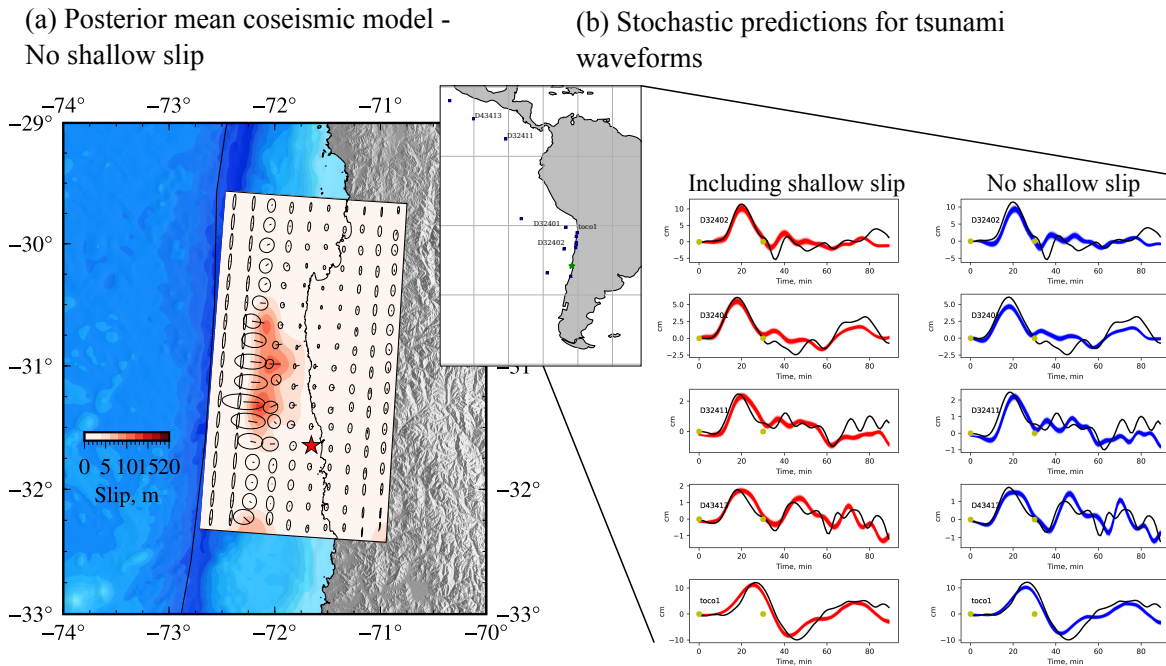


Figure 3.12: (a) Posterior mean coseismic slip model for a static inversion with a non shallow slip *a priori*. Arrows represent the slip directions and the ellipses its corresponding uncertainty. (b) Comparisons between tsunami observations (black) and stochastic predictions with shallow slip (red) and without shallow slip (blue). The tsunami waveform signal used in the inversion is shown between yellow dots. The map shows the depicted tsunami stations.

of splitting of rupture fronts, occurring both before reaching 60 seconds. This effect is known as a "double encircling pincer movement" and was previously reported by Das and Kostrov [1983]. The first episode reported by Meng et al. [2018] is between 15 and 35 seconds, and the second, around 45 and 60 seconds. The first encircling is colocated with the static coseismic model of An and Meng [2017]. However, such a model could miss rupture features retrieved by our joint inversion that incorporates kinematic data. For both episodes, Meng et al. [2018] suggest encircling effects that are northern than the encircling patches that we obtained. We report the first encircling episode approximately at 40 seconds, at least 20 seconds later than Meng et al. [2018]. The later presence of slip on the slip animation and Figure 3.13 indicate the presence of an asperity/barrier region [Das and Kostrov, 1983, Madariaga, 1983], as previously suggested by Meng et al. [2018]. Both encircling episodes are contouring regions with small final slip amplitudes and are resulting in large slip where the slip-rate pulses are focusing. This is quite consistent with numerical modeling results of Kato [2007] showing such focusing effect around a circular asperity, which supports the existence of such phenomena. The encircling effect can be also produced by a hierarchical asperity model or cascade-up growth model. This means that small weaker patches are embedded inside larger stronger

3.6. DISCUSSION

fault areas [Noda et al., 2013].

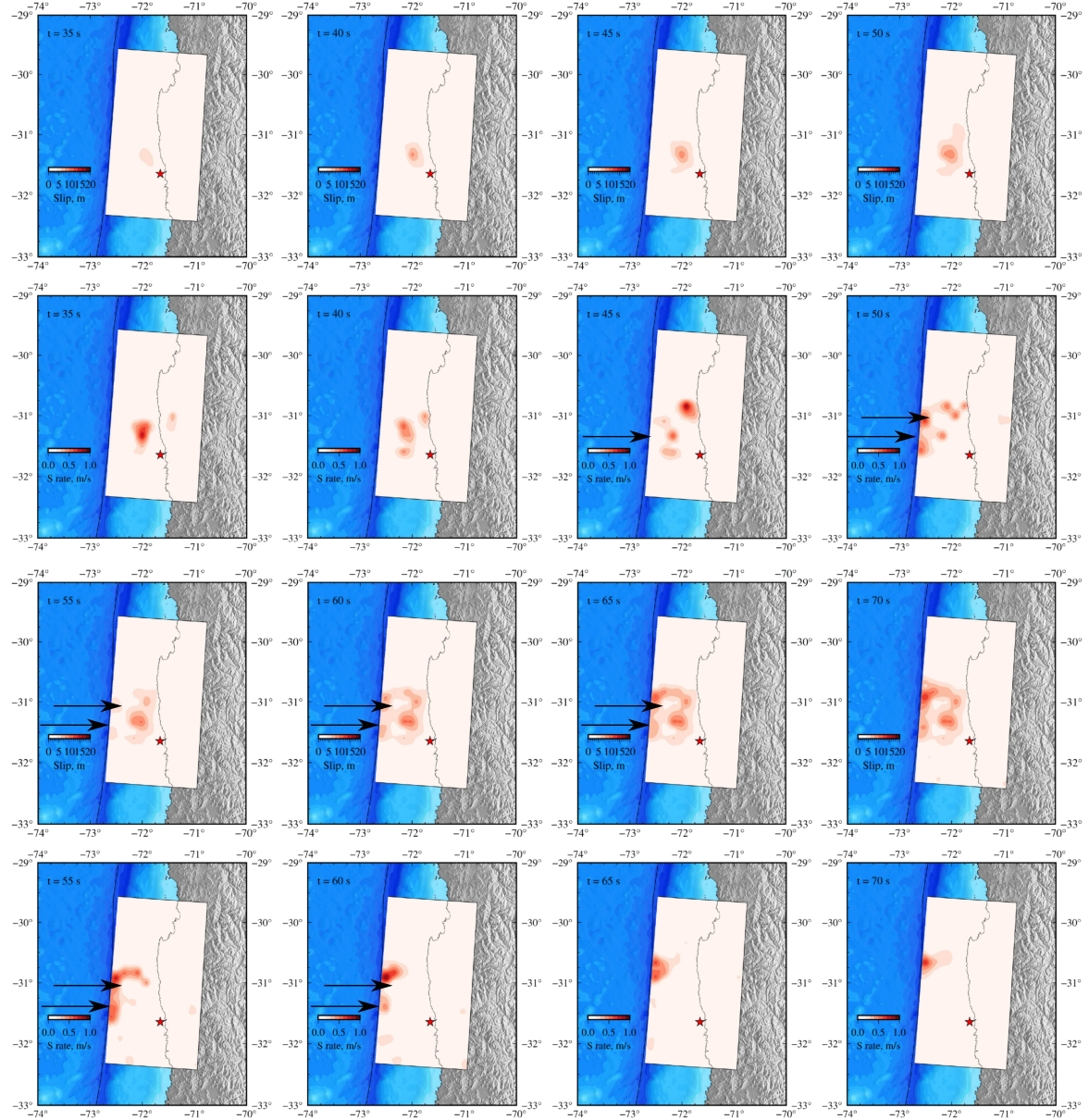


Figure 3.13: Five seconds snapshots of slip (first and third row) and slip rate (second and fourth row) evolution. Slip and slip rate are calculated using the posterior mean coseismic model using the 2nd order C_p solution. The red star is the inverted hypocenter location. Arrows represent the possible encircling locations.

3.6.3 Breakdown work of the 2015 $M_W = 8.3$ Illapel earthquake

Some studies have reported a low radiation efficiency for tsunami earthquakes [Venkataraman and Kanamori, 2004]. This is due to the presence of sediments, which dissipate a large part of the available energy. This is relevant for the 2015 Illapel earthquake as our solution suggests large slip at shallow depth. To further

3.6. DISCUSSION

investigate the rupture dynamics of the 2015 Illapel earthquake, we follow an approach similar to Tinti et al. [2005a], and use kinematic models to compute dynamic parameters. Consequently, we use kinematic model samples from our posterior distribution as a boundary condition to compute stress evolution following the methodology of Aochi et al. [2000]. Using these stress evolution computations, we can obtain the corresponding breakdown work following Tinti et al. [2005a]:

$$\mathbf{W}_b = \int_0^{T_b} (\tau(t) - \tau_{\min}) \cdot \nu(t) dt, \quad (3.12)$$

where \mathbf{W}_b is the breakdown work, τ is the traction, ν is the slip rate, and T_b is the time where the minimum traction τ_{\min} is reached.

Following this approach, we were able to recover slip weakening distance D_c and breakdown work \mathbf{W}_b for an ensemble of samples driven from the *a posteriori* PDF of the 2015 $M_W = 8.3$ Illapel earthquake. It is worth mentioning that the breakdown work is also called the fracture energy in seismology studies [Tinti et al., 2005a]. However in fact, it is different from what is commonly used in fracture mechanics (where it is strictly defined as the energy used to produce a new crack surface). As pointed out by Kanamori and Rivera [2006] and Tinti et al. [2005a], what is generally referred to as fracture energy in seismology includes different types of energy such as the energies used for off-fault cracking, and various thermal processes. To avoid any confusion, we follow Tinti et al. (2005) and refer to it as breakdown energy. Beyond the interest of estimating \mathbf{W}_b for Illapel, we focus on studying \mathbf{W}_b since different studies have pointed out the dependence of D_c on the final slip, making D_c a not reliable parameter [Guatteri and Spudich, 2000, Piatanesi et al., 2004, Tinti et al., 2009]. We follow the same methodology to obtain breakdown work of the 2014 $M_W = 8.1$ Iquique earthquake to compare it with the Illapel event since the Iquique earthquake is located almost in the same region and has a similar magnitude. We use the solution of Duputel et al. [2015] because it was also obtained using a similar Bayesian approach. We compare the average breakdown energy of both earthquakes with the solution and scaling relationship from Tinti et al. [2005a] (Figure 3.14 a). Both breakdown energies follow the proposed scaling relationship. This result suggests that even though the scaling relationship was calculated using smaller magnitude events, such a relationship can be extrapolated to larger magnitudes. We compare our breakdown estimations with those of Aochi and Ruiz [2021]. In their work, Aochi and Ruiz [2021] create a simplified kinematic slip inversion using ellipses and then used this inversion to make a dynamic model. Their estimation of total fracture energy E_G is 8.5×10^{16} J. Our breakdown energy for the Illapel earthquake is $1.89 \pm 0.11 \times 10^{18}$, which is about one order of magnitude

3.6. DISCUSSION

larger. The estimation of Aochi and Ruiz [2021] followed the scaling relationship of Aochi and Twardzik [2020], which is built using events with magnitudes between $M_W = 6.0 - 7.8$. Such events can possibly be modelled by simplified models (one or two ellipses). However, given the complexity of the Illapel earthquake, different patches are needed to recover the complete rupture fracture energy. We can use the estimate of radiated energy $E_R = 2.93 \times 10^{16}$ J from Ye et al. [2017] and compute the radiation efficiency as:

$$\eta_R = \frac{E_R}{E_R + (E_G \text{ or } \mathbf{W}_b)}. \quad (3.13)$$

If we use the results of Aochi and Ruiz [2021], we obtain $\eta_R = 0.256$. On the other hand, with our calculated breakdown energy we estimate a radiation efficiency of $\eta_R = 0.015$. Venkataraman and Kanamori [2004] reported radiation efficiencies smaller than 0.25 for tsunami earthquakes (such as the 1992 Nicaragua earthquake). Such low radiation efficiency is consistent with our modelling results requiring significant slip at shallow depth to explain tsunami observations.

Moreover, we compare the average breakdown work of both earthquakes with the solution and scaling relationship from Tinti et al. [2005a] and the scaling relationship from Causse et al. [2014] (Figure 3.14 b). Even though there is a general agreement, we can clearly see that the breakdown work averaged over the fault is small compared with the scaling relationships. We think that such underestimation results from the fact that the averaging of \mathbf{W}_b is done over the entire fault used for slip inversion (even in regions that did not slip). To mitigate this effect, we decided to weight the averaging of the breakdown work by the corresponding slip in subfaults. We see that for the Illapel earthquake, the estimated value is more consistent with the aforementioned scaling relationships. In the case of the Iquique earthquake, there is still a significant offset, which could be then due to the compactness of the rupture [Duputel et al., 2015]. We compare again with the aforementioned study of Aochi and Ruiz [2021]. They report an average breakdown work of 7.5 MJ/m^2 , while our estimates are $34.4 \pm 2.04 \text{ MJ/m}^2$, and $122.8 \pm 14.7 \text{ MJ/m}^2$ for the average and weighted average breakdown work respectively. The approach of Aochi and Ruiz [2021] smoothens any possible heterogeneity inside the patch and is limited in low frequencies. These limitations would explain the differences with our average breakdown estimates, since posterior coseismic mean models show a very heterogeneity rupture (Figures 3.6 and 3.8).

We carry out a final comparison between individual subfault slip and the analogous breakdown work (Figure 3.15). We find the same behavior that was reported by Tinti et al. [2005a], where the breakdown work scales as u^2 . To get insights about

3.7. CONCLUSION

breakdown work scaling relationships, we calculate the fracture energy G for a self-healing slip pulse model [Rice et al., 2005]. For this model, the fracture energy is calculated as:

$$G = G^* \left(\frac{\mu u^2}{\pi L} \right), \quad (3.14)$$

where μ is the shear modulus, L the sliding zone, and u the corresponding displacement. The expression G^* depends of two terms:

$$G^* = g(\theta) F(v_r), \quad (3.15)$$

where $g(\theta)$ is a function of the ratio R/L , with L being the sliding zone, and R the slip weakening zone. On the other hand, $F(v_r)$ depends of the velocity rupture v_r and the fracture mode, i.e, the function is different for mode II and mode III. For the Illapel event we choose to use mode II, while for the Iquique earthquake we adopt mode III. The function $g(\theta)$ varies from 1, when $R/L \rightarrow 0$, to 2 when $R/L = 1$. In this work we decide to make the conservative assumption of having $R/L = 1$, hence having the maximum G . We approximate the corresponding sliding zone L as $L = v_r \times T_s$, where v_r and T_s are the inverted rupture velocity and rise time for each model subfault. In case this value is bigger than the corresponding subfault length, i.e., $L > 18$, we keep this last value.

Fracture energy for the 2015 $M_W = 8.3$ Illapel earthquake and the 2014 $M_W = 8.1$ Iquique earthquake are shown in Figure 3.15. In both case, the same scaling relationship seems to be valid with breakdown work estimates that evolves similarly as fracture energy from the scaling relationship in equation 3.14. However, fracture energy is consistently smaller than its corresponding value of breakdown work. An explanation for this offset could be the fact that the calculation of breakdown work involves a mixture of energies, i.e., heat and surface energy. On the contrary, the model of a self-healing slip pulse only includes fracture energy.

3.7 Conclusion

Using extensive static and kinematic data sets, and a realistic uncertainty model, we obtain fully Bayesian joint inversions of the 2015 $M_W = 8.3$ Illapel earthquake. We employ a non-linear parameterization (inverting for slip, rupture velocity, rise time and hypocenter location), which allows us to resolve the complexity of the rupture. We also explore three approaches to evaluate prediction uncertainty due to inaccuracies in the Earth model. We use an empirical estimate of the prediction error covariance matrix C_p along with 1st order and 2nd order perturbation approaches.

3.7. CONCLUSION

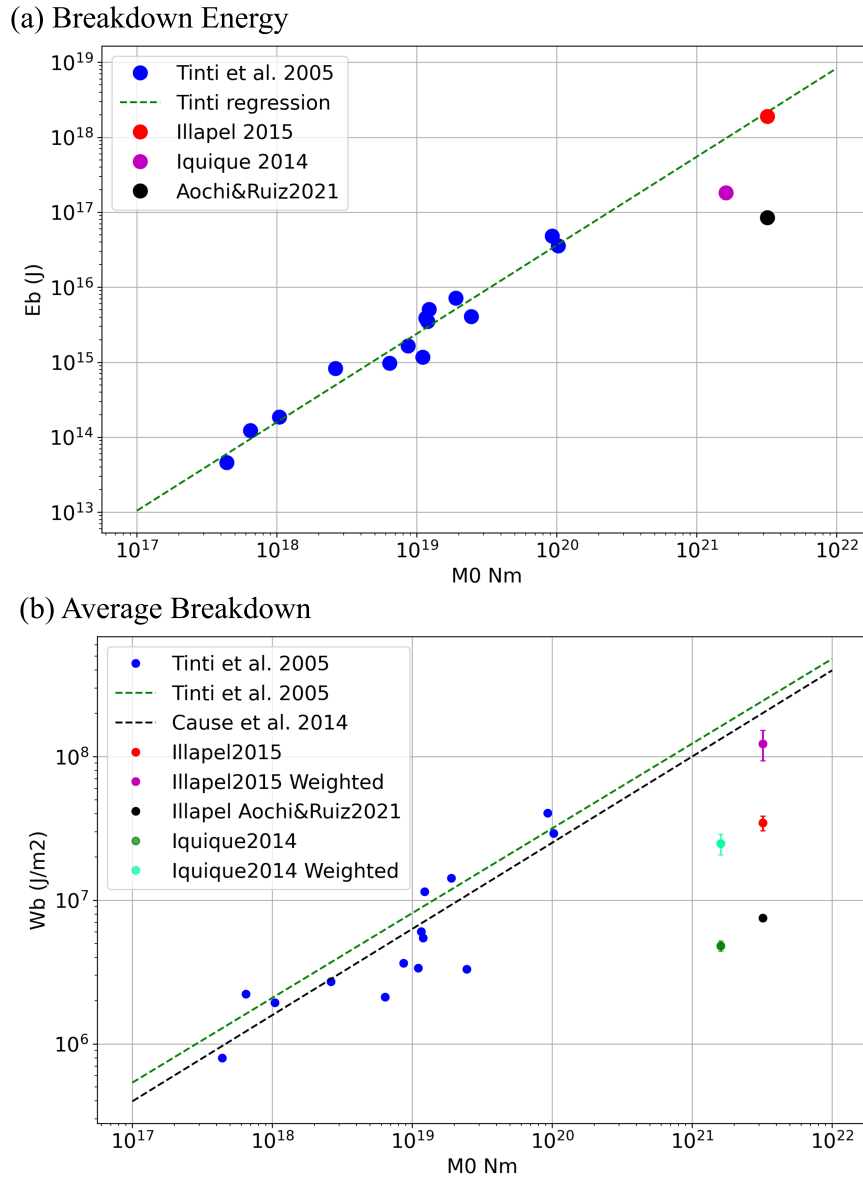


Figure 3.14: Average breakdown energies (a) and average breakdown work (b) for the 2015 $M_W = 8.3$ Illapel earthquake and the 2014 $M_W = 8.1$ Iquique earthquake. For the breakdown energy, purple and red dots represent the average breakdown energies calculated in this study. For the breakdown work, green and red dots represent the average breakdown work calculated in this study. Cyan and purple dots represent the average breakdown work weighted by the corresponding slip. Blue dots represent the breakdown energies and breakdown work calculated by Tinti et al. [2005a] respectively. The dashed green line represents the scaling relationship from the same study while the dashed black line represents the scaling relationship is from Causse et al. [2014].

Results suggest that 2nd order approximation can provide results that are similar to those obtained using an empirical C_p , which can help to save computing time.

Our kinematic slip models indicate two main slip asperities : a first asperity close to

3.7. CONCLUSION

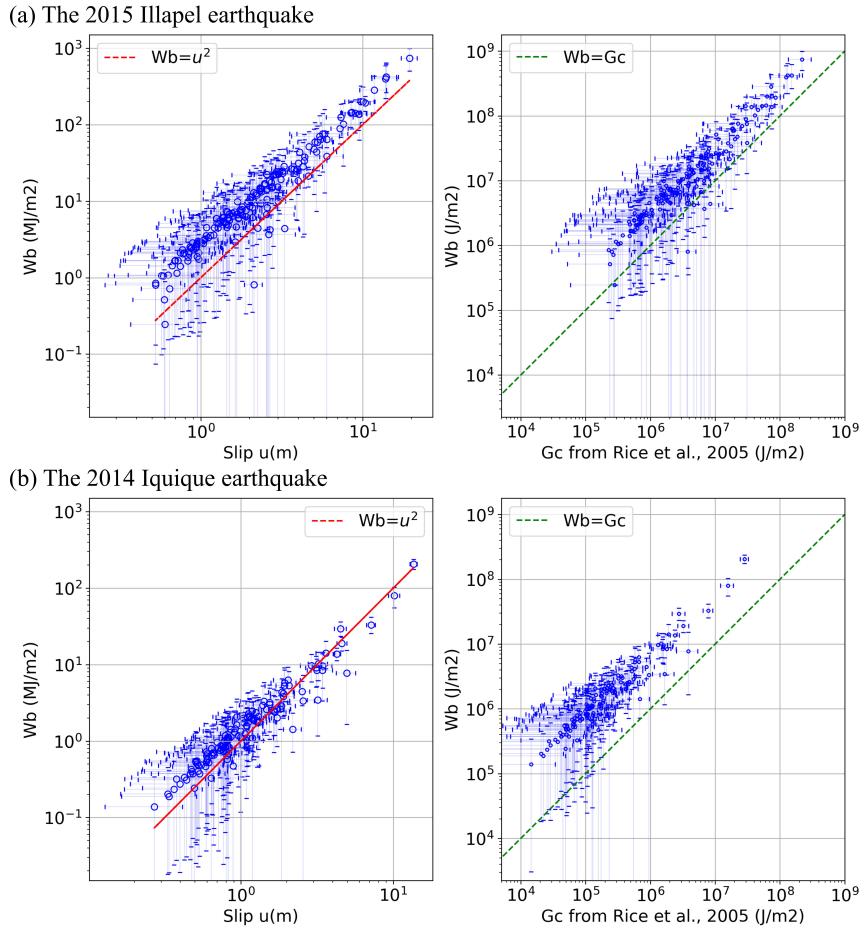


Figure 3.15: Scaling of breakdown work density with slip and Fracture energy estimates from Rice et al. (2005). (a) Scaling relationships for the 2015 $M_W = 8.3$ Illapel earthquake. (b) Scaling relationships for the 2014 $M_W = 8.1$ Iquique earthquake.

the hypocenter and another one at a shallow depth. Results show that the rupture propagated slowly at shallow depth. Analysis of an inversion imposing a small slip amplitude close to the trench suggests that shallow slip is necessary to fit tsunami observations. Historical records suggest that such shallow slip did not occur during the 1943 earthquake that affected the same region of the Chilean megathrust.

Estimation of rupture and centroid times suggests that an encircling rupture behavior takes place in the westward region. This phenomenon has been previously suggested by back-projection studies, and depict a focusing effect that is consistent with dynamic simulations of encircling ruptures. The 2015 $M_W = 8.3$ Illapel earthquake and the 2014 $M_W = 8.1$ Iquique earthquake exhibit a breakdown work density that scales as u^2 and is in good agreement with scaling relationships previously reported by Tinti et al. [2005a] and Rice et al. [2005]. The total breakdown energy is consistent with scaling relationships suggested for smaller earthquakes.

3.8 Acknowledgments

We thank L. Rivera and H. Bhat for helpful discussion. This project has received funding from the European Research Council (ERC, under the European Union's Horizon 2020 research and innovation programme under grant agreement No. 805256 and grant agreement No 758210) and from Agence Nationale de la Recherche (project ANR-17-ERC3-0010). This research was also supported by the Mexican National Council for Science and Technology (CONACYT), scholarship 2018-000003-01EXTF-00012. RJ acknowledges funding from the Institut Universitaire de France.

3.8. ACKNOWLEDGMENTS

General conclusions

In this work, we explored both the rupture nucleation and propagation using various types of observations, including seismic, geodetic and tsunami data. The joint interpretation of these different observations is a challenging task as each data set is affected by different uncertainties and is sensitive to different fault processes. In the framework of this PhD work, a particular effort was made to characterize the observational and prediction uncertainties, which provide a natural weighting between disparate data sets.

As we discussed in section 2, the origin of foreshock sequences distinguishing between the current conceptual models (foreshocks cascaded model or aseismic preslip triggering) is an ongoing matter of study. New experimental and numerical studies, such as McLaskey [2019], show that both conceptual models could actually be coexisting. Studies for the 2014 $M_W = 8.2$ Iquique earthquake suggest the occurrence of an aseismic preslip up to 8 months before the mainshock [Socquet et al., 2017]. At the same time, a series of self-triggered foreshocks have been observed [Herman et al., 2016]. The corresponding foreshock seismicity rate can be explained using the temporal ETAS seismicity model [Schurr et al., 2014]. Our work regarding the initiation phase of the 2017 $M_W = 6.9$ Valparaíso earthquake suggests that the transient displacements prior to the mainshock cannot be explained only with foreshock induced displacements, even when accounting for prediction and observation uncertainties. This implies the presence of a seismic and an aseismic contribution. We estimate that $\sim 50 \pm 11\%$ of GPS displacements are likely caused by an aseismic slip, a ratio that is fairly consistent for different stations in the vicinity of the Valparaíso sequence. We assess the aseismic preslip distribution

by performing a slip inversion following a Bayesian scheme. The aseismic preslip has a scalar moment of $M_0 = 3.08 \times 10^{18}$ N.m, which corresponds to a magnitude $M_w = 6.3$. Given the cumulative moment of foreshocks ($M_0 = 1.48 \times 10^{18}$ N.m), we estimate that nearly 70% of the scalar moment released during the preparation phase of the Valparaíso mainshock is aseismic, which is roughly in agreement with estimates from Ruiz et al. [2017].

Even if the results suggest that aseismic preslip is one of the mechanisms triggering foreshocks, part of the foreshock activity likely results from cascading phenomena due to stress changes of neighboring events. Why some earthquakes are preceded by foreshocks while others are not is still an open question in seismology. The absence of a systematic precursory activity might partly be due to an observational gap due to the incompleteness of the current seismicity catalog [as suggested by Mignan, 2014]. In this regard, the need of conducting statistical studies using a highly complete earthquake catalog, such as the Southern California catalog. Trugman and Ross [2019] showed that 72% of $M_W \geq 4$ earthquakes in this region are preceded by an elevated seismic activity compared with the background seismicity rate, suggesting that foreshock activity is less exceptional than previously thought. However, Moutote et al. [2021] reanalyzed the same catalog and found that only 18% of these foreshock sequences were really anomalous and could not be attributed to temporal fluctuations in background seismicity rate. Even though we take into account the contribution of missing events in GPS displacement time-series, we could use these more complete catalogs to have a better estimation of the seismic missing contribution in the transient displacement. Likewise, in the Valparaíso sequence analysis, we correct the GPS time-series removing the seismic contribution to estimate the overall partitioning between aseismic and seismic slip. However, it would be interesting to jointly invert for seismic data and geodetic time-series (instead of correcting geodetic time-series using source models derived independently from seismic data). Besides, laboratory-driven and theoretical models show that earthquakes are preceded by the growth of self-accelerating aseismic slip that smoothly reaches co-seismic slip-rates [e.g., Ohnaka, 1992, Latour et al., 2013]. One objective of future studies should be to use geodetic time-series to assess if slip evolution before mainshocks follow what is predicted by these studies.

As the second project of this thesis, we obtained fully Bayesian joint inversions of the 2015 $M_W = 8.3$ Illapel earthquake. The 2015 $M_W = 8.3$ Illapel earthquake is an interesting earthquake for which more than ten different kinematic models have been published. Nevertheless, these models exhibit significant variability. Some models exhibit almost no shallow slip [An and Meng, 2017], contrarily to other studies [Lay et al., 2016]. Delimiting the amount of shallow slip turns out to be crucial

as it can generate hazardous tsunami waves. This variation can be attributed to differences in methodology and employed observations. We employ a non-linear parameterization (inverting for slip, rupture velocity, rise time, and hypocenter location), which allows us to resolve the complexity of the rupture. Since computing forward problem uncertainties is computationally expensive, we explore three approaches to predict uncertainty due to inaccuracies in the Earth model: using an empirical covariance matrix C_p , a covariance matrix C_p calculated using the 1st order approximation, and a new approach, the 2nd order approximation approach. Results using a 2nd order approach are similar to those obtained using an empirical matrix, which can save computing time.

Our kinematic solution shows a rupture with two main slip areas, a first asperity close to the hypocenter, and another one at shallow depth, with an important amount of shallow slip, in agreement with previous studies including tsunami observations [Lay et al., 2016, Melgar et al., 2016b]. Analysis of an inversion imposing a small slip amplitude close to the trench confirms that shallow slip is necessary to fit tsunami observations. Rupture times suggest a rupture that propagates slowly at shallow depth, with a northwestward direction. Rupture times also indicate that an encircling rupture occurs westward of the hypocenter. Encircling effects have been previously suggested by previous back-projection studies [Meng et al., 2018] and depict a focusing effect consistent with dynamic simulations of encircling ruptures. To gain insight into rupture dynamics we use kinematic models to compute the stress evolution on the fault as a function of time. We compute the breakdown work density from the stress evolution and compare the resulting probability density estimates with similar calculations done for the 2014 $M_W = 8.1$ Iquique earthquake. Both earthquakes exhibit a breakdown work density that scales as u^2 and is in good agreement with scaling relationships previously reported by Tinti et al. [2005a] and Rice et al. [2005]. The total breakdown energy is consistent with scaling relationships suggested for smaller earthquakes.

In this work, we obtain more reliable estimates for the 2015 $M_W = 8.3$ Illapel earthquake by employing a Bayesian scheme. This allows us to have robust slip distribution solutions on the fault. Furthermore, we have developed a methodology to calculate estimations of breakdown work W_b and energy E_b by using our posterior ensemble of models. In this regard, an interesting perspective would be to use the same methodology (Bayesian slip inversion and dynamic parameters evaluation) to analyze many other earthquakes. Beyond having a detailed description of various ruptures, such approach would allow us to have interesting insights into scaling relationships and energy budget for different earthquakes (intraplate events, megathrust and tsunami earthquakes along with shallow and deep events). This

kind of studies have been conducted using single finite fault inversion models [Ye et al., 2016], which limits the estimation of uncertainties. Similarly, we could compare our estimates of breakdown work with scaling relationships developed using laboratory earthquakes and numerical modeling [e.g., Lambert and Lapusta, 2020, Paglialunga et al., 2022, Viesca and Garagash, 2015].

Appendices

Supporting Information for Seismic and aseismic fault slip during the initiation phase of the 2017 Mw=6.9 Valparaíso earthquake

Contents of this file

1. Text S1 to S2
2. Figures S1 to S12
3. Tables S1 to S2

Introduction

S1. GPS processing

68 continuous GPS (cGPS) were processed in South America (66 stations) and Nazca (2 stations) Plates (Figures A.1 and A.2), from different networks that are listed below:

- 13 cGPS from the International GNSS service (www.igs.org): ANTC, AREQ, BRAZ, BRFT, CHPI, GLPS, ISPA, KOUR, LPGS, RIO2, SANT, UFPR, UNSA.
- 3 cGPS from the Instituto Geográfico Militar of Bolivia (www.igmbolivia.gob.bo): SCRZ, URUS, YCBA.
- 11 cGPS from the Brazilian Network (RBMC-IP, www.ibge.gov.br): CUIB, MABA, MSCG, NAUS, POAL, POVE, PRCV, ROCD, RSAL, SAVO, TOPL.
- 15 cGPS from Argentinian National Network (RAMSAC, www.ign.gob.ar [Piñón et al., 2018]) AZUL, BCAR, CATA, DINO, EBYP, ESQU, MA01, NESA, PEJO, RWSN, SL01, TUCU, UNRO, UNSJ, VBCA
- 5 cGPS from the Chilean - French cooperation through LIA “Montessus de Ballore” (www.lia-mb.net): CONS, JRGN, OVLL, UAPE, UDAT.
- 2 cGPS from the Ministerio de Bienes Nacionales of Chile (www.bienesnacionales.cl): BN05, BN13
- 18 cGPS from the Centro Sismológico Nacional de Chile (CSN, www.csn.uchile.cl [Baez et al., 2018]): CHDA, CTPC, CUVI, DGF1, LVIL, MPLA, NAVI, PORT, QTAY, RCSD, ROB1, QTAY, SLMC, TLGT, TRPD, UAIB, VALN, ZAPA.

All these data were processed in double differences using GAMIT 10.7 software to obtain daily, 12 and 6 hours estimates of station positions, choosing ionosphere-free combination and fixing the ambiguities to integer values. The precise orbits from the International GNSS Service for Geodynamics, precise EOPs from the IERS bulletin B, IGS tables to describe the phase centers of the antennas, FES2004 ocean-tidal loading corrections, as well as atmospheric loading corrections (tidal and non-tidal). We used precise orbits from the International GNSS Service for Geodynamics, precise EOPs from the IERS bulletin B, IGS tables to describe the phase centers of the antennas, FES2004 ocean-tidal loading corrections, as well as atmospheric loading corrections (tidal and non-tidal). One tropospheric vertical delay parameter and two horizontal gradients per stations are estimated every 2 hours. Daily solutions and position time series are combined using the PYACS software [Nocquet, 2017] in a

regional stabilization process. The results are mapped into ITRF 2014 reference frame [Altamimi et al., 2016] and then put in the South-American frame using the Euler pole at -83.4° E, 15.2° N, and angular velocity $0.287^{\circ}\text{my}^{-1}$ [Nocquet et al., 2014].

S2. Prediction error covariance matrix

We focus on prediction uncertainties due to inaccuracies in the Earth model. These uncertainties are represented by the matrix C_p . We note the forward model $g(\Psi, \mathbf{m})$ for a source model \mathbf{m} , and Earth model parameters Ψ (i.e., P and S wave velocities, density). We can estimate C_p empirically from an ensemble of random models $\Psi_i, (i = 1, \dots, n)$ as:

$$C_p = \frac{1}{n-1} \sum_{i=1}^n (g(\Psi_i, \mathbf{m}) - \bar{g}(\Psi, \mathbf{m}))(g(\Psi_i, \mathbf{m}) - \bar{g}(\Psi, \mathbf{m}))^T, \quad (\text{A.1})$$

where \bar{g} is the mean of the ensemble of predictions $g(\Psi_i, \mathbf{m})$. In the following, we refer to C_p estimated in equation (1) as the empirical prediction error covariance matrix. Alternatively, we can compute C_p following a linearized perturbation approach. We assume that our forward model $g(\Psi, \mathbf{m})$ is well approximated by linearized perturbations of our predictions. For an a priori Earth model $\tilde{\Psi}$ we write:

$$g(\Psi, \mathbf{m}) \approx g(\tilde{\Psi}, \mathbf{m}) + K_\Psi(\tilde{\Psi}, \mathbf{m}) \cdot (\Psi - \tilde{\Psi}), \quad (\text{A.2})$$

where $K_\Psi(\tilde{\Psi}, \mathbf{m})$ is the sensitivity kernels of the predictions with respect to elastic parameters used to compute forward predictions:

$$K_\Psi(\tilde{\Psi}, \mathbf{m}) = \frac{\partial g_i}{\partial \Psi_j}(\tilde{\Psi}, \mathbf{m}). \quad (\text{A.3})$$

In this first order approximation, we use the sensitivity kernel $K_\Psi(\tilde{\Psi}, \mathbf{m})$ to estimate the covariance matrix C_p [Duputel et al., 2014]:

$$C_p = K_\Psi \cdot C_\Psi \cdot K_\Psi^T, \quad (\text{A.4})$$

where C_Ψ is the covariance matrix describing uncertainty in the Earth model. To analyze both approaches, we consider a simple test case limited to an uncertain in S-wave velocity in a single layer (at 30 km depth) using the source parameters of the $M_W = 6.0$ foreshock on 2017-04-23 (see section 3 of the main text). For comparison, we calculate prediction error covariance matrices C_p using equation (1) and equation (4). We plot in Figure S7 the diagonal components of both matrices for a representative station. We observe that there is an overall good agreement between our first order C_p and the empirical C_p matrix. We notice some discrepancies in the variance amplitudes and a time-shift in the late part of the waveforms (after 75s in Figure S7). To explore the origin of these effects, we compare synthetic waveforms predicted from the stochastic models and the waveforms calculated with

the first order approach. The results shown in Figure S8 indicate that the time-shift and amplitude difference in Figure S7 are related to the fact that the first order approach is unable to perfectly reproduce large perturbations in the Earth model.

To correct these differences, we can also estimate a covariance matrix using a second order approximation of the forward model as:

$$g(\Psi, \mathbf{m}) \approx g(\tilde{\Psi}, \mathbf{m}) + \mathbf{K}_{\Psi}(\tilde{\Psi}, \mathbf{m}) \cdot (\Psi - \tilde{\Psi}) + \frac{1}{2!} (\Psi - \tilde{\Psi}) \cdot \mathbf{H}_{\Psi}(\tilde{\Psi}, \mathbf{m}) \cdot (\Psi - \tilde{\Psi}), \quad (\text{A.5})$$

where \mathbf{H}_{Ψ} is the second order derivative with respect to the elastic parameters:

$$\mathbf{H}_{\Psi}(\tilde{\Psi}, \mathbf{m}) = \frac{\partial^2 g_i}{\partial \Psi_k \partial \Psi_j}(\tilde{\Psi}, \mathbf{m}). \quad (\text{A.6})$$

The computation of H involves evaluating n^2 derivatives, where n is the number of elastic parameters (e.g., 3 parameters per layer for a 1D Earth model). However, assuming that cross-terms are negligible, we can reduce the number of 2nd order derivatives to be evaluated to n .

As shown in Figure S7 and S8, some of the imperfections obtained with the first order approach can be corrected by employing a second order approach neglecting cross-terms. In practice, these discrepancies are more significant when we apply larger perturbations to the velocity model. Despite the fact that the inaccuracies of the first order approach have been corrected, we notice in Figure S8 that the differences between the first and second order approach are relatively small given the 1 Hz sampling frequency used in our moment tensor inversions. Our tests show that the differences are more visible when inverting waveforms with a higher sampling rate.

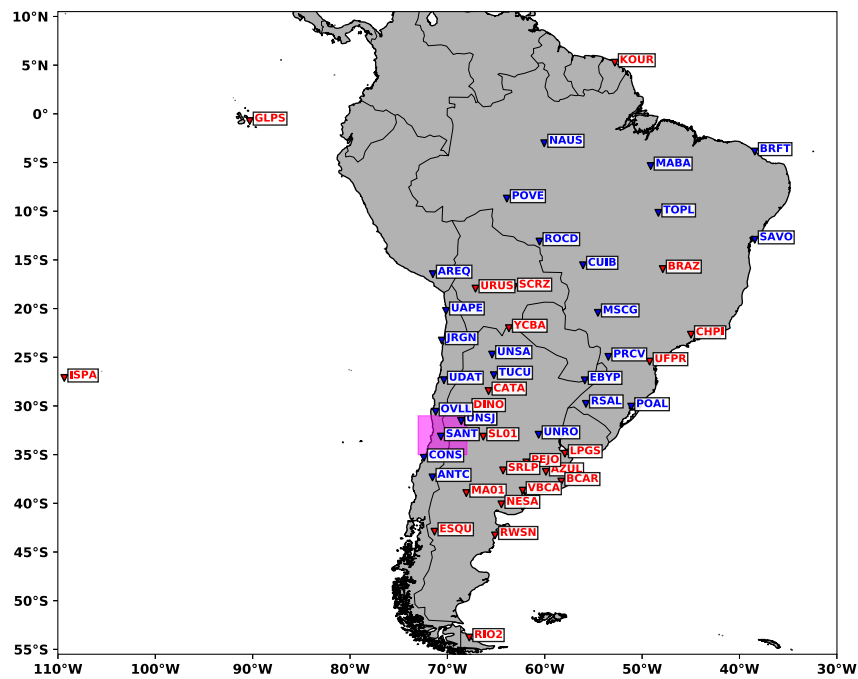


Figure A.1: Map of the GPS stations processed in South America and Nazca Plates. The red stations are those ones used to define the Reference Frame, while the blue ones are just used on the processing. The pink box denotes the study area (see Figure A.2 to look at the stations processed in this region).

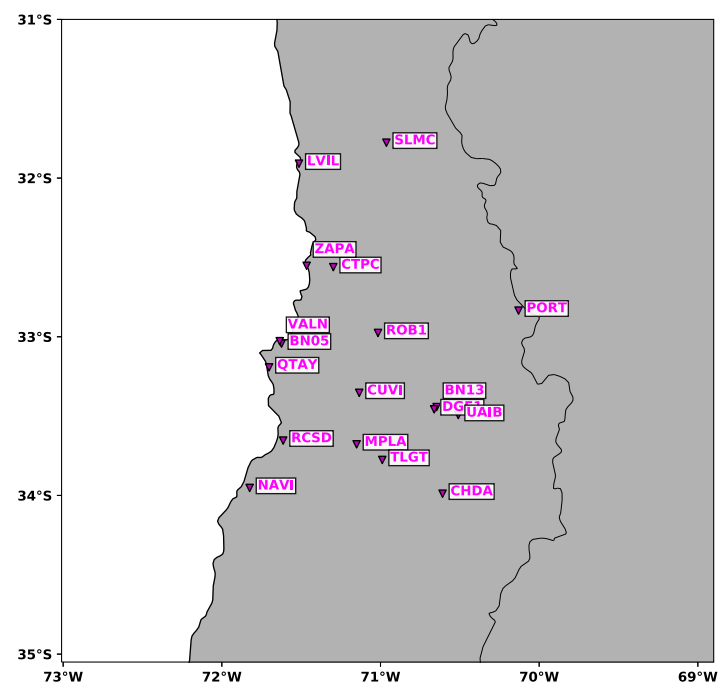


Figure A.2: Map of the GPS stations processed in the study area.

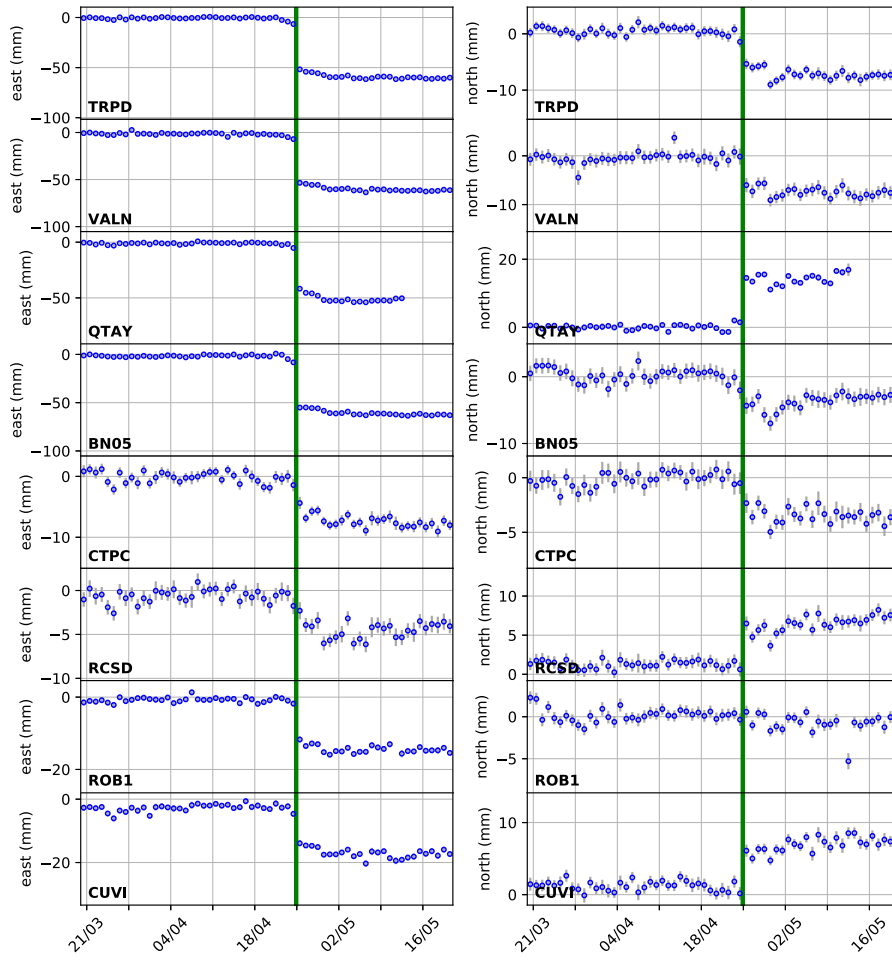


Figure A.3: GPS time series for the Valparaíso region network for north and east component. The images show the time series before and after the mainshock (green line) of the sequence.

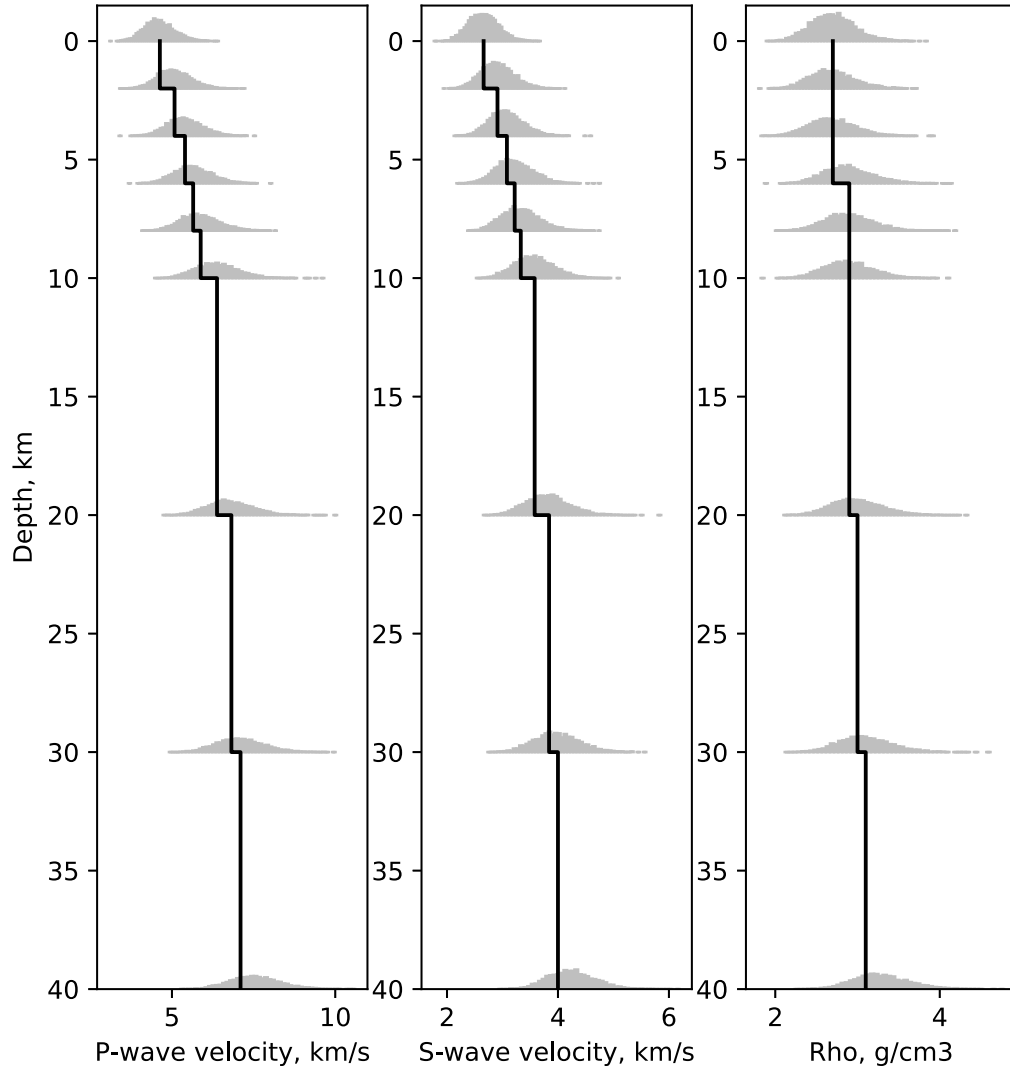


Figure A.4: Model variability of the P-wave, S-wave, and density as a function of depth in Valparaíso region. Black line represents the velocity layered model used for Green's Function (GF) calculation. Grey histograms are the probability density function for each parameter as a function of depth as described in Cp.

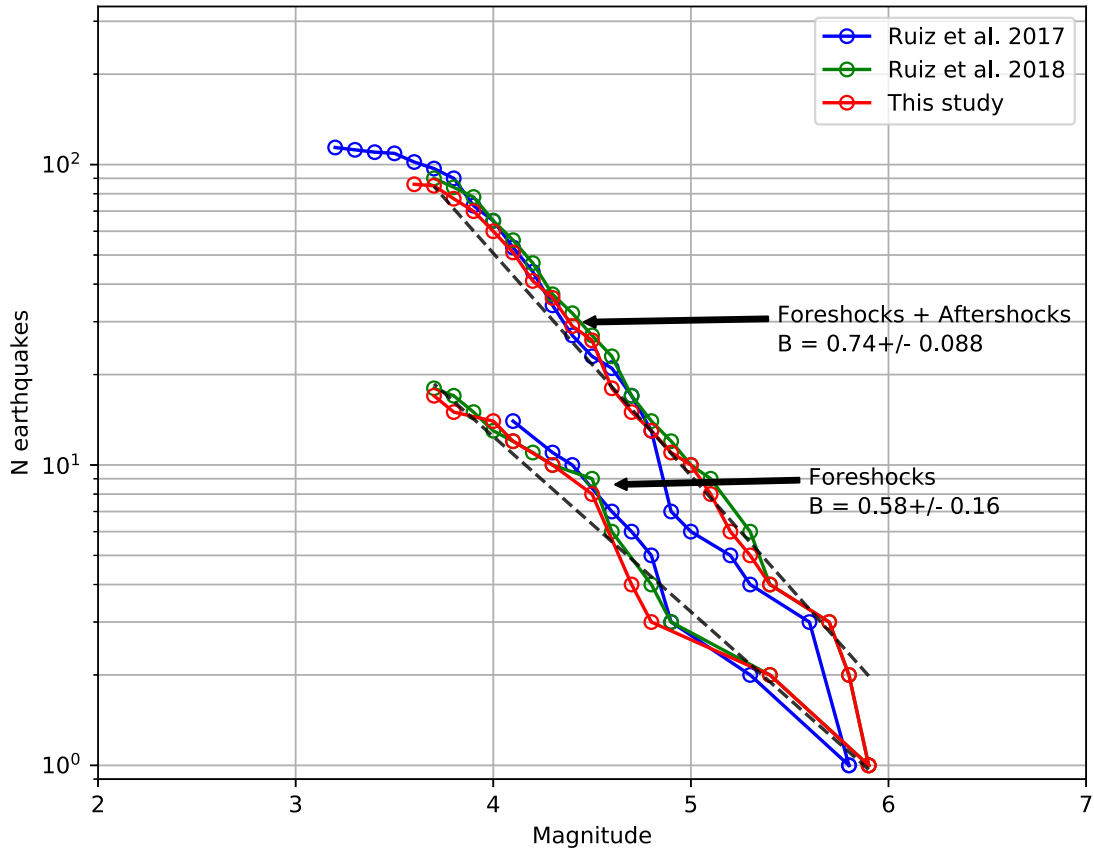


Figure A.5: Gutenberg-Richter law for the 2017 Valparaíso earthquake sequence. Three different catalogs of the sequence are shown: Our CMT catalog, S. Ruiz et al. (2017) catalog, and J. A. Ruiz et al. (2018) catalog. For each catalog, both the whole sequence (foreshocks and aftershocks), and the foreshocks sequence are represented.

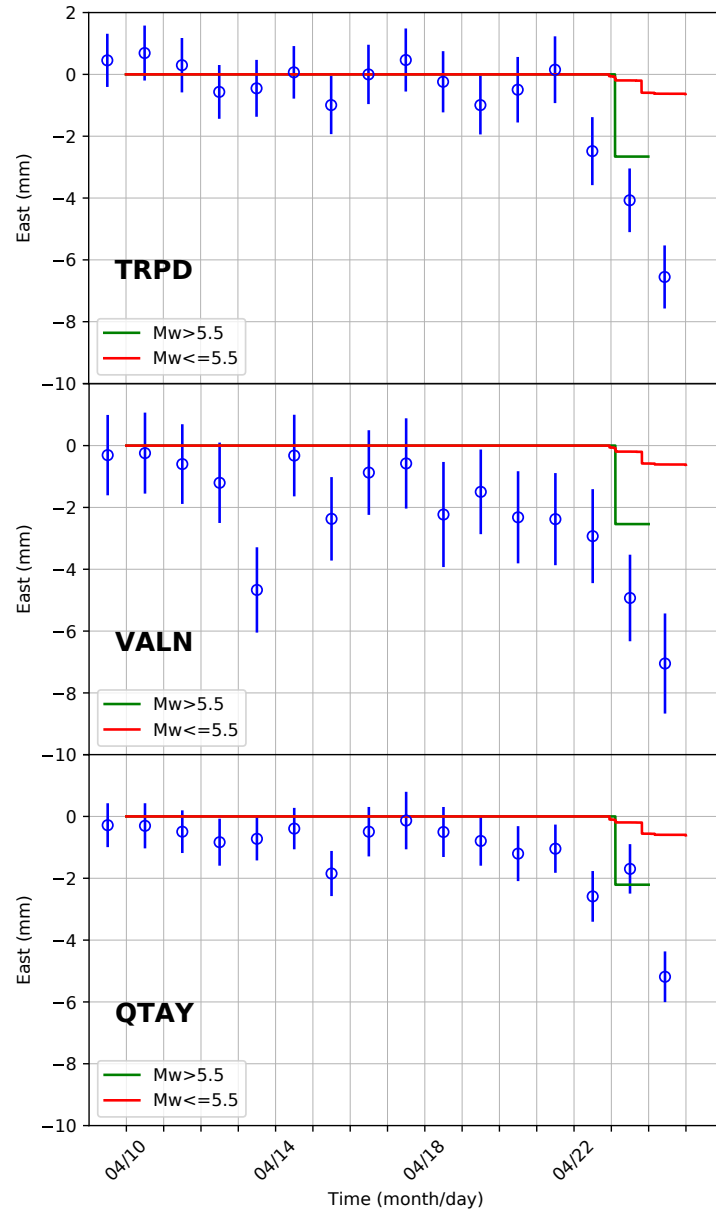


Figure A.6: Synthetic surface displacement for different ranges of magnitude, foreshocks with $M_w \geq 5.5$ (largest foreshock $M_w = 6.0$) and foreshocks with $M_w \leq 5.5$. The $M_w = 6.0$ contribution appears to dominate the signal, with respect to the cumulative contribution of smaller foreshocks.

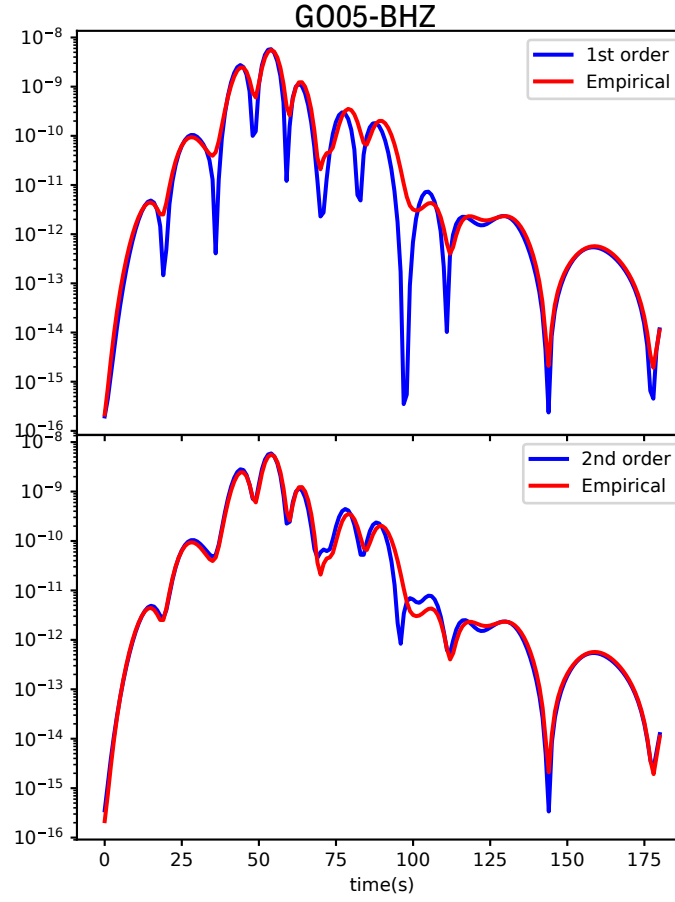


Figure A.7: Diagonal of the C_p matrix for the vertical component of the station G005. The matrix is calculated for the $M_W = 6.0$ foreshock of the Valparaíso sequence (see section 3 of the main text). The red line represents the diagonal matrix for the empirical covariance matrix (i.e., the matrix created from an ensemble of models). The blue line represents the first (top) and second-order (bottom) approaches used to compute C_p .

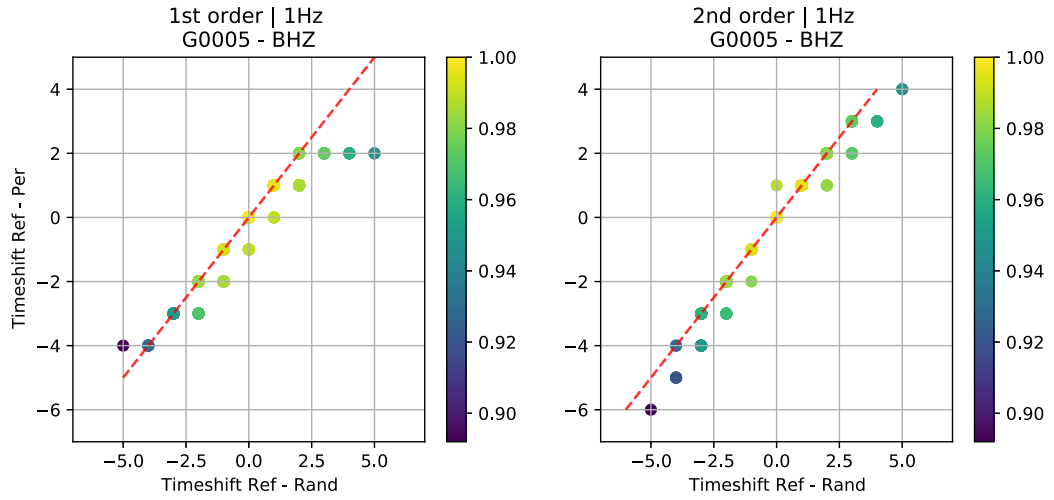
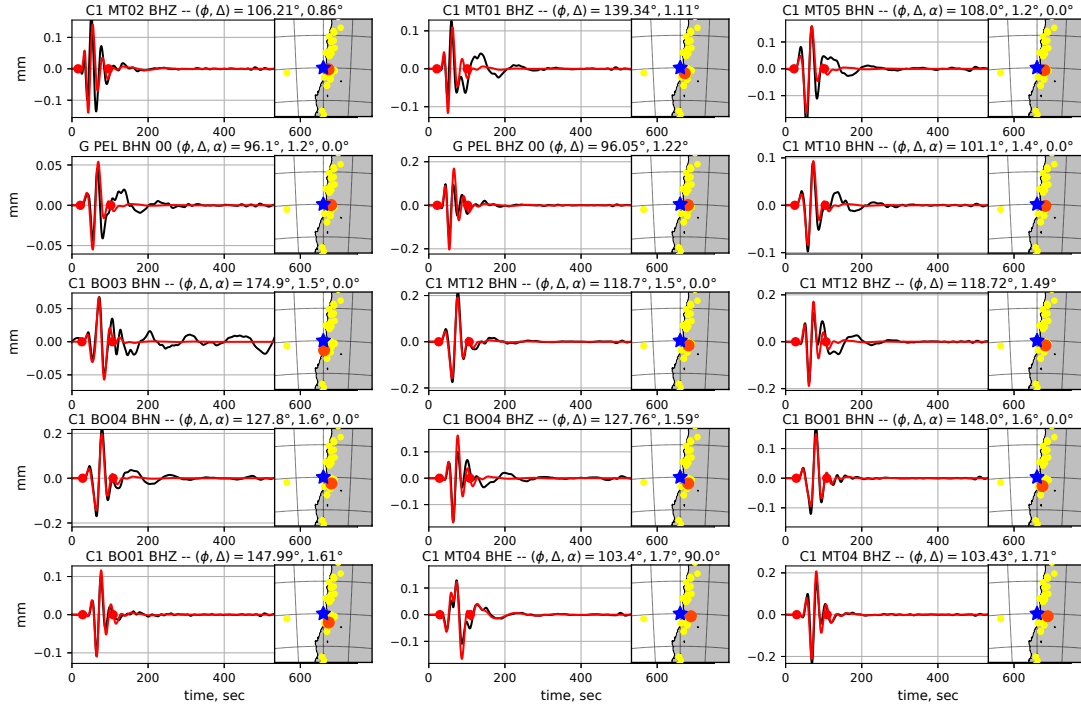
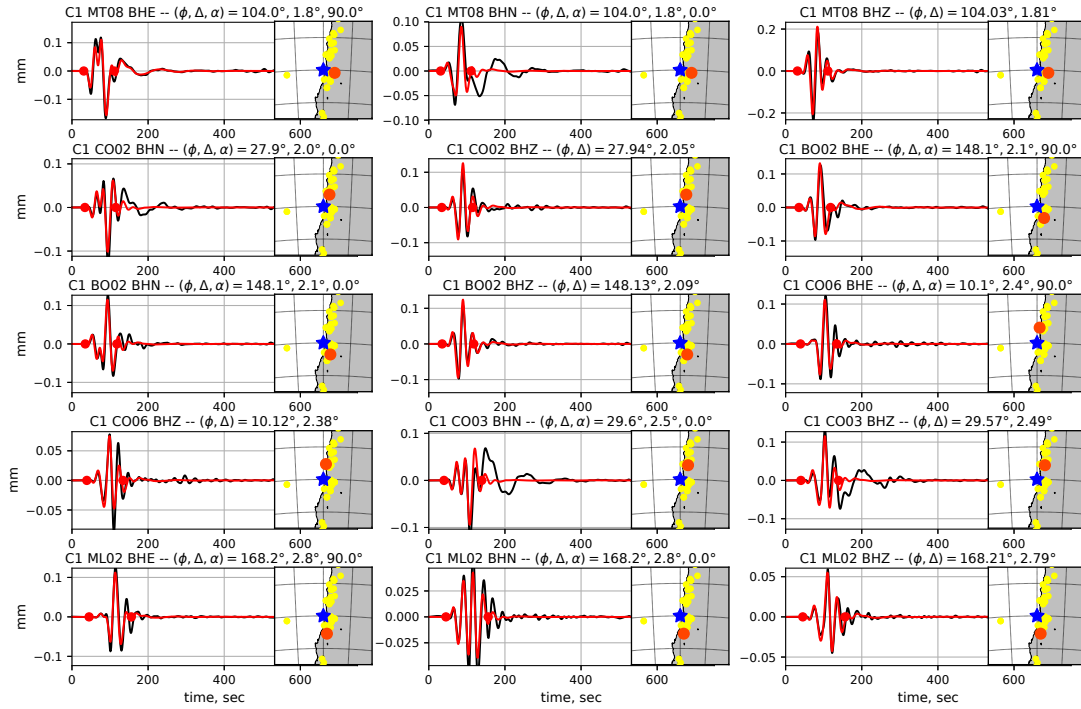


Figure A.8: Comparison between synthetic waveforms predicted from stochastic models calculated with a log-normal distribution, and synthetic waveforms calculated using the first and second order C_p matrix. The waveforms are generated using the source model of the $M_W = 6.0$ foreshock presented in section 3 of the main text. The X-axis represents time shifts between waveforms generated with the average velocity model of the region (figure S4) and waveform predicted for randomly perturbed velocity models. The Y-axis represents time shifts between waveforms generated with the average velocity model and waveforms generated either with the first or the second order approximation (see equations (2) and (5) of text S2). The color represents the correlation coefficient of each pair of waveforms. If the comparison follows the $y = x$ line, it means that the perturbation approximation properly estimates the empirical covariance matrix. We can observe that the second order approach better approximates actual synthetics (especially when there is a significant time-delay between waveforms).

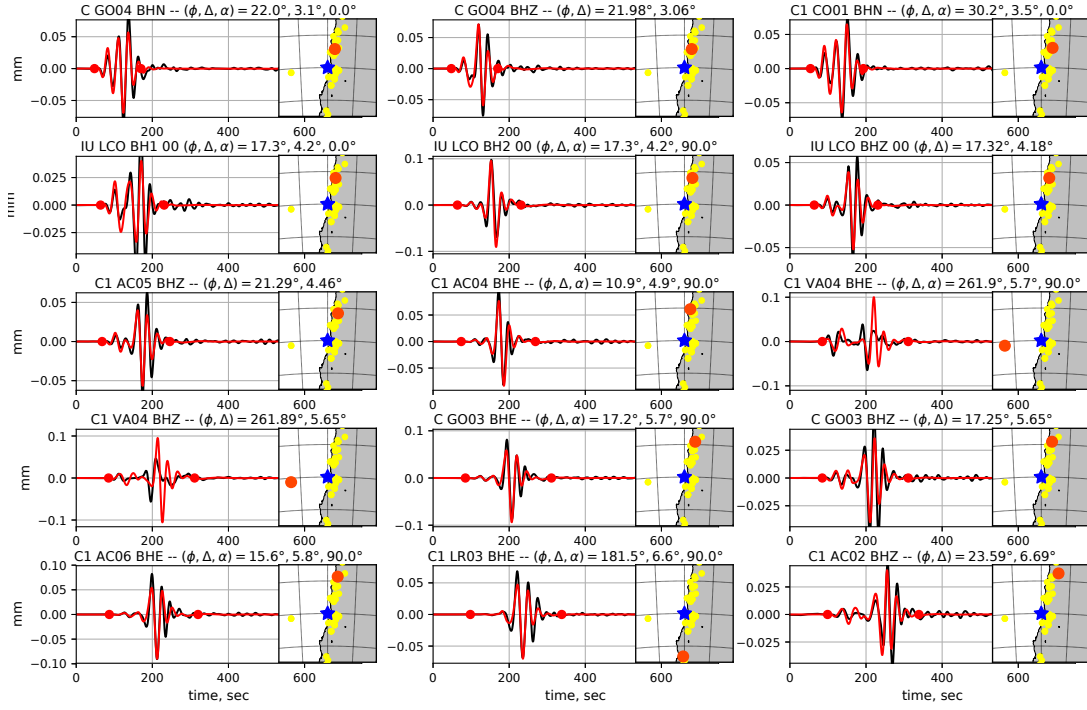
OFF_COAST_CENTRAL_CHILE, filter = (0.01, 0.04, 4, 1), p 1/4



OFF_COAST_CENTRAL_CHILE, filter = (0.01, 0.04, 4, 1), p 2/4



OFF_COAST_CENTRAL_CHILE, filter = (0.01, 0.04, 4, 1), p 3/4



OFF_COAST_CENTRAL_CHILE, filter = (0.01, 0.04, 4, 1), p 4/4

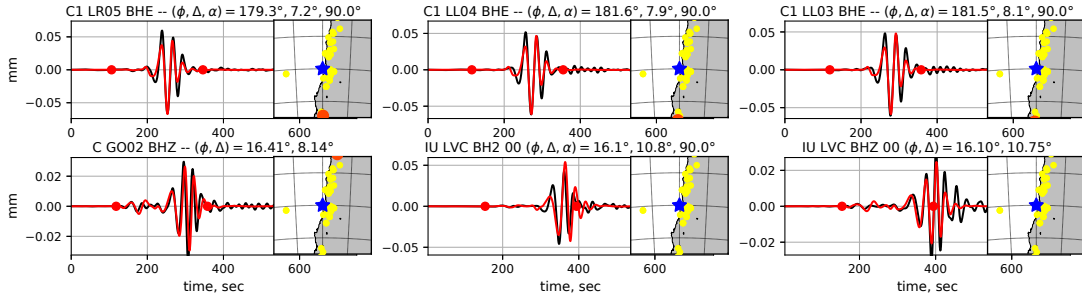


Figure A.9: Waveforms fit for the $M_W = 6.0$ foreshock using CMT solution from our catalog. Observed (black) and synthetic (red) waveforms for a given station (orange). The fit (inversion) is made between red dots. The blue star represents the CMT location. Yellow dots correspond to the ensemble of stations used in the inversion.

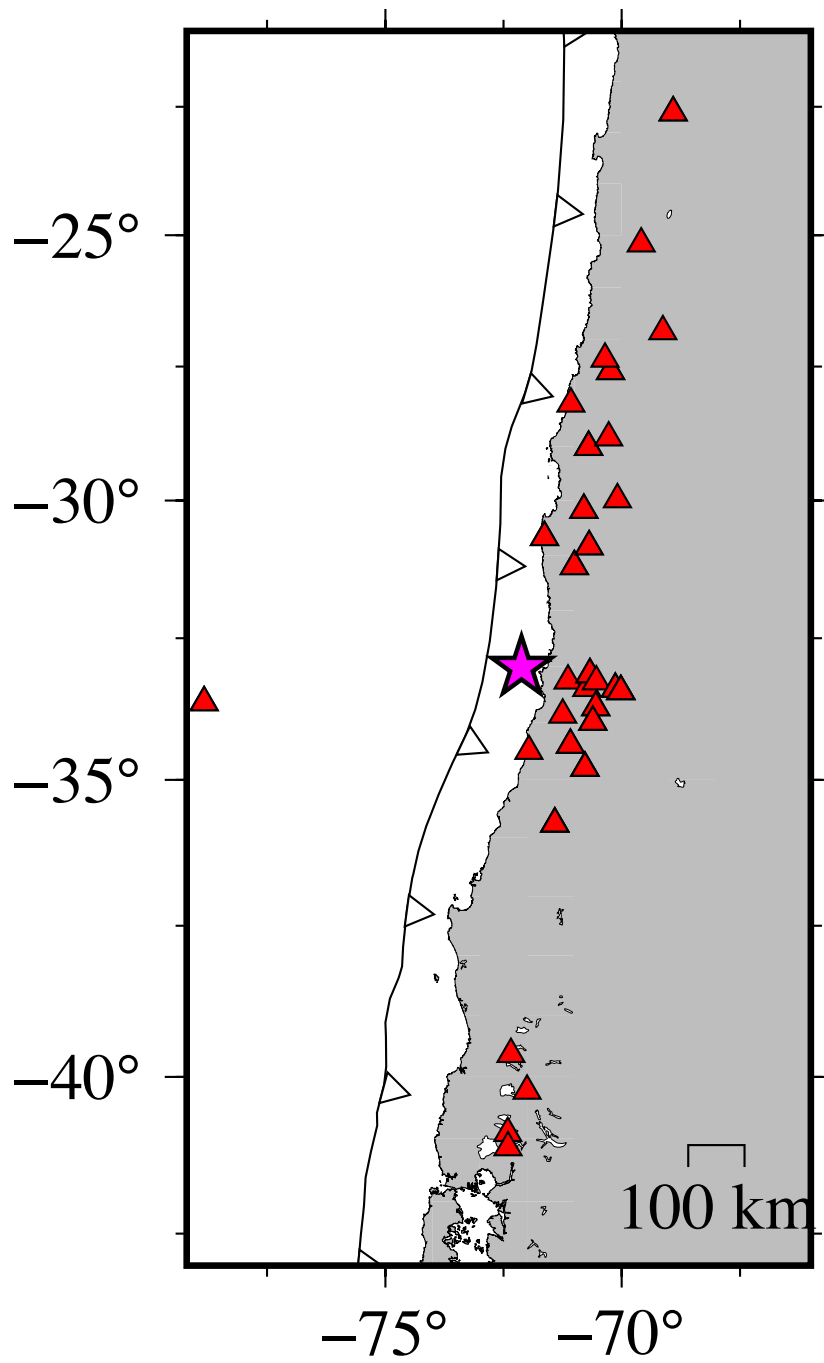


Figure A.10: Stations used for the $M_W = 6$ foreshock CMT inversion. The CMT location is shown in purple.

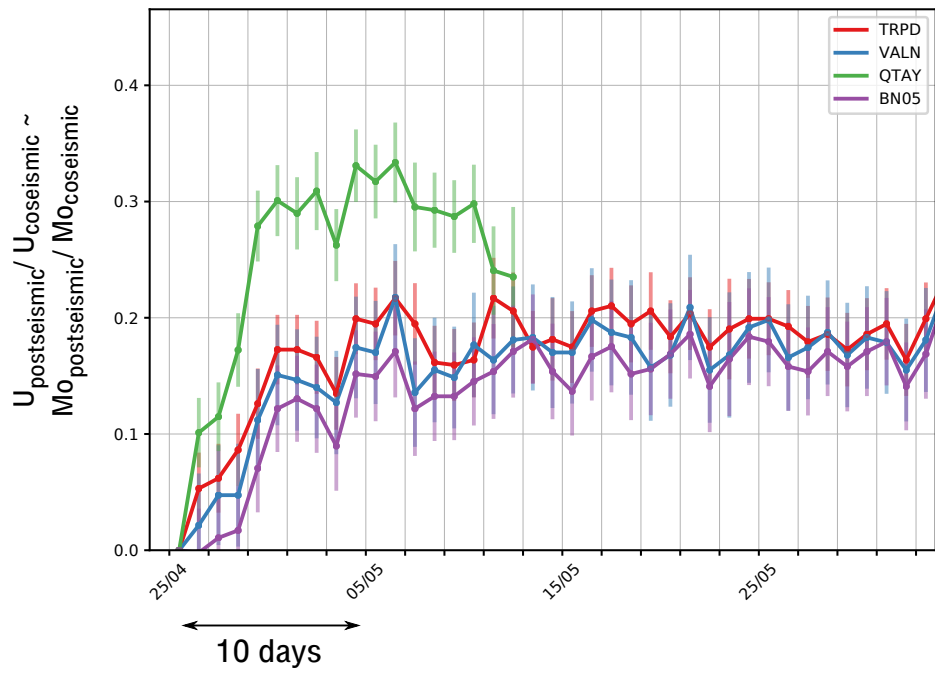


Figure A.11: Mainshock postseismic surface displacement normalized by the coseismic displacement at each GPS station. This ratio approximates the moment ratio between postseismic and coseismic terms.

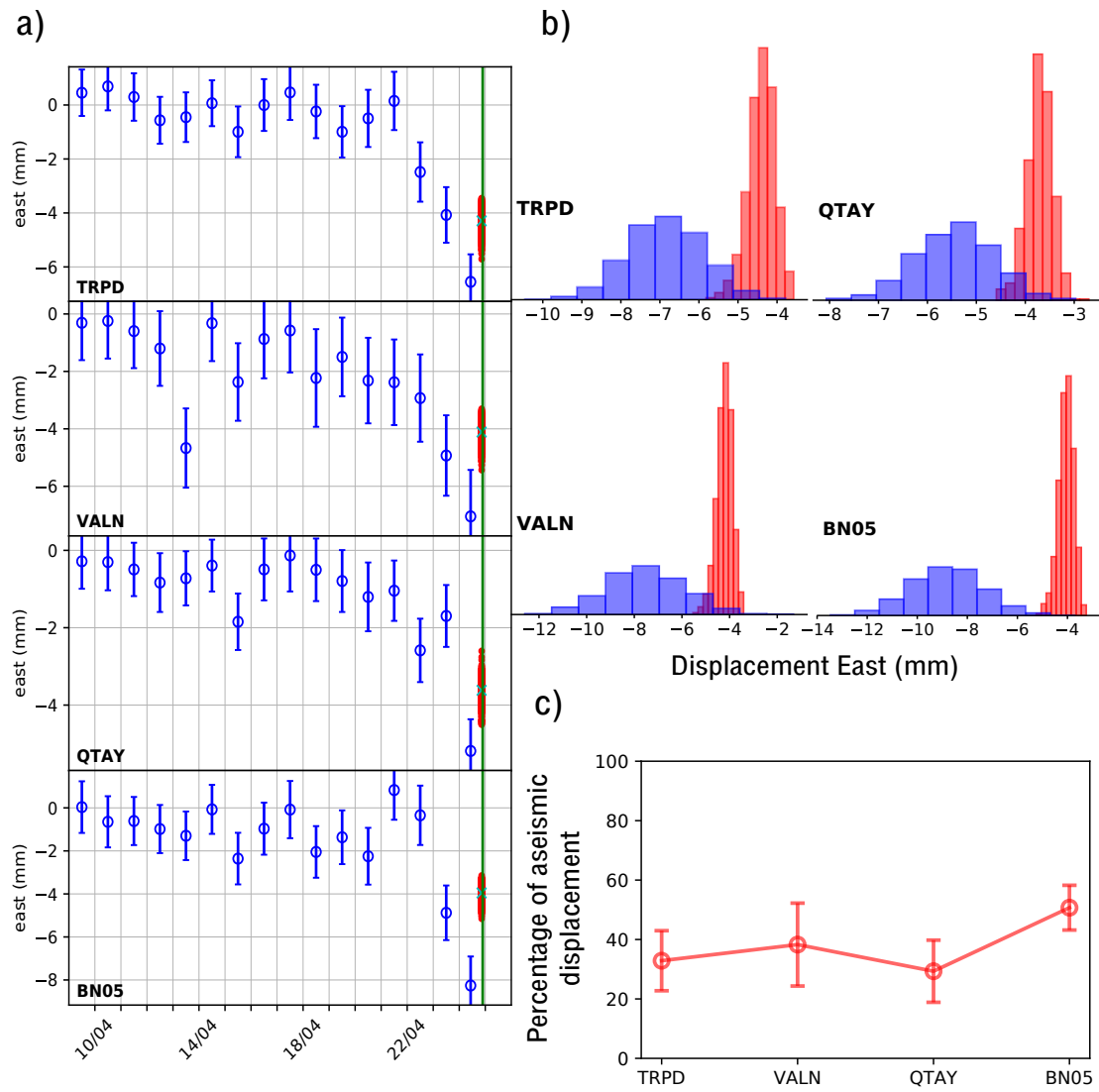


Figure A.12: Same as Figure 4 of main text but with the quick postseismic contribution produced by the largest foreshock.

Table A.1: Bandpass filter corner frequencies used for CMT inversion

Magnitude	Low Corner Freq (Hz)	High Corner Freq (Hz)
< 4.5	0.02	0.08
> 4.5	0.015	0.06
6.0	0.01	0.04

Table A.2: CMT solutions of our catalog.

Date	Time	Lon °	Lat °	Depth km	M0 N·m	Mw	Mrr N·m	Mtt N·m	Mpp N·m	Mrt N·m	Mrp N·m	Mtp N·m
2017-04-15	01:50:23	-70.85	-31.93	35.5	3.56e+14	3.63	-1.49e+20	-8.60e+20	1.01e+21	-1.82e+20	-1.83e+21	2.927e+21
2017-04-22	22:46:44	-71.96	-33.14	17.5	2.21e+16	4.83	1.76e+23	-1.58e+22	-1.60e+23	-2.78e+22	-1.41e+23	3.324e+21
2017-04-22	23:57:13	-72.03	-33.05	21.5	2.10e+15	4.15	1.28e+22	-1.07e+21	-1.17e+22	-8.45e+20	-1.70e+22	9.225e+20
2017-04-23	01:49:12	-72.06	-33.03	22.5	8.47e+15	4.55	5.58e+22	2.57e+21	-5.83e+22	-5.42e+21	-6.24e+22	9.259e+20
2017-04-23	02:36:06	-72.10	-33.03	19.5	1.16e+18	6.0	7.45e+24	-3.96e+23	-7.05e+24	4.10e+23	-9.06e+24	-5.981e+22
2017-04-23	02:43:18	-71.89	-33.05	21.5	1.76e+16	4.76	7.84e+22	2.41e+22	-1.03e+23	-1.86e+22	-1.44e+23	-4.994e+22
2017-04-23	02:52:38	-72.00	-33.05	25.5	8.02e+15	4.54	6.41e+22	-5.19e+20	-6.36e+22	1.29e+21	-4.66e+22	-1.311e+22
2017-04-23	03:00:12	-71.97	-32.86	14.5	5.04e+15	4.40	3.97e+22	-7.83e+21	-3.19e+22	-9.10e+21	-3.43e+22	4.470e+21
2017-04-23	03:02:17	-72.02	-33.07	26.5	8.48e+15	4.55	7.48e+22	-5.13e+21	-6.97e+22	6.45e+21	-4.39e+22	-2.778e+21
2017-04-23	12:52:15	-71.99	-33.07	26.5	5.42e+14	3.76	3.07e+21	2.78e+20	-3.34e+21	4.33e+20	-4.30e+21	-6.063e+20
2017-04-23	16:12:54	-71.96	-32.99	25.5	1.93e+15	4.12	1.12e+22	-2.14e+21	-9.07e+21	-7.36e+20	-1.63e+22	-9.098e+20
2017-04-23	19:40:10	-72.16	-33.05	21.5	2.10e+17	5.5	1.69e+24	-1.06e+23	-1.59e+24	5.75e+22	-1.31e+24	8.445e+22
2017-04-23	20:30:50	-72.10	-33.06	30.5	1.50e+15	4.05	5.58e+21	1.06e+22	-1.62e+22	2.95e+21	-5.86e+21	-3.027e+20
2017-04-24	01:19:42	-72.04	-33.11	22.5	1.31e+15	4.01	6.16e+21	9.72e+20	-7.14e+21	4.68e+20	-1.12e+22	-1.181e+21
2017-04-24	03:50:50	-72.14	-33.09	24.5	4.53e+15	4.37	3.42e+22	-3.71e+21	-3.05e+22	3.65e+21	-3.11e+22	4.655e+21
2017-04-24	03:54:11	-72.05	-33.10	21.5	7.87e+15	4.53	5.58e+22	-2.75e+21	-5.30e+22	8.92e+21	-5.55e+22	-8.387e+21
2017-04-24	06:54:36	-72.06	-33.11	23.5	7.69e+14	3.86	4.85e+21	-7.75e+20	-4.07e+21	1.17e+21	-6.13e+21	4.638e+20
2017-04-24	13:17:02	-71.93	-33.00	28.5	5.03e+14	3.73	2.19e+21	1.04e+21	-3.23e+21	-7.60e+18	-4.09e+21	-1.127e+21
2017-04-24	23:54:45	-71.93	-33.29	35.5	1.43e+16	4.70	5.65e+22	3.38e+22	-9.04e+22	2.77e+22	-1.16e+23	-1.953e+22
2017-04-25	00:17:36	-72.04	-33.17	20.5	7.58e+15	4.52	6.05e+22	-5.41e+21	-5.51e+22	-5.64e+21	-4.85e+22	5.282e+21

Continued on next page

Table A.2 – Continued from previous page

Date	Time	Lon °	Lat °	Depth km	M0 N·m	Mw	Mrr N·m	Mtt N·m	Mpp N·m	Mrt N·m	Mrp N·m	Mtp N·m
2017-04-25	01:33:15	-72.04	-33.16	22.5	1.56e+16	4.73	1.27e+23	-3.88e+21	-1.23e+23	1.73e+22	-9.06e+22	6.894e+21
2017-04-25	01:43:03	-72.09	-33.16	22.5	6.78e+16	5.15	5.20e+23	-3.77e+22	-4.82e+23	2.10e+22	-4.56e+23	5.773e+21
2017-04-25	01:54:30	-72.11	-33.10	22.5	1.45e+15	4.04	2.60e+21	2.37e+21	-4.97e+21	8.85e+20	-1.22e+22	-6.659e+21
2017-04-25	02:33:05	-71.89	-33.00	32.5	9.88e+14	3.93	8.24e+21	-2.88e+21	-5.36e+21	1.11e+21	-7.10e+21	-3.851e+20
2017-04-25	03:02:23	-72.08	-33.16	23.5	9.33e+15	4.58	7.71e+22	-1.13e+22	-6.58e+22	8.15e+21	-5.93e+22	3.680e+21
2017-04-25	05:56:26	-72.28	-33.03	17.5	2.43e+15	4.19	2.26e+22	-5.64e+21	-1.70e+22	-6.61e+19	-1.27e+22	4.963e+21
2017-04-25	06:34:15	-71.93	-32.97	25.5	4.88e+14	3.73	3.60e+21	-5.02e+20	-3.10e+21	-6.10e+20	-3.50e+21	4.637e+19
2017-04-25	08:15:17	-71.98	-32.97	24.5	9.43e+14	3.92	5.98e+21	-5.54e+20	-5.43e+21	1.41e+20	-7.48e+21	-6.557e+20
2017-04-25	08:29:06	-72.09	-33.15	19.5	1.21e+15	3.99	8.03e+21	7.54e+20	-8.78e+21	3.61e+20	-8.67e+21	-1.002e+20
2017-04-25	09:33:31	-72.00	-33.10	27.5	3.85e+15	4.32	2.18e+22	-3.06e+21	-1.87e+22	5.88e+21	-3.20e+22	-3.549e+21
2017-04-25	10:20:23	-72.11	-32.92	21.5	1.95e+15	4.13	8.25e+21	-2.08e+20	-8.04e+21	-1.85e+21	-1.76e+22	-2.089e+20
2017-04-25	10:24:35	-72.14	-32.90	22.5	2.28e+15	4.17	1.90e+22	-2.81e+21	-1.62e+22	-1.29e+21	-1.43e+22	-2.237e+21
2017-04-25	11:22:02	-72.20	-33.03	19.5	1.03e+15	3.94	8.45e+21	-1.21e+21	-7.24e+21	3.36e+19	-6.50e+21	1.057e+21
2017-04-25	11:24:09	-72.27	-33.12	19.5	1.70e+15	4.09	1.50e+22	-2.19e+21	-1.28e+22	3.35e+21	-9.24e+21	2.462e+20
2017-04-25	12:13:23	-72.21	-33.12	19.5	1.21e+16	4.65	1.02e+23	-1.01e+22	-9.21e+22	1.81e+22	-6.92e+22	2.311e+21
2017-04-25	12:37:37	-72.16	-33.05	21.5	1.31e+15	4.01	8.31e+21	-3.74e+20	-7.94e+21	1.08e+20	-1.02e+22	1.217e+21
2017-04-25	14:26:35	-72.10	-33.17	21.5	2.76e+15	4.23	1.34e+22	7.15e+20	-1.41e+22	2.13e+21	-2.37e+22	2.934e+21
2017-04-25	15:32:07	-72.21	-33.10	19.5	1.18e+15	3.98	1.15e+22	-2.05e+21	-9.41e+21	-5.21e+20	-4.93e+21	2.174e+21
2017-04-25	16:38:53	-72.18	-33.07	19.5	1.41e+15	4.03	9.02e+21	4.71e+20	-9.49e+21	4.63e+20	-1.06e+22	-5.471e+20
2017-04-25	16:48:36	-72.01	-33.31	24.5	1.99e+15	4.13	9.15e+21	6.87e+20	-9.84e+21	7.19e+21	-1.58e+22	1.966e+21
2017-04-25	20:57:54	-72.15	-33.13	19.5	1.16e+15	3.98	9.76e+21	-9.29e+20	-8.83e+21	1.11e+21	-6.90e+21	-3.074e+19

Continued on next page

Table A.2 – Continued from previous page

Date	Time	Lon °	Lat °	Depth km	M0 N·m	Mw	Mrr N·m	Mtt N·m	Mpp N·m	Mrt N·m	Mrp N·m	Mtp N·m
2017-04-25	21:03:13	-72.06	-33.12	17.5	8.67e+14	3.89	6.93e+21	-2.24e+21	-4.69e+21	1.96e+21	-6.05e+21	6.534e+20
2017-04-25	23:58:11	-71.98	-32.95	26.5	1.25e+15	4.00	1.04e+22	-1.85e+21	-8.51e+21	1.59e+20	-8.10e+21	1.225e+21
2017-04-26	00:43:00	-71.96	-32.94	26.5	4.63e+14	3.71	1.77e+21	2.60e+20	-2.03e+21	-4.96e+20	-4.19e+21	-5.287e+19
2017-04-26	10:05:34	-72.21	-33.14	21.5	4.05e+15	4.34	3.21e+22	-3.83e+21	-2.82e+22	6.22e+21	-2.64e+22	1.765e+20
2017-04-26	14:45:55	-71.85	-33.29	27.5	4.49e+15	4.37	3.33e+22	-2.38e+20	-3.31e+22	3.36e+21	-3.00e+22	1.143e+21
2017-04-26	15:14:01	-71.99	-33.30	31.5	4.64e+15	4.38	3.80e+22	7.82e+20	-3.88e+22	9.17e+21	-2.42e+22	2.401e+21
2017-04-27	01:55:05	-71.81	-33.13	32.5	1.05e+15	3.95	9.92e+21	-3.26e+20	-9.59e+21	9.98e+20	-3.61e+21	1.043e+21
2017-04-27	05:09:22	-71.90	-33.31	27.5	4.06e+16	5.01	3.31e+23	1.23e+22	-3.43e+23	8.57e+21	-2.13e+23	7.488e+22
2017-04-27	06:55:45	-71.88	-33.29	25.5	1.86e+15	4.11	1.23e+22	-7.08e+20	-1.16e+22	1.08e+21	-1.42e+22	-1.304e+20
2017-04-27	08:24:41	-71.89	-33.28	28.5	1.34e+16	4.68	1.04e+23	7.86e+21	-1.12e+23	6.07e+21	-7.88e+22	3.411e+21
2017-04-27	08:46:34	-72.06	-33.10	23.5	1.70e+15	4.09	8.60e+21	-5.83e+20	-8.01e+21	1.44e+21	-1.47e+22	-4.253e+20
2017-04-27	21:17:33	-71.92	-33.30	29.5	8.93e+14	3.90	5.29e+21	1.21e+21	-6.50e+21	2.02e+20	-6.69e+21	-4.765e+20
2017-04-28	15:30:05	-72.02	-33.26	23.5	7.43e+17	5.85	5.32e+24	-2.17e+23	-5.10e+24	1.60e+24	-5.03e+24	5.323e+23
2017-04-28	15:33:30	-71.96	-33.32	23.5	2.32e+16	4.84	1.72e+23	-1.56e+22	-1.57e+23	4.19e+22	-1.58e+23	-1.243e+22
2017-04-28	15:40:24	-71.91	-33.26	28.5	8.66e+15	4.56	4.40e+22	1.25e+22	-5.65e+22	4.84e+22	-4.91e+22	-2.064e+22
2017-04-28	15:49:44	-71.91	-33.31	26.5	2.89e+16	4.91	1.74e+23	2.36e+22	-1.98e+23	3.56e+22	-2.18e+23	1.129e+22
2017-04-28	15:58:34	-72.05	-33.26	27.5	1.32e+17	5.35	9.24e+23	-2.51e+22	-8.98e+23	3.88e+23	-8.39e+23	2.300e+23
2017-04-28	16:05:57	-71.66	-33.17	29.5	5.06e+17	5.74	3.37e+24	-4.38e+23	-2.93e+24	-6.71e+23	-3.88e+24	5.465e+23
2017-04-28	17:09:40	-71.93	-33.25	20.5	7.87e+15	4.53	2.26e+22	1.64e+22	-3.91e+22	2.52e+22	-6.67e+22	-3.073e+21
2017-04-28	17:21:48	-72.06	-33.23	24.5	3.25e+15	4.27	1.51e+22	2.05e+21	-1.72e+22	9.80e+21	-2.64e+22	-6.374e+19
2017-04-28	17:38:09	-71.93	-33.35	29.5	4.21e+15	4.35	-1.54e+22	-8.40e+21	2.38e+22	2.62e+22	-8.34e+21	-2.420e+22

Continued on next page

Table A.2 – Continued from previous page

Date	Time	Lon °	Lat °	Depth km	M0 N·m	Mw	Mrr N·m	Mtt N·m	Mpp N·m	Mrt N·m	Mrp N·m	Mtp N·m
2017-04-28	17:41:50	-71.98	-33.30	25.5	1.11e+17	5.30	7.98e+23	-2.82e+22	-7.70e+23	2.17e+21	-7.79e+23	-3.052e+22
2017-04-28	17:57:07	-71.94	-33.36	30.5	2.57e+15	4.21	1.60e+22	1.97e+21	-1.79e+22	-3.88e+21	-1.88e+22	3.429e+20
2017-04-28	18:28:23	-71.96	-33.28	29.5	2.68e+15	4.22	1.30e+22	9.66e+20	-1.39e+22	3.90e+21	-2.28e+22	-1.247e+21
2017-04-29	01:06:23	-72.02	-33.25	20.5	4.87e+14	3.73	1.49e+21	1.13e+21	-2.63e+21	2.44e+21	-3.40e+21	-1.148e+21
2017-04-29	01:08:35	-71.99	-33.37	27.5	5.34e+15	4.42	3.22e+22	2.74e+21	-3.49e+22	-3.80e+21	-4.03e+22	-9.976e+21
2017-04-29	01:37:16	-72.07	-33.23	25.5	5.16e+15	4.41	3.27e+22	4.71e+21	-3.74e+22	2.14e+22	-3.01e+22	7.211e+21
2017-04-29	01:46:00	-72.02	-33.22	24.5	5.41e+16	5.09	4.98e+23	-4.40e+22	-4.54e+23	8.74e+22	-2.43e+23	1.079e+22
2017-04-29	02:36:24	-71.73	-33.12	32.5	7.30e+14	3.84	7.48e+21	-1.76e+21	-5.71e+21	-7.30e+20	2.43e+21	1.489e+21
2017-04-29	04:50:34	-72.07	-33.24	22.5	7.66e+14	3.86	4.21e+21	-9.67e+19	-4.11e+21	3.07e+21	-5.62e+21	6.726e+20
2017-04-29	08:30:43	-72.05	-33.25	24.5	2.92e+15	4.24	8.79e+21	7.25e+21	-1.60e+22	1.38e+22	-2.17e+22	-1.908e+20
2017-04-29	08:54:02	-72.03	-33.24	22.5	2.54e+15	4.20	6.44e+21	4.24e+21	-1.07e+22	8.88e+21	-2.20e+22	1.113e+20
2017-04-30	17:55:34	-72.02	-33.37	26.5	8.74e+14	3.89	5.89e+21	-2.22e+20	-5.67e+21	-6.18e+20	-5.07e+21	-4.335e+21
2017-04-30	21:49:02	-72.26	-32.97	22.5	1.04e+15	3.95	1.05e+22	-1.74e+21	-8.73e+21	4.23e+20	-4.01e+21	-3.070e+20
2017-05-01	23:38:45	-72.21	-33.01	18.5	1.79e+15	4.10	1.49e+22	-1.38e+21	-1.35e+22	1.76e+21	-1.07e+22	-1.596e+20
2017-05-03	16:50:22	-72.26	-33.08	21.5	5.62e+15	4.43	5.74e+22	-1.11e+22	-4.63e+22	2.43e+21	-2.16e+22	1.035e+21
2017-05-04	14:31:43	-72.15	-33.09	22.5	5.62e+14	3.77	4.83e+21	-2.63e+20	-4.57e+21	6.57e+20	-2.99e+21	3.640e+20
2017-05-05	01:34:46	-72.24	-32.90	18.5	1.04e+15	3.95	6.92e+21	5.61e+20	-7.48e+21	8.32e+20	-7.45e+21	9.744e+20
2017-05-05	04:42:01	-71.99	-32.82	22.5	4.92e+14	3.73	2.14e+21	8.61e+19	-2.23e+21	9.84e+20	-4.22e+21	8.527e+20
2017-05-05	10:48:21	-72.18	-32.94	16.5	6.36e+14	3.80	5.53e+21	-1.53e+20	-5.37e+21	1.07e+21	-3.11e+21	-1.131e+20
2017-05-09	09:22:31	-72.27	-33.75	21.5	7.49e+14	3.85	5.79e+21	1.88e+20	-5.98e+21	-4.60e+19	-4.54e+21	9.364e+20
2017-05-09	11:28:32	-72.25	-33.05	19.5	4.44e+14	3.70	4.06e+21	-9.09e+20	-3.15e+21	1.48e+19	-2.55e+21	4.498e+20

Continued on next page

Table A.2 – Continued from previous page

Date	Time	Lon °	Lat °	Depth km	M0 N·m	Mw	Mrr N·m	Mtt N·m	Mpp N·m	Mrt N·m	Mrp N·m	Mtp N·m
2017-05-13	16:54:46	-72.06	-32.94	26.5	6.48e+16	5.14	5.42e+23	-3.86e+22	-5.04e+23	-5.74e+22	-3.78e+23	-6.968e+21
2017-05-16	02:16:29	-72.21	-32.96	16.5	1.99e+15	4.13	-2.93e+21	1.90e+21	1.03e+21	3.93e+21	-1.01e+22	-1.707e+22
2017-05-16	04:36:15	-71.65	-32.00	27.5	4.20e+15	4.35	1.60e+21	9.87e+20	-2.59e+21	2.57e+20	-4.18e+22	3.070e+21
2017-05-18	00:44:56	-72.32	-33.03	17.5	2.20e+15	4.16	2.37e+22	-3.86e+21	-1.98e+22	7.27e+20	-2.60e+21	1.786e+21
2017-05-23	01:05:12	-72.16	-32.94	19.5	1.61e+15	4.07	6.78e+21	-7.61e+20	-6.02e+21	9.26e+21	1.18e+22	1.183e+21
2017-05-29	20:39:36	-71.86	-32.16	26.5	5.78e+14	3.77	-2.65e+21	2.71e+21	-6.71e+19	-1.05e+21	-5.11e+21	1.094e+21
2017-05-30	06:45:58	-72.19	-32.98	18.5	8.59e+14	3.89	7.53e+21	-1.20e+21	-6.34e+21	1.74e+21	-4.68e+21	7.912e+20

Supporting Information for Revisiting the 2015 Mw=8.3 Illapel earthquake. From kinematic rupture inversion to rupture dynamics.

Contents of this file

1. Text S1 to S2
2. Figures S1 to S10

Text S1. Data processing

InSAR images. InSAR data consist of a descending pair (20150824-20150917) and an ascending pair (20150826-20150919) acquired by the Sentinel-1A satellite operated by the European Space Agency under the Copernicus program. We used ISCE software [Rosen et al., 2012] to process the data, and Snaphu to unwrap the interferograms [Chen and Zebker, 2002]. We used SRTM DEM [Farr et al., 2007] to coregister the InSAR pairs, remove topographic phase and geocode the interferograms. To improve computational efficiency, we use a resolution-based resampling of InSAR observations [Lohman and Simons, 2005]. In the resampling process, displacement measurements are averaged over windows of sizes ranging from 0.6 to 10 km.

Tsunami data. We use seven tide gauges (buca1, chnr1, juan1, meji1, papo1, talt1,

toco1) and seven sea-bottom pressure sensor records (D32401, D32402, D32411, D32412, D43412, D43413, D51407) at NOAA DART (Deep-ocean Assessment and Reporting of Tsunamis) stations [Mungov et al., 2013]. We remove tidal signals at each station by fitting and subtracting a sinusoidal function over a time window of 25 hr before and 20 hr after the earthquake initiation time. We then lowpass-filter the data at 240 sec, with one sample per minute. For the inversion, we only use the first 30 min time-window after tsunami arrival.

The tsunami Green's functions are computed using COMCOT [Cornell Multi-grid Coupled Tsunami Model code Liu et al., 1995] with the GEBCO (General Bathymetric Chart of the Oceans) 30-sec bathymetry (The GEBCO_2014 Grid, version 20141103, <http://www.gebco.net>). We downsample the 30-sec bathymetry data to a 0.4 min and 1 min grid size for near-field (D32401, D32402, D32411, and tide gauges) and far-field (other stations) simulations, respectively. We compute seafloor deformation for each slip source using a modified 1D elastic structure, where we assume that the shallowest layer of 2.6 km is ocean water. We apply a spatial filter when predicting seafloor deformation for unit slip, as a way to approximate the effect of water layer attenuation [Geist and Dmowska, 1999, Kajiura, 1981]. To account for long-period dispersion [Watada, 2013] that is not incorporated in COMCOT, each simulated tsunami waveform is corrected with a frequency-dependent shift in arrival times calculated along ray paths (near-field stations) or great-circle paths (far-field stations), following the method in Jiang and Simons [2016].

Text S2. Observation measurement uncertainties.

The observed uncertainties are represented by the matrix C_d . In the case of GPS data, we used the associated standard errors and incorporate them in C_d . For the InSAR images, we use a two steps approach to calculate the corresponding C_d . First, we compute residuals from a preliminary slip inversion, and from them, we compute an empirical covariance function as a function of the distance between observation points. Secondly, we estimate the best-fit exponential function of the covariance to build the full data covariance Jolivet et al. [2012]. Given the correlation between InSAR images pixels, The obtained exponential function is:

$$C(i, j) = \sigma^2 e^{-\frac{\|i, j\|_2}{\lambda}}, \quad (\text{B.1})$$

where σ and λ are 0.00605 m 7.75 km respectively.

For the kinematic data, we compute the observational uncertainty in two steps. First, we use an *a priori* solution to compute synthetic waveforms and we obtain

the residual between synthetic and observed data. Then, based on residual length, we calculate an exponential correlation function with a length of 10% and 6% for HRGPS and strong motion data respectively. From this exponential correlation function, we compute the 20% of relative error and we add it to the standard errors calculated from the waveform.

Data Set S1.

Movie S1.

Audio S1.

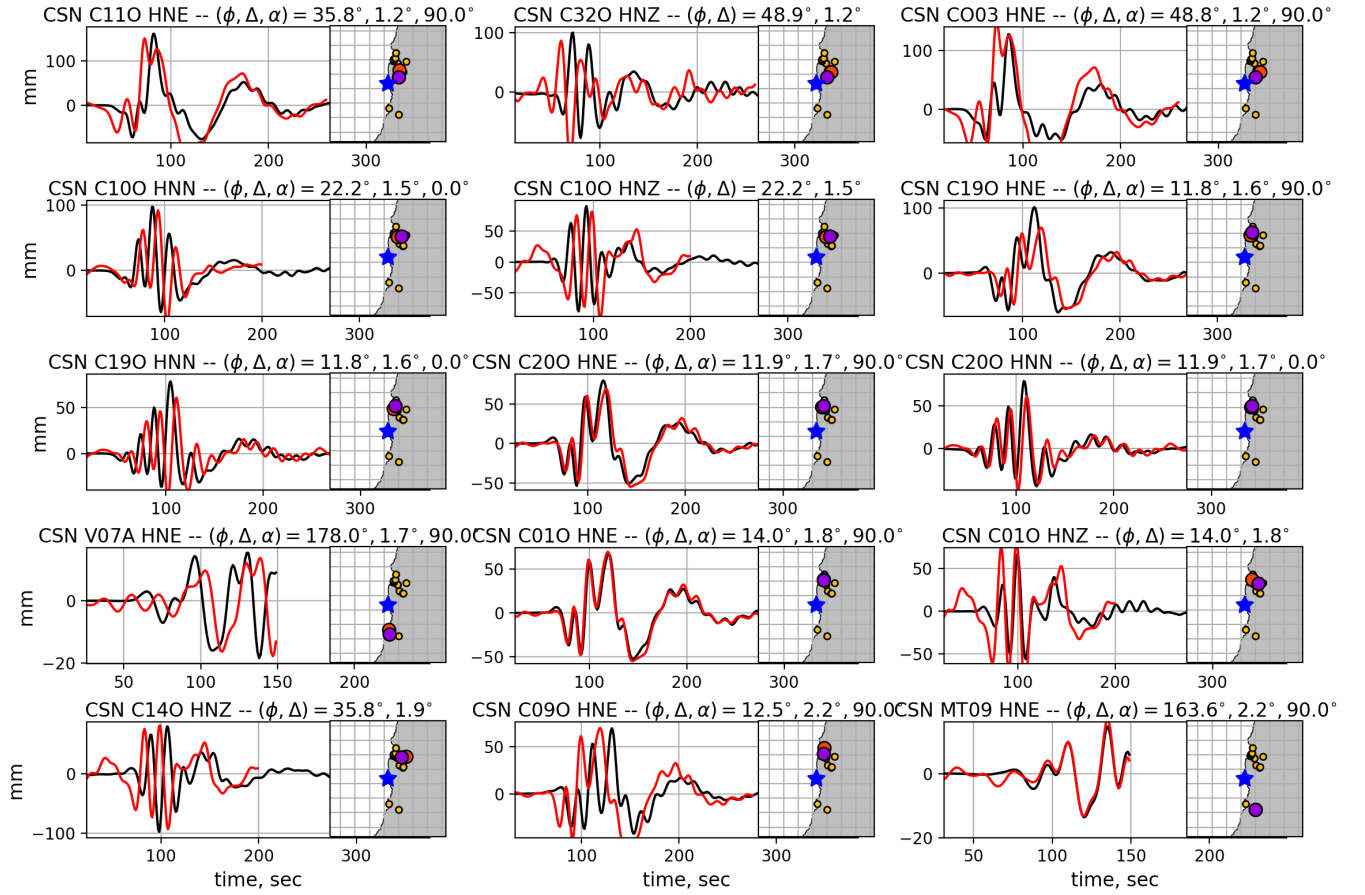


Figure B.1: Comparison between displacements corrected from ground motion records and HRGPS displacements. Red and black waveforms represent HRGPS and strong motion respectively. On the maps, the blue star represents the CSN hypocenter while circles indicate station location (orange for the strong motion station depicted, yellow for the ensemble of strong motion stations, and purple for HRGPS stations). Variation in waveforms is mostly due to differences in colocation.

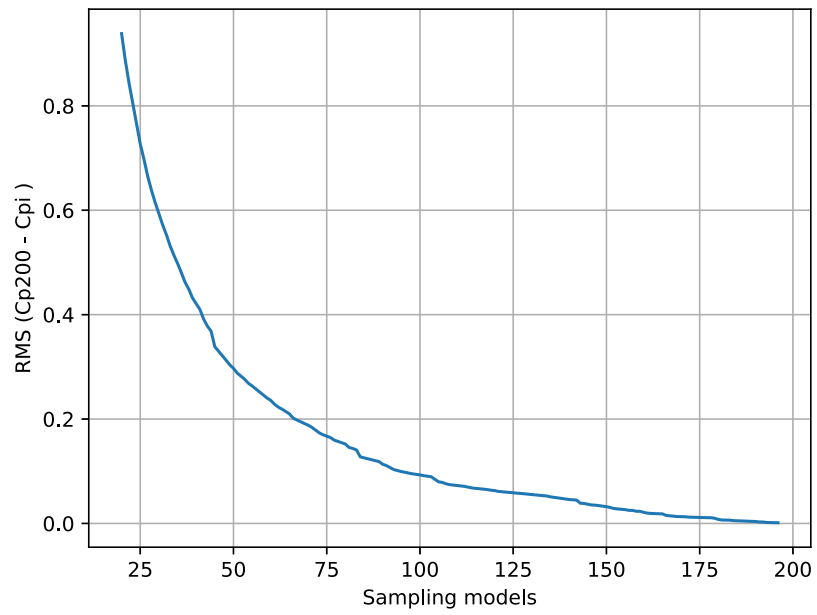


Figure B.2: Difference between final empirical covariance matrix and intermediate covariance matrix calculated using a number of samples.

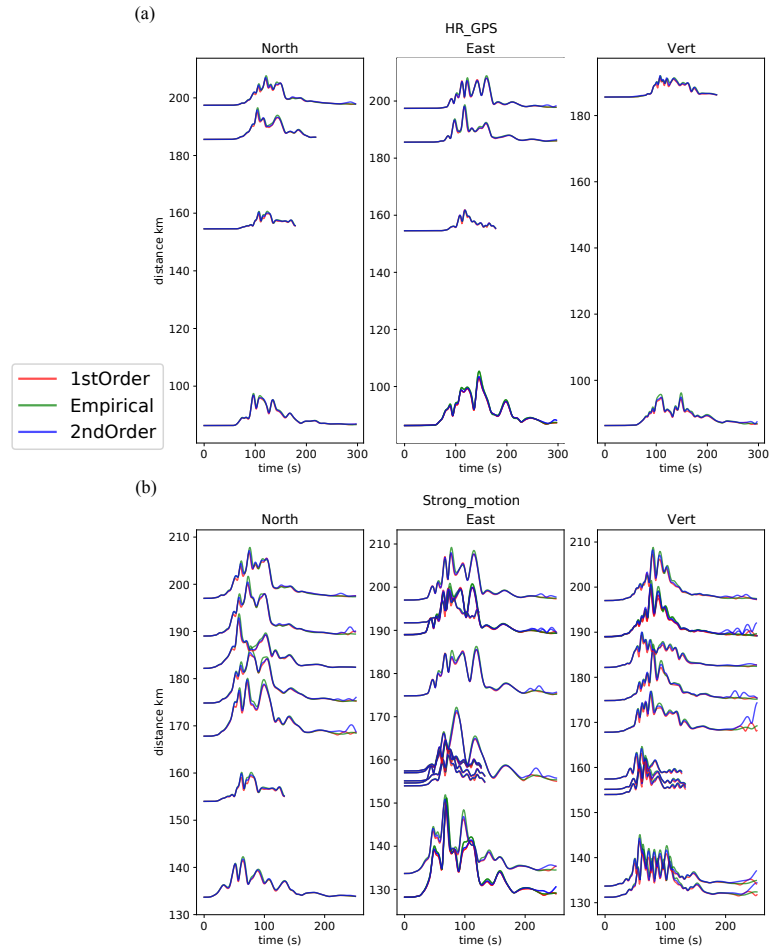


Figure B.3: Covariance matrix comparison for HRGPS records (a) and Strong Motion stations (b) at hypocenter distances greater < 200 km. The green line represents the diagonal of the empirical covariance matrix (i.e., the matrix created from an ensemble of models). The red and blue line represents the diagonal of the matrix calculated using the 1st and 2nd order approximation approach.

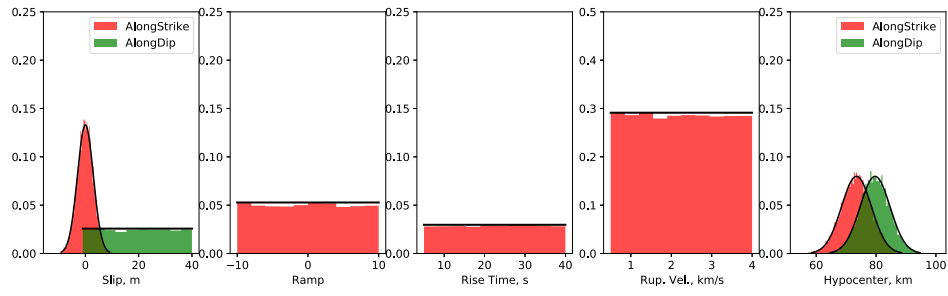


Figure B.4: *A priori* probability density function (PDF) distributions. *A priori* PDFs are shown for the inverted parameters. We include nuisance parameters to include a linear ramp to account for InSAR orbital errors and translation parameters for each GPS data set.

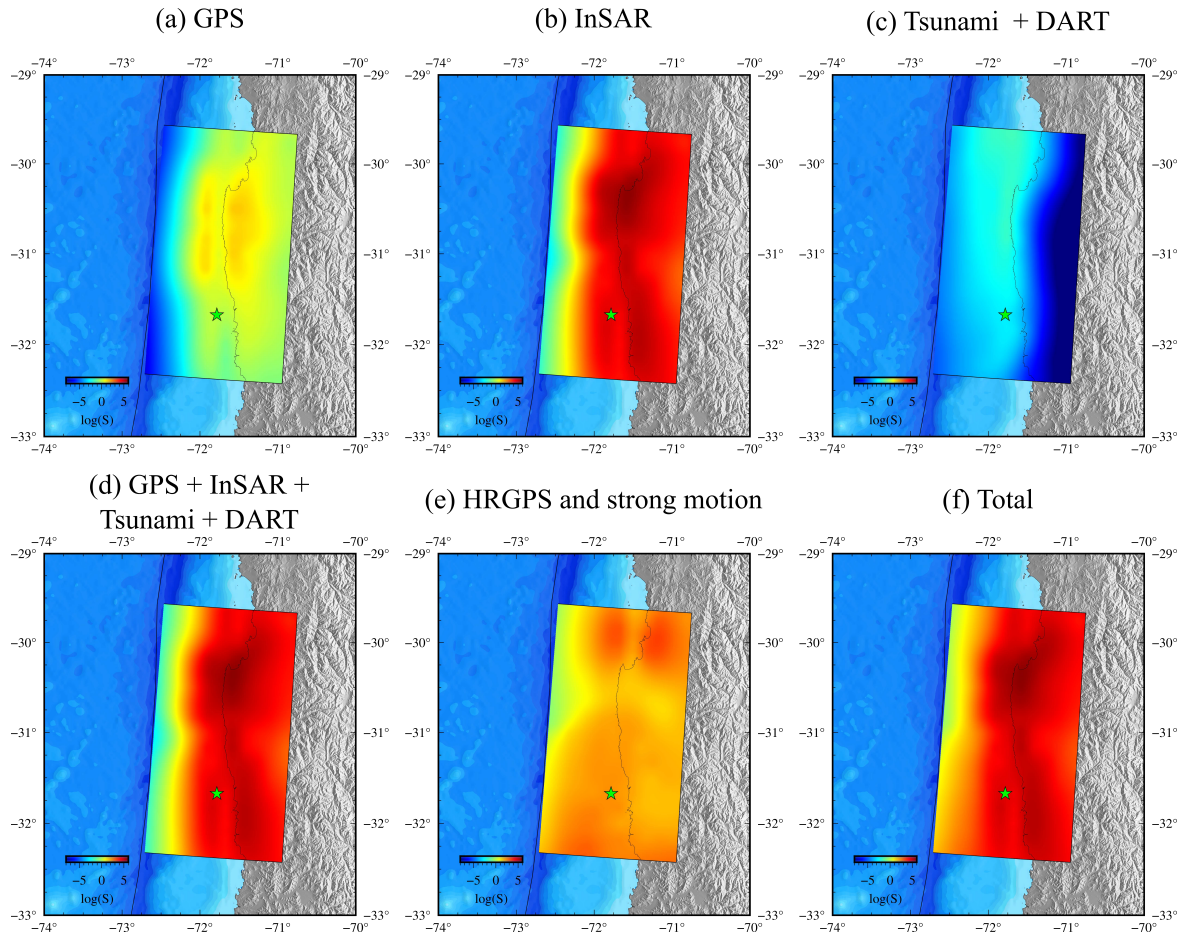


Figure B.5: Sensitivity for each data set. The sensitivity is shown for (a) GPS, (b) InSAR, (c) Tsunami and dart data, (d) tsunami, InSAR, GPS and tide-gauges, (e) High rate GPS and strong motion, and (f) The ensemble of data sets.

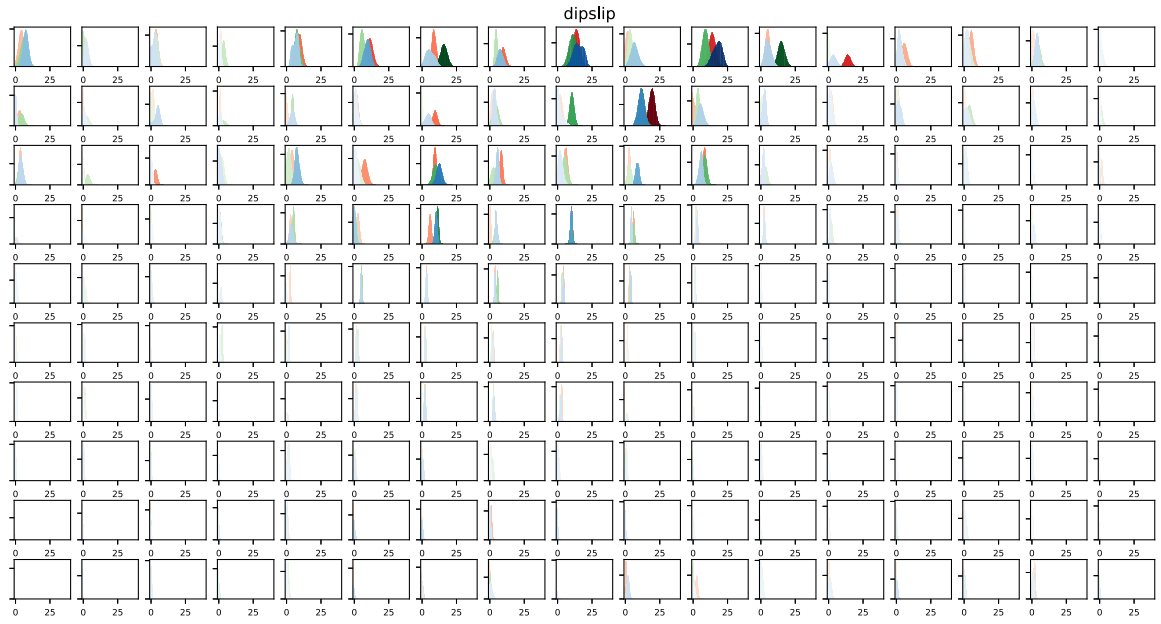


Figure B.6: Posterior mean distributions for the dip slip parameters. The colors represent the empirical C_p matrix (green), the first order approximation matrix (red), and the second order approximation matrix (blue). The strength of the colors are proportional to the magnitude of the slip.

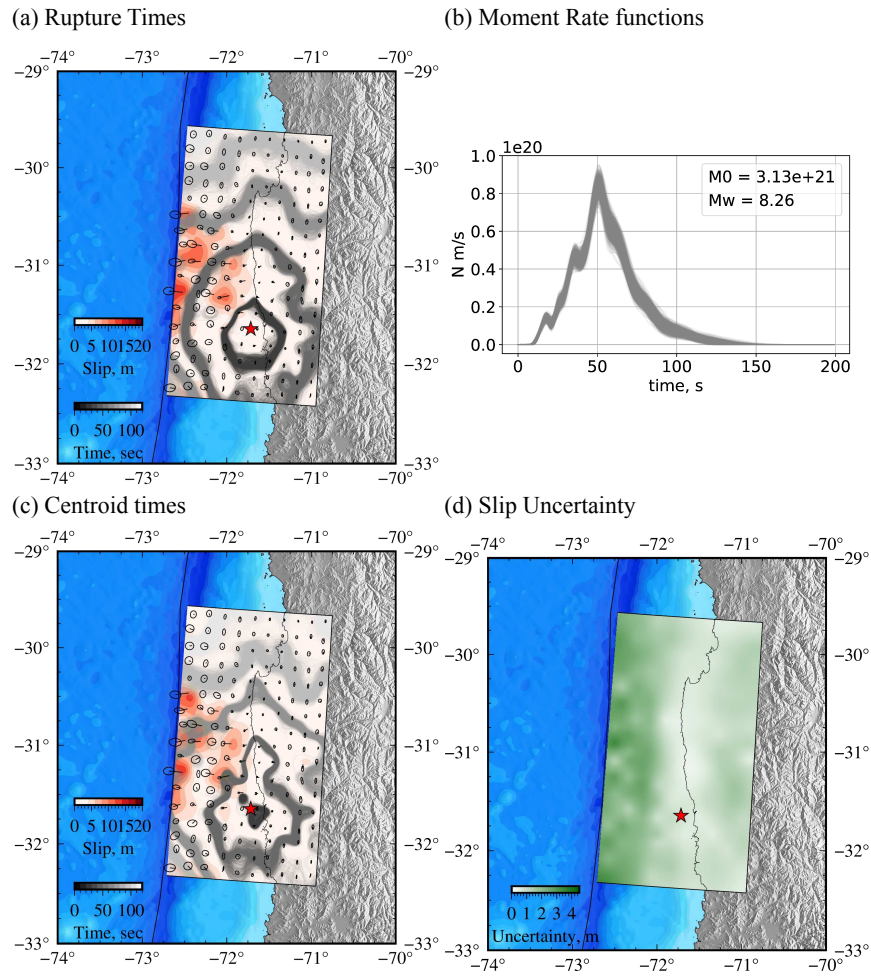


Figure B.7: Impact of using an empirical covariance matrix C_p in slip inversion. (a) Posterior mean coseismic slip model, arrows represent the slip directions and the ellipses its corresponding uncertainty. Contours show stochastic rupture fronts samples from the *a posteriori* distribution. (b) Stochastic moment rate functions. (c) Posterior mean coseismic slip model with contours that represent stochastic centroid time fronts samples from the *a posteriori* distribution. (d) Uncertainty of the ensemble of coseismic slip models. The red star in the figures represents the inverted hypocenter location.

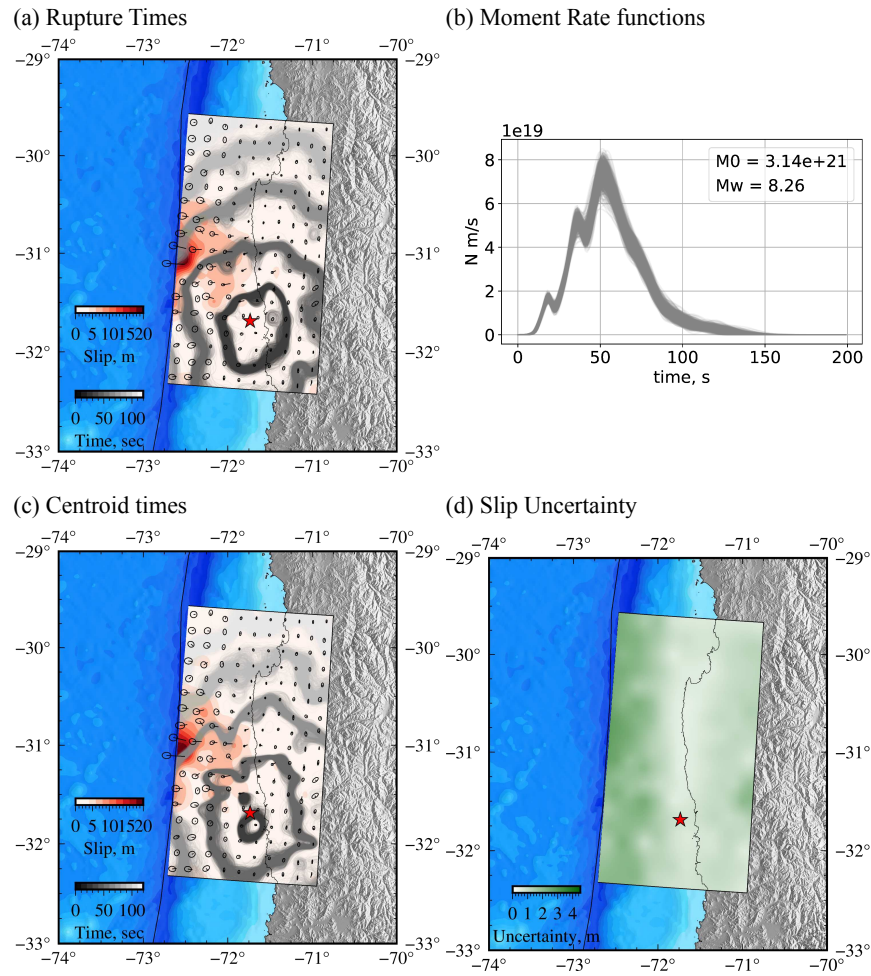


Figure B.8: Impact of using a 1st order approximation C_p in slip inversion. (a) Posterior mean coseismic slip model, arrows represent the slip directions and the ellipses its corresponding uncertainty. Contours show stochastic rupture fronts samples from the *a posteriori* distribution. (b) Stochastic moment rate functions. (c) Posterior mean coseismic slip model with contours that represent stochastic centroid time fronts samples from the *a posteriori* distribution. (d) Uncertainty of the ensemble of coseismic slip models. The red star in the figures represents the inverted hypocenter location.

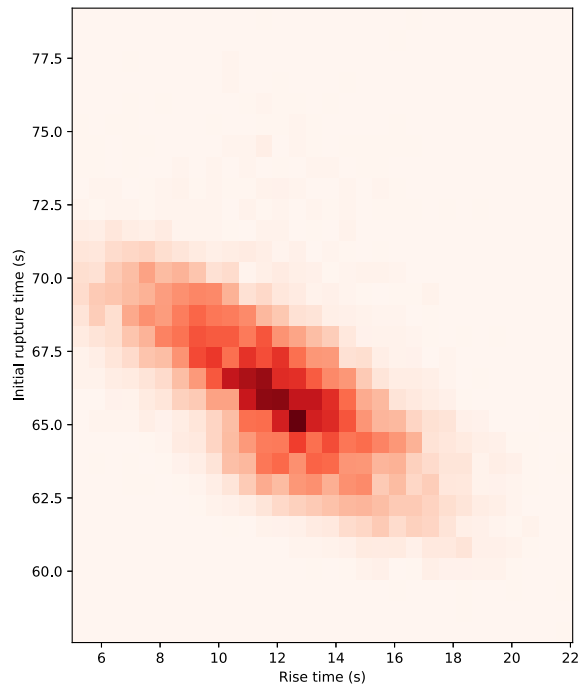
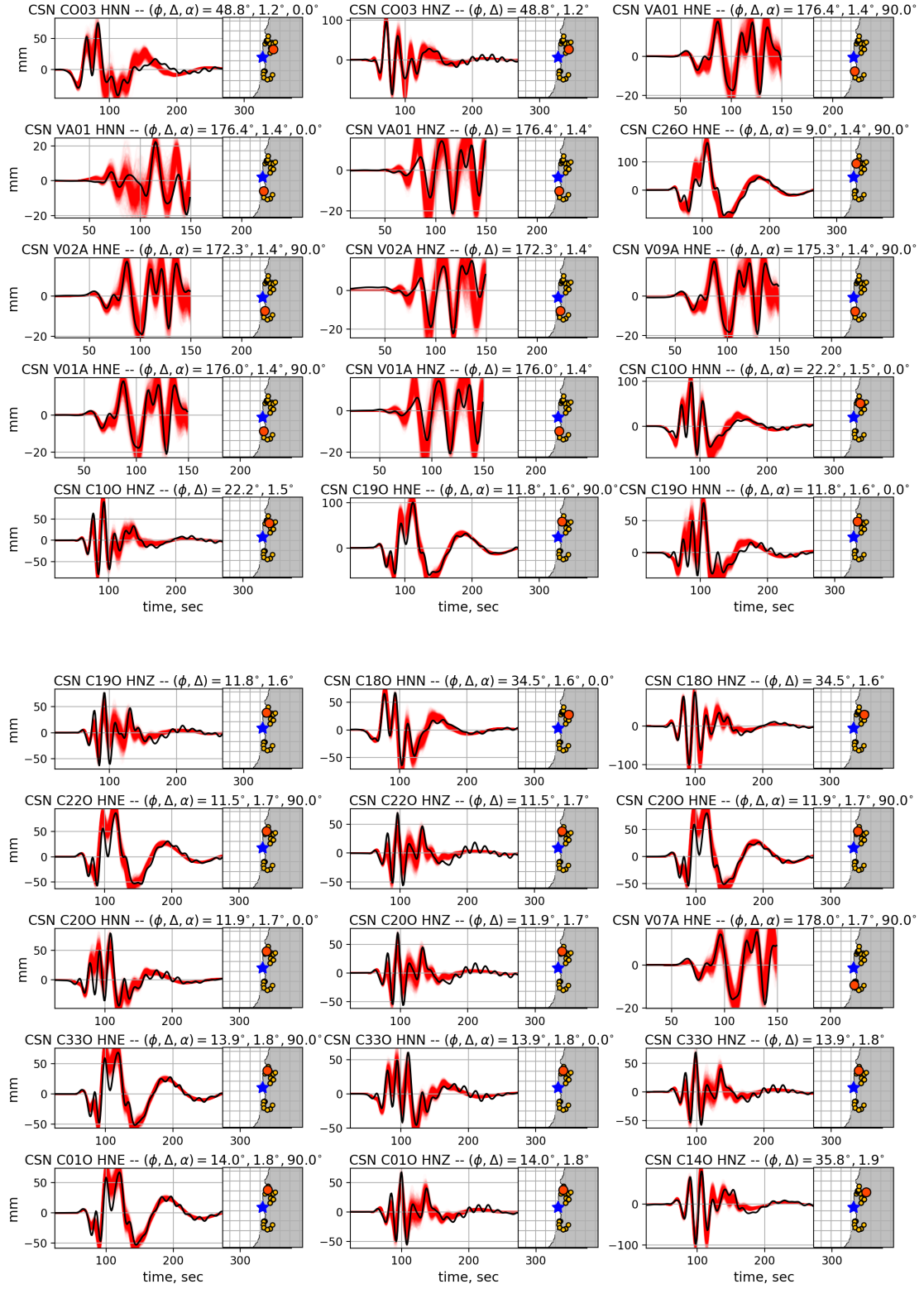


Figure B.9: Comparison between rupture and rise times for the patch with maximum slip.



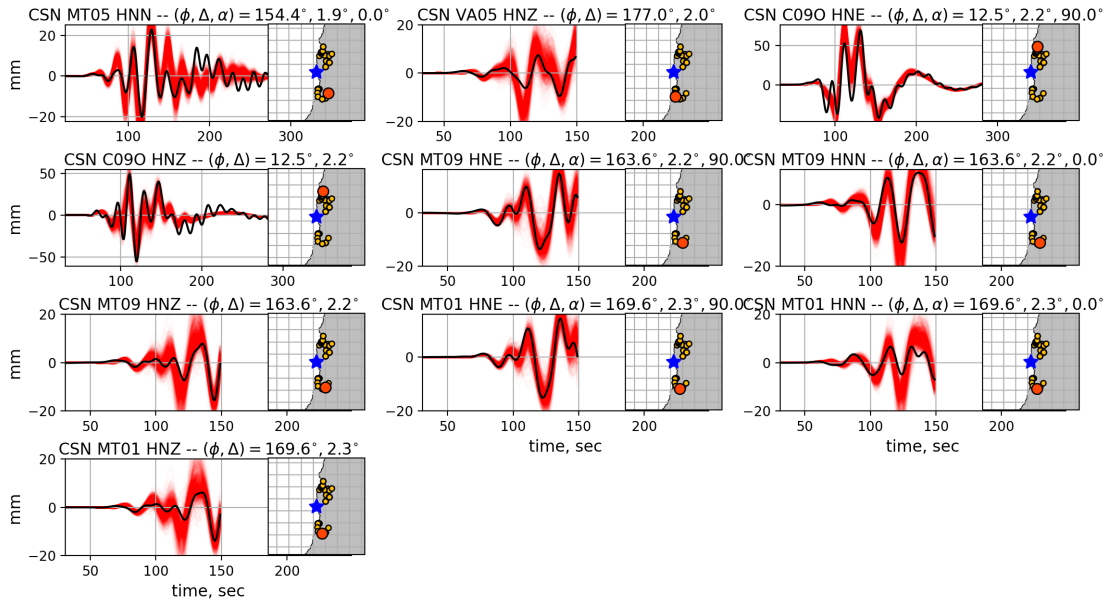


Figure B.10: Examples of comparisons between data (black) and stochastic predictions (red) for HRGPS and Strong Motion stations using a 2nd order approximation C_p . On the maps, the blue star represents the hypocenter while circles indicate station location (orange for the station depicted and yellow for the other stations).

List of Figures

1	The 2017 Valparaiso earthquake sequence. (a) Earthquake locations including foreshocks (blue circles), mainshock (green star), and aftershocks (white circles). The red colormap indicates the preslip distribution resulting from the inversion of GPS data. The black arrows show the cumulative observed GPS surface displacements (up to one hour before the mainshock). Orange dots indicate the seismicity distribution from 2017/01/01 until 2017/10/05 according to the microseismicity catalog obtained by S. Ruiz et al. (2017). (b) GPS Time-series in the vicinity of Valparaíso. The vertical red dashed line indicates approximate onset of the transient displacement visible on the timeseries. The cumulative number of earthquakes from S. Ruiz et al. (2017) is shown at the bottom of the figure. The purple star represents the largest $M_W = 6.0$ foreshock.	4
2	CMT solutions of the 2017 Valparaíso earthquake sequence and cumulative moment (a) CMT solutions of the 2017 Valparaíso earthquake sequence. Focal mechanisms are contoured in blue and black for foreshocks and aftershocks respectively. The size of beach balls scales with the moment magnitude. Color of the compressive quadrants represents the event depth. (b) Cumulative scalar seismic moment of the 2017 Valparaíso sequence. The mainshock scalar moment is not included in this figure. The red dashed line outlines the approximate onset of transient displacements visible on GPS time-series. The green line indicates the origin time.	5

LIST OF FIGURES

- 3 Slip during the Valparaíso foreshock sequence. a) Time series of GNSS data (blue) and stochastic foreshock-induced co-seismic displacement (gray). Red dots represent the average of stochastic co-seismic offsets. Green cross corresponds to the total foreshock displacement, including the contribution of earthquakes below the magnitude of completeness. b) Distributions of observed pre-seismic displacement and predicted cumulative co-seismic offsets caused by foreshocks. Blue histograms represent observations assuming Gaussian uncertainties from standard errors estimated at each station. Red histograms correspond to the posterior distribution of cumulative foreshock-induced co-seismic displacement. c) Percentage of aseismic displacement for each station. d) Average postseismic signal measured on stations TRPD, VALN, BN05 and QTAY. e) Slip inversion of pre-seismic GPS data. f) Slip inversion of GPS data after removing foreshock-induced displacement. Black and blue arrows are observed and predicted horizontal GPS displacements along with their ellipses (representing observational and prediction uncertainties, respectively). Colored circles are observed (outer circles) and predicted (inner circles) vertical displacements from GPS. 7
- 4 Covariance matrix comparison for HRGPS records (a) and Strong Motion stations (b). The green line represents the diagonal of the empirical covariance matrix (i.e., the matrix created from an ensemble of models). The red and blue line represents the diagonal of the matrix calculated using the 1st and 2nd order approximation approach. 9
- 5 Comparison of co-seismic slip distributions obtained using different prediction error covariances C_p . Red colors are the final slip distributions. Arrows represent the slip directions with their corresponding uncertainty. The red star is the inverted hypocenter location (empirical, 1st, and 2nd order approximation, respectively). The blue star is the CSN hypocenter, and the green star is the USGS hypocenter. . . 10
- 6 Impact of using a 2nd order approximation C_p in slip inversion. (a) Posterior mean coseismic slip model, arrows represent the slip directions and the ellipses its corresponding uncertainty. Contours show stochastic rupture fronts samples from the *a posteriori* distribution. (b) Stochastic moment rate functions. (c) Posterior mean coseismic slip model with contours that represent stochastic centroid time fronts samples from the *a posteriori* distribution. (d) Uncertainty of the ensemble of coseismic slip models. The red star in the figures represents the inverted hypocenter location. 11

- 7 Average breakdown energies (a) and average breakdown work (b) for the 2015 $M_W = 8.3$ Illapel earthquake and the 2014 $M_W = 8.1$ Iquique earthquake. For the breakdown energy, purple and red dots represent the average breakdown energies calculated in this study. For the breakdown work, green and red dots represent the average breakdown work calculated in this study. Cyan and purple dots represent the average breakdown work weighted by the corresponding slip. Blue dots represent the breakdown energies and breakdown work calculated by Tinti et al. [2005a] respectively. The dashed green line represents the scaling relationship from the same study while the dashed black line represents the scaling relationship is from Causse et al. [2014]. 13
- 8 La séquence du séisme de Valparaíso de 2017. (a) Localisations des séismes, y compris les pré-chocs (cercles bleus), le choc principal (étoile verte) et les répliques (cercles blancs). La carte de couleur rouge indique la distribution de glissement présismique résultant de l'inversion des données GPS. Les flèches noires montrent les déplacements GPS observés cumulés (jusqu'à une heure avant le choc principal). Les points orange indiquent la distribution de la sismicité du 2017/01/01 au 2017/10/05 selon le catalogue de microsismicité obtenu par S. Ruiz et al. (2017). (b) Séries temporelles GPS dans les environs de Valparaíso. La ligne verticale en pointillés rouges indique le début approximatif du déplacement transitoire visible sur la série temporelle. Le nombre cumulé de séismes de S. Ruiz et al. (2017) est indiqué en bas de la figure. L'étoile violette représente le plus grand pré-choc $M_W = 6.0$ 16
- 9 Solutions CMT de la séquence du séisme de Valparaíso de 2017 et moment cumulé. (a) Solutions CMT de la séquence du séisme de Valparaíso de 2017. Les mécanismes aux foyers sont délimités en bleu et en noir pour les pré-chocs et les répliques respectivement. La taille de chaque mécanisme est proportionnelle à la magnitude du moment. La couleur des mécanismes représente la profondeur de l'événement. (b) Moment sismique scalaire cumulé de la séquence Valparaíso 2017. Le moment scalaire du choc principal n'est pas inclus dans cette figure. La ligne pointillée rouge souligne le début approximatif des déplacements transitoires visibles sur les séries temporelles GPS. La ligne verte indique l'heure d'origine. 17

- 10 Glissement pendant la séquence de séismes pré-chocs de Valparaíso. a) Séries temporelle des données GNSS (bleu) et déplacement co-sismique stochastique induit par le pré-choc $M_W = 6.0$ (gris). Les points rouges représentent les déplacements moyens cosismiques stochastiques. La croix verte correspond au déplacement présismique total, y compris la contribution des séismes inférieurs à la magnitude de complétude. b) Distributions des déplacements présismiques observés (bleu) et des déplacements cosismiques cumulés générés pour les séismes pré-chocs (rouge) une heure avant le choc principal. Pour les observations, on suppose des incertitudes gaussiennes à partir des erreurs standard estimées à chaque station. c) Pourcentage de déplacement asismique pour chaque station. d) Signal post-sismique moyen mesuré sur les stations TRPD, VALN, BN05 et QTAY. e) Inversion de glissement des données GPS présismiques. f) Inversion de glissement des données GPS sans la contribution des séismes pré-chocs. Les flèches noires et bleues représentent les déplacements GPS horizontaux observés et prédits, ainsi que leurs ellipses $1-\sigma$ (représentant les incertitudes respectives). Les cercles colorés représentent les déplacements verticaux observés (cercles extérieurs) et prédits (cercles intérieurs) à partir du GPS. 19
- 11 Comparaison des matrices de covariance pour les signaux HRGPS (a) et les stations Strong Motion (b). La ligne verte représente la diagonale de la matrice de covariance empirique (c'est-à-dire la matrice créée à partir d'un ensemble de modèles). La ligne rouge et bleue représente la diagonale de la matrice calculée en utilisant l'approche d'approximation de 1er et 2ème ordre, respectivement. 21
- 12 Comparaison des distributions de glissement cosismique obtenues en utilisant différentes matrices de covariance d'erreur de prédiction C_p . Les couleurs rouges représentent les distributions de glissement finales. Les flèches représentent les directions de glissement avec leur incertitude correspondante. L'étoile rouge représente la localisation de l'hypocentre inversé. L'étoile bleue est l'hypocentre du CSN, et l'étoile verte est l'hypocentre de l'USGS. 22

LIST OF FIGURES

- 13 Impact de l'utilisation d'une approximation de 2ème ordre C_p dans l'inversion du glissement. (a) Modèle moyen *a posteriori* du glissement cosismique, les flèches représentent les directions de glissement et les ellipses l'incertitude correspondante. Les contours montrent les fronts de rupture stochastiques échantillonnés à partir de la distribution *a posteriori*. (b) Fonctions de taux de moment stochastique. (c) Modèle moyen *a posteriori* du glissement cosismique avec des contours qui représentent des échantillons de fronts de temps centroïdes stochastiques échantillonnés de la distribution *a posteriori*. (d) Incertitude de l'ensemble des modèles de glissement cosismique. L'étoile rouge dans les figures représente la localisation de l'hypocentre inversé. 23

- 14 Energies moyennes de rupture (a) et travail moyen de rupture (b) pour le séisme de 2015 $M_W = 8.3$ Illapel et le séisme de 2014 $M_W = 8.1$ Iquique. Pour l'énergie de rupture, les points violets et rouges représentent les énergies de rupture moyennes calculées dans cette étude. Pour le travail de rupture, les points verts et rouges représentent le travail de rupture moyen calculé dans cette étude. Les points cyan et violet représentent le travail de rupture moyen pondéré par le glissement correspondant. Les points bleus représentent les énergies de rupture et le travail de rupture calculés par Tinti et al. [2005a] respectivement. La ligne verte en pointillé représente la relation d'échelle de la même étude tandis que la ligne noire en pointillé représente la relation d'échelle de Causse et al. [2014]. 25

- 15 Example of Elastic Rebound theory for the San Andreas fault. In a first stage, stress is accumulated on the fault as a consequence of plates interaction. Then energy will be accumulated until reaching the yield stress. Finally, the fault will liberate this energy. Figure from USGS website <https://earthquake.usgs.gov/>. 2

- 16 Simple models of recurring earthquakes parameterized by a yield stress level σ_2 (related to the static friction on the fault) and a post earthquake stress level σ_1 (related to the dynamic friction on the fault). This diagram is based on [Shimazaki and Nakata, 1980]. Figure from Shearer [2019]. 3

LIST OF FIGURES

17	Schematic characterization of the megathrust frictional environment. Domain description is as follows: A: near-trench domain where tsunami earthquakes or anelastic deformation and stable sliding occur; B: central megathrust domain where large slip occurs with minor short-period seismic radiation; C: down-dip domain where moderate slip occurs with significant coherent short-period seismic radiation; and D: transitional domain, only present in some areas, typically with a young subducting plate, where SSEs, LFEs and tectonic tremors occur. Regions of unstable frictional sliding are red regions labeled “seismic”. Regions of aseismic stable or episodic sliding are white regions labeled “aseismic”. Orange areas are conditional stability [Scholz, 1998] regions, which displace aseismically except when accelerated by failure of adjacent seismic patches. Figure from Lay [2015].	4
18	Selected finite-source rupture models for the 1999 $M_W = 7.6$ Izmit earthquake (Turkey), obtained using different inversion strategies and different datasets. Black stars mark the hypocenter. Colors indicate fault slip (in meters). Note the pronounced dissimilarities of the slip distributions for this event. The inversion results are from (a) Bouchon et al. [2002], (b) Sekiguchi and Iwata [2002], (c) Delouis et al. [2002], and (d) Yagi and Kikuchi [2000]. Figure from Mai et al. [2016].	5
1.1	Scheme of inversion theory.	8
1.2	A simple inertial seismometer for measuring vertical motion. Movement of the suspended magnet induces a voltage in the coil; this signal is then amplified and recorded. Figure from Shearer [2019].	10
1.3	Velocity response functions for four different vertical-component instruments (old IDA station ALE, long and short-period channels for the GDSN station COL, and IRIS/IDA station ALE). Figure from Shearer [2019].	11
1.4	Example of velocitogram integrated from an accelerometer record at station 51JYC (31.96° N, 104.98° E) from the 2008 Wenchuan earthquake with inconstant baseline shift. The smooth line shows the non-linear trend correction on velocity determined using the automatic scheme presented in Wang et al. [2011]. Figure from Wang et al. [2011].	12

LIST OF FIGURES

- 1.5 Detrended daily displacement time series of four continuous GPS (cGPS) stations spanning nearly 15 years in the Parkfield, California region, in north, east, and up components. The region experienced two earthquakes in this period (26 December 2003 $M_W = 6.6$ San Simeon and 28 September 2004 $M_W = 6.0$ Parkfield), which generated both coseismic and postseismic deformation. The stations span both sides of the San Andreas fault. Prepared by Lina Su. Figure from Bock and Melgar [2016]. 14

- 1.6 (a) Descending and (b) ascending interferograms showing the deformation of the Hector Mine earthquake. Each color cycle represents 10 cm of line-of-sight (LOS) displacement toward (yellow–red–blue) or away from (yellow–blue–red) the satellite. Arrows show the horizontal component of the look direction from the radar satellites. Purple + and - signs point to areas of positive and negative LOS displacement. The mapped fault trace is shown as thick line and the epicenter is denoted with a star. Coordinates are universal transverse Mercator (UTM) coordinates (zone 115) in kilometers. Figure from Jónsson et al. [2002]. 15

- 1.7 The nine force couples which are the components of the seismic moment tensor. Each consists of two opposite forces separated by a distance d (dashed line), so the net force is always zero. Figure from Stein and Wysession [2009]. 18

- 1.8 W phase from the 2001 Peruvian earthquake ($M_W = 8.4$) recorded at HRV, and the synthetic W phase computed by mode summation using the GCMT solution. Figure from Kanamori and Rivera [2008]. . 21

- 1.9 Schematic illustrations showing how to parameterize spatiotemporal slip distribution. The initial time of time function is shown by contours in each of the top figures. (a) Typical linear expression of the multi-time-window analysis. Unknown parameters are amplitude for each window. (b) An example of nonlinear expression, in which rupture time is also an unknown parameter. Figure from Ide [2015]. 23

- 1.10 Slip-velocity functions of delta, boxcar, Gaussian, truncated Kostrov, and Yoffe are shown on the left. The corresponding slip functions of Heaviside, ramp, smoothed ramp, square root, and Yoffe in slip are shown on the right. Figure from Tinti et al. [2005b]. 26

1.11	Reference k-2 static slip distribution and inverted models for different values of the smoothing parameter l . The inversion process is performed by assuming that all the model and source parameters are known except the static slip. Mean slip equals 0.7 m. The space between the contour lines is 0.5 m. Figure from Causse et al. [2010].	29
1.12	TMCMC algorithm schematic: This cartoon illustrates one complete cooling stage of the TMCMC algorithm. The five samples from β_m are resampled and then the Metropolis algorithm is run to replace the unique samples lost through resampling. Numbers indicate the frequency of each model after resampling. The five red samples comprise the posterior distribution for β_{m+1} . The algorithm is plotted with a 100% acceptance rate for simplicity. Figure from Minson [2010].	36
1.13	CATMIP algorithm schematic. This cartoon illustrates one complete cooling stage of the CATMIP algorithm. The five samples from β_m are resampled and then an instance of the Metropolis algorithm is run for each of the resulting samples. Numbers indicate the frequency of each model after resampling. The five red samples comprise the posterior distribution for β_{m+1} . The algorithm is plotted with very short Markov chains and a 100 per cent acceptance rate for simplicity. In applications, the Markov chains would be much longer and the acceptance rate much lower. Figure from Minson et al. [2013].	38
1.14	The relation between slip and stress on the fault plane, determined for the 1995 Kobe earthquake [Ide and Takeo, 1997]. Each trace is the function calculated at the corresponding location in the middle figure that shows final slip distribution by contours. Figure from Ide [2015].	40
2.1	An asperity model indicating the different nature of stress distribution in each subduction zone category. The hatched areas indicate the zones of strong coupling. Figure from Lay and Kanamori [1981].	43
2.2	Schematic depiction of two possible mechanisms for foreshock generation. (a) Foreshocks triggered by previous foreshocks finally trigger the mainshock in a cascade of failures. (b) Foreshocks occur within the nucleation zone as asperities are loaded by the aseismic nucleation. The mainshock rupture is in Red and Foreshocks are in Blue. Figure courtesy of Z. Duputel.	44

LIST OF FIGURES

2.3	Plots of the logarithm of the rupture growth rate V against the logarithm of the rupture growth length L during the nucleation for events on the smooth fault. L_{sc} denotes the critical length beyond which the rupture grows at accelerating speeds, and the times $t_1 = 106.255$ and $t_2 = 106.560465$. Figure from Ohnaka and Shen [1999].	46
2.4	Photograph of the polycarbonate plate with the acoustic array, in the loading apparatus. Figure from Latour et al. [2013].	46
2.5	Examples of videograms showing three spontaneous laboratory earthquakes at increasingly higher normal prestresses – Gray scale indicates the light intensity change since time $t = 0$. Red curves highlight the position of rupture tips as a function of time (from Latour et al. [2013]). Blue dashed lines are the predicted position of rupture fronts in numerical simulations conducted by Kaneko et al. [2016]. Rupture nucleation can be decomposed into a quasi- static phase followed by an acceleration phase before dynamic (seismic) rupture propagation. Notice that the characteristics of rupture nucleation depend on the level of imposed normal stress (indicated on top of each subplot). Figure modified from Kaneko et al. [2016], courtesy of Z. Duputel.	47
2.6	Normalized stacks of the cumulative seismic moments of all the interplate sequences. Each sequence carries the same weight. Figure from Bouchon et al. [2013].	48
2.7	Motion of coastal GPS stations preceding the Iquique earthquake. (A) North and (B) east components relative to a linear evolution model with seasonal variations estimated since 2012. The thick red line denotes the origin time of the mainshock, whereas the black dotted lines show the occurrence times of the $M_W > 6$ foreshocks. Error bars indicate 1σ formal uncertainty. Figure from Ruiz et al. [2014].	50
2.8	East–west cross sections of the evolving shear stress changes on the fault plane during the foreshock sequence to the 1999 Izmit earthquake. a–d, Each frame corresponds to the origin time of one of the four largest foreshocks and adds the stress change from that event. Stress change based on a previously reported source model [Madariaga and Ruiz, 2016]. Red squares and error-bars show hypocentroids and 2σ location uncertainty of events occurring through the time indicated in the figure heading. Green diamonds denote the hypocentroid of the next foreshock in the sequence (a–c) and the mainshock hypocentre (d). Figure from Ellsworth and Bulut [2018].	53
2.9	Map of earthquake density in the QTM catalog (bins: 2 km by 2 km). Figure from Ross et al. [2019]	54

LIST OF FIGURES

2.10 Anomalous foreshock-mainshock sequences. Left) Poisson distribution model from Trugman and Ross [2019]. Center) Gamma distribution model Differences between models from van den Ende and Ampuero [2020]. Right) ETAS model from Moutote et al. [2021]. Figure courtesy of Z. Duputel and L. Moutote.	55
2.11 Three earthquake initiation models, their relationship to L_c , and their implications for foreshocks. The preslip model (a) and cascade model (b) illustrate endmember behavior where L_c is large (>10 km) or small (<1 m). (c) The laboratory observations suggest a rate-dependent cascade up model, which contains attributes of both end members. Figure from McLaskey [2019].	56
2.12 The 2017 Valparaíso earthquake sequence. (a) Earthquake locations including foreshocks (blue circles), mainshock (green star), and aftershocks (white circles). The red colormap indicates the preslip distribution resulting from the inversion of GPS data (see section 2.8.6). The black arrows show the cumulative observed GPS surface displacements (up to one hour before the mainshock). Orange dots indicate the seismicity distribution from 2017/01/01 until 2017/10/05 according to the microseismicity catalog obtained by S. Ruiz et al. (2017). (b) GPS Time-series in the vicinity of Valparaíso. The vertical red dashed line indicates approximate onset of the transient displacement visible on the timeseries. The cumulative number of earthquakes from S. Ruiz et al. (2017) is shown at the bottom of the figure. The purple star represents the largest $M_W = 6.0$ foreshock.	61
2.13 CMT solutions of the 2017 Valparaíso earthquake sequence and cumulative moment (a) CMT solutions of the 2017 Valparaíso earthquake sequence. Focal mechanisms are contoured in blue and black for foreshocks and aftershocks respectively. The size of beach balls scales with the moment magnitude. Color of the compressive quadrants represents the event depth. (b) Cumulative scalar seismic moment of the 2017 Valparaíso sequence. The mainshock scalar moment is not included in this figure. The red dashed line outlines the approximate onset of transient displacements visible on GPS time-series. The green line indicates the origin time.	63

2.14 Bayesian point-source model for the $M_W=6.0$ foreshock on 2017-04-23. Blue circles and lines in the figure represent model samples randomly drawn from the posterior distribution. a) Samples from the posterior PDF depicting uncertainties in the point source location. The red and orange stars are the initial solution (i.e. starting model) and the posterior mean model respectively. b) Focal mechanism uncertainty. c) Marginal posterior PDF of the scalar seismic moment. The red and orange lines are the initial and the posterior mean model. 67

2.15 Slip during the Valparaíso foreshock sequence. a) Time series of GNSS data (blue) and stochastic foreshock-induced co-seismic displacement (gray). Red dots represent the average of stochastic co-seismic offsets. Green cross corresponds to the total foreshock displacement, including the contribution of earthquakes below the magnitude of completeness. b) Distributions of observed pre-seismic displacement and predicted cumulative co-seismic offsets caused by foreshocks. Blue histograms represent observations assuming Gaussian uncertainties from standard errors estimated at each station. Red histograms correspond to the posterior distribution of cumulative foreshock-induced co-seismic displacement. c) Percentage of aseismic displacement for each station. d) Average postseismic signal measured on stations TRPD, VALN, BN05 and QTAY (see Figure S11). e) Slip inversion of pre-seismic GPS data. f) Slip inversion of GPS data after removing foreshock-induced displacement. Black and blue arrows are observed and predicted horizontal GPS displacements along with their $1-\sigma$ ellipses (representing observational and prediction uncertainties, respectively). Colored circles are observed (outer circles) and predicted (inner circles) vertical displacements from GPS and tide gauges, respectively. 72

3.1 General overview of the studied region with data sets used in this study (a). Green star represents the hypocenter obtained by the Chilean Seismological Center (CSN). Ascending (b) and descending (c) Sentinel 1-A InSAR images. 77

LIST OF FIGURES

3.2	Comparison between displacements corrected from ground motion records and HRGPS displacements. Red and black waveforms represent HRGPS and strong motion respectively. On the maps, the blue star represents the CSN hypocenter while circles indicate station location (orange for the strong motion station depicted, yellow for the ensemble of strong motion stations, and purple for HRGPS stations). Variation in waveforms is mostly due to differences in colocation. . .	78
3.3	Model variability of the P-wave, S-wave, and density as a function of depth in the Illapel region. The black line represents the velocity layered model used for Green's Function (GF) calculation. Grey histograms are the probability density function for each parameter as a function of depth.	81
3.4	Covariance matrix comparison for HRGPS records (a) and Strong Motion stations (b). The green line represents the diagonal of the empirical covariance matrix (i.e., the matrix created from an ensemble of models). The red and blue line represents the diagonal of the matrix calculated using the 1st and 2nd order approximation approach.	83
3.5	Posterior mean coseismic slip model for the static data set. Arrows represent the slip directions and the ellipses its corresponding uncertainty.	85
3.6	Comparison of co-seismic slip distributions obtained using different prediction error covariances C_p . Red colors are the final slip distributions. Arrows represent the slip directions with their corresponding uncertainty. The red star is the inverted hypocenter location (empirical, 1st, and 2nd order approximation, respectively). The blue star is the CSN hypocenter, and the green star is the USGS hypocenter. . .	86
3.7	Rupture times comparison between different C_p inversion solutions. Comparison between the empirical covariance matrix and the first order (a) and 2nd order (b) approaches.	86
3.8	Impact of using a 2nd order approximation C_p in slip inversion. (a) Posterior mean coseismic slip model, arrows represent the slip directions and the ellipses its corresponding uncertainty. Contours show stochastic rupture fronts samples from the <i>a posteriori</i> distribution. (b) Stochastic moment rate functions. (c) Posterior mean coseismic slip model with contours that represent stochastic centroid time fronts samples from the <i>a posteriori</i> distribution. (d) Uncertainty of the ensemble of coseismic slip models. The red star in the figures represents the inverted hypocenter location.	88

- 3.9 (a) Observed displacement GPS (black arrows) and predictions for the posterior mean model (red arrows) using a 2nd order approximation C_p . The colormap indicates vertical component displacements for observed (outer circle) and synthetic (inner circle) data. (b) Comparisons between tsunami observations (black) and stochastic predictions (red) using a 2nd order approximation C_p . The tsunami waveform signal used in the inversion is shown between blue dots. The map corresponds to each tsunami station. 89
- 3.10 InSAR images misfit using the posterior coseismic model using the 2nd order C_p matrix solution. Observed ascending (a) and descending (d) Sentinel 1-A images. We show the corresponding synthetic displacement for ascending (b) and descending (c) images and the respective residual, ((c) for ascending, and (f) for descending images). 90
- 3.11 Examples of comparisons between data (black) and stochastic predictions (red) for HRGPS and Strong Motion stations using a 2nd order approximation C_p . On the maps, the blue star represents the hypocenter while circles indicate station location (orange for the station depicted and yellow for the other stations) 91
- 3.12 (a) Posterior mean coseismic slip model for a stati inversion with a non shallow slip *a priori*. Arrows represent the slip directions and the ellipses its corresponding uncertainty. (b) Comparisons between tsunami observations (black) and stochastic predictions with shallow slip (red) and without shallow slip (blue). The tsunami waveform signal used in the inversion is shown between yellow dots. The map shows the depicted tsunami stations. 92
- 3.13 Five seconds snapshots of slip (first and third row) and slip rate (second and fourth row) evolution. Slip and slip rate are calculated using the posterior mean coseismic model using the 2nd order C_p solution. The red star is the inverted hypocenter location. Arrows represent the possible encircling locations. 93

LIST OF FIGURES

3.14 Average breakdown energies (a) and average breakdown work (b) for the 2015 $M_W = 8.3$ Illapel earthquake and the 2014 $M_W = 8.1$ Iquique earthquake. For the breakdown energy, purple and red dots represent the average breakdown energies calculated in this study. For the breakdown work, green and red dots represent the average breakdown work calculated in this study. Cyan and purple dots represent the average breakdown work weighted by the corresponding slip. Blue dots represent the breakdown energies and breakdown work calculated by Tinti et al. [2005a] respectively. The dashed green line represents the scaling relationship from the same study while the dashed black line represents the scaling relationship is from Causse et al. [2014].	97
3.15 Scaling of breakdown work density with slip and Fracture energy estimates from Rice et al. (2005). (a) Scaling relationships for the 2015 $M_W = 8.3$ Illapel earthquake. (b) Scaling relationships for the 2014 $M_W = 8.1$ Iquique earthquake.	98
A.1 Map of the GPS stations processed in South America and Nazca Plates. The red stations are those ones used to define the Reference Frame, while the blue ones are just used on the processing. The pink box denotes the study area (see Figure A.2 to look at the stations processed in this region).	112
A.2 Map of the GPS stations processed in the study area.	113
A.3 GPS time series for the Valparaíso region network for north and east component. The images show the time series before and after the mainshock (green line) of the sequence.	114
A.4 Model variability of the P-wave, S-wave, and density as a function of depth in Valparaíso region. Black line represents the velocity layered model used for Green's Function (GF) calculation. Grey histograms are the probability density function for each parameter as a function of depth as described in Cp.	115
A.5 Gutenberg-Richter law for the 2017 Valparaíso earthquake sequence. Three different catalogs of the sequence are shown: Our CMT catalog, S. Ruiz et al. (2017) catalog, and J. A. Ruiz et al. (2018) catalog. For each catalog, both the whole sequence (foreshocks and aftershocks), and the foreshocks sequence are represented.	116

LIST OF FIGURES

- A.6 Synthetic surface displacement for different ranges of magnitude, foreshocks with $M_w \geq 5.5$ (largest foreshock $M_w = 6.0$) and foreshocks with $M_w \leq 5.5$. The $M_w = 6.0$ contribution appears to dominate the signal, with respect to the cumulative contribution of smaller foreshocks. 117
- A.7 Diagonal of the C_p matrix for the vertical component of the station G005. The matrix is calculated for the $M_W = 6.0$ foreshock of the Valparaíso sequence (see section 3 of the main text). The red line represents the diagonal matrix for the empirical covariance matrix (i.e., the matrix created from an ensemble of models). The blue line represents the first (top) and second-order (bottom) approaches used to compute C_p 118
- A.8 Comparison between synthetic waveforms predicted from stochastic models calculated with a log-normal distribution, and synthetic waveforms calculated using the first and second order C_p matrix. The waveforms are generated using the source model of the $M_W = 6.0$ foreshock presented in section 3 of the main text. The X-axis represents time shifts between waveforms generated with the average velocity model of the region (figure S4) and waveform predicted for randomly perturbed velocity models. The Y-axis represents time shifts between waveforms generated with the average velocity model and waveforms generated either with the first or the second order approximation (see equations (2) and (5) of text S2). The color represents the correlation coefficient of each pair of waveforms. If the comparison follows the $y = x$ line, it means that the perturbation approximation properly estimates the empirical covariance matrix. We can observe that the second order approach better approximates actual synthetics (especially when there is a significant time-delay between waveforms). 119
- A.9 Waveforms fit for the $M_W = 6.0$ foreshock using CMT solution from our catalog. Observed (black) and synthetic (red) waveforms for a given station (orange). The fit (inversion) is made between red dots. The blue star represents the CMT location. Yellow dots correspond to the ensemble of stations used in the inversion. 121
- A.10 Stations used for the $M_W = 6$ foreshock CMT inversion. The CMT location is shown in purple. 122
- A.11 Mainshock postseismic surface displacement normalized by the coseismic displacement at each GPS station. This ratio approximates the moment ratio between postseismic and coseismic terms. 123

LIST OF FIGURES

A.12	Same as Figure 4 of main text but with the quick postseismic contribution produced by the largest foreshock.	124
B.1	Comparison between displacements corrected from ground motion records and HRGPS displacements. Red and black waveforms represent HRGPS and strong motion respectively. On the maps, the blue star represents the CSN hypocenter while circles indicate station location (orange for the strong motion station depicted, yellow for the ensemble of strong motion stations, and purple for HRGPS stations). Variation in waveforms is mostly due to differences in colocation. . .	134
B.2	Difference between final empirical covariance matrix and intermediate covariance matrix calculated using a number of samples. . . .	135
B.3	Covariance matrix comparison for HRGPS records (a) and Strong Motion stations (b) at hypocenter distances greater < 200 km. The green line represents the diagonal of the empirical covariance matrix (i.e., the matrix created from an ensemble of models). The red and blue line represents the diagonal of the matrix calculated using the 1st and 2nd order approximation approach.	136
B.4	<i>A priori</i> probability density function (PDF) distributions. <i>A priori</i> PDFs are shown for the inverted parameters. We include nuisance parameters to include a linear ramp to account for InSAR orbital errors and translation parameters for each GPS data set.	137
B.5	Sensitivity for each data set. The sensitivity is shown for (a) GPS, (b) InSAR, (c) Tsunami and dart data, (d) tsunami, InSAR, GPS and tide-gauges, (e) High rate GPS and strong motion, and (f) The ensemble of data sets.	138
B.6	Posterior mean distributions for the dip slip parameters. The colors represent the empirical C_p matrix (green), the first order approximation matrix (red), and the second order approximation matrix (blue). The strength of the colors are proportional to the magnitude of the slip.139	
B.7	Impact of using an empirical covariance matrix C_p in slip inversion. (a) Posterior mean coseismic slip model, arrows represent the slip directions and the ellipses its corresponding uncertainty. Contours show stochastic rupture fronts samples from the <i>a posteriori</i> distribution. (b) Stochastic moment rate functions. (c) Posterior mean coseismic slip model with contours that represent stochastic centroid time fronts samples from the <i>a posteriori</i> distribution. (d) Uncertainty of the ensemble of coseismic slip models. The red star in the figures represents the inverted hypocenter location.	140

LIST OF FIGURES

B.8	Impact of using a 1st order approximation C_p in slip inversion. (a) Posterior mean coseismic slip model, arrows represent the slip directions and the ellipses its corresponding uncertainty. Contours show stochastic rupture fronts samples from the <i>a posteriori</i> distribution. (b) Stochastic moment rate functions. (c) Posterior mean coseismic slip model with contours that represent stochastic centroid time fronts samples from the <i>a posteriori</i> distribution. (d) Uncertainty of the ensemble of coseismic slip models. The red star in the figures represents the inverted hypocenter location.	141
B.9	Comparison between rupture and rise times for the patch with maximum slip.	142
B.10	Examples of comparisons between data (black) and stochastic predictions (red) for HRGPS and Strong Motion stations using a 2nd order approximation C_p . On the maps, the blue star represents the hypocenter while circles indicate station location (orange for the station depicted and yellow for the other stations).	144

List of Tables

1.1	Rejection method	33
1.2	Metropolis algorithm	33
1.3	TMCMC algorithm	36
1.4	CATMIP algorithm	37
3.1	Approaches to calculate C_p (for 36 parameters)	83
A.1	Bandpass filter corner frequencies used for CMT inversion	125
A.2	CMT solutions of our catalog.	126

Bibliography

- Brad T Aagaard, Matthew G Knepley, and Charles A Williams. A domain decomposition approach to implementing fault slip in finite-element models of quasi-static and dynamic crustal deformation. *Journal of Geophysical Research: Solid Earth*, 118(6):3059–3079, 2013.
- Rachel E Abercrombie and Jim Mori. Occurrence patterns of foreshocks to large earthquakes in the western united states. *Nature*, 381(6580):303–307, 1996.
- Duncan Carr Agnew, WHK Lee, H Kanamori, PC Jennings, and C Kisslinger. History of seismology. *International handbook of earthquake and engineering seismology*, 81(A):3–11, 2002.
- PS Agram and M Simons. A noise model for insar time series. *Journal of Geophysical Research: Solid Earth*, 120(4):2752–2771, 2015.
- Keiiti Aki. Maximum likelihood estimate of b in the formula $\log n = a - bm$ and its confidence limits. *Bull. Earthq. Res. Inst., Tokyo Univ.*, 43:237–239, 1965.
- Keiiti Aki. Characterization of barriers on an earthquake fault. *Journal of Geophysical Research: Solid Earth*, 84(B11):6140–6148, 1979.
- Keiiti Aki and Paul G Richards. *Quantitative seismology*. University Science Books, 2002.
- Albuquerque Seismological Laboratory (ASL)/USGS. Global seismograph network - iris/usgs (gsn). international federation of digital seismograph networks, 1988.
- Albuquerque Seismological Laboratory (ASL)/USGS. Global telemetered seismograph network (usaf/usgs). international federation of digital seismograph networks., 1993.
- SCR Allen and DJM Greenslade. Developing tsunami warnings from numerical model output. *Natural Hazards*, 46(1):35–52, 2008.

BIBLIOGRAPHY

- Zuheir Altamimi, Paul Rebischung, Laurent Métivier, and Xavier Collilieux. ITRF2014: A new release of the International Terrestrial Reference Frame modeling nonlinear station motions. *Journal of Geophysical Research: Solid Earth*, 121(8):6109–6131, 2016. ISSN 21699356. doi: 10.1002/2016JB013098.
- Mohamed A Alwahedi and Jessica C Hawthorne. Intermediate-magnitude post-seismic slip follows intermediate-magnitude (m 4 to 5) earthquakes in california. *Geophysical Research Letters*, 46(7):3676–3687, 2019.
- Jean-Paul Ampuero and Allan M Rubin. Earthquake nucleation on rate and state faults—aging and slip laws. *Journal of Geophysical Research: Solid Earth*, 113(B1), 2008.
- Chao An and Lingsen Meng. Time reversal imaging of the 2015 illapel tsunami source. *Geophysical Research Letters*, 44(4):1732–1739, 2017.
- Chao An, Han Yue, Jianbao Sun, Lingsen Meng, and Juan Carlos Báez. The 2015 mw 8.3 illapel, chile, earthquake: Direction-reversed along-dip rupture with localized water reverberationthe 2015 mw 8.3 illapel, chile, earthquake. *Bulletin of the Seismological Society of America*, 107(5):2416–2426, 2017.
- JA Anderson and Harry Oscar Wood. Description and theory of the torsion seismometer. *Bulletin of the Seismological Society of America*, 15(1):1–72, 1925.
- DJ Andrews. Rupture propagation with finite stress in antiplane strain. *Journal of Geophysical Research*, 81(20):3575–3582, 1976.
- D Angermann, Juergen Klotz, and Ch Reigber. Space-geodetic estimation of the nazca-south america euler vector. *Earth and Planetary Science Letters*, 171(3):329–334, 1999.
- Hideo Aochi and Sergio Ruiz. Early stage and main ruptures of the 2015 mw8.3 illapel, chile, megathrust earthquake: Kinematic elliptical inversions and dynamic rupture simulations. *Journal of Geophysical Research: Solid Earth*, page e2020JB021207, 2021.
- Hideo Aochi and Cédric Twardzik. Imaging of seismogenic asperities of the 2016 ml 6.0 amatrice, central italy, earthquake through dynamic rupture simulations. *Pure and Applied Geophysics*, 177(5):1931–1946, 2020.
- Hideo Aochi, Eiichi Fukuyama, and Mitsuhiro Matsu’ura. Spontaneous rupture propagation on a non-planar fault in 3-d elastic medium. *pure and applied geophysics*, 157(11-12):2003–2027, 2000.

BIBLIOGRAPHY

- Richard C Aster, Brian Borchers, and Clifford H Thurber. *Parameter estimation and inverse problems*. Elsevier, 2018.
- George Backus and Marjorie Mulcahy. Moment tensors and other phenomenological descriptions of seismic sources—i. continuous displacements. *Geophysical Journal International*, 46(2):341–361, 1976.
- Juan CARLOS Baez, Felipe Leyton, C Troncoso, F del Campo, M Bevis, C Vigny, M Moreno, M Simons, E Kendrick, H Parra, et al. The chilean gnss network: Current status and progress toward early warning applications. *Seismological Research Letters*, 89(4):1546–1554, 2018.
- James L Beck and Siu-Kui Au. Bayesian updating of structural models and reliability using markov chain monte carlo simulation. *Journal of engineering mechanics*, 128(4):380–391, 2002.
- Susan Beck, Sergio Barrientos, Eduardo Kausel, and M Reyes. Source characteristics of historic earthquakes along the central chile subduction askew et alzone. *Journal of South American Earth Sciences*, 11(2):115–129, 1998.
- Jonathan Bedford, Marcos Moreno, Bernd Schurr, Mitja Bartsch, and Onno Oncken. Investigating the final seismic swarm before the iquique-pisagua 2014 mw 8.1 by comparison of continuous gps and seismic foreshock data. *Geophysical Research Letters*, 42(10):3820–3828, 2015.
- Igor A Beresnev. Uncertainties in finite-fault slip inversions: to what extent to believe?(a critical review). *Bulletin of the Seismological Society of America*, 93(6):2445–2458, 2003.
- Gregory C Beroza and Satoshi Ide. Slow earthquakes and nonvolcanic tremor. *Annual review of Earth and planetary sciences*, 39:271–296, 2011.
- Wolfgang Betz, Iason Papaioannou, and Daniel Straub. Transitional markov chain monte carlo: observations and improvements. *Journal of Engineering Mechanics*, 142(5):04016016, 2016.
- Christopher M Bishop. *Pattern recognition and machine learning*. springer, 2006.
- Quentin Bletery, Anthony Sladen, Junle Jiang, and Mark Simons. A bayesian source model for the 2004 great sumatra-andaman earthquake. *Journal of Geophysical Research: Solid Earth*, 121(7):5116–5135, 2016.
- Yehuda Bock and Diego Melgar. Physical applications of gps geodesy: A review. *Reports on Progress in Physics*, 79(10):106801, 2016.

BIBLIOGRAPHY

- Yehuda Bock, Rosanne M Nikolaidis, Paul J de Jonge, and Michael Bevis. Instantaneous geodetic positioning at medium distances with the global positioning system. *Journal of Geophysical Research: Solid Earth*, 105(B12):28223–28253, 2000.
- Yehuda Bock, Diego Melgar, and Brendan W Crowell. Real-time strong-motion broadband displacements from collocated gps and accelerometers. *Bulletin of the Seismological Society of America*, 101(6):2904–2925, 2011.
- David M Boore and Julian J Bommer. Processing of strong-motion accelerograms: needs, options and consequences. *Soil Dynamics and Earthquake Engineering*, 25(2):93–115, 2005.
- Michel Bouchon. The state of stress on some faults of the san andreas system as inferred from near-field strong motion data. *Journal of Geophysical Research: Solid Earth*, 102(B6):11731–11744, 1997.
- Michel Bouchon, M Nafi Toksoz, Hayrullah Karabulut, Marie-Paule Bouin, Michel Dietrich, Mustafa Aktar, and Margaret Edie. Space and time evolution of rupture and faulting during the 1999 izmit (turkey) earthquake. *Bulletin of the Seismological Society of America*, 92(1):256–266, 2002.
- Michel Bouchon, Hayrullah Karabulut, Mustafa Aktar, Serdar Özalaybey, Jean Schmittbuhl, and Marie-Paule Bouin. Extended nucleation of the 1999 mw 7.6 izmit earthquake. *science*, 331(6019):877–880, 2011.
- Michel Bouchon, Virginie Durand, David Marsan, Hayrullah Karabulut, and Jean Schmittbuhl. The long precursory phase of most large interplate earthquakes. *Nature geoscience*, 6(4):299–302, 2013.
- David D Bowman and Geoffrey CP King. Accelerating seismicity and stress accumulation before large earthquakes. *Geophysical Research Letters*, 28(21):4039–4042, 2001.
- Emily E Brodsky and Thorne Lay. Recognizing foreshocks from the 1 april 2014 chile earthquake. *Science*, 344(6185):700–702, 2014.
- R Burridge and L Knopoff. Body force equivalents for seismic dislocations. *Bulletin of the Seismological Society of America*, 54(6A):1875–1888, 1964.
- Emmanuel Caballero, Agnes Chounet, Zacharie Duputel, Jorge Jara, Cedric Twardzik, and Romain Jolivet. Seismic and aseismic fault slip during the initiation phase of the 2017 mw= 6.9 valparaíso earthquake. *Geophysical research letters*, 48(6):e2020GL091916, 2021.

BIBLIOGRAPHY

- M Causse, LA Dalguer, and Paul Martin Mai. Variability of dynamic source parameters inferred from kinematic models of past earthquakes. *Geophysical Journal International*, 196(3):1754–1769, 2014.
- Mathieu Causse, Fabrice Cotton, and P Martin Mai. Constraining the roughness degree of slip heterogeneity. *Journal of Geophysical Research: Solid Earth*, 115(B5), 2010.
- Wei-An Chao, Yih-Min Wu, and Li Zhao. An automatic scheme for baseline correction of strong-motion records in coseismic deformation determination. *Journal of seismology*, 14(3):495–504, 2010.
- Curtis W Chen and Howard A Zebker. Phase unwrapping for large sar interferograms: Statistical segmentation and generalized network models. *IEEE Transactions on Geoscience and Remote Sensing*, 40(8):1709–1719, 2002.
- Siddhartha Chib and Edward Greenberg. Understanding the metropolis-hastings algorithm. *The american statistician*, 49(4):327–335, 1995.
- Jianye Ching and Yi-Chu Chen. Transitional markov chain monte carlo method for bayesian model updating, model class selection, and model averaging. *Journal of engineering mechanics*, 133(7):816–832, 2007.
- Mohamed Chlieh, Jean-Philippe Avouac, Vala Hjorleifsdottir, Teh-Ru Alex Song, Chen Ji, Kerry Sieh, Anthony Sladen, Helene Hebert, Linette Prawirodirdjo, Yehuda Bock, et al. Coseismic slip and afterslip of the great mw 9.15 sumatra–andaman earthquake of 2004. *Bulletin of the Seismological Society of America*, 97(1A):S152–S173, 2007.
- A Cochard and R Madariaga. Complexity of seismicity due to highly rate-dependent friction. *Journal of Geophysical Research: Solid Earth*, 101(B11):25321–25336, 1996.
- Diana Comte, A Eisenberg, E Lorca, M Pardo, L Ponce, R Saragoni, SK Singh, and G Suárez. The 1985 central chile earthquake: A repeat of previous great earthquakes in the region? *Science*, 233(4762):449–453, 1986.
- Brendan W Crowell, Yehuda Bock, and Diego Melgar. Real-time inversion of gps data for finite fault modeling and rapid hazard assessment. *Geophysical Research Letters*, 39(9), 2012.
- Víctor M Cruz-Atienza, Josué Tago, Carlos Villafuerte, Meng Wei, Ricardo Garza-Girón, Luis A Dominguez, Vladimir Kostoglodov, Takuya Nishimura, SI Franco,

BIBLIOGRAPHY

- Jorge Real, et al. Short-term interaction between silent and devastating earthquakes in Mexico. *Nature communications*, 12(1):1–14, 2021.
- John C Curlander and Robert N McDonough. *Synthetic aperture radar*, volume 11. Wiley, New York, 1991.
- N D’agostino, D Cheloni, G Fornaro, R Giuliani, and D Reale. Space-time distribution of afterslip following the 2009 l’aquila earthquake. *Journal of Geophysical Research: Solid Earth*, 117(B2), 2012.
- M Dalaison and Romain Jolivet. A kalman filter time series analysis method for insar. *Journal of Geophysical Research: Solid Earth*, 125(7):e2019JB019150, 2020.
- S Das and BV Kostrov. Breaking of a single asperity: rupture process and seismic radiation. *Journal of Geophysical Research: Solid Earth*, 88(B5):4277–4288, 1983.
- Sh Das and CH Scholz. Theory of time-dependent rupture in the earth. *Journal of Geophysical Research: Solid Earth*, 86(B7):6039–6051, 1981.
- Shamita Das and Keiiti Aki. Fault plane with barriers: A versatile earthquake model. *Journal of geophysical research*, 82(36):5658–5670, 1977.
- Steven M Day, Guang Yu, and David J Wald. Dynamic stress changes during earthquake rupture. *Bulletin of the Seismological Society of America*, 88(2):512–522, 1998.
- B Delouis, D Giardini, P Lundgren, and J Salichon. Joint inversion of insar, gps, teleseismic, and strong-motion data for the spatial and temporal distribution of earthquake slip: Application to the 1999 izmit mainshock. *Bulletin of the Seismological Society of America*, 92(1):278–299, 2002.
- Jan Dettmer, Roberto Benavente, Phil R Cummins, and Malcolm Sambridge. Trans-dimensional finite-fault inversion. *Geophysical Journal International*, 199(2):735–751, 2014.
- James H Dieterich. Time-dependent friction and the mechanics of stick-slip. In *Rock friction and earthquake prediction*, pages 790–806. Springer, 1978.
- Douglas A Dodge, Gregory C Beroza, and WL Ellsworth. Detailed observations of California foreshock sequences: Implications for the earthquake initiation process. *Journal of Geophysical Research: Solid Earth*, 101(B10):22371–22392, 1996.

BIBLIOGRAPHY

- Herb Dragert, Kelin Wang, and Thomas S James. A silent slip event on the deeper cascadia subduction interface. *Science*, 292(5521):1525–1528, 2001.
- Zacharie Duputel, Luis Rivera, Yukitoshi Fukahata, and Hiroo Kanamori. Uncertainty estimations for seismic source inversions. *Geophysical Journal International*, 190(2):1243–1256, 2012a.
- Zacharie Duputel, Luis Rivera, Hiroo Kanamori, and Gavin Hayes. W phase source inversion for moderate to large earthquakes (1990–2010). *Geophysical Journal International*, 189(2):1125–1147, 2012b.
- Zacharie Duputel, Piyush S Agram, Mark Simons, Sarah E Minson, and James L Beck. Accounting for prediction uncertainty when inferring subsurface fault slip. *Geophysical Journal International*, 197(1):464–482, 2014.
- Zacharie Duputel, Junle Jiang, Romain Jolivet, Mark Simons, Luis Rivera, J-P Ampuero, Bryan Riel, Susan E Owen, Angelyn W Moore, and Sergey V Samsonov. The iquique earthquake sequence of april 2014: Bayesian modeling accounting for prediction uncertainty. *Geophysical Research Letters*, 42(19):7949–7957, 2015.
- Tina Dura, Marco Cisternas, Benjamin P Horton, Lisa L Ely, Alan R Nelson, Robert L Wesson, and Jessica E Pilarczyk. Coastal evidence for holocene subduction-zone earthquakes and tsunamis in central chile. *Quaternary Science Reviews*, 113:93–111, 2015.
- Adam M Dziewonski, T-A Chou, and John H Woodhouse. Determination of earthquake source parameters from waveform data for studies of global and regional seismicity. *Journal of Geophysical Research: Solid Earth*, 86(B4):2825–2852, 1981.
- Göran Ekström, Meredith Nettles, and AM Dziewoński. The global cmt project 2004–2010: Centroid-moment tensors for 13,017 earthquakes. *Physics of the Earth and Planetary Interiors*, 200:1–9, 2012.
- William L Ellsworth and Fatih Bulut. Nucleation of the 1999 izmit earthquake by a triggered cascade of foreshocks. *Nature Geoscience*, 11(7):531–535, 2018.
- WL Ellsworth and GC Beroza. Seismic evidence for an earthquake nucleation phase. *Science*, 268(5212):851–855, 1995.
- Tom G Farr, Paul A Rosen, Edward Caro, Robert Crippen, Riley Duren, Scott Hensley, Michael Kobrick, Mimi Paller, Ernesto Rodriguez, Ladislav Roth, et al. The shuttle radar topography mission. *Reviews of geophysics*, 45(2), 2007.

BIBLIOGRAPHY

- Jun'ichi Fukuda and Kaj M Johnson. A fully bayesian inversion for spatial distribution of fault slip with objective smoothing. *Bulletin of the Seismological Society of America*, 98(3):1128–1146, 2008.
- Eiichi Fukuyama and Raúl Madariaga. Rupture dynamics of a planar fault in a 3d elastic medium: rate-and slip-weakening friction. *Bulletin of the Seismological Society of America*, 88(1):1–17, 1998.
- Eric L Geist and Renata Dmowska. Local tsunamis and distributed slip at the source. In *Seismogenic and tsunamigenic processes in shallow subduction zones*, pages 485–512. Springer, 1999.
- Jianghui Geng, Yehuda Bock, Diego Melgar, Brendan W Crowell, and Jennifer S Haase. A new seismogeodetic approach applied to gps and accelerometer observations of the 2012 brawley seismic swarm: Implications for earthquake early warning. *Geochemistry, Geophysics, Geosystems*, 14(7):2124–2142, 2013.
- Steven J Gibbons and Frode Ringdal. The detection of low magnitude seismic events using array-based waveform correlation. *Geophysical Journal International*, 165(1):149–166, 2006.
- Baptiste Gombert, Zacharie Duputel, Romain Jolivet, C Doubre, L Rivera, and Mark Simons. Revisiting the 1992 landers earthquake: a bayesian exploration of coseismic slip and off-fault damage. *Geophysical Journal International*, 212(2):839–852, 2018a.
- Baptiste Gombert, Zacharie Duputel, Romain Jolivet, Mark Simons, Junle Jiang, Cunren Liang, Eric J Fielding, and Luis Rivera. Strain budget of the ecuador–colombia subduction zone: A stochastic view. *Earth and Planetary Science Letters*, 498:288–299, 2018b.
- VM Graizer. Determination of the true displacement of the ground from strong-motion recordings. *izv ussr acad sci. Physics Solid Earth*, 15(12):875–885, 1979.
- Mariagiovanna Guatteri and Paul Spudich. Coseismic temporal changes of slip direction: the effect of absolute stress on dynamic rupture. *Bulletin of the Seismological Society of America*, 88(3):777–789, 1998.
- Mariagiovanna Guatteri and Paul Spudich. What can strong-motion data tell us about slip-weakening fault-friction laws? *Bulletin of the Seismological Society of America*, 90(1):98–116, 2000.

BIBLIOGRAPHY

- Sebastian Hainzl, Frank Scherbaum, and Celine Beauval. Estimating background activity based on interevent-time distribution. *Bulletin of the Seismological Society of America*, 96(1):313–320, 2006.
- John F Hall and James L Beck. Structural damage in mexico city. *Geophysical Research Letters*, 13(6):589–592, 1986.
- Miroslav Hallo and František Gallovič. Fast and cheap approximation of green function uncertainty for waveform-based earthquake source inversions. *Geophysical Journal International*, 207(2):1012–1029, 2016.
- Per Christian Hansen and Dianne Prost O’Leary. The use of the l-curve in the regularization of discrete ill-posed problems. *SIAM journal on scientific computing*, 14(6):1487–1503, 1993.
- Stephen Hartzell and Donald V Helmberger. Strong-motion modeling of the imperial valley earthquake of 1979. *Bulletin of the Seismological Society of America*, 72(2):571–596, 1982.
- Stephen H Hartzell and Thomas H Heaton. Inversion of strong ground motion and teleseismic waveform data for the fault rupture history of the 1979 imperial valley, california, earthquake. *Bulletin of the Seismological Society of America*, 73(6A): 1553–1583, 1983.
- NA Haskell. Total energy and energy spectral density of elastic wave radiation from propagating faults. *Bulletin of the Seismological Society of America*, 54(6A): 1811–1841, 1964.
- W. K. Hastings. Monte Carlo sampling methods using Markov chains and their applications. *Biometrika*, 57(1):97–109, 1970. ISSN 0006-3444. doi: 10.1093/biomet/57.1.97. URL <https://doi.org/10.1093/biomet/57.1.97>.
- Jens Havskov and Gerardo Alguacil. *Instrumentation in earthquake seismology*, volume 358. Springer, 2004.
- Jens Havskov and Lars Ottemoller. *Routine data processing in earthquake seismology: with sample data, exercises and software*. Springer Science & Business Media, 2010.
- Gavin P Hayes, Luis Rivera, and Hiroo Kanamori. Source inversion of the w-phase: real-time implementation and extension to low magnitudes. *Seismological Research Letters*, 80(5):817–822, 2009.

BIBLIOGRAPHY

- Gavin P Hayes, David J Wald, and Rebecca L Johnson. Slab1. 0: A three-dimensional model of global subduction zone geometries. *Journal of Geophysical Research: Solid Earth*, 117(B1), 2012.
- Thomas H Heaton. Evidence for and implications of self-healing pulses of slip in earthquake rupture. *Physics of the Earth and Planetary Interiors*, 64(1):1–20, 1990.
- Mohammad Heidarzadeh, Satoko Murotani, Kenji Satake, Takeo Ishibe, and Aditya Riadi Gusman. Source model of the 16 september 2015 illapel, chile, mw 8.4 earthquake based on teleseismic and tsunami data. *Geophysical Research Letters*, 43(2):643–650, 2016.
- Agnès Helmstetter and Didier Sornette. Foreshocks explained by cascades of triggered seismicity. *Journal of Geophysical Research: Solid Earth*, 108(B10), 2003.
- Matthew W Herman, Kevin P Furlong, Gavin P Hayes, and Harley M Benz. Fore-shock triggering of the 1 april 2014 mw 8.2 iquique, chile, earthquake. *Earth and Planetary Science Letters*, 447:119–129, 2016.
- T A Herring, R.W. King, M.A. Floyd, and S C McClusky. GAMIT Reference Manual. GPS Analysis at MIT GLOBK, Release 10.7. (June):168, 2018.
- Robert B Herrmann. Computer programs in seismology: An evolving tool for instruction and research. *Seismological Research Letters*, 84(6):1081–1088, 2013.
- Moujahed I Husseini, Dushan B Jovanovich, MJ Randall, and LB Freund. The fracture energy of earthquakes. *Geophysical Journal International*, 43(2):367–385, 1975.
- Yoshiaki Ida. Cohesive force across the tip of a longitudinal-shear crack and griffith’s specific surface energy. *Journal of Geophysical Research*, 77(20):3796–3805, 1972.
- S Ide. 4.09-slip inversion. *Treatise on geophysics, 2nd edn. Elsevier, Oxford*, pages 215–241, 2015.
- Satoshi Ide and Minoru Takeo. Determination of constitutive relations of fault slip based on seismic wave analysis. *Journal of Geophysical Research: Solid Earth*, 102(B12):27379–27391, 1997.
- Toshihiro Igarashi, Toru Matsuzawa, and Akira Hasegawa. Repeating earthquakes and interplate aseismic slip in the northeastern japan subduction zone. *Journal of Geophysical Research: Solid Earth*, 108(B5), 2003.

BIBLIOGRAPHY

- Institut de Physique du Globe de Paris and Ecole et Observatoire des Sciences de la Terre de Strasbourg (EOST). Geoscope - french global network of broadband seismic stations., 1982.
- Yoshihiro Ito, Kazushige Obara, Katsuhiko Shiomi, Shutaro Sekine, and Hitoshi Hirose. Slow earthquakes coincident with episodic tremors and slow slip events. *Science*, 315(5811):503–506, 2007.
- Yoshihiro Ito, Ryota Hino, Motoyuki Kido, Hiromi Fujimoto, Yukihiro Osada, Daisuke Inazu, Yusaku Ohta, Takeshi Iinuma, Mako Ohzono, Satoshi Miura, et al. Episodic slow slip events in the japan subduction zone before the 2011 tohoku-oki earthquake. *Tectonophysics*, 600:14–26, 2013.
- Wilfred D Iwan, Michael A Moser, and Chia-Yen Peng. Some observations on strong-motion earthquake measurement using a digital accelerograph. *Bulletin of the Seismological Society of America*, 75(5):1225–1246, 1985.
- David D Jackson and Mitsuhiro Matsu'Ura. A bayesian approach to nonlinear inversion. *Journal of Geophysical Research: Solid Earth*, 90(B1):581–591, 1985.
- Steven C Jaumé and Lynn R Sykes. Evolving towards a critical point: A review of accelerating seismic moment/energy release prior to large and great earthquakes. *Seismicity patterns, their statistical significance and physical meaning*, pages 279–305, 1999.
- Edwin T Jaynes. *Probability theory: The logic of science*. Cambridge university press, 2003.
- Junle Jiang and Mark Simons. Probabilistic imaging of tsunamigenic seafloor deformation during the 2011 tohoku-oki earthquake. *Journal of Geophysical Research: Solid Earth*, 121(12):9050–9076, 2016.
- R Jolivet, M Simons, PS Agram, Z Duputel, and Z-K Shen. Aseismic slip and seismogenic coupling along the central san andreas fault. *Geophysical Research Letters*, 42(2):297–306, 2015.
- Romain Jolivet. *Déformation intersismique le long de la faille de Haiyuan, Chine: variations spatio-temporelles contraintes par interférométrie SAR*. PhD thesis, Université de Grenoble, 2011.
- Romain Jolivet and Mark Simons. A multipixel time series analysis method accounting for ground motion, atmospheric noise, and orbital errors. *Geophysical Research Letters*, 45(4):1814–1824, 2018.

BIBLIOGRAPHY

- Romain Jolivet, Cécile Lasserre, M-P Doin, Stéphane Guillaso, Gilles Peltzer, R Dailu, Jimin Sun, Z-K Shen, and X Xu. Shallow creep on the haiyuan fault (gansu, china) revealed by sar interferometry. *Journal of Geophysical Research: Solid Earth*, 117(B6), 2012.
- Romain Jolivet, M Simons, Z Duputel, J-A Olive, HS Bhat, and Quentin Bletery. Interseismic loading of subduction megathrust drives long-term uplift in northern chile. *Geophysical Research Letters*, 47(8):e2019GL085377, 2020.
- Lucile Jones and Peter Molnar. Frequency of foreshocks. *Nature*, 262(5570):677–679, 1976.
- Sigurjón Jónsson, Howard Zebker, Paul Segall, and Falk Amelung. Fault slip distribution of the 1999 m w 7.1 hector mine, california, earthquake, estimated from satellite radar and gps measurements. *Bulletin of the Seismological Society of America*, 92(4):1377–1389, 2002.
- ML u Jost and RB Herrmann. A student’s guide to and review of moment tensors. *Seismological Research Letters*, 60(2):37–57, 1989.
- Ya Ya Kagan and Leon Knopoff. Stochastic synthesis of earthquake catalogs. *Journal of Geophysical Research: Solid Earth*, 86(B4):2853–2862, 1981.
- Yan Y Kagan and L Knopoff. Statistical short-term earthquake prediction. *Science*, 236(4808):1563–1567, 1987.
- Kinjiro Kajiura. 20. tsunami energy in relation to parameters of the earthquake fault model. *Bulletin of the Earthquake Research Institute*, 56, 1981.
- Hiroo Kanamori. Mechanism of tsunami earthquakes. *Physics of the earth and planetary interiors*, 6(5):346–359, 1972.
- Hiroo Kanamori. Seismic and aseismic slip along subduction zones and their tectonic implications. *Island Arcs, Deep Sea Trenches and Back-Arc Basins*, 1:163–174, 1977.
- Hiroo Kanamori. W phase. *Geophysical research letters*, 20(16):1691–1694, 1993.
- Hiroo Kanamori and Luis Rivera. Energy partitioning during an earthquake. *Earthquakes: Radiated Energy and the Physics of Faulting*, 2006.
- Hiroo Kanamori and Luis Rivera. Source inversion of wphase: speeding up seismic tsunami warning. *Geophysical Journal International*, 175(1):222–238, 2008.

BIBLIOGRAPHY

- Y Kaneko and J-P Ampuero. A mechanism for preseismic steady rupture fronts observed in laboratory experiments. *Geophysical Research Letters*, 38(21), 2011.
- Yoshihiro Kaneko, Jean-Philippe Avouac, and Nadia Lapusta. Towards inferring earthquake patterns from geodetic observations of interseismic coupling. *Nature Geoscience*, 3(5):363–369, 2010.
- Yoshihiro Kaneko, Stefan B Nielsen, and Brett M Carpenter. The onset of laboratory earthquakes explained by nucleating rupture on a rate-and-state fault. *Journal of Geophysical Research: Solid Earth*, 121(8):6071–6091, 2016.
- Aitaro Kato and Shigeki Nakagawa. Multiple slow-slip events during a foreshock sequence of the 2014 iquique, chile mw 8.1 earthquake. *Geophysical Research Letters*, 41(15):5420–5427, 2014.
- Aitaro Kato, Kazushige Obara, Toshihiro Igarashi, Hiroshi Tsuruoka, Shigeki Nakagawa, and Naoshi Hirata. Propagation of slow slip leading up to the 2011 mw 9.0 tohoku-oki earthquake. *Science*, 335(6069):705–708, 2012.
- Aitaro Kato, Jun’ichi Fukuda, Takao Kumazawa, and Shigeki Nakagawa. Accelerated nucleation of the 2014 iquique, chile mw 8.2 earthquake. *Scientific reports*, 6:24792, 2016.
- Naoyuki Kato. How frictional properties lead to either rupture-front focusing or crack-like behavior. *Bulletin of the Seismological Society of America*, 97(6):2182–2189, 2007.
- Motoki Kazama and Toshihiro Noda. Damage statistics (summary of the 2011 off the pacific coast of tohoku earthquake damage). *Soils and Foundations*, 52(5):780–792, 2012.
- Masayuki Kikuchi and Hiroo Kanamori. Inversion of complex body waves—iii. *Bulletin of the Seismological Society of America*, 81(6):2335–2350, 1991.
- Scott Kirkpatrick, C Daniel Gelatt Jr, and Mario P Vecchi. Optimization by simulated annealing. *science*, 220(4598):671–680, 1983.
- Emilie Klein, Christophe Vigny, Luce Fleitout, Raphael Grandin, Romain Jolivet, Efrain Rivera, and Marianne Métois. A comprehensive analysis of the illapel 2015 mw8. 3 earthquake from gps and insar data. *Earth and Planetary Science Letters*, 469:123–134, 2017.
- Levshina Knopoff, T Levshina, VI Keilis-Borok, and C Mattoni. Increased long-range intermediate-magnitude earthquake activity prior to strong earthquakes in

BIBLIOGRAPHY

- california. *Journal of Geophysical Research: Solid Earth*, 101(B3):5779–5796, 1996.
- Valère Lambert and Nadia Lapusta. Rupture-dependent breakdown energy in fault models with thermo-hydro-mechanical processes. *Solid Earth*, 11(6):2283–2302, 2020.
- Nadia Lapusta and Yi Liu. Three-dimensional boundary integral modeling of spontaneous earthquake sequences and aseismic slip. *Journal of Geophysical Research: Solid Earth*, 114(B9), 2009.
- Nadia Lapusta and James R Rice. Nucleation and early seismic propagation of small and large events in a crustal earthquake model. *Journal of Geophysical Research: Solid Earth*, 108(B4), 2003.
- S Latour, A Schubnel, S Nielsen, R Madariaga, and S Vinciguerra. Characterization of nucleation during laboratory earthquakes. *Geophysical Research Letters*, 40(19):5064–5069, 2013.
- Thorne Lay. The surge of great earthquakes from 2004 to 2014. *Earth and Planetary Science Letters*, 409:133–146, 2015.
- Thorne Lay and Hiroo Kanamori. An asperity model of large earthquake sequences. *Earthquake prediction: an international review*, 1981.
- Thorne Lay, Hiroo Kanamori, and Larry Ruff. *The asperity model and the nature of large subduction zone earthquakes*. na, 1982.
- Thorne Lay, Hiroo Kanamori, Charles J Ammon, Meredith Nettles, Steven N Ward, Richard C Aster, Susan L Beck, Susan L Bilek, Michael R Brudzinski, Rhett Butler, et al. The great sumatra-andaman earthquake of 26 december 2004. *Science*, 308(5725):1127–1133, 2005.
- Thorne Lay, Han Yue, Emily E Brodsky, and Chao An. The 1 april 2014 iquique, chile, mw 8.1 earthquake rupture sequence. *Geophysical Research Letters*, 41(11):3818–3825, 2014.
- Thorne Lay, Linyan Li, and Kwok Fai Cheung. Modeling tsunami observations to evaluate a proposed late tsunami earthquake stage for the 16 september 2015 illapel, chile, mw 8.3 earthquake. *Geophysical Research Letters*, 43(15):7902–7912, 2016.
- Xavier Le Pichon. Sea-floor spreading and continental drift. *Journal of Geophysical Research*, 73(12):3661–3697, 1968.

BIBLIOGRAPHY

- Shiann-Jong Lee, Te-Yang Yeh, Tzu-Chi Lin, Yen-Yu Lin, Teh-Ru Alex Song, and Bor-Shouh Huang. Two-stage composite megathrust rupture of the 2015 mw8.4 Illapel, Chile, earthquake identified by spectral-element inversion of teleseismic waves. *Geophysical Research Letters*, 43(10):4979–4985, 2016.
- Linyan Li, Thorne Lay, Kwok Fai Cheung, and Lingling Ye. Joint modeling of teleseismic and tsunami wave observations to constrain the 16 September 2015 Illapel, Chile, mw 8.3 earthquake rupture process. *Geophysical Research Letters*, 43(9):4303–4312, 2016.
- Yu-nung Nina Lin, Anthony Sladen, Francisco Ortega-Culaciati, Mark Simons, Jean-Philippe Avouac, Eric J Fielding, Benjamin A Brooks, Michael Bevis, Jeff Genrich, Andreas Rietbrock, et al. Coseismic and postseismic slip associated with the 2010 Maule earthquake, Chile: Characterizing the Arauco Peninsula barrier effect. *Journal of Geophysical Research: Solid Earth*, 118(6):3142–3159, 2013.
- Eric O Lindsey, Rishav Mallick, Judith A Hubbard, Kyle E Bradley, Rafael V Almeida, James DP Moore, Roland Bürgmann, and Emma M Hill. Slip rate deficit and earthquake potential on shallow megathrusts. *Nature Geoscience*, 14(5):321–326, 2021.
- Philip L-F Liu, Yong-Sik Cho, SB Yoon, and SN Seo. Numerical simulations of the 1960 Chilean tsunami propagation and inundation at Hilo, Hawaii. In *Tsunami: Progress in prediction, disaster prevention and warning*, pages 99–115. Springer, 1995.
- Rowena B Lohman and Mark Simons. Some thoughts on the use of InSAR data to constrain models of surface deformation: Noise structure and data downsampling. *Geochemistry, Geophysics, Geosystems*, 6(1), 2005.
- Cinna Lomnitz. Major earthquakes of Chile: a historical survey, 1535-1960. *Seismological Research Letters*, 75(3):368–378, 2004.
- Raul Madariaga. High frequency radiation from dynamic earthquake. *Ann. Geophys.*, 1:17, 1983.
- Raul Madariaga and Sergio Ruiz. Earthquake dynamics on circular faults: A review 1970–2015. *Journal of Seismology*, 20(4):1235–1252, 2016.
- P Martin Mai and Gregory C Beroza. Source scaling properties from finite-fault-rupture models. *Bulletin of the Seismological Society of America*, 90(3):604–615, 2000.

BIBLIOGRAPHY

- P Martin Mai, Danijel Schorlemmer, Morgan Page, Jean-Paul Ampuero, Kimiyuki Asano, Mathieu Causse, Susana Custodio, Wenyan Fan, Gaetano Festa, Martin Galis, et al. The earthquake-source inversion validation (siv) project. *Seismological Research Letters*, 87(3):690–708, 2016.
- Isabelle Manighetti, Michel Campillo, C Sammis, PM Mai, and G King. Evidence for self-similar, triangular slip distributions on earthquakes: Implications for earthquake and fault mechanics. *Journal of Geophysical Research: Solid Earth*, 110 (B5), 2005.
- Lou Marill, David Marsan, Anne Socquet, Mathilde Radiguet, Nathalie Cotte, and Baptiste Rousset. Fourteen-year acceleration along the japan trench. *Journal of Geophysical Research: Solid Earth*, 126(11):e2020JB021226, 2021.
- Chris Marone. Laboratory-derived friction laws and their application to seismic faulting. *Annual Review of Earth and Planetary Sciences*, 26(1):643–696, 1998.
- D Marsan and B Enescu. Modeling the foreshock sequence prior to the 2011, mw9.0 tohoku, japan, earthquake. *Journal of Geophysical Research: Solid Earth*, 117 (B6), 2012.
- Warner Marzocchi and Jiancang Zhuang. Statistics between mainshocks and foreshocks in italy and southern california. *Geophysical Research Letters*, 38(9), 2011.
- Didier Massonnet, Marc Rossi, César Carmona, Frédéric Adragna, Gilles Peltzer, Kurt Feigl, and Thierry Rabaute. The displacement field of the landers earthquake mapped by radar interferometry. *nature*, 364(6433):138–142, 1993.
- Mitsuhiro Matsu'ura, Akemi Noda, and Yukitoshi Fukahata. Geodetic data inversion based on bayesian formulation with direct and indirect prior information. *Geophysical Journal International*, 171(3):1342–1351, 2007.
- Andreas P Mavrommatis, Paul Segall, and Kaj M Johnson. A decadal-scale deformation transient prior to the 2011 mw 9.0 tohoku-oki earthquake. *Geophysical Research Letters*, 41(13):4486–4494, 2014.
- Andreas P Mavrommatis, Paul Segall, Naoki Uchida, and Kaj M Johnson. Long-term acceleration of aseismic slip preceding the mw 9 tohoku-oki earthquake: Constraints from repeating earthquakes. *Geophysical Research Letters*, 42(22): 9717–9725, 2015.

BIBLIOGRAPHY

- Jeffrey J McGuire, Margaret S Boettcher, and Thomas H Jordan. Foreshock sequences and short-term earthquake predictability on east pacific rise transform faults. *Nature*, 434(7032):457–461, 2005.
- Dan P McKenzie and Robert L Parker. The north pacific: an example of tectonics on a sphere. *Nature*, 216(5122):1276–1280, 1967.
- Gregory C McLaskey. Earthquake initiation from laboratory observations and implications for foreshocks. *Journal of Geophysical Research: Solid Earth*, 124(12):12882–12904, 2019.
- Gregory C McLaskey and Brian D Kilgore. Foreshocks during the nucleation of stick-slip instability. *Journal of Geophysical Research: Solid Earth*, 118(6):2982–2997, 2013.
- M-A Meier, JP Ampuero, and Thomas H Heaton. The hidden simplicity of subduction megathrust earthquakes. *Science*, 357(6357):1277–1281, 2017.
- Christian Meinig, Scott E Stalin, Alex I Nakamura, and Hugh B Milburn. Real-time deep-ocean tsunami measuring, monitoring, and reporting system: The noaa dart ii description and disclosure. *NOAA, Pacific Marine Environmental Laboratory (PMEL)*, pages 1–15, 2005.
- Diego Melgar, Brendan W Crowell, Jianghui Geng, Richard M Allen, Yehuda Bock, Sebastian Riquelme, Emma M Hill, Marino Protti, and Athanassios Ganas. Earthquake magnitude calculation without saturation from the scaling of peak ground displacement. *Geophysical Research Letters*, 42(13):5197–5205, 2015.
- Diego Melgar, Richard M Allen, Sebastian Riquelme, Jianghui Geng, Francisco Bravo, Juan Carlos Baez, Hector Parra, Sergio Barrientos, Peng Fang, Yehuda Bock, et al. Local tsunami warnings: Perspectives from recent large events. *Geophysical Research Letters*, 43(3):1109–1117, 2016a.
- Diego Melgar, Wenyan Fan, Sebastian Riquelme, Jianghui Geng, Cunren Liang, Mauricio Fuentes, Gabriel Vargas, Richard M Allen, Peter M Shearer, and Eric J Fielding. Slip segmentation and slow rupture to the trench during the 2015, mw8.3 illapel, chile earthquake. *Geophysical Research Letters*, 43(3):961–966, 2016b.
- Lingsen Meng, Hui Huang, Roland Bürgmann, Jean Paul Ampuero, and Anne Strader. Dual megathrust slip behaviors of the 2014 iquique earthquake sequence. *Earth and Planetary Science Letters*, 411:177–187, 2015.

BIBLIOGRAPHY

- Lingsen Meng, Han Bao, Hui Huang, Ailin Zhang, Andrew Bloore, and Zhipeng Liu. Double pincer movement: Encircling rupture splitting during the 2015 mw 8.3 illapel earthquake. *Earth and Planetary Science Letters*, 495:164–173, 2018.
- William Menke. *Geophysical data analysis: discrete inverse theory: MATLAB edition*, volume 45. Academic press, 2012.
- Marianne Metois, C Vigny, and A Socquet. Interseismic coupling, megathrust earthquakes and seismic swarms along the chilean subduction zone (38–18 s). *Pure and Applied Geophysics*, 173(5):1431–1449, 2016.
- Nicholas Metropolis, Arianna W Rosenbluth, Marshall N Rosenbluth, Augusta H Teller, and Edward Teller. Equation of state calculations by fast computing machines. *The journal of chemical physics*, 21(6):1087–1092, 1953.
- Sean P Meyn and Richard L Tweedie. *Markov chains and stochastic stability*. Springer Science & Business Media, 2012.
- Arnaud Mignan. The debate on the prognostic value of earthquake foreshocks: A meta-analysis. *Scientific reports*, 4(1):1–5, 2014.
- Sarah Minson. *A Bayesian approach to earthquake source studies*. California Institute of Technology, 2010.
- SE Minson, M Simons, and JL Beck. Bayesian inversion for finite fault earthquake source models i—theory and algorithm. *Geophysical Journal International*, 194(3):1701–1726, 2013.
- Shin’ichi Miyazaki, Jeffery J McGuire, and Paul Segall. Seismic and aseismic fault slip before and during the 2011 off the pacific coast of tohoku earthquake. *Earth, planets and space*, 63(7):637–642, 2011.
- Catalina Morales-Yañez, Zacharie Duputel, and Luis Rivera. Impact of 3d earth structure on w-phase cmt parameters. *Geophysical Journal International*, 2020.
- Marcelo Spegiorin Moreno, John Bolte, Juergen Klotz, and Daniel Melnick. Impact of megathrust geometry on inversion of coseismic slip from geodetic data: Application to the 1960 chile earthquake. *Geophysical Research Letters*, 36(16), 2009.
- Luc Moutote, David Marsan, Olivier Lengliné, and Zacharie Duputel. Rare occurrences of non-cascading foreshock activity in southern california. *Geophysical research letters*, 48(7):e2020GL091757, 2021.

BIBLIOGRAPHY

- George Mungov, Marie Eblé, and Richard Bouchard. Dart® tsunameter retrospective and real-time data: A reflection on 10 years of processing in support of tsunami research and operations. *Pure and Applied Geophysics*, 170(9):1369–1384, 2013.
- Robert M Nadeau, W Foxall, and TV McEvilly. Clustering and periodic recurrence of microearthquakes on the san andreas fault at parkfield, california. *Science*, 267(5197):503–507, 1995.
- J. M. Nocquet, J. C. Villegas-Lanza, M. Chlieh, P. A. Mothes, F. Rolandone, P. Jarrin, D. Cisneros, A. Alvarado, L. Audin, F. Bondoux, X. Martin, Y. Font, M. Régnier, M. Vallée, T. Tran, C. Beauval, J. M. Maguiña Mendoza, W. Martinez, H. Tavera, and H. Yepes. Motion of continental slivers and creeping subduction in the northern Andes. *Nature Geoscience*, 7(4):287–291, 2014. ISSN 17520908. doi: 10.1038/ngeo2099.
- Jean-Mathieu Nocquet. Pyacs: a set of python tools for gps analysis and tectonic modelling. In *Colloque G2*, 2017.
- Hiroyuki Noda, Masao Nakatani, and Takane Hori. Large nucleation before large earthquakes is sometimes skipped due to cascade-up—implications from a rate and state simulation of faults with hierarchical asperities. *Journal of Geophysical Research: Solid Earth*, 118(6):2924–2952, 2013.
- Kazushige Obara. Nonvolcanic deep tremor associated with subduction in southwest japan. *Science*, 296(5573):1679–1681, 2002.
- Kazushige Obara and Aitaro Kato. Connecting slow earthquakes to huge earthquakes. *Science*, 353(6296):253–257, 2016.
- Yoshihiko Ogata. Statistical models for earthquake occurrences and residual analysis for point processes. *Journal of the American Statistical association*, 83(401):9–27, 1988.
- Mitiyasu Ohnaka. Earthquake source nucleation: a physical model for short-term precursors. *Tectonophysics*, 211(1-4):149–178, 1992.
- Mitiyasu Ohnaka. A physical scaling relation between the size of an earthquake and its nucleation zone size. *pure and applied geophysics*, 157(11-12):2259–2282, 2000.
- Mitiyasu Ohnaka and Lin-feng Shen. Scaling of the shear rupture process from nucleation to dynamic propagation: Implications of geometric irregularity of the

- rupturing surfaces. *Journal of Geophysical Research: Solid Earth*, 104(B1):817–844, 1999.
- Yusaku Ohta, Tatsuya Kobayashi, Hiroaki Tsushima, Satoshi Miura, Ryota Hino, Tomoji Takasu, Hiromi Fujimoto, Takeshi Iinuma, Kenji Tachibana, Tomotsugu Demachi, et al. Quasi real-time fault model estimation for near-field tsunami forecasting based on rtk-gps analysis: Application to the 2011 tohoku-oki earthquake (mw 9.0). *Journal of Geophysical Research: Solid Earth*, 117(B2), 2012.
- Yoshimitsu Okada. Surface deformation due to shear and tensile faults in a half-space. *Bulletin of the seismological society of America*, 75(4):1135–1154, 1985.
- Ryo Okuwaki, Yuji Yagi, Rafael Aránguiz, Juan González, and Gabriel González. Rupture process during the 2015 illapel, chile earthquake: Zigzag-along-dip rupture episodes. *Pure and Applied Geophysics*, 173(4):1011–1020, 2016.
- Allen H Olson and Randy J Apsel. Finite faults and inverse theory with applications to the 1979 imperial valley earthquake. *Bulletin of the Seismological Society of America*, 72(6A):1969–2001, 1982.
- Shinzaburo Ozawa, Takuya Nishimura, Hiroshi Munekane, Hisashi Suito, Tomokazu Kobayashi, Mikio Tobita, and Tetsuro Imakiire. Preceding, coseismic, and post-seismic slips of the 2011 tohoku earthquake, japan. *Journal of Geophysical Research: Solid Earth*, 117(B7), 2012.
- Federica Paglialunga, François X Passelègue, Nicolas Brantut, Fabian Barras, Mathias Lebihain, and Marie Violay. On the scale dependence in the dynamics of frictional rupture: Constant fracture energy versus size-dependent breakdown work. *Earth and Planetary Science Letters*, 584:117442, 2022.
- H Perfettini and J-P Avouac. Postseismic relaxation driven by brittle creep: A possible mechanism to reconcile geodetic measurements and the decay rate of aftershocks, application to the chi-chi earthquake, taiwan. *Journal of Geophysical Research: Solid Earth*, 109(B2), 2004.
- Hugo Perfettini, Jean-Philippe Avouac, Hernando Tavera, Andrew Kositsky, Jean-Mathieu Nocquet, Francis Bondoux, Mohamed Chlieh, Anthony Sladen, Laurence Audin, Daniel L Farber, et al. Seismic and aseismic slip on the central peru megathrust. *Nature*, 465(7294):78–81, 2010.
- Alessio Piatanesi, Elisa Tinti, Massimo Cocco, and Eiichi Fukuyama. The dependence of traction evolution on the earthquake source time function adopted in kinematic rupture models. *Geophysical research letters*, 31(4), 2004.

BIBLIOGRAPHY

- Diego A Piñón, Demián D Gómez, Robert Smalley Jr, Sergio R Cimbaro, Eduardo A Lauría, and Michael G Bevis. The history, state, and future of the argentine continuous satellite monitoring network and its contributions to geodesy in latin america. *Seismological Research Letters*, 89(2A):475–482, 2018.
- Mathilde Radiguet, Fabrice Cotton, Mathilde Vergnolle, Michel Campillo, Bernard Valette, Vladimir Kostoglodov, and Nathalie Cotte. Spatial and temporal evolution of a long term slow slip event: the 2006 guerrero slow slip event. *Geophysical Journal International*, 184(2):816–828, 2011.
- Théa Ragon, Anthony Sladen, and Mark Simons. Accounting for uncertain fault geometry in earthquake source inversions–i: theory and simplified application. *Geophysical Journal International*, 214(2):1174–1190, 2018.
- Hoby NT Razafindrakoto and P Martin Mai. Uncertainty in earthquake source imaging due to variations in source time function and earth structure. *Bulletin of the Seismological Society of America*, 104(2):855–874, 2014.
- Paul A Reasenber. Foreshock occurrence before large earthquakes. *Journal of Geophysical Research: Solid Earth*, 104(B3):4755–4768, 1999.
- E von Rebeur-Paschwitz. Horizontalpendel-beobachtungen auf der kaiserlichen universitäts-sterne-warte zu strassburg 1892–1894. *Beiträge zur Geophysik*, 2: 211–536, 1895.
- Harry Fielding Reid. The california earthquake of april 18, 1906. *Report of the state earthquake investigation commission*, 2:16–18, 1910.
- James R Rice and Yehuda Ben-Zion. Slip complexity in earthquake fault models. *Proceedings of the National Academy of Sciences*, 93(9):3811–3818, 1996.
- James R Rice, Charles G Sammis, and Robert Parsons. Off-fault secondary failure induced by a dynamic slip pulse. *Bulletin of the Seismological Society of America*, 95(1):109–134, 2005.
- Paul A Rosen, Eric Gurrola, Gian Franco Sacco, and Howard Zebker. The insar scientific computing environment. In *EUSAR 2012; 9th European conference on synthetic aperture radar*, pages 730–733. VDE, 2012.
- Zachary E Ross, Daniel T Trugman, Egill Hauksson, and Peter M Shearer. Searching for hidden earthquakes in southern california. *Science*, 364(6442):767–771, 2019.

BIBLIOGRAPHY

- Baptiste Rousset, Romain Jolivet, Mark Simons, Cécile Lasserre, Bryan Riel, Pietro Milillo, Ziyadin Çakir, and François Renard. An aseismic slip transient on the north anatolian fault. *Geophysical Research Letters*, 43(7):3254–3262, 2016.
- Allan Mattathias Rubin and J-P Ampuero. Earthquake nucleation on (aging) rate and state faults. *Journal of Geophysical Research: Solid Earth*, 110(B11), 2005.
- Javier A Ruiz, Eduardo Contreras-Reyes, Francisco Ortega-Culaciati, and Paula Manríquez. Rupture process of the april 24, 2017, mw 6.9 valparaíso earthquake from the joint inversion of teleseismic body waves and near-field data. *Physics of the Earth and Planetary Interiors*, 279:1–14, 2018.
- S Ruiz and R Madariaga. Historical and recent large megathrust earthquakes in chile. *Tectonophysics*, 733:37–56, 2018.
- Sergio Ruiz, M Metois, A Fuenzalida, J Ruiz, F Leyton, R Grandin, C Vigny, R Madariaga, and J Campos. Intense foreshocks and a slow slip event preceded the 2014 iquique mw 8.1 earthquake. *Science*, 345(6201):1165–1169, 2014.
- Sergio Ruiz, Emilie Klein, Francisco del Campo, Efrain Rivera, Piero Poli, Marianne Metois, Vigny Christophe, Juan Carlos Baez, Gabriel Vargas, Felipe Leyton, et al. The seismic sequence of the 16 september 2015 m w 8.3 illapel, chile, earthquake. *Seismological Research Letters*, 87(4):789–799, 2016.
- Sergio Ruiz, F Aden-Antoniow, JC Baez, C Otarola, B Potin, F del Campo, P Poli, C Flores, C Satriano, F Leyton, R Madariaga, and Bernard P. Nucleation phase and dynamic inversion of the mw 6.9 valparaíso 2017 earthquake in central chile. *Geophysical Research Letters*, 44(20):10–290, 2017.
- Malcolm Sambridge. Geophysical inversion with a neighbourhood algorithm—ii. appraising the ensemble. *Geophysical Journal International*, 138(3):727–746, 1999.
- Malcolm Sambridge and Klaus Mosegaard. Monte carlo methods in geophysical inverse problems. *Reviews of Geophysics*, 40(3):3–1, 2002.
- Kenji Satake. Inversion of tsunami waveforms for the estimation of heterogeneous fault motion of large submarine earthquakes: The 1968 tokachi-oki and 1983 japan sea earthquakes. *Journal of Geophysical Research: Solid Earth*, 94(B5): 5627–5636, 1989.
- Kenji Satake and Mohammad Heidarzadeh. A review of source models of the 2015 illapel, chile earthquake and insights from tsunami data. *Pure and Applied Geophysics*, 174(1):1–9, 2017.

BIBLIOGRAPHY

- CH Scholz. Mechanism of creep in brittle rock. *Journal of Geophysical Research*, 73(10):3295–3302, 1968.
- CH Scholz, Max Wyss, and SW Smith. Seismic and aseismic slip on the san andreas fault. *Journal of geophysical research*, 74(8):2049–2069, 1969.
- Christopher H Scholz. Earthquakes and friction laws. *Nature*, 391(6662):37–42, 1998.
- Bernd Schurr, Günter Asch, Sebastian Hainzl, Jonathan Bedford, Andreas Hoechner, Mauro Palo, Rongjiang Wang, Marcos Moreno, Mitja Bartsch, Yong Zhang, et al. Gradual unlocking of plate boundary controlled initiation of the 2014 iquique earthquake. *Nature*, 512(7514):299–302, 2014.
- Paul Segall and Ruth Harris. Earthquake deformation cycle on the san andreas fault near parkfield, california. *Journal of Geophysical Research: Solid Earth*, 92(B10):10511–10525, 1987.
- Haruko Sekiguchi and Tomotaka Iwata. Rupture process of the 1999 kocaeli, turkey, earthquake estimated from strong-motion waveforms. *Bulletin of the Seismological Society of America*, 92(1):300–311, 2002.
- Peter M Shearer. *Introduction to seismology*. Cambridge university press, 2019.
- David R Shelly, Gregory C Beroza, Satoshi Ide, and Sho Nakamura. Low-frequency earthquakes in shikoku, japan, and their relationship to episodic tremor and slip. *Nature*, 442(7099):188–191, 2006.
- David R Shelly, Gregory C Beroza, and Satoshi Ide. Non-volcanic tremor and low-frequency earthquake swarms. *Nature*, 446(7133):305–307, 2007.
- Kunihiko Shimazaki and Takashi Nakata. Time-predictable recurrence model for large earthquakes. *Geophysical Research Letters*, 7(4):279–282, 1980.
- Paul G Silver and Thomas H Jordan. Optimal estimation of scalar seismic moment. *Geophysical Journal International*, 70(3):755–787, 1982.
- Mark Simons and P A Rosen. 3.12 - Interferometric Synthetic Aperture Radar Geodesy. In *Treatise on Geophysics*. Elsevier, Amsterdam, 2007. URL http://www.gps.caltech.edu/~simons/pdfs/Simons_2007.pdf.
- S Krishna Singh, E a Mena, and Raul Castro. Some aspects of source characteristics of the 19 september 1985 michoacan earthquake and ground motion amplification in and near mexico city from strong motion data. *Bulletin of the Seismological society of America*, 78(2):451–477, 1988.

BIBLIOGRAPHY

- Anne Socquet, Jesus Piña Valdes, Jorge Jara, Fabrice Cotton, Andrea Walpersdorf, Nathalie Cotte, Sebastian Specht, Francisco Ortega-Culaciati, Daniel Carrizo, and Edmundo Norabuena. An 8 month slow slip event triggers progressive nucleation of the 2014 chile megathrust. *Geophysical Research Letters*, 44(9): 4046–4053, 2017.
- Seth Stein and Michael Wysession. *An introduction to seismology, earthquakes, and earth structure*. John Wiley & Sons, 2009.
- JA Steketee. On volterra’s dislocations in a semi-infinite elastic medium. *Canadian Journal of Physics*, 36(2):192–205, 1958.
- Fleur O Strasser, MC Arango, and Julian J Bommer. Scaling of the source dimensions of interface and intraslab subduction-zone earthquakes with moment magnitude. *Seismological Research Letters*, 81(6):941–950, 2010.
- Josué Tago, Víctor M Cruz-Atienza, Carlos Villafuerte, Takuya Nishimura, Vladimir Kostoglodov, Jorge Real, and Yoshihiro Ito. Adjoint slip inversion under a constrained optimization framework: revisiting the 2006 guerrero slow slip event. *Geophysical Journal International*, 226(2):1187–1205, 2021.
- Carl Tape, Michael West, Vipul Silwal, and Natalia Ruppert. Earthquake nucleation and triggering on an optimally oriented fault. *Earth and Planetary Science Letters*, 363:231–241, 2013.
- Albert Tarantola. *Inverse problem theory and methods for model parameter estimation*, volume 89. siam, 2005.
- Albert Tarantola and Bernard Valette. Inverse problems = quest for information. *Journal of geophysics*, 50(1):159–170, 1982.
- Andrei Nikolaevich Tikhonov. On the solution of ill-posed problems and the method of regularization. In *Doklady Akademii Nauk*, volume 151, pages 501–504. Russian Academy of Sciences, 1963.
- F Tilmann, Y Zhang, M Moreno, Joachim Saul, Felix Eckelmann, M Palo, Z Deng, A Babeyko, Kejie Chen, JC Baez, et al. The 2015 illapel earthquake, central chile: A type case for a characteristic earthquake? *Geophysical Research Letters*, 43(2):574–583, 2016.
- E Tinti, P Spudich, and M Cocco. Earthquake fracture energy inferred from kinematic rupture models on extended faults. *Journal of Geophysical Research: Solid Earth*, 110(B12), 2005a.

BIBLIOGRAPHY

- Elisa Tinti, Eiichi Fukuyama, Alessio Piatanesi, and Massimo Cocco. A kinematic source-time function compatible with earthquake dynamics. *Bulletin of the Seismological Society of America*, 95(4):1211–1223, 2005b.
- Elisa Tinti, Massimo Cocco, Eiichi Fukuyama, and Alessio Piatanesi. Dependence of slip weakening distance (d_c) on final slip during dynamic rupture of earthquakes. *Geophysical Journal International*, 177(3):1205–1220, 2009.
- MD Trifunac. A three-dimensional dislocation model for the san fernando, california, earthquake of february 9, 1971. *Bulletin of the Seismological Society of America*, 64(1):149–172, 1974.
- Jeroen Tromp, Carl Tape, and Qinya Liu. Seismic tomography, adjoint methods, time reversal and banana-doughnut kernels. *Geophysical Journal International*, 160(1):195–216, 2005.
- Daniel T Trugman and Zachary E Ross. Pervasive foreshock activity across southern california. *Geophysical Research Letters*, 46(15):8772–8781, 2019.
- Victor C Tsai, Gavin P Hayes, and Zacharie Duputel. Constraints on the long-period moment-dip tradeoff for the tohoku earthquake. *Geophysical Research Letters*, 38(7), 2011.
- Cedric Twardzik, Mathilde Vergnolle, Anthony Sladen, and Louisa LH Tsang. Very early identification of a bimodal frictional behavior during the post-seismic phase of the 2015 m w 8.3 illapel, chile, earthquake. *Solid Earth Discussions*, pages 1–24, 2021.
- Naoki Uchida and Toru Matsuzawa. Pre-and postseismic slow slip surrounding the 2011 tohoku-oki earthquake rupture. *Earth and Planetary Science Letters*, 374: 81–91, 2013.
- Naoki Uchida, Takeshi Iinuma, Robert M Nadeau, Roland Bürgmann, and Ryota Hino. Periodic slow slip triggers megathrust zone earthquakes in northeastern japan. *Science*, 351(6272):488–492, 2016.
- Universidad de Chile. Red sismologica nacional. international federation of digital seismograph networks., 2012.
- Mehmet Utku. Resolving a complex seismic moment tensor into a series of simple double couple sources: A case of turkey. *International Journal of Physical Sciences*, 6(10):2550–2564, 2011.

BIBLIOGRAPHY

- Tokuji Utsu. Magnitudes of earthquakes and occurrence of their aftershocks. *Zisin, Ser. 2*, 10:35–45, 1957.
- Tokuji Utsu, Yoshihiko Ogata, et al. The centenary of the omori formula for a decay law of aftershock activity. *Journal of Physics of the Earth*, 43(1):1–33, 1995.
- Martin Vallée, Jean Charléty, Ana MG Ferreira, Bertrand Delouis, and Julien Vergoz. Scardec: a new technique for the rapid determination of seismic moment magnitude, focal mechanism and source time functions for large earthquakes using body-wave deconvolution. *Geophysical Journal International*, 184(1):338–358, 2011.
- Martijn PA van den Ende and J-P Ampuero. On the statistical significance of foreshock sequences in southern california. *Geophysical Research Letters*, 47(3): e2019GL086224, 2020.
- Anupama Venkataraman and Hiroo Kanamori. Observational constraints on the fracture energy of subduction zone earthquakes. *Journal of Geophysical Research: Solid Earth*, 109(B5), 2004.
- Robert C Viesca and Dmitry I Garagash. Ubiquitous weakening of faults due to thermal pressurization. *Nature Geoscience*, 8(11):875–879, 2015.
- Christophe Vigny, Alain Rudloff, Jean-Claude Ruegg, Raul Madariaga, Jaime Campos, and Manuel Alvarez. Upper plate deformation measured by gps in the coquimbo gap, chile. *Physics of the Earth and Planetary Interiors*, 175(1-2):86–95, 2009.
- John Von Neumann. 13. various techniques used in connection with random digits. *Appl. Math Ser*, 12(36-38):3, 1951.
- David J Wald and Robert W Graves. Resolution analysis of finite fault source inversion using one-and three-dimensional green’s functions: 2. combining seismic and geodetic data. *Journal of Geophysical Research: Solid Earth*, 106(B5):8767–8788, 2001.
- Rongjiang Wang, Bernd Schurr, Claus Milkereit, Zhigang Shao, and Mingpei Jin. An improved automatic scheme for empirical baseline correction of digital strong-motion records. *Bulletin of the Seismological Society of America*, 101(5):2029–2044, 2011.
- Shingo Watada. Tsunami speed variations in density-stratified compressible global oceans. *Geophysical Research Letters*, 40(15):4001–4006, 2013.

BIBLIOGRAPHY

- Charles A Williams and Laura M Wallace. Effects of material property variations on slip estimates for subduction interface slow-slip events. *Geophysical Research Letters*, 42(4):1113–1121, 2015.
- Yuji Yagi and Yukitoshi Fukahata. Introduction of uncertainty of green’s function into waveform inversion for seismic source processes. *Geophysical Journal International*, 186(2):711–720, 2011.
- Yuji Yagi and Masayuki Kikuchi. Source rupture process of the kocaeli, turkey, earthquake of august 17, 1999, obtained by joint inversion of near-field data and tele-seismic data. *Geophysical Research Letters*, 27(13):1969–1972, 2000.
- Lingling Ye, Thorne Lay, Hiroo Kanamori, and Luis Rivera. Rupture characteristics of major and great ($M_w \geq 7.0$) megathrust earthquakes from 1990 to 2015: 1. source parameter scaling relationships. *Journal of Geophysical Research: Solid Earth*, 121(2):826–844, 2016.
- Lingling Ye, Thorne Lay, Hiroo Kanamori, and Keith D Koper. Rapidly estimated seismic source parameters for the 16 september 2015 illapel, chile m w 8.3 earthquake. In *The Chile-2015 (Illapel) Earthquake and Tsunami*, pages 11–22. Springer, 2017.
- Jiuxun Yin, Hongfeng Yang, Huajian Yao, and Huihui Weng. Coseismic radiation and stress drop during the 2015 mw 8.3 illapel, chile megathrust earthquake. *Geophysical Research Letters*, 43(4):1520–1528, 2016.
- Yusuke Yokota and Kazuki Koketsu. A very long-term transient event preceding the 2011 tohoku earthquake. *Nature communications*, 6(1):1–5, 2015.
- Howard A Zebker, Paul A Rosen, Richard M Goldstein, Andrew Gabriel, and Charles L Werner. On the derivation of coseismic displacement fields using differential radar interferometry: The landers earthquake. *Journal of Geophysical Research: Solid Earth*, 99(B10):19617–19634, 1994.
- Xu Zhao, Zacharie Duputel, and Zhenxing Yao. Regional w-phase source inversion for moderate to large earthquakes in china and neighboring areas. *Journal of Geophysical Research: Solid Earth*, 122(12):10–052, 2017.
- Lupei Zhu and Luis A Rivera. A note on the dynamic and static displacements from a point source in multilayered media. *Geophysical Journal International*, 148(3): 619–627, 2002.

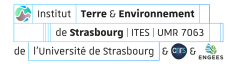
BIBLIOGRAPHY

Jiancang Zhuang, David S Harte, Maximilian J Werner, Sebastian Hainzl, and Shiyong Zhou. Basic models of seismicity: Temporal models. *Community Online Resource for Statistical Seismicity Analysis*, 2012. doi: <http://dx.doi.org/10.5078/corssa-79905851>.

Dimitri Zigone, Diane Rivet, Mathilde Radiguet, Michel Campillo, Christophe Voisin, Nathalie Cotte, Andrea Walpersdorf, Nikolai M Shapiro, Glenn Cougoulat, Philippe Roux, et al. Triggering of tremors and slow slip event in guerrero, mexico, by the 2010 mw 8.8 maule, chile, earthquake. *Journal of Geophysical Research: Solid Earth*, 117(B9), 2012.

Emmanuel CABALLERO LEYVA

Caractérisation bayésienne de la source sismique: De l'initiation du séisme à la rupture sismique



Résumé

L'objectif général de cette thèse est de mener une étude approfondie de la source, couvrant différents aspects de la caractérisation des séismes. Premièrement, je me suis focalisé sur la phase d'initiation des tremblements de terre. Spécifiquement, j'ai analysé la phase d'initiation du séisme de Valparaíso en 2017 (magnitude $M_w=6.9$). Ce séisme est un cas d'étude intéressant car il a été précédé par un déplacement transitoire accompagnée par de nombreux séismes pré-chocs. Nous montrons que ce séisme a vraisemblablement été précédé par un glissement asismique sur la faille. Dans une deuxième partie de ma thèse, je me suis intéressé à la caractérisation détaillée de la distribution de glissement co-sismique associée aux grands séismes. En particulier, j'examine le séisme d'Illapel en 2014 ($M_w=8.3$). La caractérisation cinématique de la source de ce séisme est donc effectuée via une approche d'échantillonnage bayésien qui s'est avérée utile pour caractériser l'incertitude a posteriori. Nos modèles cinématiques indiquent une forte complexité dans le processus de rupture, associé à des "encerclements d'aspérités" qui ont été précédemment suggérées par des études précédentes.

Mots-clés: Phase d'initiation, séisme de Valparaíso, séisme d'Illapel, inversion cinématique

Résumé en anglais

The general objective of this thesis is to conduct a thorough source study covering different aspects of earthquake characterization. First, I focused on the initiation phase of earthquakes. Specifically, I analyzed the initiation phase of the 2017 Valparaíso earthquake (magnitude $M_w=6.9$). This earthquake is an interesting case study because it was preceded by a transient displacement accompanied by many pre-shock earthquakes. We show that this earthquake was probably preceded by an aseismic slip on the fault. In a second part of my thesis, I am interested in the detailed characterization of the co-seismic slip distribution associated with large earthquakes. In particular, I examine the 2014 Illapel earthquake ($M_w=8.3$). The kinematic characterization of the source of this earthquake is therefore performed via a Bayesian sampling approach, which has proven useful in characterizing the a posteriori uncertainty. Our kinematic models indicate a high complexity in the rupture process, associated with "encircling asperities" that have been previously suggested by previous studies.

Keywords: Initiation phase, Valparaíso earthquake, Illapel earthquake, kinematic inversion